TIME-LAPSE V_P/V_S ANALYSIS FOR RESERVOIR CHARACTERIZATION, RULISON FIELD, COLORADO

by

Ramses G. Meza

A thesis submitted to the Faculty and the Board of Trustees of the Colorado School of Mines in partial fulfillment of the requirements for the degree of Master of Science (Geophysics).

Golden, Colorado

Date: April 7, 2008

Signed: ____________________

Ramses Gabriel Meza

Approved: ____________________

Dr. Thomas L. Davis

Thesis Advisor

____

Dr. Terence K. Young

Department Head

Geophysics

ABSTRACT

I obtained high-resolution time-lapse $\boldsymbol{V_P/V_S}$ volumes from post-stack inversion of P- and S- wave datasets from three (3) time-lapse dedicated 9C surveys acquired in 2003, 2004 and 2006 by the Reservoir Characterization Project (RCP) in Rulison Field. Rulison is a basin-centered gas accumulation located in western Colorado and is operated by Williams Production Co RMT. The reservoir consists of stacked fluvial sands and coals of the Cretaceous Williams Fork Formation. The clastics represent the primary target for development and they are considered tight-gas sandstones due to their low porosity (6%-12%) and permeability (0.1 μd- 2 μd). This unconventional reservoir due to its low connectivity needs interconnected natural and induced fractures in order to produce at economic rates, so enhanced seismic imaging techniques are required to improve the recovery efficiency of this field. It has been demonstrated in previous studies (Rojas, 2005; Guliyev, 2007) that there is a potential of using $\boldsymbol{V_P/V_S}$ as an effective attribute to describe important reservoir variables such as lithology and pressure. To the best of my knowledge this is the first time time-lapse multi-component seismic is used to help with reservoir characterization of tight gas sands via time-lapse $\boldsymbol{V_P/V_S}$ volumes.

After cross-equalization of the three (3) time-lapse vintages on separate wave-modes (PP, fast-shear S11 and slow-shear S22) I performed post-stack inversion of the corresponding datasets to obtain impedances $\boldsymbol{Z_P}$, $\boldsymbol{Z_{S11}}$ and $\boldsymbol{Z_{S22}}$. 3D interactive multi-component registration was carried out to register the pure-shear volumes to compressional (PP) time scale. This procedure allowed me to obtain two (2) $\boldsymbol{V_P/V_S}$ volumes per each vintage: fast or $\boldsymbol{V_P/V_{S1}}$ and slow or $\boldsymbol{V_P/V_{S2}}$. In the case of areas characterized by one dominant vertical fracture set, the slow-shear mode attributes (i.e. $\boldsymbol{Z_{S22}}$ and $\boldsymbol{V_P/V_{S2}}$) are more sensitive to time lapse changes than the fast-shear mode attributes, but in case of multiple fracture sets or even one fracture set with different orientation the fast-shear mode attributes need to be considered too.

Using a mapping function and effective stress concepts, I estimated reservoir pressure volumes from $\boldsymbol{V_P/V_S}$ volumes. These volumes predict actual reservoir pressure only in those cases of high reservoir pressure, which is supported by analysis of rock physics measurements. Time-lapse anomalies seen on $\boldsymbol{V_P/V_S}$ volumes are clearly defined more than using another attributes. Most of the anomalies are associated with producing wells, indicating pressure drawdown of specific producing sandstones. Many of these time-lapse changes are not symmetric about the wells, indicating elliptical drainage associated with hydraulic fracturing or drainage interference with nearby wells, or stratigraphic control on production.

I propose a classification scheme of time-lapse $\boldsymbol{V_P/V_S}$ anomalies based on rock physics observations and the base and monitor $\boldsymbol{V_P/V_S}$ values that created those features. This procedure may help identify zones still in high pressure (type I anomalies) or considerably depleted (type II anomalies). This technique can provide important insights about the current development schemes and practices in the field, and how to potentially increase recovery efficiency. I use a procedure involving impedance-filtered $\boldsymbol{V_P/V_S}$ to help identify sandstones, which is based on the parent impedances of the $\boldsymbol{V_P/V_S}$ volume and petrophysical cross-plotting. The inclusion of the different forms of $\boldsymbol{V_P/V_S}$ in the geo-statistical, geo-mechanical and reservoir simulation models can help to constrain the corresponding static and dynamic variables of the reservoir model in order to optimize the development of gas resources in this reservoir, by implementing best practices for well placing and hydraulic fracturing.

TABLE OF CONTENTS

LIST OF FIGURES

LIST OF TABLES

ACKNOWLEDGEMENTS

I deeply thank my thesis advisor Tom Davis for his continuous support and confidence from the very beginning of my stay at Mines, also I would like to thank the RCP consortia sponsors for their financial and technical support. Thanks also to Robert (Bob) Benson for his support in terms of technical advisory and applications.

I am also really thankful with my mentor Reinaldo Michelena (iReservoir.com), whose questions and pieces of advice helped me to achieve most of the thesis goals. He played the role of the devil's advocate that everyone needs. Thanks also to Murray Roth (Transform Software) for his guidance through the multi-component registration world.

Thanks to my committee members: Steve Hill, Mike Batzle and John Curtis for their advice and also for their questions. Also thanks to Colorado School of Mines, especially the department of geophysics headed by Terry Young for their efforts on our education improvement, including faculty members and staff like Susan Venable and Sara Summers. I also thanks to my fellow RCP students, especially Matt Casey, Kurt Wikel, Nelson Rojas, Praj Mazumdar, Liz LaBarre and the former students Eldar Guliyev and Elmar Safarov. Among the former RCP students I must include Ludmila Adam and Gerardo Franco, close friends without whom it wouldn't have been possible for me to stay in Mines safely!

As usual, my family supported me in the same way they have done during decades, especially my parents…there are no words enough to thank you. Thanks also to my Venezuelan friends around the globe, including the Venezuelan gang here in Mines: Fernando & Angelica, Hector & Veronica, and Christopher. Finally, I would like to deeply thank my lovely wife Maria Gabriela, without whom I wouldn't have gone through my masters successfully…this thesis is dedicated to her to honor her love and support.

CHAPTER 1
INTRODUCTION

1.1 Reservoir Characterization Project (RCP) Phase XI

This thesis project is part of the ongoing research projects of the Reservoir Characterization Project (RCP), headquartered in the Department of Geophysics at Colorado School of Mines in Golden. The RCP is an industry-funded research consortium focused on the development and application of 4-D multi-component seismic and other related techniques to enhance both static and dynamic description of complex oil & gas reservoirs (http://www.mines.edu/academic/geophysics/rcp/).

This research is associated with RCP Phase XI, which consists of the enhancement of the dynamic characterization of reservoirs in Rulison Field, Colorado (Figure 1.1). RCP acquired time-lapse dedicated 9C-3D surveys in the years 2003, 2004 and 2006.

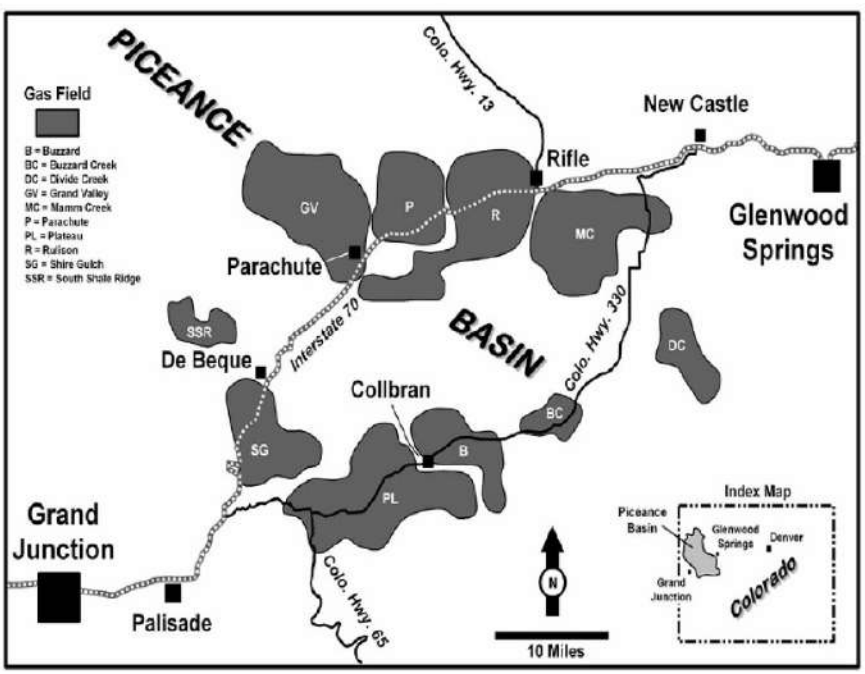

Figure 1.1. Relative location of Rulison Field (R) (from Rumon, 2006).

Rulison Field, operated by Williams Production RMT Company, is a basin-centered onshore gas accumulation in the Piceance Basin, Western Colorado. It is characterized as an unconventional gas field since most of the gas (98%) is being produced from tight-gas sandstones and coals from Williams Fork Formation (Late Cretaceous). Figure 1.2 shows a generalized stratigraphic column of Piceance Basin showing the intervals of interest for this project. The tight-gas sands interval is labeled as reservoir level 2 (main research target) and the coal interval as reservoir level 3 (secondary research target).

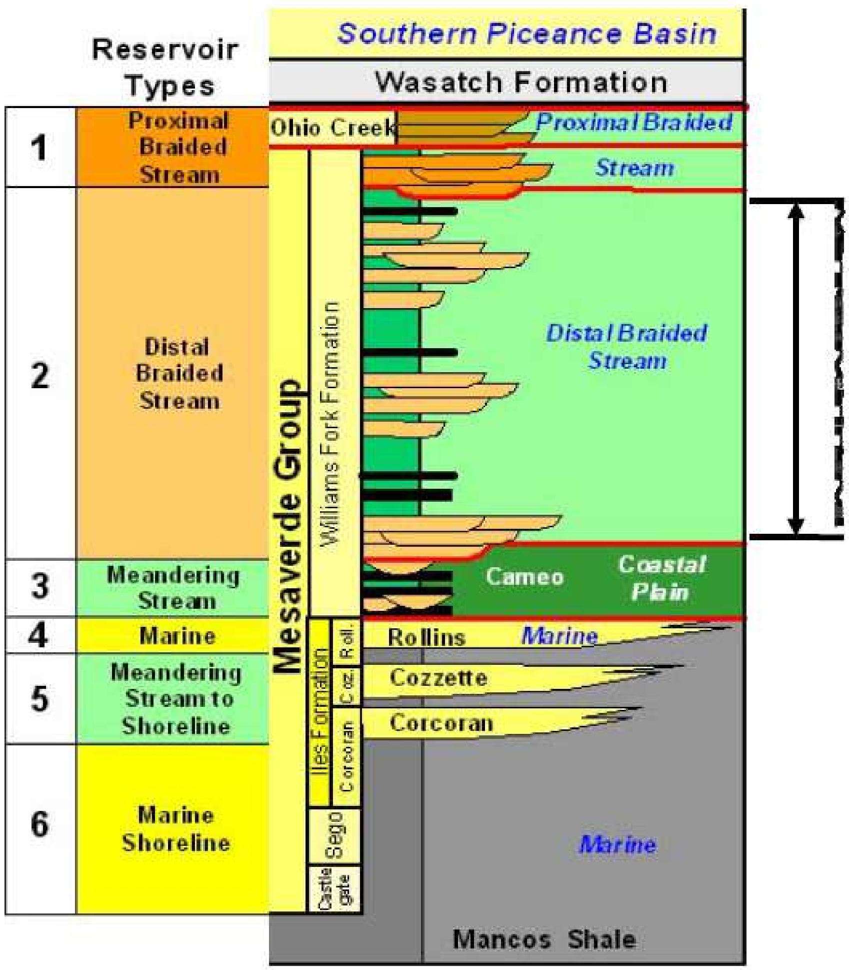

Figure 1.2. Depositional and stratigraphic framework of the Piceance Basin (from Guliyev, 2007)

.

Historically, it has been recognized that the Williams Fork Formation contains significant gas resources, but the low primary porosity and permeability, in addition to the strong lateral discontinuity of the stacked sand bodies makes it difficult to complete wells that could produce at economic rates (Cumella and Ostby, 2003). Production in Rulison field dates back to 1960's, however it was during 1980's when enhanced completion techniques, mainly hydraulic fracturing, allowed obtaining the successive completion of producing wells at economic rates, as noticed on the production history chart shown on Figure 1.3. There is a sharp rise of fluids production during the late 1970's-early 1980's (Cluff and Graff, 2003).

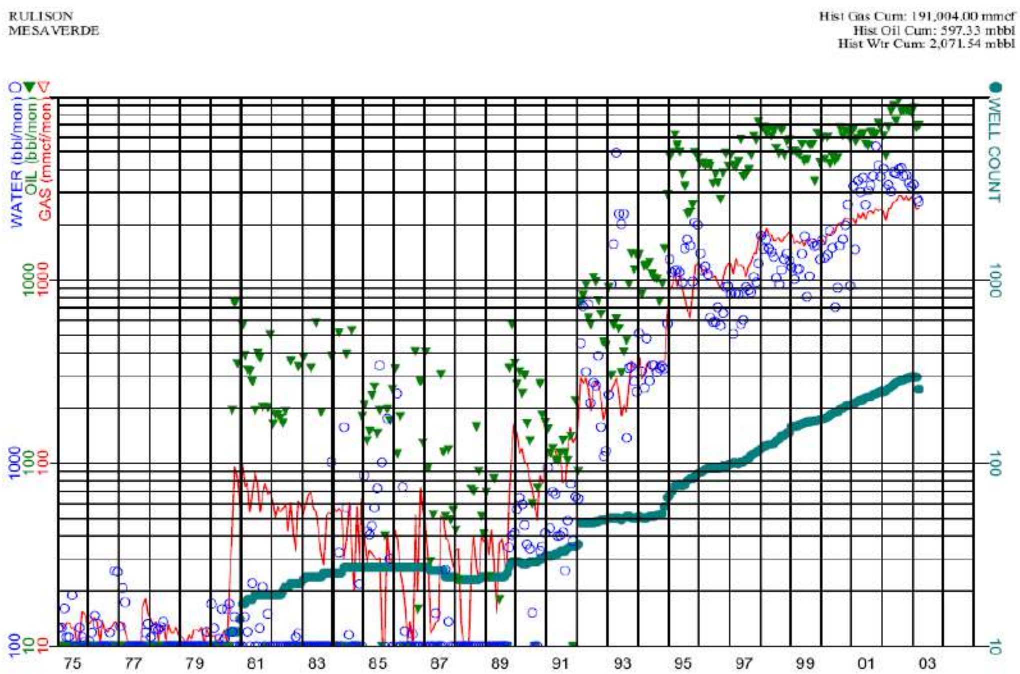

Figure 1.3. Rulison Field Production Chart from Mesa Verde Group Reservoirs (from Cluff and Graff, 2003).

The low lateral continuity of the fluvial sand bodies as well as the low internal connectivity (primary porosity and permeability) constrain the drainage area of each well completed. This is better illustrated by seeing the main reservoir properties shown on Table 1.1.

RESERVOIR PROPERTY	VALUE/RANGE OF PROPERTY
Primary Porosity	**6% - 12%**
Permeability	**0.1 μd - 2μd**
Irreducible Water Saturation	**40% - 65%**
Gross gas thickness (average)	**2400 ft.**
Net gas thickness (average)	**300 ft. – 400 ft.**
Production Mechanism	**Primary Depletion**

Table 1.1. Main Reservoir Properties of Williams Fork Formation in Rulison Field (Cumella and Ostby, 2003).

Having these characteristics, it has been stated that natural fracturing controls the productivity of the wells (Cumella and Ostby, 2003). It has been a common development pattern to induce hydraulic fracturing and use 20-acre well density or finer, in order to improve the productivity of the wells and the connectivity among the different sandstone bodies as well.

In order to improve the efficiency of such a development scheme it is necessary to enhance both static and dynamic reservoir characterization before drilling and completion, focused mainly on:

- Perform lithologic discrimination.
- Enhance the fracture characterization (fracture density and orientation).
- Identify areas already drained and/or containing bypassed gas resources.

In order to accomplish these goals, RCP has conducted several research projects, some of them considered to be milestones for this current thesis project. Based on core lab measurements and well-log data Rojas (2005) showed that seismic attributes can be used to infer reservoir properties, especially the ratio between the compressional-wave velocity and the shear-wave velocity, best known as V_P/V_S. By using cross-dipole sonic logs on well RU-7 Rojas demonstrated, via cross-plotting, that V_P/V_S can be used to discriminate both lithology (sands versus shales) and, to a lesser degree, fluid content.

Both discrimination cases show that low V_P/V_S values (<1.6) can be associated either with low GR values (high sand content) and/or low S_W (high gas saturation). A third variable of interest for reservoir characterization explored by Rojas was reservoir pressure. In this case Rojas used ultrasonic lab measurement on un-fractured core plug samples from the area, varying the pressure conditions for the velocity measurements. Rojas found out, under realistic fluid substitution conditions, that low V_P/V_S values correlate to over-pressure regimes, and high V_P/V_S values tend to correlate to a pressure drop or a depletion regime. The main conclusion derived from Rojas' research is the correlation of low V_P/V_S values to either higher sand content, higher gas saturation, higher reservoir pressure or a combination of two or three of them.

Taking advantage of the 2003 and 2004 time-lapse multi-component surveys available at the time, Keighley (2006) and Rumon (2006), using P-wave and S-wave (fast and slow or S11 and S22) surface seismic data respectively, showed that is possible to interpret time-lapse anomalies on these wave-modes, despite the high stiffness of the reservoir that could reduce the expectations about any interpretable time-lapse anomalies. They demonstrated that the main time-lapse anomalies are associated with pressure depletion. Both of them faced some issues that affected the repeatability between the 2003 and 2004 surveys, and subsequently, the interpretation of anomalies.

Guliyev (2007) calculated V_P/V_S volumes based on the P- and S- wave impedances obtained through the post-stack inversion of the 2004 PP (compressional), S11 (fast shear) and PS1 (fast converted) volumes. The correlation of the obtained V_P/V_S values and the GR values from wells away from the control well RU-7 allowed Guliyev to conclude that V_P/V_S, as a seismic attribute, can help to reduce uncertainty about lithology characterization.

The research project I conducted represents the next step: taking advantage of having three (3) time-lapse dedicated 9C surveys in order to obtain time-lapse V_P/V_S volumes that may handle the dynamic component of the reservoir (mainly pressure) rather than the static component researched by Guliyev, due to the fact he set the methodology using only one vintage, the 2004 survey. By doing this, RCP looks for a way to enhance the imaging of time-lapse changes taking into account most of the seismic information using an attribute that is consistent with core lab measurements and well-log data.

1.2 Why instantaneous V_P/V_S instead of intervallic V_P/V_S?

V_P/V_S, as a seismic attribute, is highly correlated to reservoir properties, especially lithology (Tatham, 1985; Eastwood and Castagna, 1986). When dealing with multi-component data, the easiest and most common way to obtain a form of V_P/V_S from seismic data is picking depth-equivalent seismic events in both seismic components: P-wave and S-wave as shown on Figure 1.4.

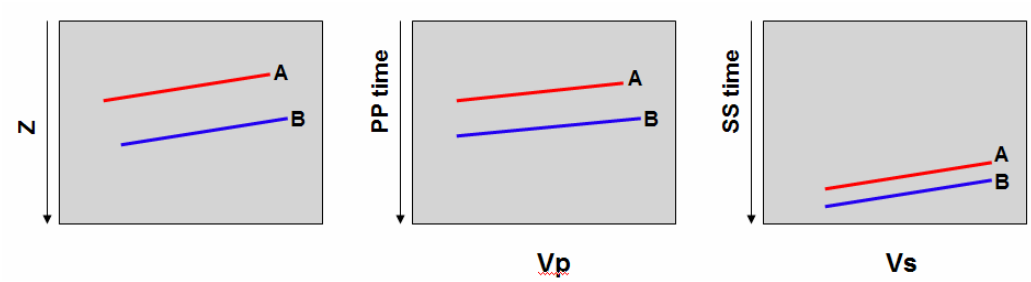

Figure 1.4. Scheme for events equivalence on multi-component seismic for intervallic V_P/V_S calculation.

The events ***A*** and ***B*** define the top and bottom of a subsurface unit the interpreter is interested in (Figure 1.4 left). By interpreting the time-equivalent events on P-wave data (middle) and S-wave data (right), using the two-way travel times of the picked events on each wave-mode is possible to obtain the value of V_P/V_S for the ***AB*** interval on each lateral position using equation 1.1:

$$\frac{V_p}{V_s}\Big|_B^A = \frac{t_{s,B} - t_{s,A}}{t_{p,B} - t_{p,A}} \qquad (1.1)$$

On this expression, $t_{S,B}$ and $t_{S,A}$ represent the two-way arrival times for the picked events ***B*** and ***A*** on shear-wave data respectively. $t_{P,B}$ and $t_{P,A}$ represent the two-way arrival times for the picked events ***B*** and ***A*** on compressional-wave data respectively. In the case the interpreter is using converted-wave data instead of pure shear data, which is the most common case on industry, equation 1.2 must be used:

$$\frac{V_p}{V_s}\Big|_B^A = \frac{2(t_{PS,B} - t_{PS,A}) - (t_{P,B} - t_{P,A})}{t_{P,B} - t_{P,A}} \tag{1.2}$$

For this expression, $t_{PS,B}$ and $t_{PS,A}$ represent the two-way arrival times for the picked events ***B*** and ***A*** on converted-wave data (PS) respectively. Theoretically, this formula must provide the same result as the PP-SS formula does.

The goal of this project is a detailed reservoir characterization of thin sandstones and time-interval measurements are not suitable. This is better understood after analyzing Figure 1.5.

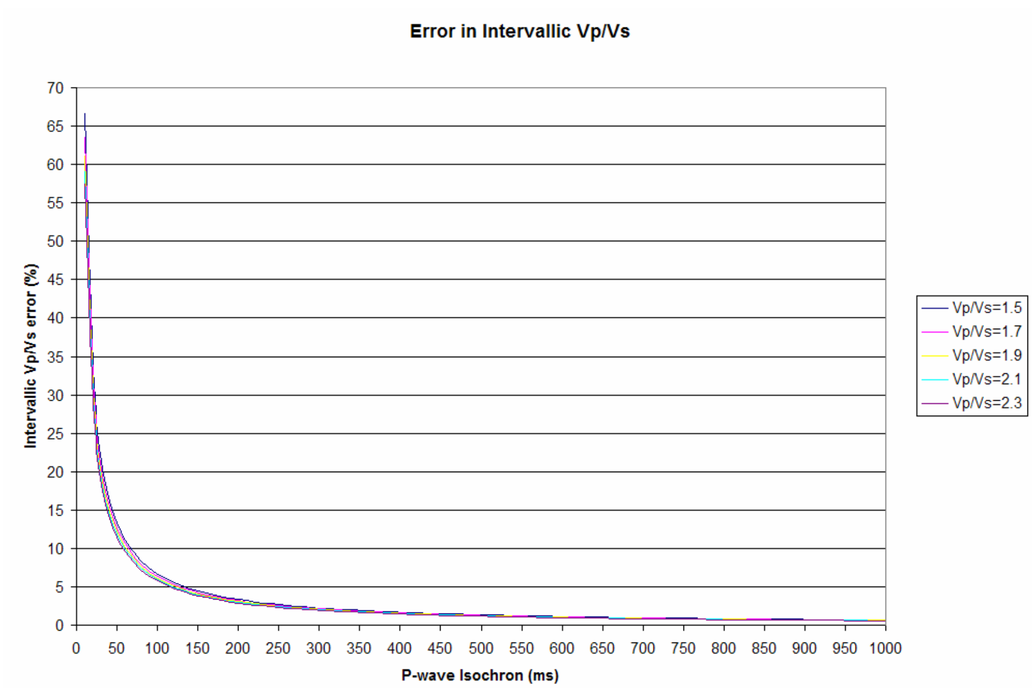

Figure 1.5. Uncertainty (Error) on Intervallic $\mathbf{V_P/V_S}$ *calculation.*

For different realistic V_P/V_S values ranging from 1.5 to 2.3, baed on error propagation from equation 1.1, I plotted the uncertainty or error (%) on the determination of intervallic V_P/V_S as a function of the interval thickness expressed as P-wave isochron time. First it should be noticed that all the curves corresponding to the different V_P/V_S values overlay each other, which means that there is no significant change of error depending on the V_P/V_S background. If it is considered that the main source of error on the horizon picking is the time-sampling, in this case 2 ms, it can be noticed that for thick intervals (> 100 ms) the error on the intervallic V_P/V_S is less than 5%. However, in case the interval becomes thinner (< 100 ms), the uncertainty rises dramatically. When considering a 30 ms interval, an error over 30% occurs. This fact becomes more important if the sampling rate is larger, because the vertical asymptote shifts towards the right, making higher the lower-limit of interval thickness to be characterized with an allowable uncertainty.

As shown on Figure 1.6, the ratio of P- and S- wave impedances can be used in order to obtain detailed V_P/V_S values in a volumetric way (Garotta, 1985), without the intervallic V_P/V_S shortcomings.

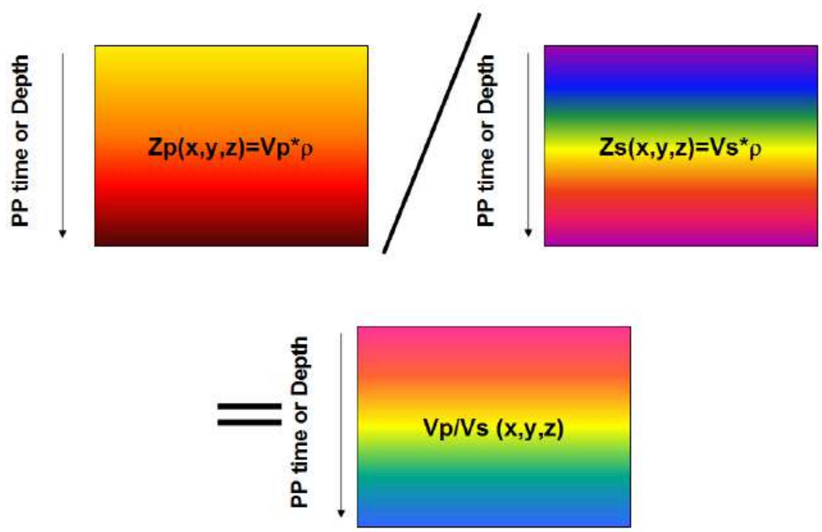

Figure 1.6. Impedance-based, Instantaneous V_P/V_S.

$\boldsymbol{V_P/V_S}$ ratio volume is obtained by dividing the corresponding volumes for P- and S- wave impedances (Garotta, 1985) as shown on the figure, and in equation 1.3:

$$\frac{Z_p}{Z_s} = \frac{V_p \rho}{V_s \rho} = \frac{V_p}{V_s} \tag{1.3}$$

There are two (2) ways to obtain both P- and S- impedances from seismic:

- In the case the interpreter only has P-wave data available, the compressional and shear wave impedances can be estimated through simultaneous inversion of pre-stack P-wave data. This procedure has the advantages of having both impedances in the same vertical domain (P-wave time) and only needs one wave-mode: P-wave, which is the one widely used in industry. The main disadvantage is that this kind of inversion is based on AVO approximations and assumptions that may not be satisfied depending on data quality and geologic settings.

- When multi-component data are available, P- and S-wave (or PS wave) components can be independently inverted in the post-stack domain to obtain their corresponding impedances in their natural time domains. The main advantage of this procedure is that is not based on approximations because we are dealing with real S-impedance obtained from S-wave data. The main disadvantages are cost of acquiring/processing multi-component data, and the need of performing data registration in order to get all datasets in the same vertical scale/domain.

This thesis research uses the independent post-stack inversion of multi-component data in order to obtain $\boldsymbol{V_P/V_S}$ volumes for each time-lapse vintage.

1.3 Research Goals and Expected Contributions

The purpose of this thesis is to explore the possibilities of improving the dynamic reservoir characterization by describing time-lapse seismic changes due to pressure changes in the reservoir. This may lead to the implementation of an enhanced development plan for Rulison Field.

The overall goal is to take advantage of the dependency of $\boldsymbol{V_P/V_S}$ with lithology and pressure in order to perform a dynamic seismic characterization in terms of reservoir pressure. The technique is implemented by comparing the 2003, 2004 and 2006 surveys in the PP and SS wave modes using post-stack inversion to generate $\boldsymbol{V_P/V_S}$ volumes as performed by Guliyev (2007), who used the 2004 vintage alone. By using just one seismic survey is not possible to decouple the effect of lithology, fluid saturation and pore pressure in $\boldsymbol{V_P/V_S}$ ratio as shown by Rojas (2005) and Guliyev (2007). Since lithology does not change during the development of the reservoir, time-lapse seismic data can be used to describe the effect of pore pressure on $\boldsymbol{V_P/V_S}$ ratio.

Through the use of the rock physics measurements performed by Rojas (2005), my thesis can work as a starting point to quantify pressure changes due to depletion using the time-lapse $\boldsymbol{V_P/V_S}$ anomalies.

The specific goals of this research project can be listed as follows:

- Obtain high-resolution $\boldsymbol{V_P/V_S}$ volumes for different 4D seismic vintages by post-stack inversion of PP and SS surface data.

- Estimate high resolution, seismically-derived reservoir pressure volumes by the use of an isotropic rock physics mapping function.

- Compare the reservoir pressure estimated from seismic data (via $\boldsymbol{V_P/V_S}$ volumes) with actual pressure tests and/or production data.

- Assess the impact of seismically-derived reservoir pressure volumes in the reservoir development.

- Investigate the potential of improved V_P/V_S volume as a lithology indicator by decoupling the effect of dynamic variables (i.e. pressure and fluid saturation) using time-lapse seismic.

By achieving these goals I have made the following contributions to RCP Phase XI:

- Demonstrate the usefulness of time-lapse V_P/V_S as a tool for enhanced seismic characterization when derived from 4D-9C seismic data.

- Contribute to seismically constrain the variables of the 3D geomechanical model (Wikel, 2007).

- Provide an additional way to describe the distribution in space of sand bodies, which could be combined with the geostatistical model (Casey, 2007).

- Constrain the history matching during reservoir simulation using the attributes obtained on this research (i.e. V_P/V_S, impedances) in order to enhance the reservoir development forecast.

- Improve the well placement and completion based on the analysis of depleted and/or bypassed zones interpreted from time-lapse seismic data.

1.4 Thesis Report Overview

The following chapters present a description of the different stages of this thesis project. Chapter 2 presents a description of the general methodology, workflows and datasets used. Chapter 3 describes the rock physics and petrophysics fundamentals/ premises of this research, as well as some results that will be used in the interpretation chapters. The post-processing of the volumes to make them suitable for time-lapse interpretation is shown in Chapter 4: cross-equalization. Since the V_P/V_S volumes are impedance-derived, Chapter 5 contains the highlights of the post-stack inversion of the cross-equalized multi-component volumes.

The vertical domain conversion of all the inverted volumes is presented in Chapter 6. The final interpreted results are contained in Chapter 7, where results are analyzed from an integrated reservoir management point of view. Finally, Chapter 8 contains the conclusions and recommendations derived from this study.

CHAPTER 2
DATASETS AND METHODOLOGY

2.1 Datasets Description

This research was conducted using proprietary surface seismic data (RCP) as well as well-log and production data (Williams RMT Production Co.). Also on these datasets are included the lab measurements resulting from un-fractured core plugs performed by Rojas (2005). The next sections present the description of each dataset.

2.1.1 Surface Seismic Datasets

As stated in the previous chapter, RCP acquired three (3) time-lapse dedicated nine-component (9C) surveys in the years 2003, 2004 and 2006. The surveys cover approximately 5.6 km^2. The relative location of the survey area along with other datasets is shown on Figure 2.1.

2.1.1.1 Acquisition

Performed by Solid State Geophysical, acquisition of the RCP surveys involved 1500 receivers placed with an inline x crossline spacing of 110 ft x 330 ft. The 36 receiver lines are perpendicular to the 12 source (vibrator) lines as shown on Figure 2.2. The reported standard deviation in stations positioning differences (Keighley, 2006) is 2.15 ft for receivers and 3.39 ft for sources as shown on Figure 2.2, which guarantees the repeatability of the surveys in terms of acquisition geometry. Due to the presence of the Roan Cliffs to the north of the survey, it was difficult to place vibrators, so data quality (fold, offset distribution, etc) is poor in this area. Figure 2.2 shows the missing source locations due to this fact. The fold distribution is shown on Figure 2.3 where the influence of missing source/receiver positions in the north is evident.

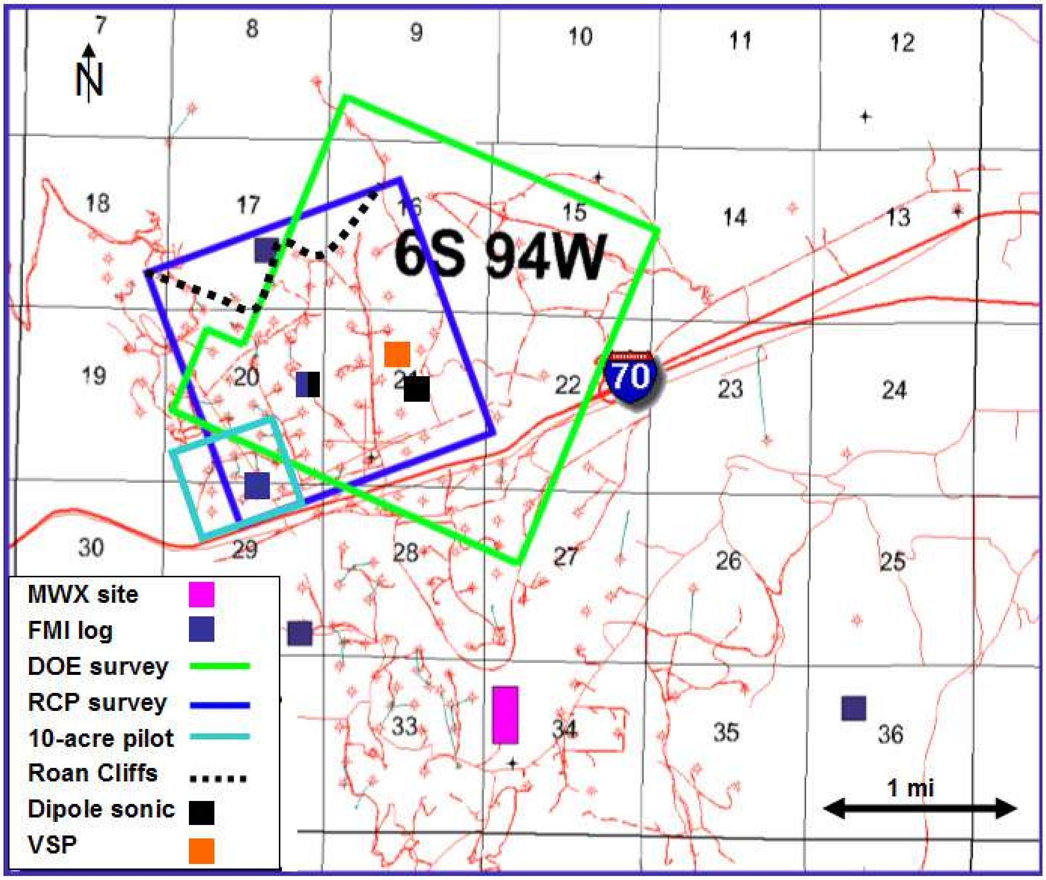

Figure 2.1. Relative location of different datasets for Rulison Field (from Keighley, 2006).

The P-wave vibrators (Mertz 18) used a sweep of 5-120 Hz during 10 seconds, while S-wave vibrators (IVI-Tri Ax) swept at 5-50 Hz during 10 seconds. I/O VectorSeis System Four single sensor digital multi-component was the sensor type used.

Although repeatability was guaranteed by geometry and equipment settings, environmental conditions during acquisition were quite different among the three vintages. During 2003 and 2006 acquisitions, dry weather conditions were reported. 2004 acquisition was characterized by a high rain fall. Also, high drilling activity was reported on the NW corner of the RCP area which introduced noise to the data and caused the removal of some gathers around the drilling area (Keighley, 2006).

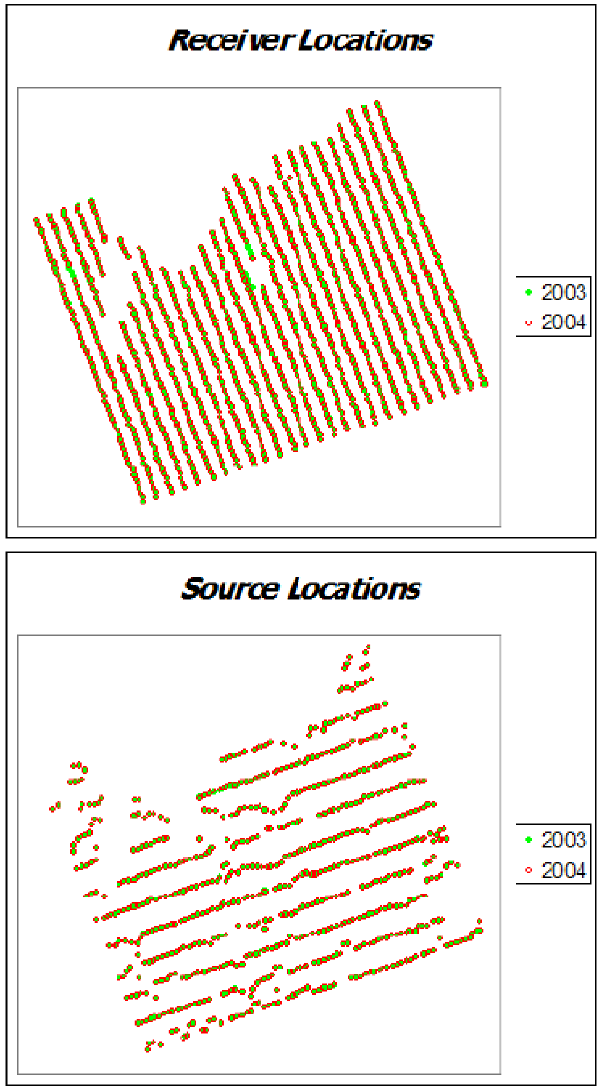

Figure 2.2. Relative location of sources and receivers. Acquisition on 2003 (green) and 2004 (red) (from Keighley, 2006).

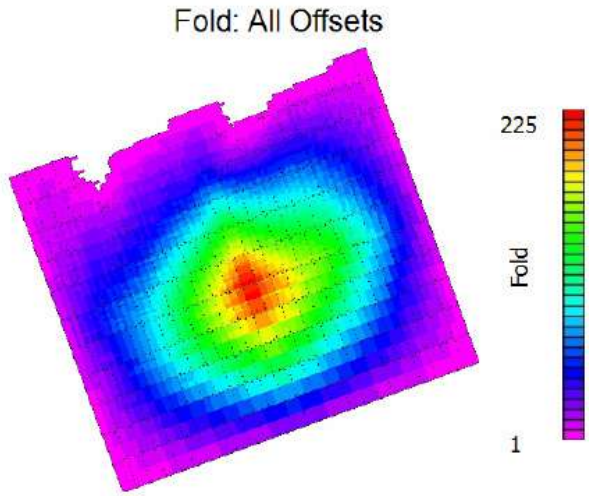

Figure 2.3. RCP survey fold (from Keighley, 2006).

2.1.1.2 Processing

The seismic volumes I used are the product of the processing by CGG-Veritas processing team. The processing was carried out on a time-lapse basis in order to maximize repeatability. The processing sequence as shown on SEGY headers for P-wave data is shown on Table 2.1, and the corresponding for S-wave data on Table 2.2.

In order to avoid introducing processing artifacts on seismic data, most of the processes were designed and applied using a common set of parameters for all the vintages within a common wave-mode. Examples of such processes are velocity analysis & NMO correction, migration and data rotation (S-wave case). Other processes such as static corrections are vintage-dependent, which means that their parameters are not common among the different vintages due to different ground conditions.

Tilt Correction applied in field
Demultiplex/reformat, 3D geometry and edits
Spreading gain recovery using t^2 function
Surface consistent scaling
Minimum phase correction
Surface consistent deconvolution
Tomostatics (weathering static)
Velocity analysis and preliminary Veritas interactive static (residual)
Constant phase rotation -180º
Final velocity analysis and Veritas interactive static (residual)
First breaks mute, static
High amplitude noise reduction
Stack
Long-wavelength static
FXY predictive deconvolution
Kirchhoff migration (using 100% of RMS velocities)
Filter 5-10-100-110 Hz @ 0-1600 ms, 5-10-80-98 Hz @ 1800-2800 ms

Table 2.1. Processing Sequence of P-wave data.

Tilt Correction applied in field
Demultiplex/reformat, 3D geometry, edits, polarity corrections (shots)
Spherical divergence correction, surface consistent amplitude equalization
Data rotation into S1 and S2 (N45ºW)
Minimum phase correction and surface consistent deconvolution
Phase and static correction on the trace vibrator +56.32º
Static correction
Velocity analysis
Radon transform
Surface consistent static
Velocity analysis
First break mutes, static
Radon Transform
Static correction
Time-lapse edits
Stack
Pre-migration scaling, Kirchhoff migration (using 100% of RMS velocities)
Filter 4-8-30-40 Hz @ 0-3000 ms, 4-8-25-35 Hz @ 3000-6000 ms

Table 2.2. Processing Sequence of S-wave data.

Regarding shear-wave data, the corresponding fold coverage above reservoir level has been reduced drastically upwards due to deep top mutes. Analysis of the overburden 2003 VSP shows that these data rotate to the same orientation as the surface seismic data (N45ºW) (Casey and Davis, 2007). Shear-wave splitting affects the distribution of shear-wave energy and arrival times of shear waves. Four (4) output volumes for shear-wave data include S11, S12, S21 and S22. Data rotation during processing performs a re-distribution of energy, maximizing the energy on those volumes polarized normal and parallel to the symmetry axes. In the case of a single orientation of vertical fractures S11 (fast shear) is going to be the shear volume with polarization parallel to the fractures, while S22 (slow shear) has an orthogonal polarization (Rumon, 2006).

2.1.2 Well-bore datasets

The RCP survey area contains over 70 drilled wells. There are two (2) wells containing cross-dipole sonic and density logs that were used for seismic control purposes. Only the well RU-7 has the log quality to be designated as a control well. As shown on Figure 2.1, this well is located close to the NE border of the survey but out from the fringe or low-fold zone. It contains most of the common log suites: GR, resistivity, check-shot (P-wave), cross-dipole sonic log (rotated for fast and slow shear-wave), density, neutron, etc.

Core data referred from Rojas (2005) corresponds to the U.S. Department of Energy well site MWX-1 containing over 2500 ft of Mesa Verde Group cores. Most of the wells in the area have production history data, but all the wells have commingled production, with no production accounted for each perforated interval. Pressure tests have been taken on some wells but not in a time-lapse basis.

2.2 Project Workflow

In order to accomplish the research specific goals stated in Chapter 1, I followed the overall general workflow shown on Figure 2.4.

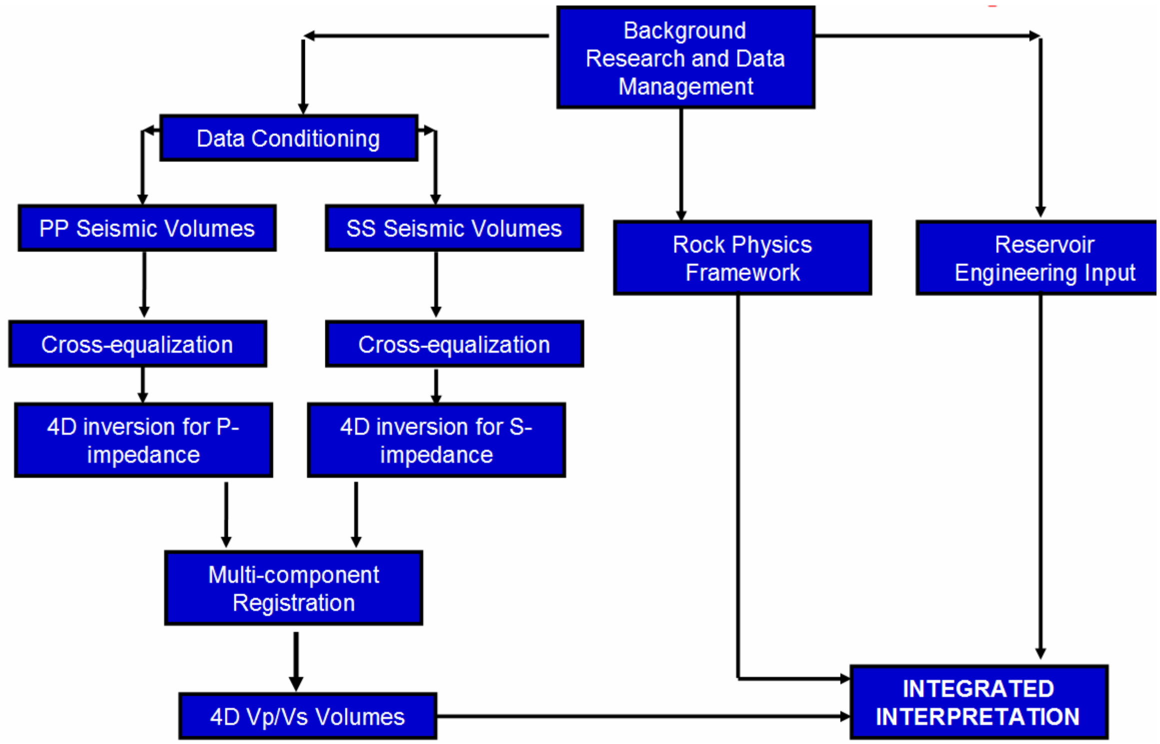

Figure 2.4. General research workflow.

This workflow is divided into three (3) main branches to be described as follows:

2.2.1 Seismic Analysis

My research is based on the analysis of the surface seismic data. The surface seismic data consists of PP and SS wave modes. Using the compressional (PP) and pure-shear wave (SS) volumes as input, I performed the cross-equalization to remove all artifacts not associated with the development of the reservoir.

The next stage involves post-stack inversion of the previous volumes to obtain P- and S- impedance. This inversion is performed in a time-lapse basis using well data to constrain the inversion. This process is followed by the multi-component registration, which allows obtaining both wave modes (PP and SS) in the same time domain (in this work, it is PP time). V_P/V_S ratio volumes are obtained simply dividing P-Impedance by S-Impedance for each seismic vintage (2003, 2004 and 2006).

2.2.2 Rock Physics & Petrophysics Framework

Based on the work done by Rojas (2005), relationships between reservoir variables (such as pressure) and seismic velocities are established. These isotropic measurements will allow quantifying and/or translating the time-lapse $\boldsymbol{V_P/V_S}$ ratio changes into pressure changes. This framework will be supported by the effective stress concepts (Hoffmann et al, 2005) mathematically expressed on equation 2.1:

$$P_e = P_c - nP_p \tag{2.1}$$

where $\boldsymbol{P_e}$ is the effective stress which affects the overall seismic wave propagation, $\boldsymbol{P_c}$ is the litho-static stress (overburden), $\boldsymbol{P_p}$ is the pore pressure, which is the reservoir parameter to be estimated in this research, and $\boldsymbol{n}$ is the effective stress coefficient, which is a function of the bulk modulus or consolidation of the rock.

In order to obtain a seismic-derived pore pressure volume it is necessary to establish a empirical relationship between $\boldsymbol{V_P/V_S}$ ratio and effective stress using existing lab measurements (Rojas, 2005) to derive an effective stress volume. The confining or litho-static stress volume is derived by integrating the density logs and extrapolating them through the space, and finally $\boldsymbol{n}$ is obtained from the 3D geomechanical model (Wikel, 2008).

The framework is isotropic. Future studies could be focused on the development of an anisotropic rock physics model.

2.2.3 Reservoir Engineering Input

The calibration of the results in terms of “realistic” values is done by comparison of the obtained seismic attributes and the seismic-derived pore pressure volume, with pressure tests and production data. Data management is necessary to properly correlate the production with seismic data. These pressure tests act as control points in terms of how good seismically derived pore pressure is describing the actual pore pressure changes in the reservoir.

CHAPTER 3
ROCK PHYSICS & PETROPHYSICS FRAMEWORK

3.1 Introduction

Rock physics describes the reservoir rock using physical properties (porosity, compressibility, rigidity, etc) that affect how seismic waves physically travel through it (Dewar, 2001). Based on this definition, rock physics links reservoir development influence on physical properties and its corresponding expression on seismic data. On the other hand, petrophysics aims to obtain reservoir parameters mostly from well-logs, and also from core and production data by using mostly empirical relations and is not usually concerned about seismic signatures (Dewar, 2001).

In order to analyze and translate time-lapse changes on seismic attributes into useful knowledge about the dynamic reservoir description, it is necessary to understand the rock physics framework behind the overall wave propagation in Rulison Field by seeing how pressure changes are related to seismic velocities. Petrophysics, in addition to rock physics, will help improving the static description, providing thresholds and correlations between seismic data and logs in order to use seismic attributes as a way to improve the spatial description of sand bodies.

3.2 Seismic wave propagation and effective stress

Seismic wave propagation is the consequence of elastic deformations the rocks undergo due to the action of a stress field (Aki and Richards, 2002). Such stress field affects the main elastic properties on rocks, in this case body-wave seismic velocities (P- and S-waves). Commonly this stress field has been known as effective stress or effective pressure (Hoffmann et al, 2005) shown in equation 3.1:

$$P_e = P_c - nP_p \tag{3.1}$$

where P_e is the effective stress or effective pressure which affects the overall seismic waves propagation, P_c is the litho-static pressure (overburden) or vertical stress, P_p is the pore pressure, which is the reservoir parameter to be estimated on this research, and n is the effective pressure coefficient (Biot's constant), which is a function of the bulk modulus or consolidation of the rock. By re-arranging equation 3.1 is possible to obtain pore pressure values from the rest of the parameters (Chopra and Huffman, 2006) as shown on equation 3.2:

$$P_p = \frac{P_c - P_e}{n} \tag{3.2}$$

The confining pressure P_c can be obtained by integrating the density logs (Sayers et al, 2006) as shown on equation 3.3, in order to account for the weight of the rocks and fluids in the pore space overlying a given depth z, being g the acceleration due to gravity and $\rho(z)$ the density at depth z:

$$P_c = g\int_0^z \rho(z)dz \tag{3.3}$$

This integrated log can be extrapolated away from wells through the area using semi-regional interpreted horizons (UMVS and Cameo) as shown on Figure 3.1. As expected, the vertical stress or confining pressure increases monotonically with depth.

Another element required for pore pressure estimation is the so-called effective pressure coefficient or Biot's constant n. Hoffman et al (2005) provided different ways to estimate such coefficient, but I used the value determined in the Rulison ongoing 3D geo-mechanical model (Wikel, 2008) n equals 0.7, which is a function of the rock primary porosity.

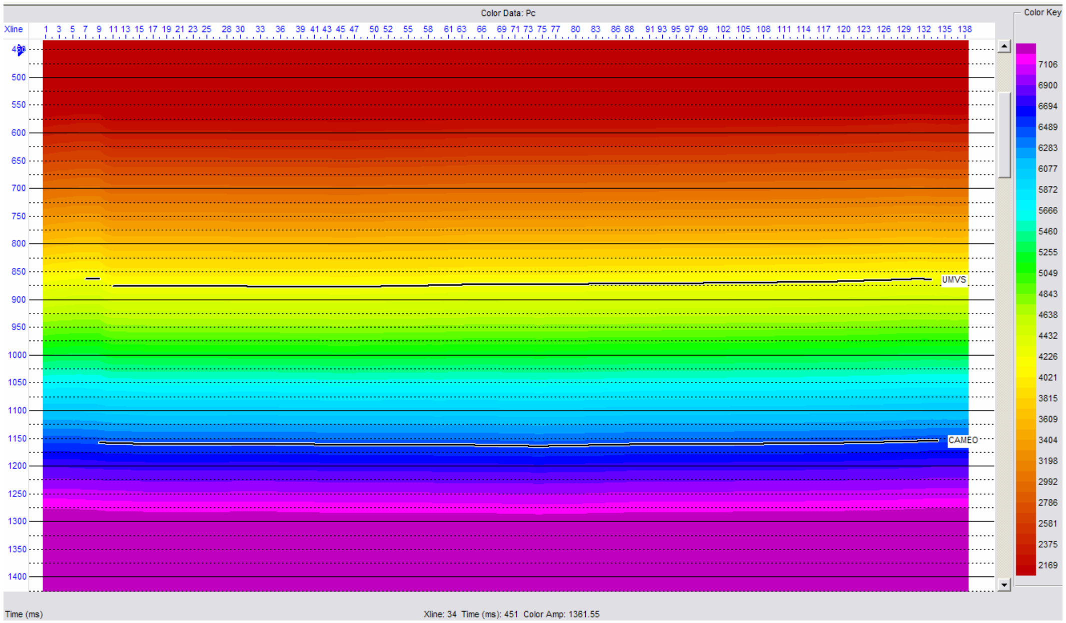

Figure 3.1. IL-19 Litho-static pressure (psi) volume.

The last variable needed for pore pressure estimation is the effective pressure, which can be obtained through an empirical relationship from ultrasonic measurements of un-fractured core plugs in the area (Rojas, 2005). Figures 3.2 and 3.3 depict the resulting measurements that relate P- and S- wave velocity values with effective pressure for a 10% porosity sample.

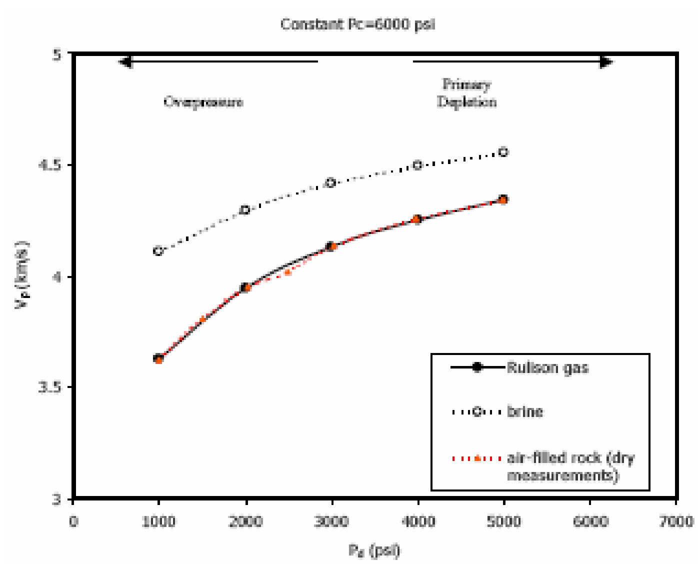

*Figure 3.2. **V$_P$** vs effective stress. Two different pore fluid saturation. (from Rojas, 2005)*

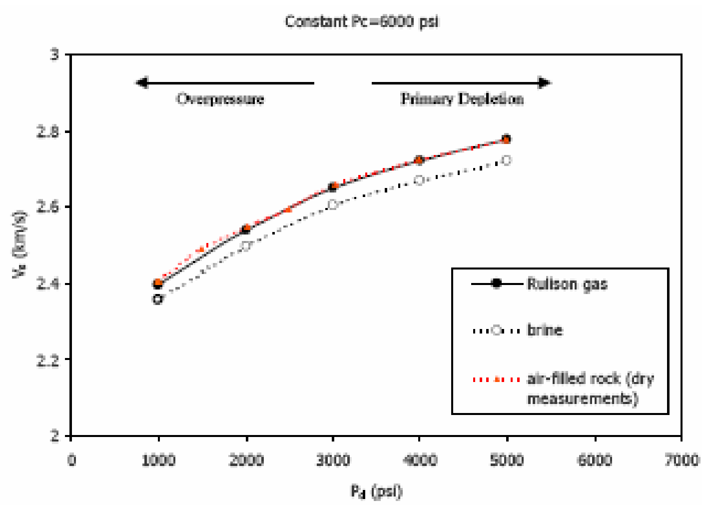

Figure 3.3. V_S vs effective stress. Two different pore fluid saturation (from Rojas, 2005).

Pressure changes directly affect rock stiffness which is related to seismic velocities (Aki and Richards, 2002). Rulison Field is being developed under a primary depletion scheme, so reservoir (pore) pressure drops are expected, causing increments on seismic velocities. Figures 3.2 and 3.3 depict the results from Rojas's research related to the change of P- and S-wave velocity with pressure respectively. At high pore pressure, the rock stiffness is lower so V_P and V_S also are lower (Mukerji et al, 2002). In case pore pressure drops (primary depletion), rock stiffness is higher and V_P and V_S are higher as well. The main difference between V_P and V_S behavior with pressure occurs at high pore pressure (low effective stress) regime, where P-wave velocity rate of change with pressure is larger than S-wave rate. V_P/V_S ratio reflects this particular behavior as seen on Figure 3.4, which additionally shows the Gassman's fluid substitution scenario worked by Rojas (2005).

In Rulison Field there is no significative active aquifer (Cumella and Ostby, 2003), so it can be assumed that water in pore space is irreducible. In addition, there is no enhanced recovery mechanism applied to the reservoir which means no fluid injection. What these premises support is the fact that under primary depletion in Rulison Field, there is no change in fluid saturation within the pore space, so the only dynamic variable that controls time-lapse responses (velocity variations with production) is reservoir pressure. This conclusion is supported by Figure 3.4; using Gassman's fluid substitution for a tight-sand core sample, Rojas (2005) showed that reservoir rock with gas saturation varying from 100% to 30% hardly changes the $\boldsymbol{V_P/V_S}$ ratio. Lower gas saturation regimes (95% brine-red curve and 100% brine-blue curve) show a very distinctive $\boldsymbol{V_P/V_S}$ response, but these saturation scenarios are not plausible in the tight-gas sand reservoir in Rulison field.

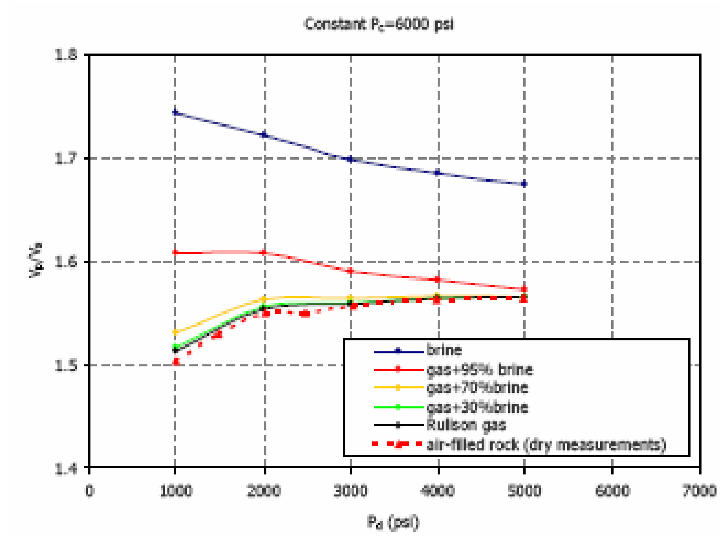

Figure 3.4. $\boldsymbol{V_P/V_S}$ vs effective stress at different pore fluid saturation (from Rojas, 2005).

Using these measurements, I plotted effective stress vs $\boldsymbol{V_P/V_S}$ and obtained a mapping function by fitting an exponential function to the experimental data. This function estimates the effective pressure when the value of $\boldsymbol{V_P/V_S}$ is known, as seen on Figure 3.5. The mapping function obtained from exponential fit to the lab data is expressed in equation 3.4:

$$P_e(x,y,z) = (7x10^{-14}) * e^{[24.545*(\frac{V_P}{V_S}(x,y,z))]} \qquad (3.4)$$

If a volume of $\boldsymbol{V_P/V_S}$ is available, then a volume of effective stress can be estimated using this formula. The main shortcoming occurs when mapping $\boldsymbol{V_P/V_S}$ values higher than 1.57, because a short range of $\boldsymbol{V_P/V_S}$ values (1.57-1.62) can be mapped into a large range of effective stress values (5000-14000 psi). This scenario corresponds to highly depleted sands where their pressures do not have an influence in their corresponding V_P/V_S values. This also could be an advantage since the low effective stress values corresponds to high-pore pressure regimes, therefore pressure estimation on this regime is more reliable when dealing with low V_P/V_S values (1.4-1.57). This mapping function was estimated from core measurements of 10% porosity samples, which means that lower porosity intervals could be over-estimated in terms of reservoir pressure estimated on this way (Hoffmann et al, 2005).

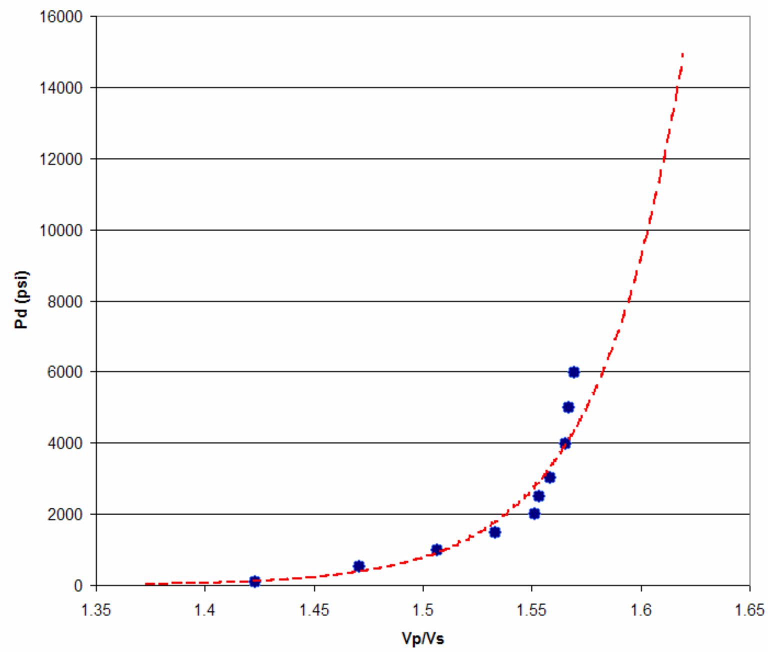

Figure 3.5. Effective stress vs V_P/V_S. Experimental points in blue (Rojas, 2005) and mapping function in dashed-red line. Regression coefficient R^2=0.9689.

3.3 Seismic sensitivity to velocity changes

Dynamic perturbations into the physical reservoir properties, such as pore pressure, are expected to have an influence on body-wave seismic velocities and seismic signals as well (Amundsen and Landrø, 2007a). To account for such influence it is necessary to establish links between seismic velocity changes and the corresponding seismic attribute changes (i.e. amplitude, impedance, etc).

I established the link between seismic amplitudes and the corresponding seismic velocities by using a zero-noise approximation (eq. 3.5a) of the seismic trace convolutional model as seen on the equation, where $\boldsymbol{A_k}$ represents the amplitude of the $\boldsymbol{k^{th}}$ interface, $\boldsymbol{w}$ the wavelet, $\boldsymbol{r_k}$ the impedance contrast at the $\boldsymbol{k^{th}}$ interface expressed only as a function (eq. 3.5b) of the upper and lower bounding layer velocities $\boldsymbol{V_k}$ and $\boldsymbol{V_{k+1}}$, and $\boldsymbol{\Delta A_k}$, $\boldsymbol{\Delta r_k}$ and $\boldsymbol{\Delta V}$ represents the changes on amplitude, impedance contrast and velocity respectively (eq. 3.5c):

$$
\begin{aligned}
A_k &= w * r_k \\
r_k &\approx \frac{V_{k+1} - V_k}{V_{k+1} + V_k} \\
\Delta A_k \approx \Delta r_k &= \frac{2}{(V_{k+1} + V_k)^2}\left[V_k \Delta V_{k+1} + V_{k+1} \Delta V_k\right]
\end{aligned}
\qquad (3.5)
$$

Equation 3.5c represents how the seismic amplitude changes at the $\boldsymbol{k^{th}}$ interface as the velocity of the layers defining that interface change. These equations apply for both P- and S-wave. Usinf the chain rule, I also obtained a similar expression for $\boldsymbol{V_P/V_S}$ changes as a function of $\boldsymbol{V_P}$ and $\boldsymbol{V_S}$ changes as shown on equation 3.6.

$$
\Delta \frac{V_p}{V_s} = \frac{1}{V_s} \Delta V_p + \frac{V_p}{V_s^2} \Delta V_s \qquad (3.6)
$$

Through knowledge of both P- and S- wave velocity changes is possible to determine the sensitivity of different attributes by using equations 3.5c and 3.6. Feasibility on amplitude-based seismic detection of time-lapse velocity changes can be also determined by 1-D forward modeling using well-log data. Rojas (2008) built 1-D synthetic seismograms using a P-wave velocity log of well RU-1. The selection of this well is based on the fact that it is the oldest well drilled in the RCP survey area, so the rock properties logged on this location are the closest to the initial reservoir conditions before significant reservoir development or production. He edited the original P-wave sonic log by increasing the velocities of sandstones on 5% and 10%, generating edited sonic logs for each relative change. For lithology discrimination during edition, he used a GR cutoff < 75 API combined with density log in order to avoid including coals and include reservoir intervals in the analysis. Figure 3.6 depicts the 1-D synthetic seismograms from the original sonic log (black traces), 5% sands P-wave velocity increase (red traces) and 10% sands P-wave velocity increase (light blue traces).

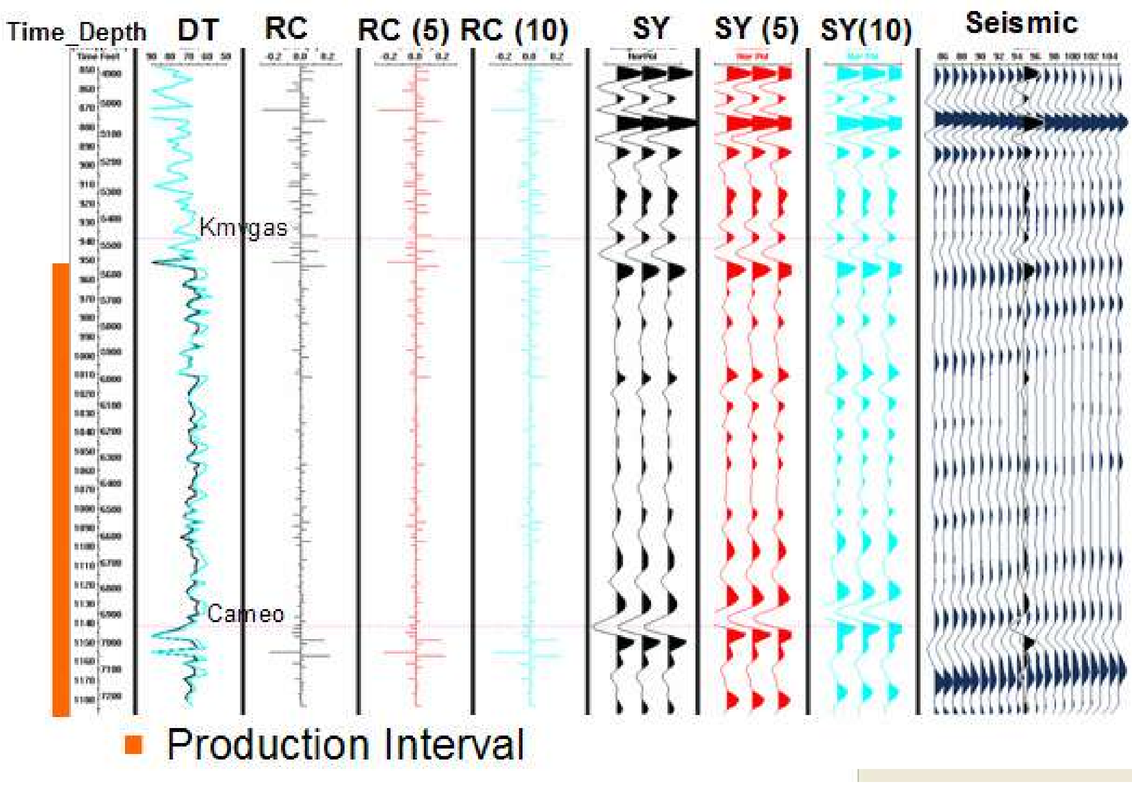

Figure 3.6. RU-1 synthetic seismograms. Track 1: Original and edited sonic logs. Track 5: Synthetic seismogram (black trace) from original log. Track 6: Synthetic seismogram (red trace) from edited log (5% velocity increase). Track 7: Synthetic seismogram (light blue trace) from edited log (10% velocity increase). N. Rojas (2008)

Figure 3.7 shows the seismic traces corresponding to the difference between the synthetic seismograms 5% velocity increase-original sonic log (left) and 10% velocity increase-original sonic log (right), where is demonstrated that such velocity changes due to pressure drop can be imaged based on P-wave amplitudes in a time-lapse basis. A shear-wave sonic log was not run on RU-1 so the 1-D forward modeling for S-wave data could not be performed, but expected to show similar results since the driver of time-lapse changes is reservoir pressure change rather than saturation change. The choice of these amounts of velocity increment was based on previous modeling work on Rulison data (Keighley, 2006).

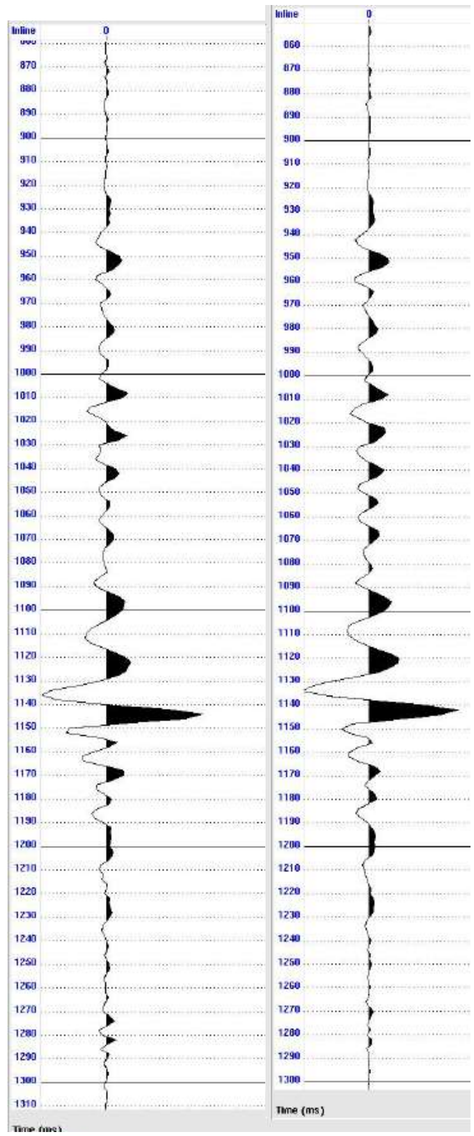

Figure 3.7. RU-1 synthetic differences relative to original P-wave sonic log. 5% velocity increase (left) and 10% velocity increase (right).

3.4 Seismic anisotropy & time-lapse seismic

Effective media concepts helped me understand the role of anisotropy on time-lapse seismic expressions since neither sand bodies nor fracture zones can be individually isolated using seismic imaging (Vasconcelos and Grechka, 2007). Effective media is modeled assuming that finite fracture openings and details on the spatial distribution of fractures can be neglected, considering fractured blocks as equivalent or effective anisotropic solids (Bakulin et al, 2000). When considering multiple vertical fracture sets embedded on an isotropic background media, the corresponding seismic expression in terms of anisotropy will be orthotropic (Grechka and Kachanov, 2006b,); which means that these multiple dry fracture sets on an isotropic matrix can be represented or modeled by two (2) mutually orthogonal vertical fracture sets under the long-wavelength assumption (Vasconcelos and Grechka, 2007), as shown on Figure 3.8. This assumption is accomplished whenever the fracture length spacing and width are considerably small compared to seismic wavelength. In this kind of media, the compliance tensor is described by four (4) independent elements, corresponding to two (2) Lamé constants for the isotropic background and two (2) fracture densities, one for each fracture set (Grechka and Kachanov, 2006a).

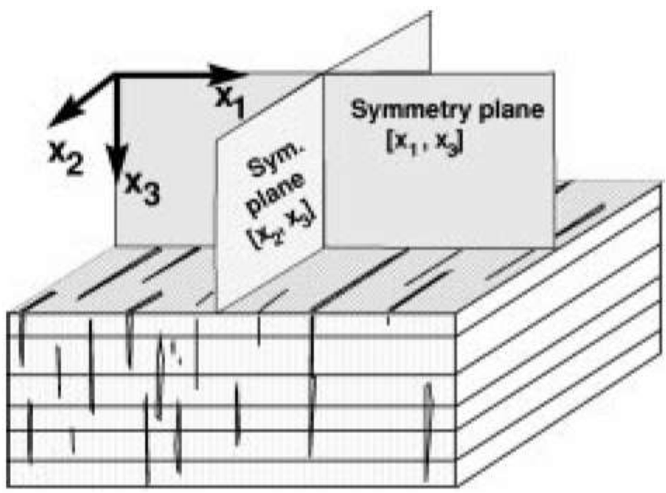

Figure 3.8. Orthorhombic model (from Tsvankin, 1997).

The existing ultrasonic lab measurements (Rojas, 2005) correspond to un-fractured core plugs from the tight-gas sand interval, which is known to be fractured in depth (Matesic, 2007). These measurements clearly show that there is no outstanding difference between the measured fast and slow shear-wave velocities ($\boldsymbol{Vs_1}$ and $\boldsymbol{Vs_2}$ respectively) as seen on Figure 3.9, since their corresponding experimental error bars overlap each other. This observation could allow assuming a closely isotropic background (matrix) rock, so the seismic anisotropy is mainly caused by natural fractures (Vasconcelos and Grechka, 2007).

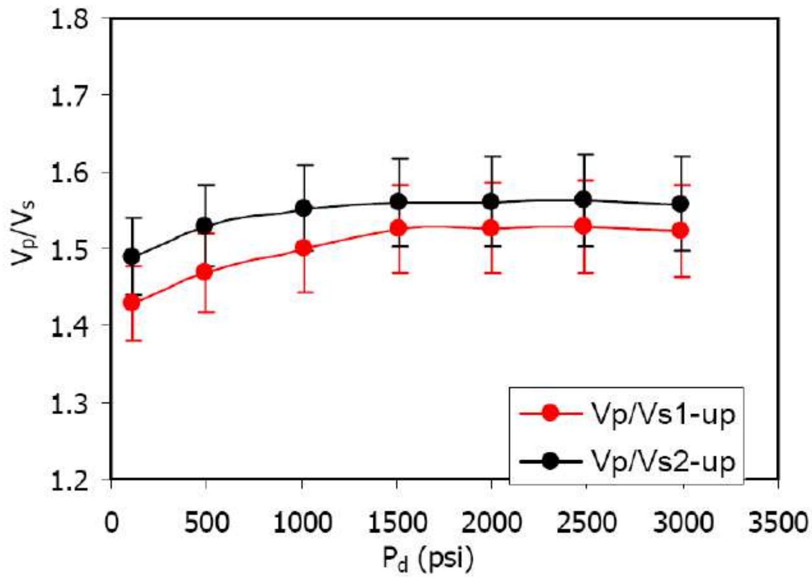

*Figure 3.9. Anisotropic **V_P/V_S** vs effective stress. Fast **V_P/V_S** in red (**V_P/V_{S1}**), slow **V_P/V_S** (**V_P/V_{S2}**) in black (from Rojas, 2005).*

It might be inferred that time-lapse signature of anisotropy is due to the change of fracture width because of the fluid pressure change within the cracks, however it has been demonstrated that the fracture aspect ratio does not influence seismic wave propagation in the case of dry (gas bearing) cracks (Schoenberg and Sayers, 1995; Bakulin et al, 2000; Grechka and Kachanov, 2006a). The anisotropy influence on time-lapse signature is controlled by the change of the normal (K_N) and tangent (K_T) compliances of the crack planes due to stress changes (Bakulin et al., 2000). Instead of open spaces within the rock matrix, fractures can be represented by inclusions or "weaknesses" on the isotropic host rock described by their corresponding compliances (Grechka and Kachanov, 2006b). The change of the reservoir fluid pressure affects the compliances of the cracks in both normal and tangential directions relative to the fracture planes, providing an imprint in the time-lapse seismic signals. This hypothesis has been supported by both theoretical and numerical modeling examples (Bakulin et al, 2000; Grechka and Kachanov 2006b).

In case of an isotropic host rock characterized by their Lamé constants λ and μ, the normal (Δ_N) and tangential (Δ_T) weaknesses are defined according to the linear-slip theory (Bakulin et al, 2000) as shown on equations 3.7a and 3.7b. These weaknesses vary from 0 to 1, whose expressions are valid for the case of fractures not hydraulically connected to the pores in the host rock.

$$\Delta_N = \frac{(\lambda + 2\mu)K_N}{1 + (\lambda + 2\mu)K_N}$$
$$\Delta_T = \frac{\mu K_T}{1 + \mu K_T} \tag{3.7}$$

In case of a fractured porous media it has to be assumed that inter-granular pores on the host rock and fractures are hydraulically connected. Under stress conditions, a fluid can move between pores and fracture space, so in case the fluid moves from fractures to pore space, cracks cannot preserve continuity of displacements normal to their faces because they are not stiff enough. If a small concentration of pores is considered, then equant porosity can be modeled as a dilute distribution of spheres into an isotropic host rock according to the Thomsen's model of fractured porous media (Bakulin et al, 2000), leading to the Thomsen's model weaknesses shown on equations 3.8a and 3.8b, as a function of the crack density ***e*** of the dominant fracture set, and the parameter ***g*** defined on equation 3.9.

$$\Delta_N = q\frac{4e}{3g(1-g)},$$
$$\Delta_T = \frac{16e}{3(3-2g)} \tag{3.8}$$

$$g \equiv \frac{\mu}{\lambda + 2\mu} = \frac{V_S^2}{V_P^2} \tag{3.9}$$

V_S and V_P are the S- and P- wave velocities for the isotropic host. The equant porosity ***q*** is a function of the bulk modulus of the fluid filling the cracks (***k'***), the Lamé constants of the isotropic host (λ and μ) and the fluid factor D_{cp} which accounts for the interconnection between cracks and pores, as shown on equation 3.10.

$$q = \left(1 - \frac{\kappa'}{\lambda + 2/3\mu}\right) D_{cp} \qquad (3.10)$$

The well-known low connectivity of inter-granular pores in Rulison reservoirs could prevent fluid flow (squirt) between cracks and pores, so the fractures could be stiff enough to maintain the continuity of displacements orthogonal to the cracks surfaces.

Since λ and μ do not change significantly on a time-lapse basis for a low-porosity host rock, the corresponding time lapse signature should be due to the change of the fracture compliances, or their corresponding weaknesses. The linear-slip model represents fractures as highly compliant (soft) thin layers or inclusions within a host isotropic rock, with border conditions allowing linear slip (not-welded) along the inclusion-host rock interfaces (Bakulin et al, 2000), which implies that there is continuity of displacements normal to the fracture planes, but the displacements tangent to the crack planes are not continuous. This assumption implies that any change on normal compliance and weakness is going to provide an imprint on shear-wave time-lapse seismic signal. In case the shear-wave surface seismic modes are properly rotated for a preferential azimuth of a dominant set of vertical fractures, the slow-shear wave mode (S22) is going to be more sensitive to changes on pressure within the fractures because it is polarized in such a way that rock particles move in a direction orthogonal to the crack surface, characterized by the normal compliance or weakness.

Shear-wave splitting (γ) can be estimated on an amplitude-based way from post-stack inversion of fast- and slow-shear wave data (Rumon, 2006). This anisotropy parameter has been frequently used in fracture characterization as an indicator of fracture density. Its expression for a HTI media (Bakulin et al, 2000) is shown on equation 3.11. It depends only on the V_P/V_S ratio of the isotropic host expressed by g, and the fracture density e.

$$\gamma = -\frac{8e}{3(3-2g)} \tag{3.11}$$

As mentioned before, $\boldsymbol{g}$ is not expected to change significantly on time-lapse for this highly consolidated reservoir, so the shear-wave splitting $\boldsymbol{\gamma}$ will be time-lapse sensitive in the same way the crack density $\boldsymbol{e}$ does. There are two realistic ways $\boldsymbol{e}$ can change in time-lapse:

- Some natural fractures can vanish due to complete closure, or
- New fractures created due to hydraulic fracturing.

The first scenario is caused by pressure drop due to depletion, leading to a lower counting of fractures in the host rock. However, this implies a change of the aspect ratio which has no influence on long-wavelength seismic signatures, and probably requires closure of a massive amount of cracks. The second scenario will provide an imprint on time-lapse analysis as far as the creation of new cracks during hydraulic fracturing is high enough to give rise of a seismically detectable change of fracture density $\boldsymbol{e}$.

Any seismic attribute based on the slow-shear wave mode, such as S22-impedance or $\boldsymbol{V_P/V_{S2}}$, is going to be sensitive in time-lapse basis whenever the vertical fracture set under analysis has an azimuth that agrees the orientation used for Alford rotation that provided the slow-shear wave mode used for analysis. There are cases where zones of the same reservoir are characterized with different fracture set orientations (Vasconcelos and Grechka, 2007), which could even provide more time-lapse sensitivity for the fast-shear wave mode, so special care has to be taken when interpreting time-lapse anomalies from slow-shear wave data.

3.5 Impedance-filtered V_P/V_S

Historically, it has been demonstrated that V_P/V_S ratio is a reliable tool for lithology discrimination in most of the cases (Tatham, 1985; Eastwood and Castagna, 1986). Rojas (2005) showed that low V_P/V_S values correlate with low-GR values (higher sand content) as shown on Figure 3.10.

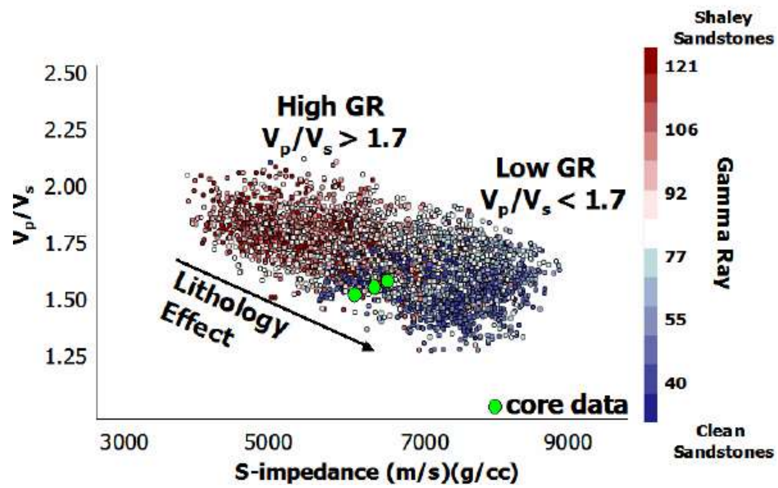

Figure 3.10. Cross-plot V_P/V_S vs S-Impedances, color coded with GR (from Rojas, 2005).

However, the range of variation of V_P/V_S for sands has a high overlap zone with that for shales. It is required to figure out new ways of cross-plotting in order to perform better lithology discrimination. The way I first proposed is based on the creation of a flag log, called ***RQI*** (Reservoir Quality Index) which is built using the volume of shale (***Vsh***) and resistivity (ILD) logs on control well RU-7 as shown on figure 3.11. ***RQI*** =1 if ***Vsh*** is equal or lower than 0.1 and ILD is equal or larger than 75 Ωm, else ***RQI*** =0. By assigning a flag to each depth in the log, the cleanest and high-resistive sands in the section can be identified. This scheme does not consider the pressure regime and it is static, but it might be refined by including high-pressure as a threshold too. Later, I cross-plotted P-impedance (Z_P) versus S11-impedance (Z_{S1}) color coded with the ***RQI*** flag log for the UMVS-Cameo interval as shown on figure 3.12.

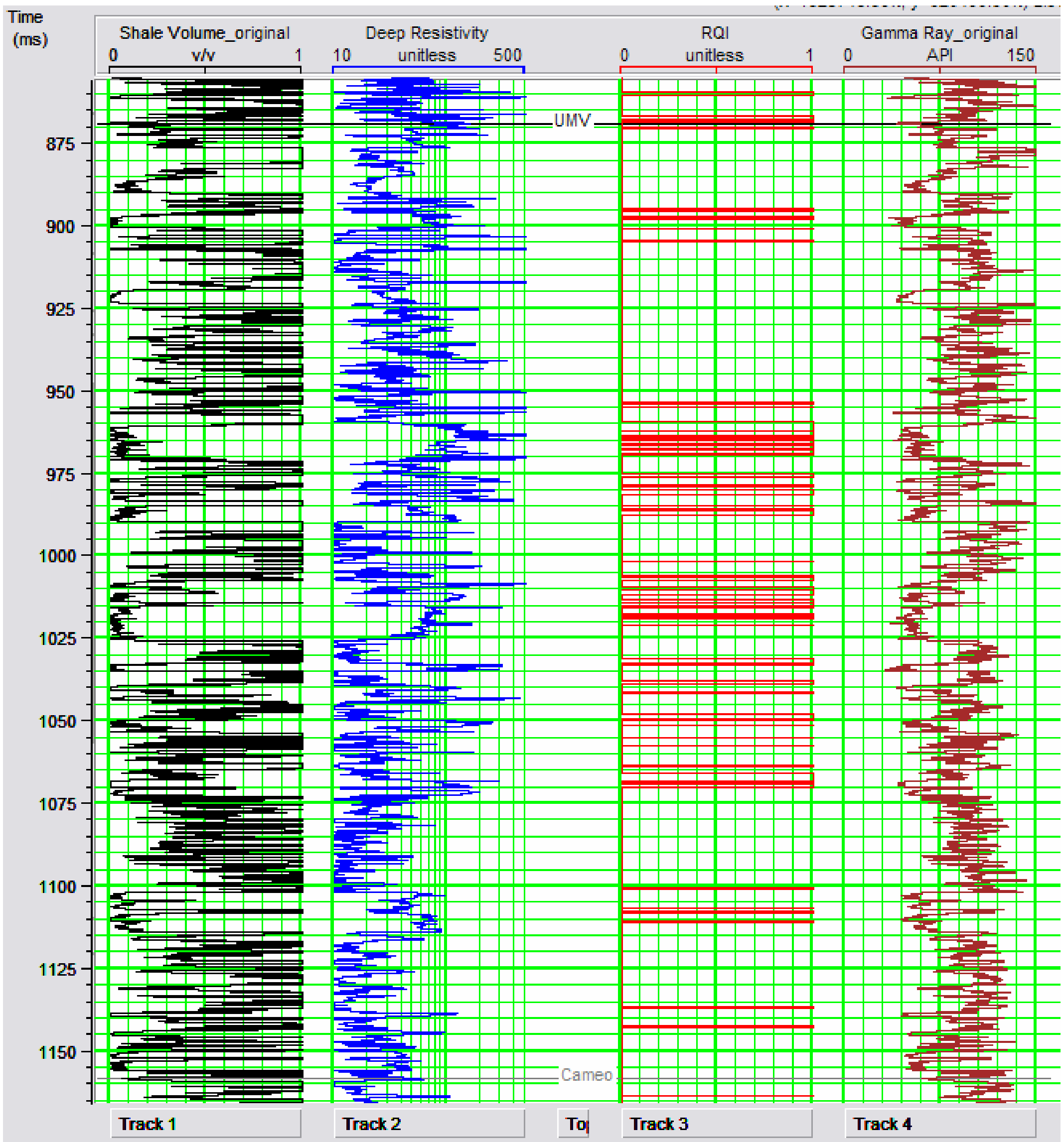

*Figure 3.11. RU-7 log suite for static characterization. Track 1: **Vsh** log (black). Track 2: ILD (blue). Track 3: **RQI** (red). Track 4: GR (brown).*

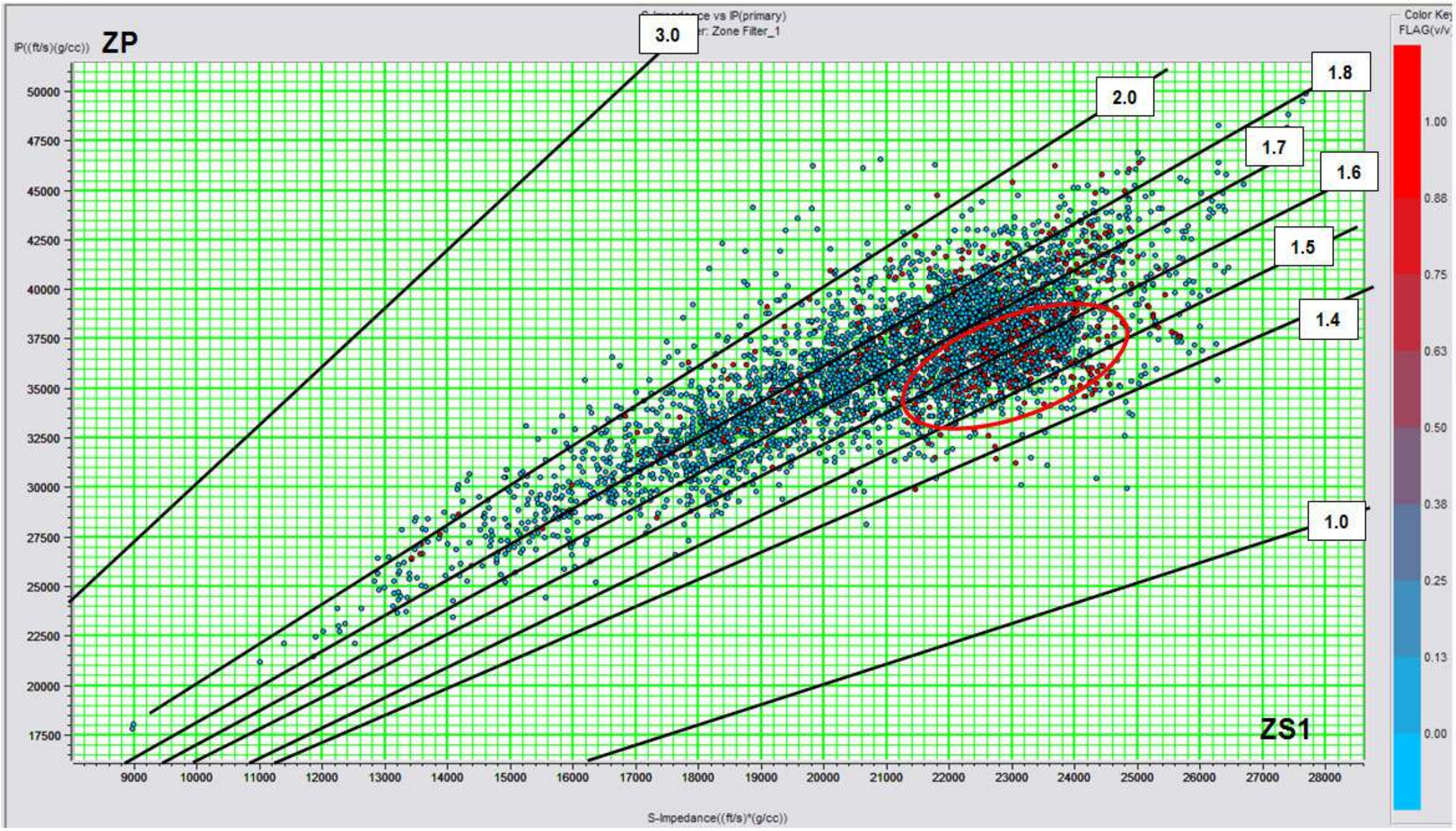

Figure 3.12. RU-7 cross-plot $\boldsymbol{Z_P}$ *vs* $\boldsymbol{Z_{S1}}$ *color coded with* ***RQI****. Constant* $\boldsymbol{V_P/V_{S1}}$ *lines overlay.*

From the previous section it was stated that the fast-shear mode has a lower time-lapse change than slow-shear mode in the UMVS-Cameo interval for a preferential fracture orientation, so the fast-shear mode could be more helpful for static characterization, which is the reason the cross-plot on Figure 3.12 is done using the fast-shear mode. Several observations can be made from this chart: First, lines of constant V_P/V_{S1} or iso-V_P/V_{S1} lines can be drawn, since the Z_P / Z_{S1} ratio is equal to V_P/V_{S1}. Second, the distribution of points shows a background linear trend with higher point dispersion at high impedances, with a cluster of points (anomaly) highlighted with the red ellipse. Also there is a high concentration of ***RQI*** =1 points in this cluster, which could allow concluding that the resistive cleanest sands of the interval could be described by the combination of the Z_P and Z_{S1} values constrained by the ellipse that highlights the high concentration of clean sands. However, this is not totally conclusive because of the distribution of points inside the ellipse that does not allow to conclude if many ***RQI*** =1 points could be overlaid by ***RQI*** =0 points or even be absent.

Figure 3.13 depicts a similar plot, but color coded with ***Vsh*** instead of ***RQI***. In this case is clearer the cluster of points (pink ellipse) out of the linear background trend, and is also clear that the vast majority of these points correspond to low ***Vsh*** values (cleanest sands). From these plots I conclude that V_P/V_S alone cannot effectively discriminate lithology, since a low V_P/V_S value can at the same time characterize sands and shales as shown on the iso- V_P/V_S lines. By combining V_P/V_S with its parents P- and S- impedance volumes it is possible to enhance the lithology discrimination by filtering the V_P/V_S values based on the impedances used for determining it, as show schematically in figure 3.14. Two (2) different pairs of realistic impedances (Z_P, Z_{S1}) can give rise to the same V_P/V_S value, but using a filter in the Z_P - Z_{S1} space as shown in the cross-plot it is possible to highlight those samples in the V_P/V_S volume that correspond to their parents impedances defined by the filter, helping to reduce the ambiguity or non-uniqueness of V_P/V_S relative to the impedances.

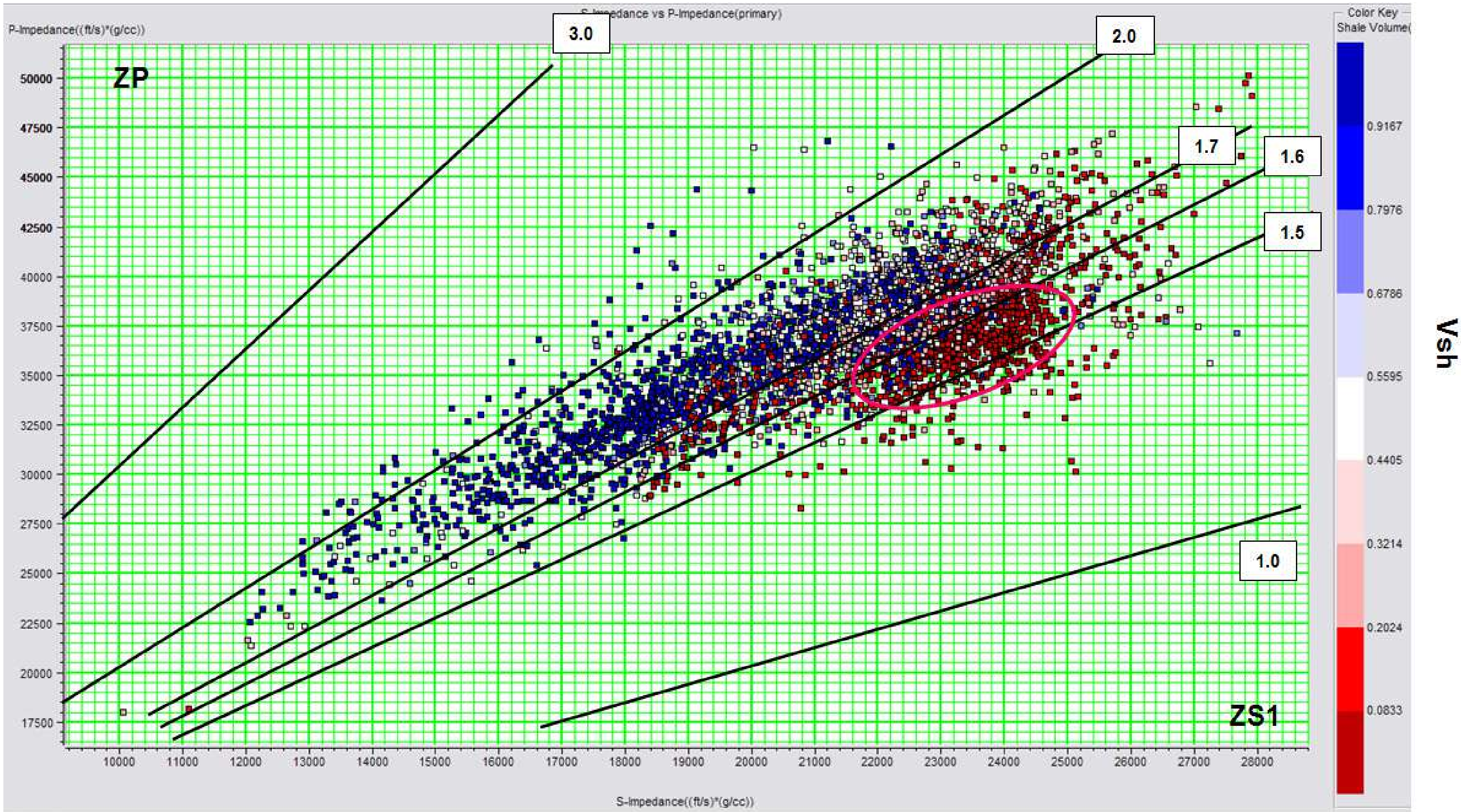

Figure 3.13. RU-7 cross-plot $\mathbf{Z_P}$ *vs* $\mathbf{Z_{S1}}$ *color coded with* ***Vsh****. Constant* $\mathbf{V_P/V_S}$ *lines overlay.*

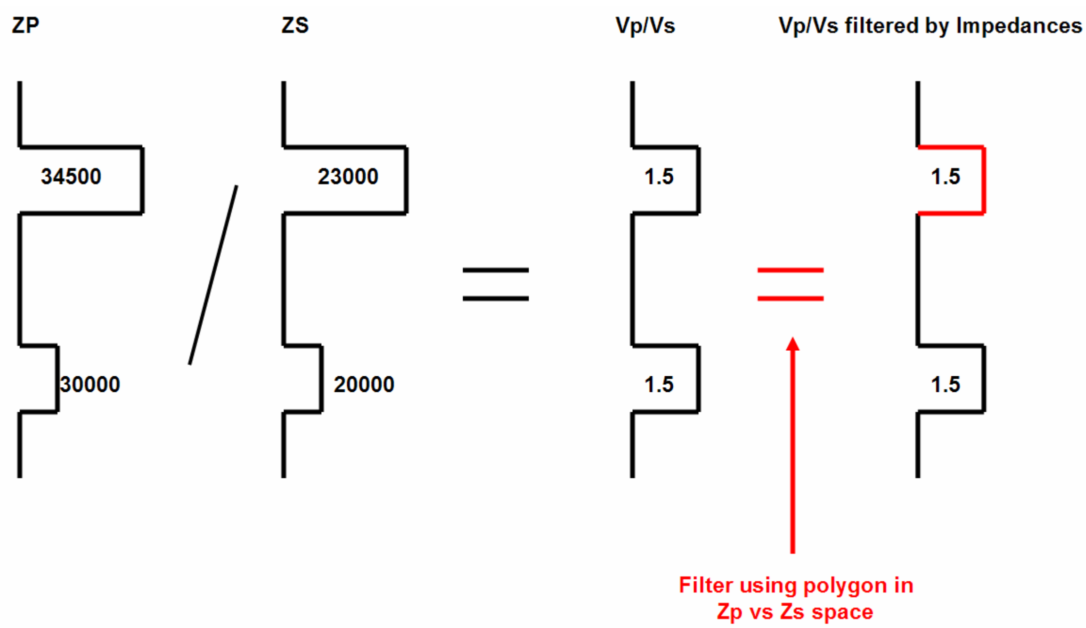

Figure 3.14. Scheme of Impedance-filtered V_P/V_S.

3.6 Summary

The analysis of existing ultrasonic measurements from un-fractured sand core plugs (figure 3.4) allows me to conclude that V_P/V_S can be useful in a time-lapse basis in order to image reservoir pressure changes and over-pressured areas, which can be done also quantitatively by translating V_P/V_S values into effective stress domain through a mapping function (eq. 3.4) derived from the data fitting of core lab measurements. The reservoir pressure changes can have an imprint into seismic velocities as expected. Both theory and modeling demonstrate the sensitivity of the seismic signals to velocity changes caused by pressure changes.

The understanding of the role of seismic anisotropy in a time-lapse basis allowed me to figure out the version of V_P/V_S to be used for dynamic characterization (V_P/V_{S2}) due to the presence of preferential orientation of fracture sets at main reservoir level, whenever the fracture preferential orientation agrees the Alford rotation azimuth applied to surface seismic data.

The static description of the main reservoir (tight gas sands) can be improved by using the impedance-filtered V_P/V_S as shown on the cross-plots, especially to image the cleanest sand bodies, reducing the ambiguity of V_P/V_S by using its parent impedances as a combined filter/highlighter based on petrophysics cross-plotting.

CHAPTER 4
CROSS-EQUALIZATION

4.1 Fundamentals

Cross-equalization can be defined as a series of processes applied to time-lapse seismic as an effort to match the involved datasets (base and monitor survey(s)) in terms of their frequency spectrum, arrival times and amplitudes in those zones that have not been changed (Sheriff, 2002). The interpreter's goal of these processes is to attenuate the time-lapse differences not related to the reservoir development (such as acquisition and processing artifacts) as a mean to enhance the real time-lapse differences associated to the reservoir development (such as primary depletion, fluid injection, thermal recovery, etc).

The way cross-equalization is performed is based on the sequential design and application of operators in time, frequency and amplitude domains. These operators are designed in what is known as the static window, which is a seismic interval depth-equivalent to a subsurface interval that has not undergone changes on its elastic properties due to the development of a hydrocarbon reservoir. This property allows a close match of time-lapse surveys in the static window, and when these operators are applied to the whole volumes allows attenuating time-lapse differences not related to reservoir development. The basic cross-equalization operators can be described as follows:

- <u>Re-binning</u>: Basically consists on matching the traces position to a common surface bin due to different acquisition geometries among the base and monitor surveys (s).

- <u>Static time-shift</u>: Once the static window has been defined, this operator applies a bulk shift to each trace in a volume (usually the monitor survey(s)) to match the reference survey (commonly the base survey) for a common seismic event or package of seismic events located in the static window, based on trace by trace cross-correlation.

- Frequency matching: Based also on cross-correlation of traces in the static window among the base and monitor survey(s), this process designs a Wiener-Levinson shaping filter that is convolved with the survey we want to match, usually applied to the volume with more abundant high frequencies, in order to avoid boosting high-frequency noise when applied in the opposite case.

- Cross-normalization: This operator applies a trace by trace gain factor to the whole monitor survey(s). This gain factor is calculated in the static window by taking the ratio of the RMS values of every common pair of traces. Its goal is to match the surveys in terms of amplitudes.

- Time-variant time shifts: If the interpreter wishes to perform time-lapse comparisons based only on amplitudes then the seismic events, even at reservoir level, need to be matched among the surveys in terms of arrival times due to the changes on the reservoir velocities. This goal is achieved by applying time-variant time shifts to the whole monitor survey(s), which is designed independently of the static window and is based also on cross-correlation of common trace pairs and a sliding window. This step applies a time-shift to every sample in the sliding window according to the maximum lag of the local cross-correlation.

The cross-equalization quality control (QC) can be done by calculating a similarity attribute known as NRMS (Normalized Root Mean Square) (Kragh and Christie, 2002) as shown on equation 4.1:

$$NRMS = \frac{2 * RMS(monitor_t - base_t)}{RMSmonitor_t + RMSbase_t} \tag{4.1}$$

where $base_t$ and $monitor_t$ represent the base and monitor samples for a given trace within the static window respectively. *RMS* is the acronym for the root-mean square taken from the corresponding data within the static window. The output is going to be a value ranging from 0 to 2 per common trace location involved, so for a common trace pair, the closer to 0 NRMS is, the more similar the base and monitor surveys are. This attribute is calculated after each cross-equalization step in order to assess the level of improvement in the repeatability of the surveys.

4.2 Cross-Equalization strategy in Rulison Field

The Reservoir Characterization Project (RCP) acquired three (3) time-lapse 3D-9C dedicated surveys in the years 2003, 2004 and 2006. These surveys were processed by CGG Veritas under a time-lapse scheme, so it is expected that cross-equalization must be highly efficient when dealing with these time-lapse dedicated surveys. Since my research is based on the PP, S11 and S22 modes for all these years, I applied the cross-equalization using the Hampson & Russell Pro4D® software for every wave mode separately using the 2003 survey as the base vintage, as shown on Figure 4.1. For each wave mode, the 2006 volume was first cross-equalized to match the 2003 volume, and then the 2004 volume match to 2003 volume. The reason for this order lies in the fact that 2004 acquisition conditions (rain) were far different from those for 2003 and 2006 (Robert Benson, personal communication) which especially affected this survey in the spectral domain (Keighley, 2006). By doing first the 2004-2003 cross-equalization would have implied to apply a strong shaping filter to the 2003 survey and also to the 2006 survey because they have lower attenuation for the higher frequencies compared to the 2004 survey.

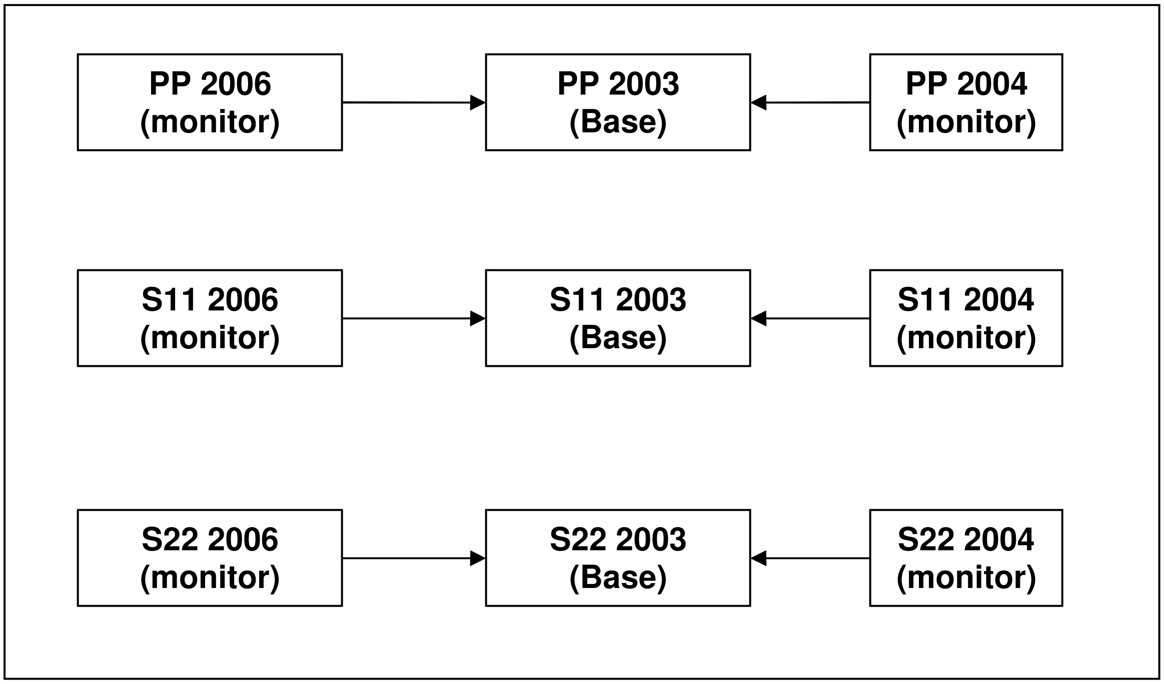

Figure 4.1: Cross-equalization of 2003, 2004 and 2006 surveys in separate wave modes.

The choice of the static window is based on the previous work in the area for PP mode (Keighley, 2006) and S11 & S22 (Rumon, 2006). Table 4.1 shows the static window top and bottom for each wave mode on their original time domains.

Wave Mode	Top of Static Window (ms)	Bottom of Static window (ms)
PP	700	926
S11	1800	1900
S22	1800	1950

Table 4.1: Static windows for cross-equalization of the different wave modes involved.

It is assumed that the overburden does not change significantly in time-lapse basis compared to the reservoir so it can be considered as static.

4.3 Cross-Equalization PP-2006 to PP-2003

As mentioned before, I first cross-equalized PP-2006 to match the PP-2003 volume as part of the cross-equalization strategy using the static window 700-926 ms, which contains the depth-equivalent events for Top Mesa Verde and UMVS. Figure 4.2 shows both PP-2003 and 2006 volumes before cross-equalization, and Figure 4.3 shows the NRMS map at this stage with its corresponding histogram seen on Figure 4.4. An overall NRMS=0.35 allows to conclude that both acquisition and processing provided a good degree of data repeatability for these datasets, repeatability improved by cross-equalization as it is shown on later figures.

4.3.1 Static Time-shift

The time shifts to the 2006 data were applied by calculating the cross-correlation between the 2006 and 2003 data using only the samples of the traces within the static window. The maximum allowed time shift was set on 20 ms. The maximum correlation found in a trace by trace basis is shown on Figure 4.5, and its corresponding histogram on Figure 4.6. On the map view can be appreciated that there is a uniform distribution of high cross-correlation values as seen on its corresponding histogram with most of the values being higher than 0.9.

The calculated and applied time-shifts are seen on Figure 4.7 as a map view and Figure 4.8 as its corresponding histogram. Most of the traces on PP-2006 survey needed a negative time shift which means that the events in the static window originally had later arrival times compared to the same events in the PP-2003 volume, which can be interpreted as lower overburden velocities in the year 2006 compared to 2003, probably due to velocity differences in the weathering layer (i.e. different weather conditions), or acquisition conditions (i.e. different source and/or receiver coupling conditions). These time-shifts were applied to the corresponding traces of the PP-2006 volume, so both the base PP-2003 and shifted PP-2206 are shown on Figure 4.9. Since the applied time shifts were very small, there is no obvious change on the PP-2006 dataset that can be seen by naked-eye. The difference PP 2006-2003 before and after the application of the static time shifts is shown on Figure 4.10. Visually, cross-equalization results can be assessed by seeing how attenuated are the differences within the static window.

This assessment is supported by the NRMS after the application of the static time-shifts shown on Figure 4.11, with its corresponding histogram depicted on Figure 4.12. The map view (Figure 4.11) presents more uniformly distributed lower NRMS values, and the histogram shows a peak shifted from around 0.35 (before application of time-shifts) to around 0.25 (after applying time-shifts) with a narrower distribution. I conclude that the repeatability has been increased through the application of static time-shifts to PP-2006.

The next common step on cross-equalization is the design and application of the shaping filter. In the case of PP data, Keighley (2006) using PP 2003 and 2004 data found out that on the PP 2004 data, high frequencies (over 50 Hz) are more attenuated than on the PP 2003 data. He applied a shaping filter to PP 2003 in order to match the PP-2004 frequency content. Considering all the datasets for PP wave mode and making a comparison as seen on Figure 4.13, I conclude that it is not necessary to apply a shaping filter to the PP data because this implies modifying the spectral content of PP 2003 and 2006 to match the PP 2004 spectral content, and this mismatch at high frequencies can be neglected since this occurs mainly in the right slope of the amplitude spectra.

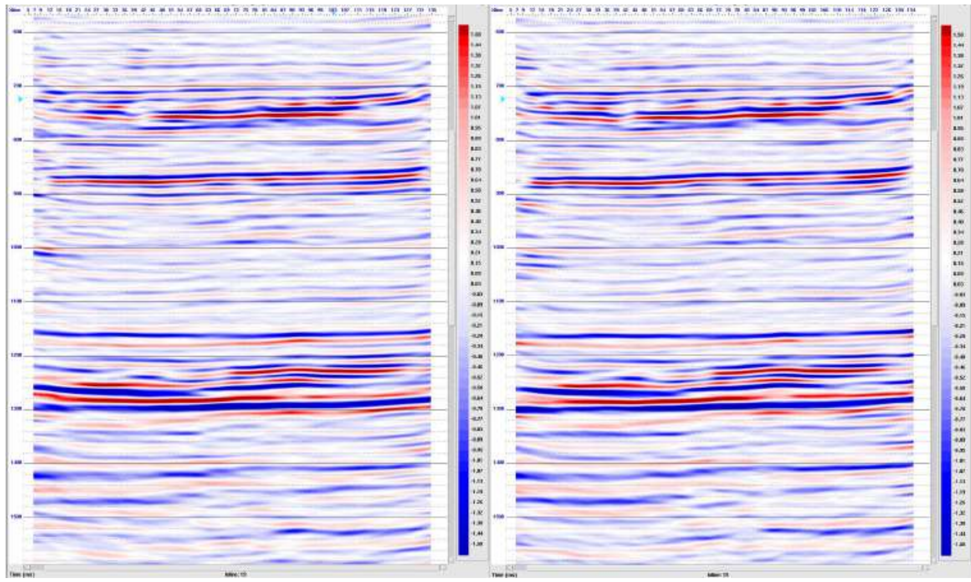

Figure 4.2. Inline 19: PP-2003 (left) and PP-2006 (right).

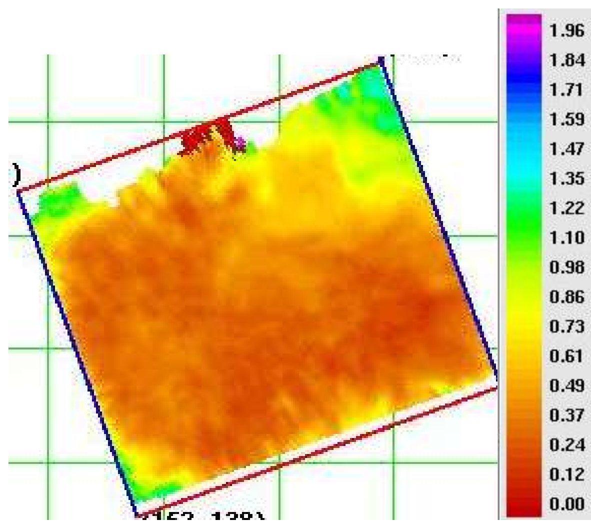

Figure 4.3. NRMS PP 2003-2006 for raw data.

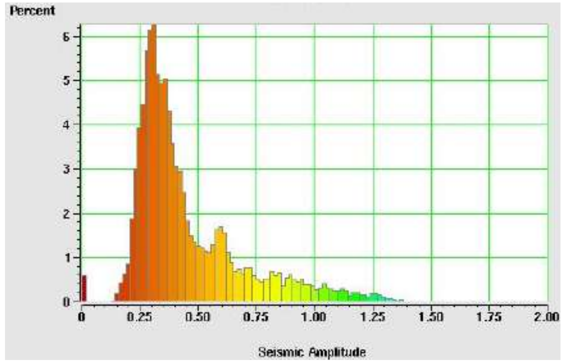

Figure 4.4. Histogram of NRMS PP 2003-2006 for raw data.

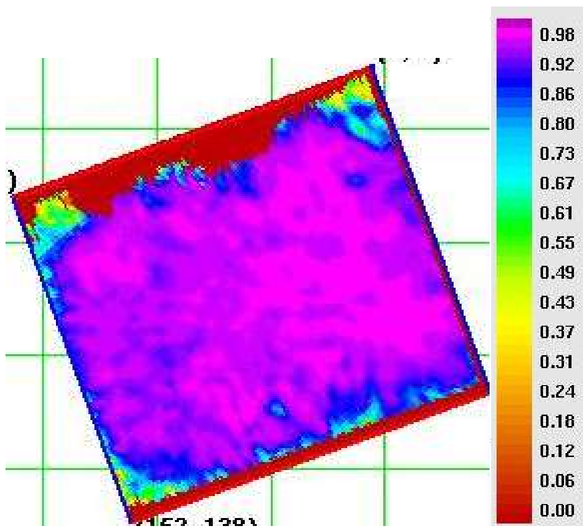

Figure 4.5. Maximum cross-correlation (PP-2003 & 2006) map distribution expressed in fraction.

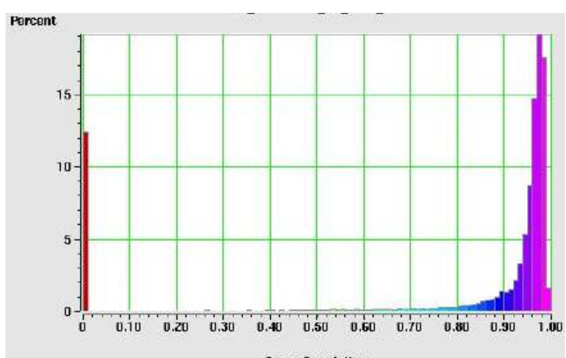

Figure 4.6. Maximum cross-correlation (PP-2003 & 2006) histogram, expressed in fraction.

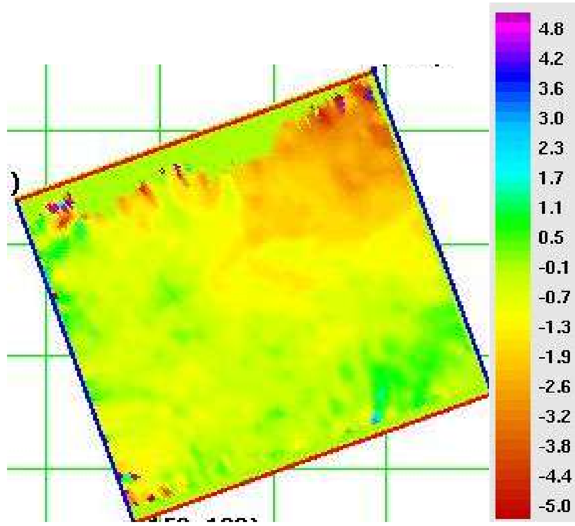

Figure 4.7. Time-shifts applied to PP-2006 relative to PP-2003.

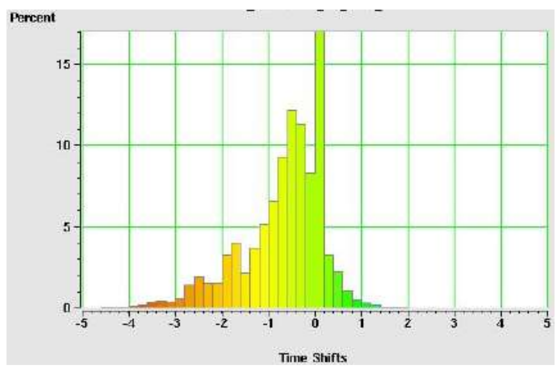

Figure 4.8. Histogram of the time-shifts applied to PP-2006 relative to PP-2003.

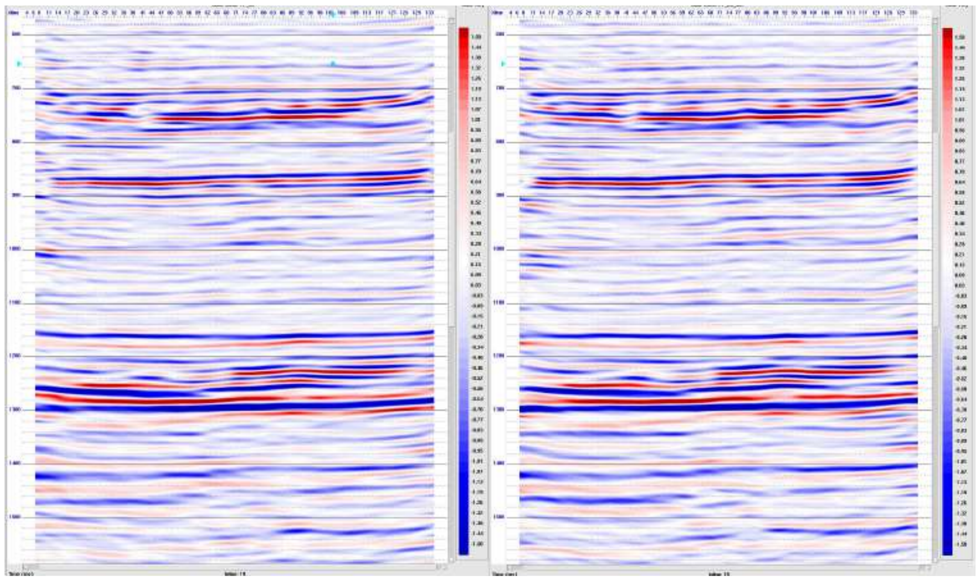

Figure 4.9. Inline 19: PP-2003 (left) and PP-2006 (right), after application of static time shifts to PP-2006.

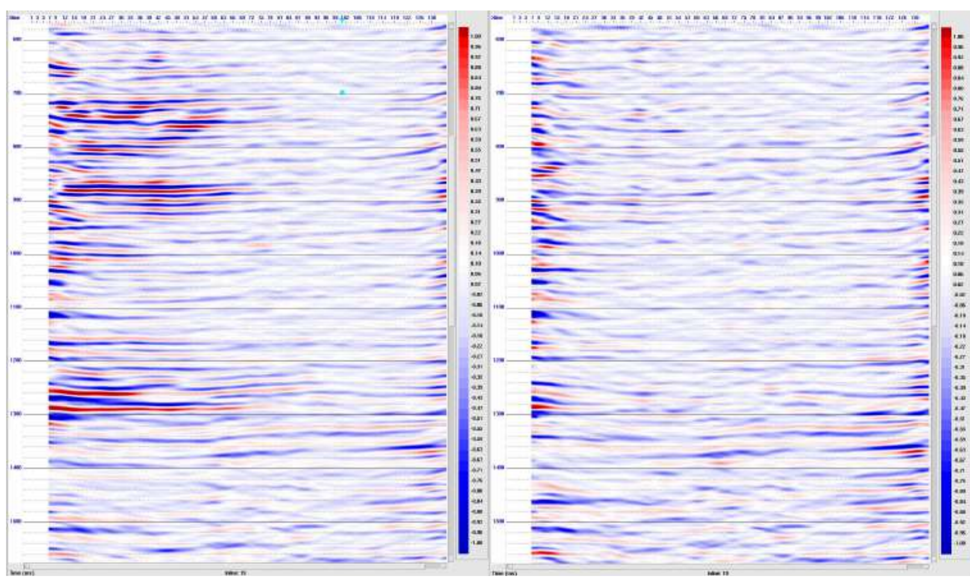

Figure 4.10. Inline 19: Difference PP 2006-2003 for raw data (left) and after application of static time shifts to PP-2006 (right).

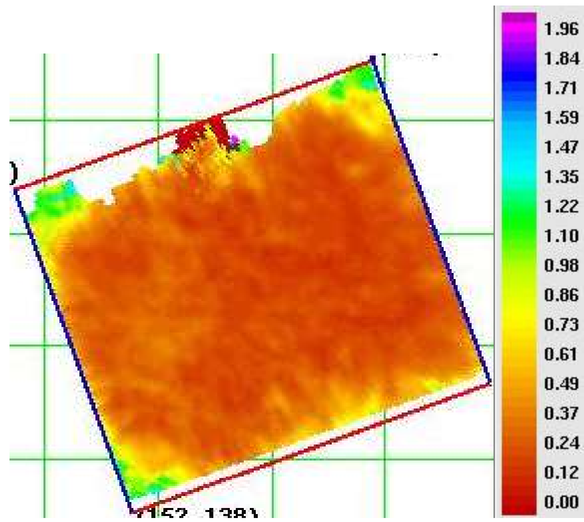

Figure 4.11. NRMS PP 2003-2006 after application of time-shifts to PP-2006.

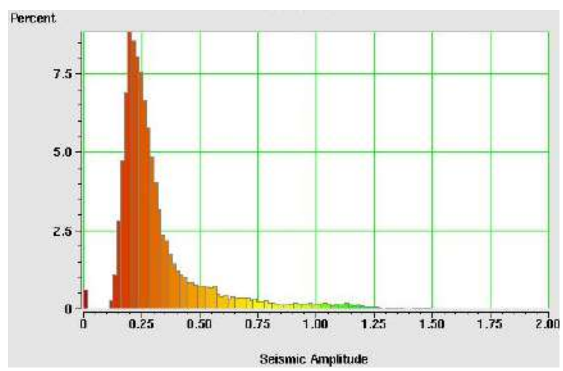

Figure 4.12. Histogram of NRMS PP 2003-2006 after application of time-shifts to PP-2006.

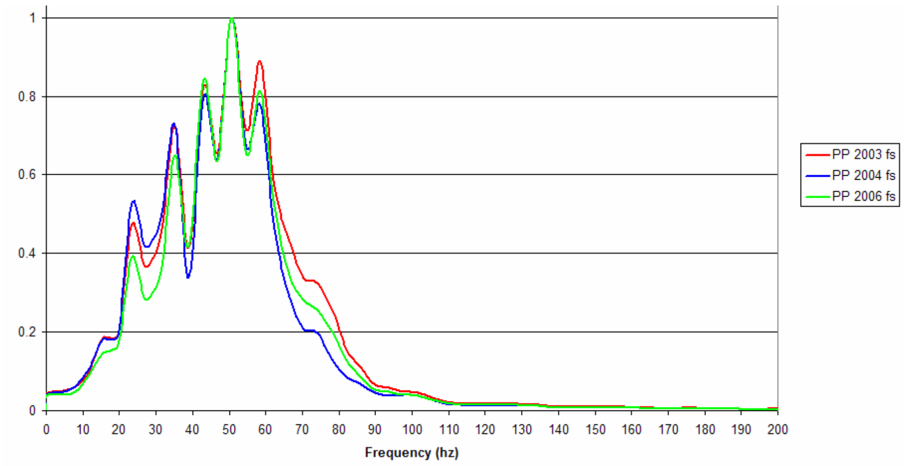

Figure 4.13. Amplitude Spectra of PP-2003 (red), PP-2004 (blue) and PP-2006 (green).

4.3.2 Cross-Normalization (Gain)

The amplitude matching between the two surveys was done by calculating the gain factors in a trace-by-trace basis within the static window. A map view of these gain factors is depicted on Figure 4.14 and its corresponding histogram on Figure 4.15. From these figures can be seen that the scaling of amplitudes applied to PP-2006 dataset to match the PP-2003 dataset is not strong since most of the gain factors are around 1, which also could be an indicative sign of the level of repeatability between the surveys.

These gain factors were applied to their corresponding traces on the PP-2006 volume, which results are shown along with PP-2003 on Figure 4.16. Using this volume, I calculated the PP 2006-2003 difference after applying the gain to PP-2006 and it can be compared to the difference before the application of the gain as seen on Figure 4.17, where no outstanding improvement can be seen. By interpreting the resulting NRMS on Figures 4.18 and 4.19 can be reinforced the point that both surveys already matched very well in terms of amplitudes before the application of the cross-normalization.

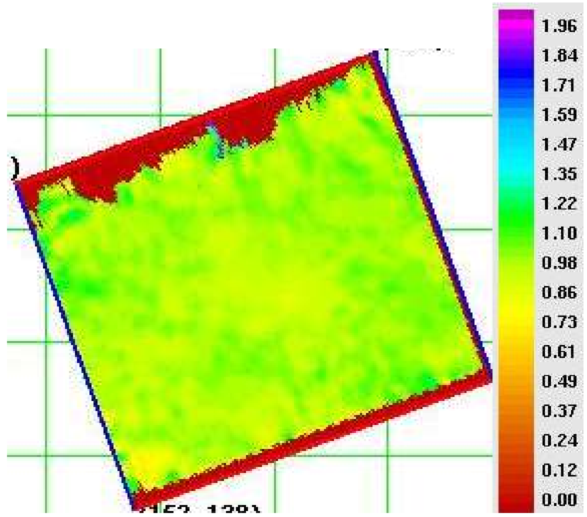

Figure 4.14. Gain factor (trace-by-trace) applied to the PP-2006 volume.

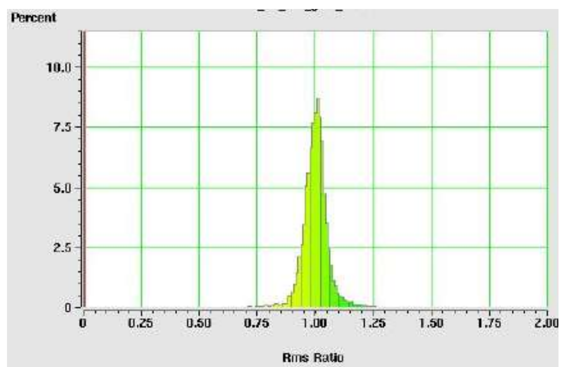

Figure 4.15. Histogram of the gain factor (trace-by-trace) applied to the PP-2006 volume.

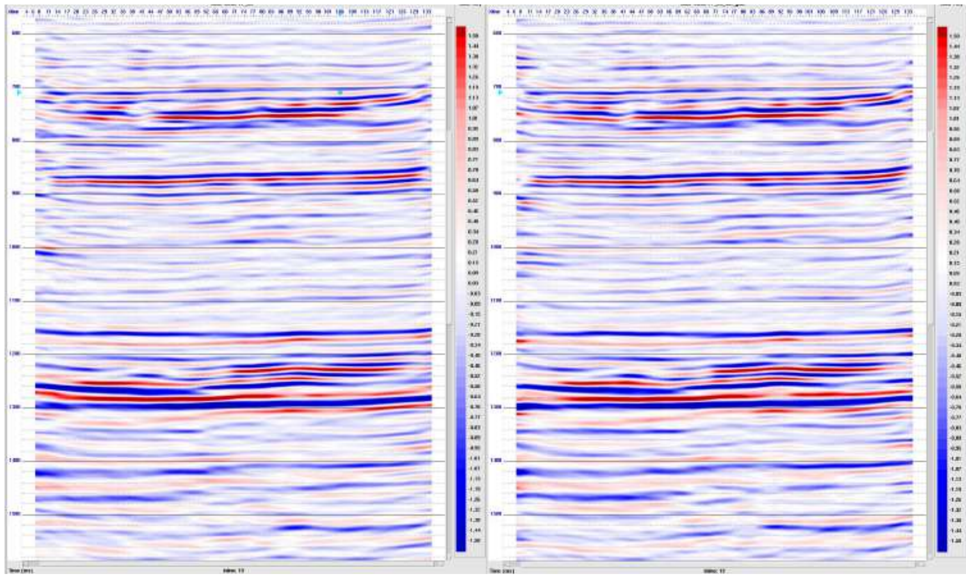

Figure 4.16. Inline 19: PP-2003 (left) and PP-2006 (right), after application of static time shifts and cross-normalization (gain) to PP-2006.

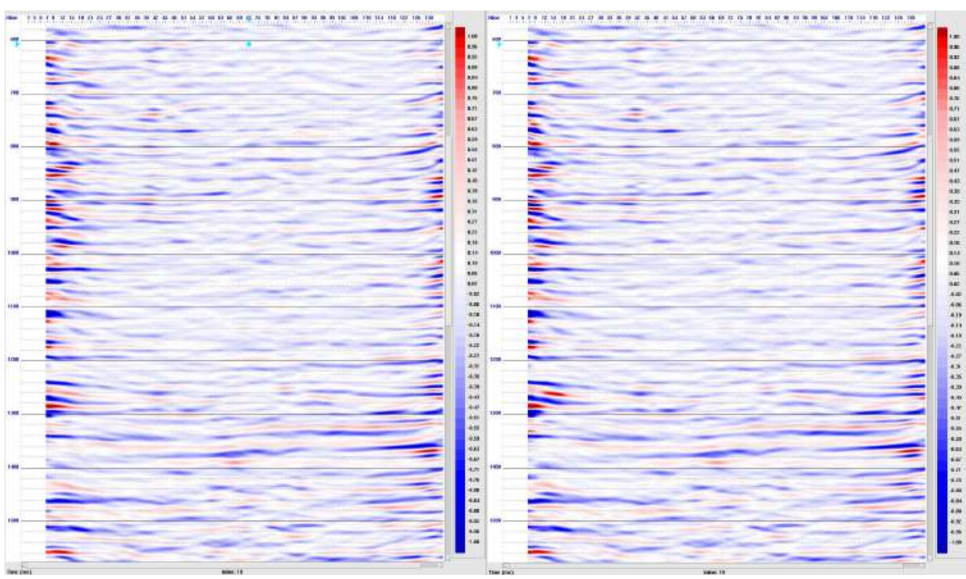

Figure 4.17. Inline 19: Difference PP 2006-2003 after application of static time shifts (left) and after application of time–shifts and cross-normalization (gain) to PP-2006 (right).

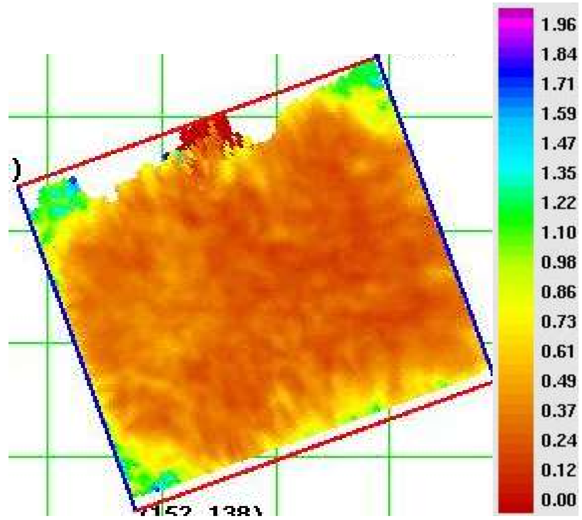

Figure 4.18. NRMS PP 2003-2006 after application of time-shifts and cross-normalization (gain) to PP-2006.

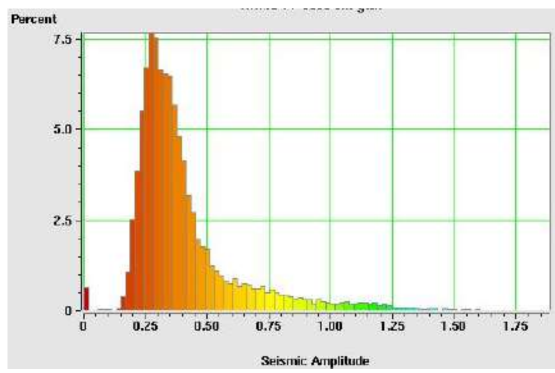

Figure 4.19. Histogram of NRMS PP 2003-2006 after application of time-shifts and cross-normalization (gain) to PP-2006.

4.3.3 Time-variant time-shifts

After testing different sets of parameters, this final stage in cross-equalization was performed by using a sliding window for correlation being 100 ms long and starting at 650 ms. This correlation window had a 1ms step and this correlation was done using 650 windows in order to cover all the seismic events-packages of interest (lower overburden, tight-gas sands interval and coals interval). The time-variant time shifts were designed to be applied to PP 2006, and the resulting volume is shown along with PP 2003 on Figure 4.20, and this was used to calculate the PP 2006-2003 differences shown on Figure 4.21 before and after applying these time-variant time shifts. Again there is no outstanding improvement in the repeatability of the surveys after the application of this last cross-equalization step, but observation of NRMS after the time-variant time-shifts as shown on Figures 4.22 and 4.23 shows that the main NRMS peak shifted toward values lower than 0.25, which means an improvement on the PP 2003-2006 surveys repeatability.

A final assessment of the PP 2003-2006 cross-equalization can be done by seeing the PP 2006-2003 before and after cross-equalization shown on Figure 4.24, where is outstanding the degree of attenuation of the differences in the static window after cross-equalization. This also is confirmed by the comparison of the NRMS before and after cross-equalization seen on Figure 4.25, where the series of processes allowed obtained a more uniform distribution of lower NRMS values, which is translated as an improvement of the repeatability of these surveys.

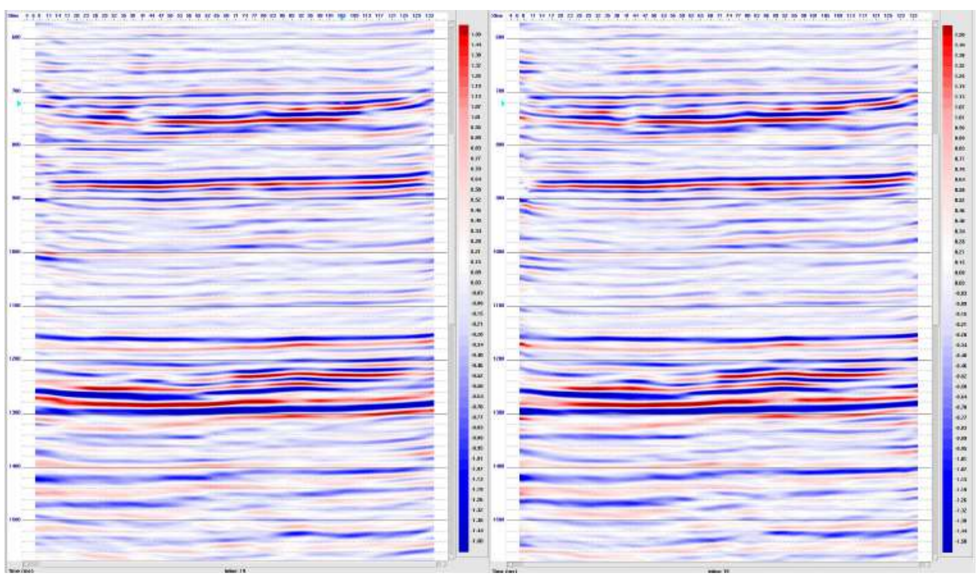

Figure 4.20. Inline 19: PP-2003 (left) and PP-2006 (right), after application of static time shifts, cross-normalization (gain) and time-variant time-shifts to PP-2006.

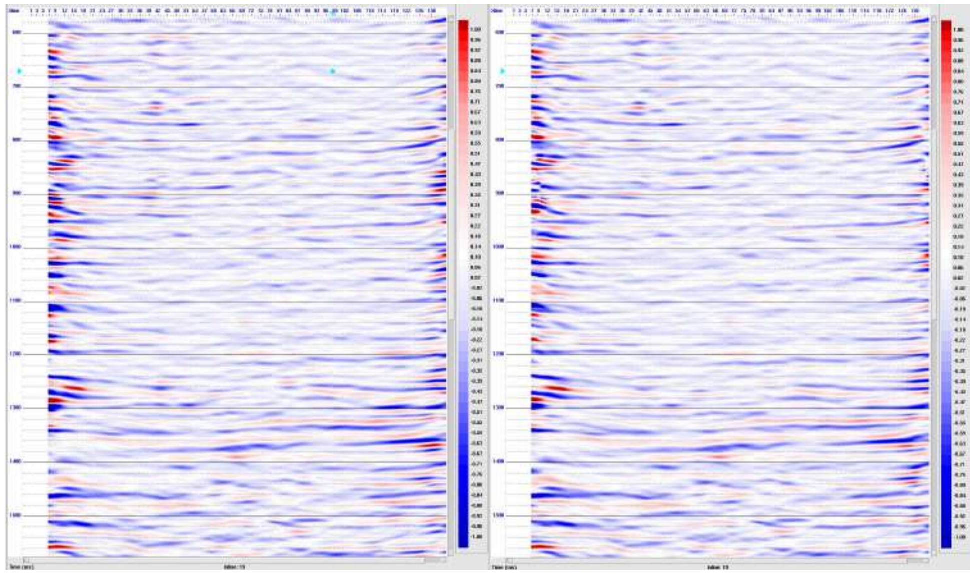

Figure 4.21. Inline 19: Difference PP 2006-2003 after application of time–shifts and cross-normalization (gain) (left), and after application of time–shifts, cross-normalization (gain) and time-variant time-shifts to PP-2006 (right).

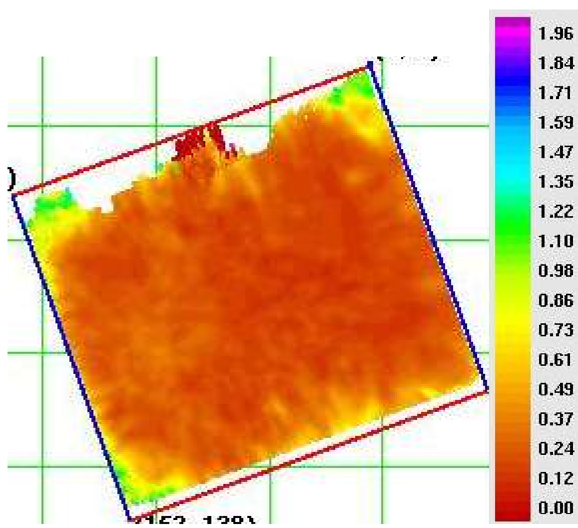

Figure 4.22. NRMS PP 2003-2006 after application of time-shifts, cross-normalization (gain) and time-variant time-shifts to PP-2006.

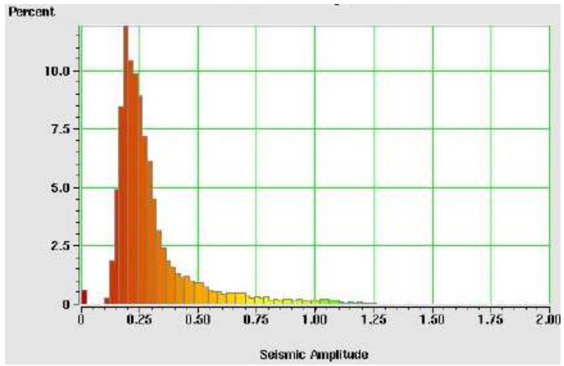

Figure 4.23. Histogram of NRMS PP 2003-2006 after application of time-shifts, cross-normalization (gain) and time-variant time-shifts to PP-2006.

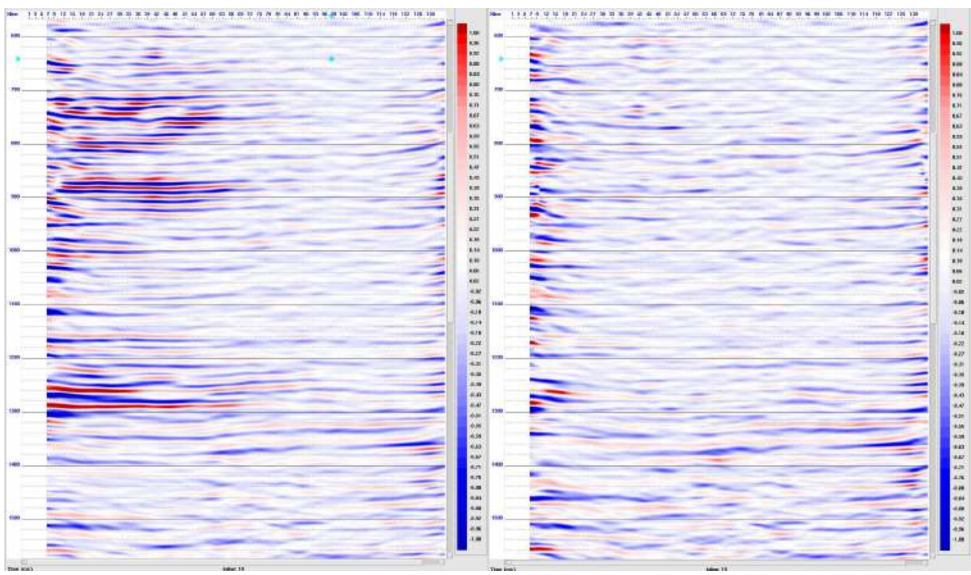

Figure 4.24. Inline 19: Difference PP 2006-2003 before cross-equalization (left) and after cross-equalization (right).

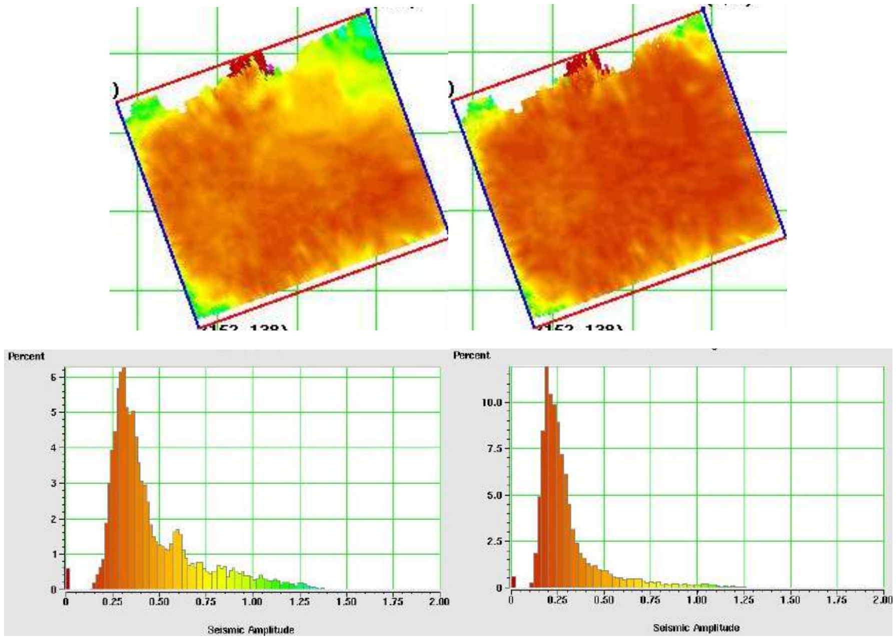

Figure 4.25. NRMS PP 2003-2006 map views before (upper left) and after cross-equalization (upper right). Histograms before (lower left) and after cross-equalization (lower right).

4.4 Cross-Equalization PP-2004 to PP-2003

Under the same considerations, I used the same static window to match the PP-2004 to the PP-2003 dataset (700-926 ms) which contains the depth-equivalent events for Top Mesa Verde and UMVS. Figure 4.26 shows both PP-2003 and 2004 volumes before cross-equalization, and Figure 4.27 shows the NRMS map at this stage with its corresponding histogram seen on Figure 4.28. Contrary to PP 2003-2006 case, the PP 2003 and 2004 datasets show a slightly broader range of NRMS, which in this case might be indicative of different conditions during 2004 acquisition that lowered the repeatability of the 2004 survey compared to 2003 and 2006. However, repeatability was improved by cross-equalization as it is shown on later figures.

4.4.1 Static Time-shift

The time shifts to the 2004 data were applied by calculating the cross-correlation between the 2004 and 2003 data using only the samples of the traces within the static window. The maximum allowed time shift was set on 20 ms. The maximum correlation found in a trace by traces basis is shown on Figure 4.29, and its corresponding histogram on Figure 4.30. On the map view can be appreciated that there is a uniform distribution of high cross-correlation values as seen on its corresponding histogram with most of the values being higher than 0.9.

The calculated and applied time-shifts are seen on Figure 4.31 as a map view and Figure 4.32 as its corresponding histogram. Most of the traces on PP-2004 survey needed a negative time shift which means that the events in the static window originally had later arrival times compared to the same events in the PP-2003 volume, which can be interpreted as lower overburden velocities in the year 2004 compared to 2003, probably due to velocity differences in the weathering layer (i.e. different weather conditions), or acquisition conditions (i.e. different source and/or receiver coupling conditions). In this case the time-shifts are higher than those for PP-2006, which could be due to the fact that 2004 acquisition was characterized by anomalous rainy conditions. These time-shifts were applied to the corresponding traces of the PP-2004 volume, so both the base PP-2003 and shifted PP-2004 are shown on Figure 4.33. Since the applied time shifts were still very small, there is no obvious change on the PP-2004 dataset that can be seen by naked-eye.

The difference PP 2004-2003 before and after the application of the static time shifts is shown on figure 4.34. Visually, cross-equalization results can be assessed by seeing how attenuated are the differences within the static window. It can be clearly seen that the static time shifts applied to PP-2004 accomplished this criteria, especially by seeing how attenuated are the differences between 700 ms and 800 ms, and around 900 ms after the application of these time shifts. This assessment is supported by the NRMS after the application of the static time-shifts shown on Figure 4.35, with its corresponding histogram depicted on Figure 4.36. The map view (Figure 4.35) presents more uniformly distributed lower NRMS values, and the histogram shows a peak shifted from around 0.35 (before application of time-shifts) to around 0.25 (after applying time-shifts) with a narrower distribution. I conclude that repeatability has been increased through the application of static time-shifts to PP-2004.

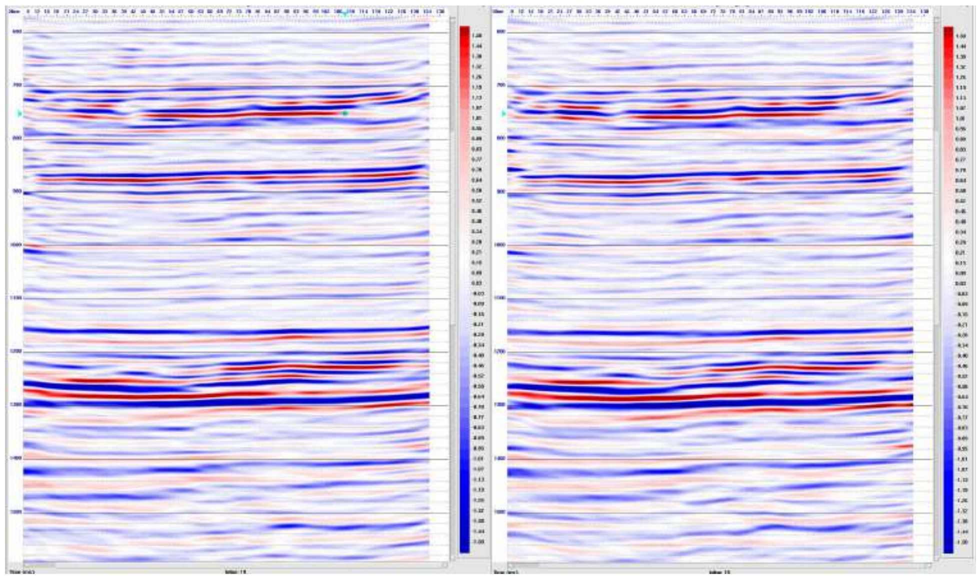

Figure 4.26. Inline 19: PP-2003 (left) and PP-2004 (right).

.

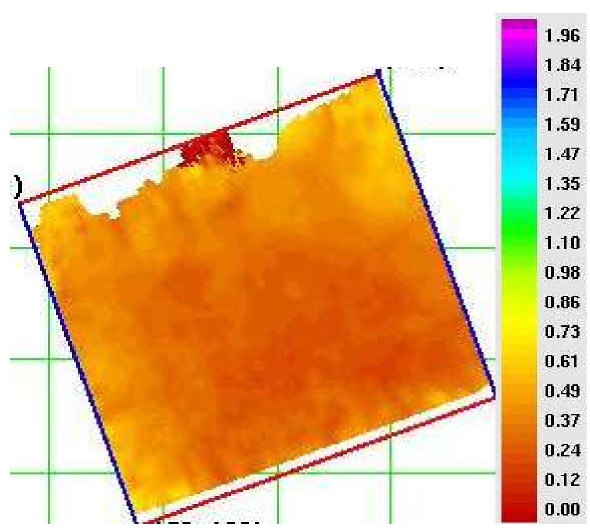

Figure 4.27. NRMS PP 2003-2004 for raw data.

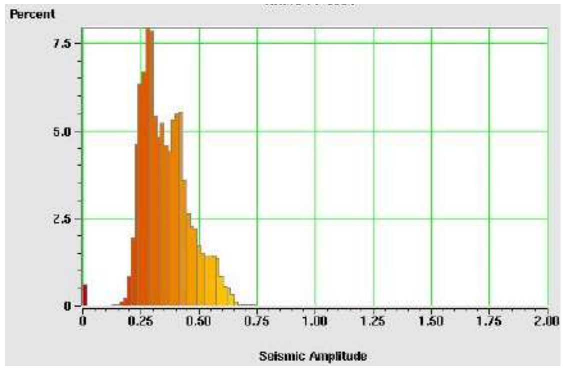

Figure 4.28. Histogram of NRMS PP 2003-2004 for raw data.

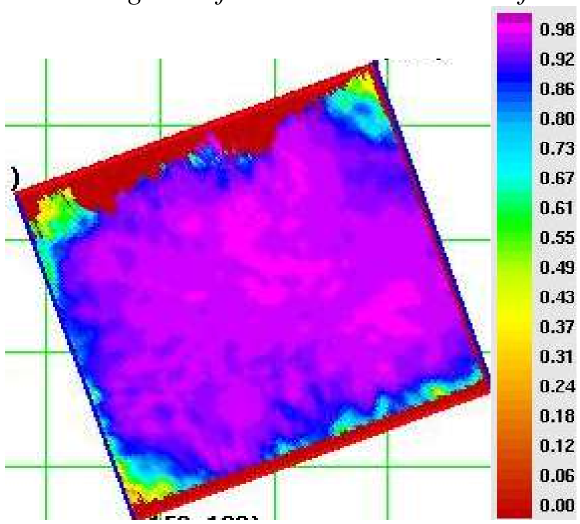

Figure 4.29. Maximum cross-correlation (PP-2003 & 2004) map distribution expressed in fraction.

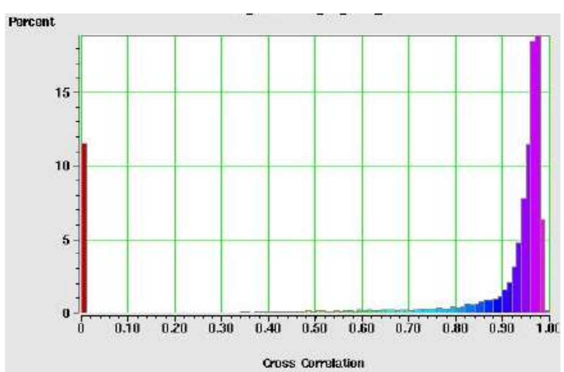

Figure 4.30. Maximum cross-correlation (PP-2003 & 2004) histogram, expressed in fraction.

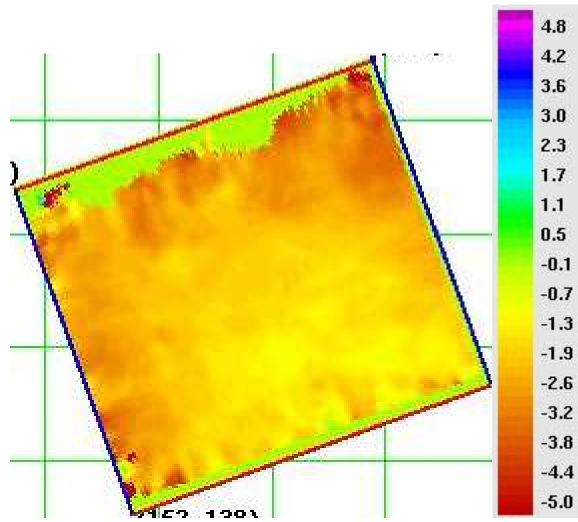

Figure 4.31. Time-shifts applied to PP-2004 relative to PP-2003.

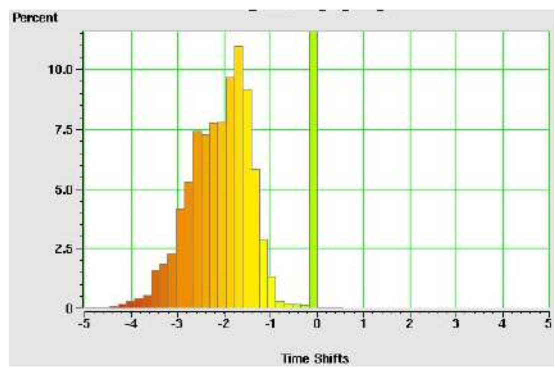

Figure 4.32. Histogram of time-shifts applied to PP-2004 relative to PP-2003.

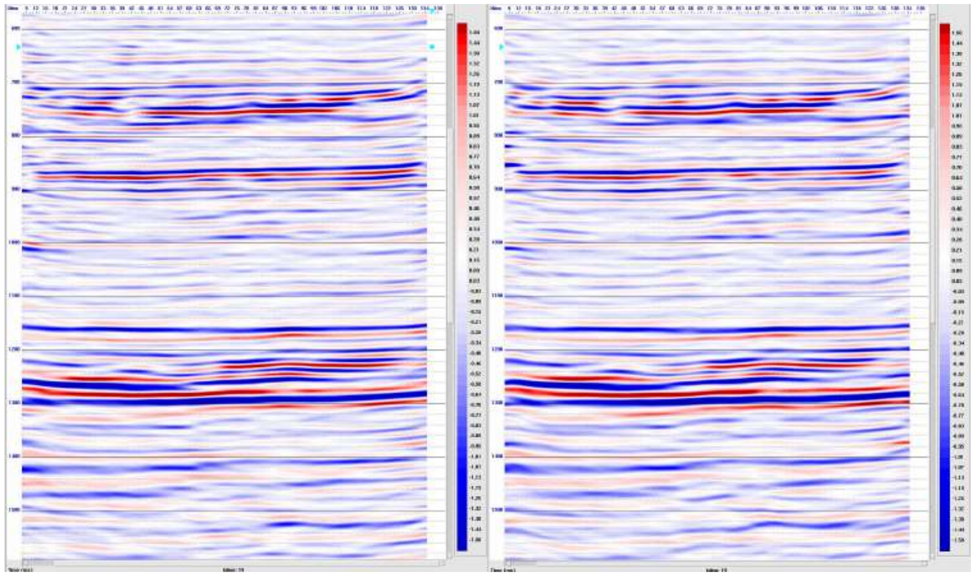

Figure 4.33. Inline 19: PP-2003 (left) and PP-2004 (right), after application of static time shifts to PP-2004.

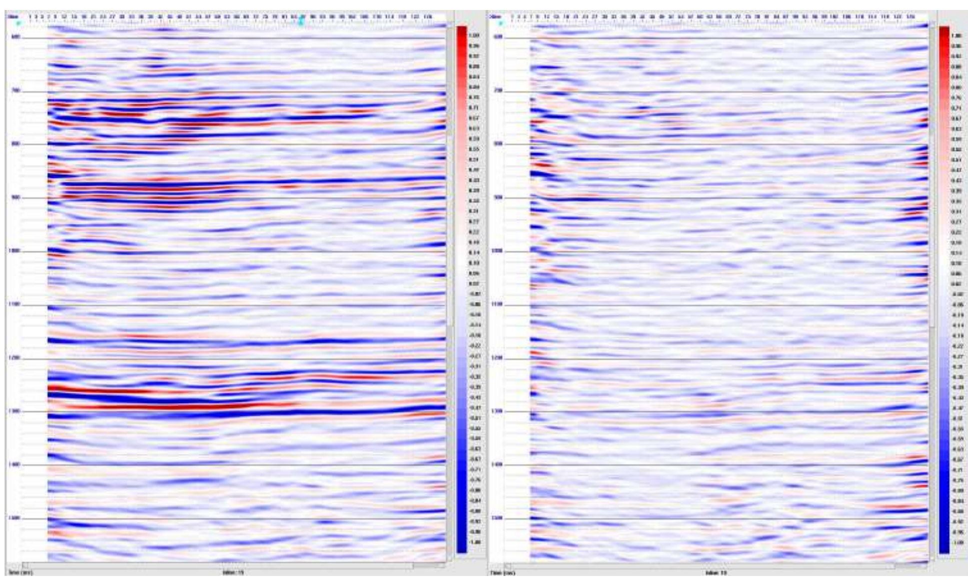

Figure 4.34. Inline 19: Difference PP 2004-2003 for raw data (left) and after application of static time shifts to PP-2004 (right).

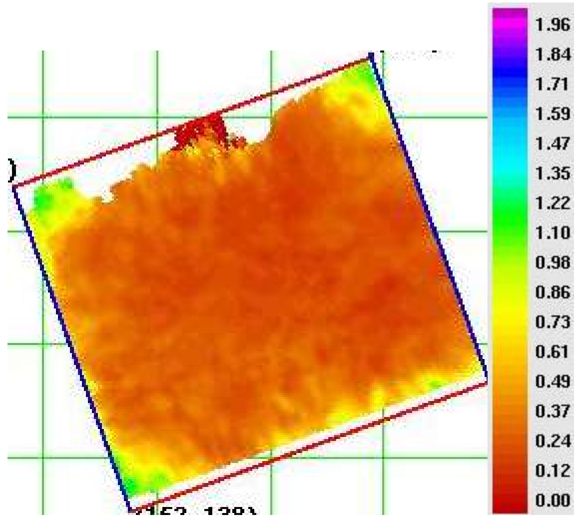

Figure 4.35. NRMS PP 2003-2004 after application of time-shifts to PP-2004.

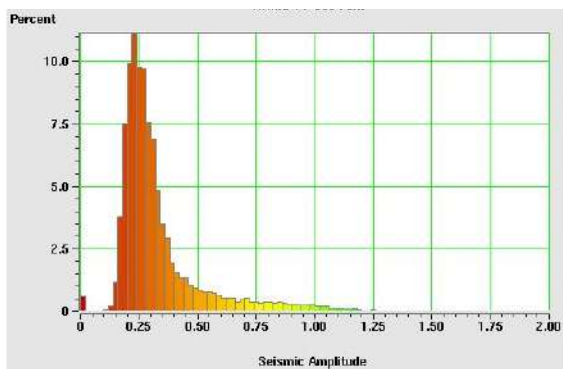

Figure 4.36. Histogram of NRMS PP 2003-2004 after application of time-shifts to PP-2004.

4.4.2 Cross-Normalization (Gain)

The amplitude matching between the two surveys was done by calculating the gain factors in a trace-by-trace basis within the static window. A map view of these gain factors is depicted on Figure 4.37 and its corresponding histogram on Figure 4.38. From these Figures it can be seen that the scaling of amplitudes applied to PP-2004 dataset to match the PP-2003 dataset is not strong since most of the gain factors are around 1. This gain factor indicates a high level of repeatability between the surveys.

These gain factors were applied to their corresponding traces on the PP-2004 volume, which results are shown along with PP-2003 on Figure 4.39. Using this resulting volume I calculated the PP 2004-2003 difference after applying the gain to PP-2004 and it can be compared to the difference before the application of the gain as seen on figure 4.40. No outstanding improvement can be seen. By interpreting the resulting NRMS on Figures 4.41 and 4.42 we can see that both surveys are already matched very well in terms of amplitudes before the application of the cross-normalization.

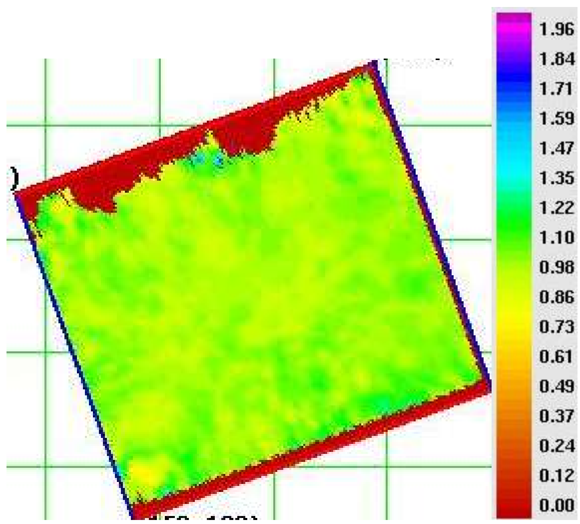

Figure 4.37. Gain factor (trace-by-trace) applied to the PP-2004 volume.

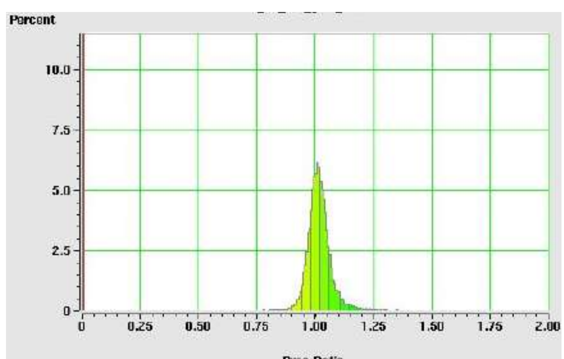

Figure 4.38. Histogram of the gain factor (trace-by-trace) applied to the PP-2004 volume.

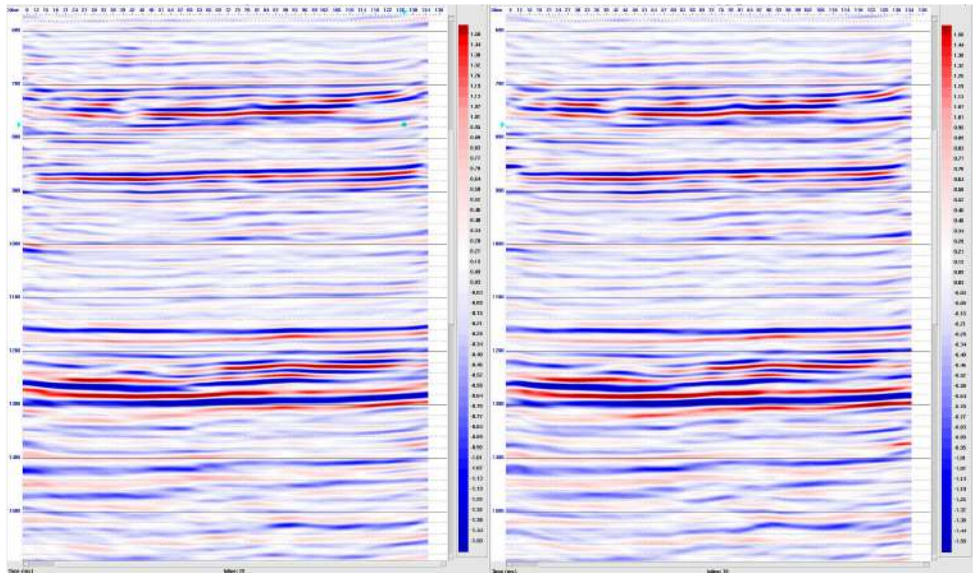

Figure 4.39. Inline 19: PP-2003 (left) and PP-2004 (right), after application of static time shifts and cross-normalization (gain) to PP-2004.

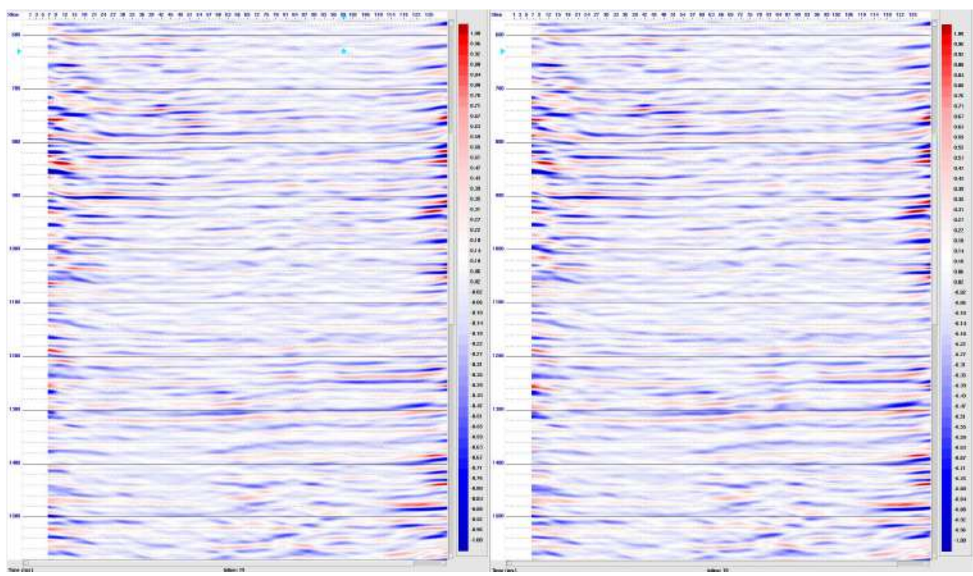

Figure 4.40. Inline 19: Difference PP 2004-2003 after application of static time shifts (left) and after application of time–shifts and cross-normalization (gain) to PP-2004 (right).

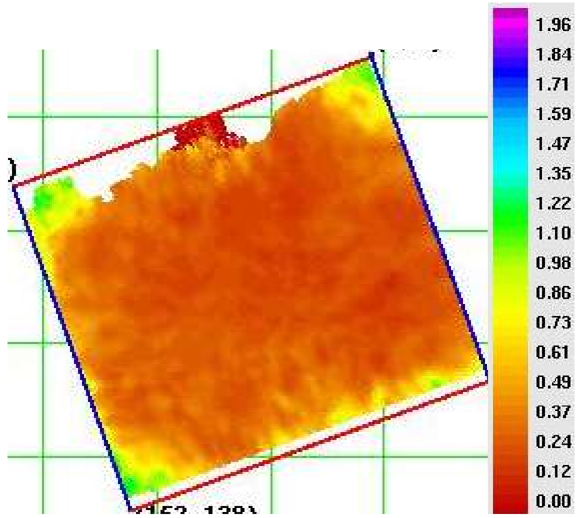

Figure 4.41. NRMS PP 2003-2004 after application of time-shifts and cross-normalization (gain) to PP-2004.

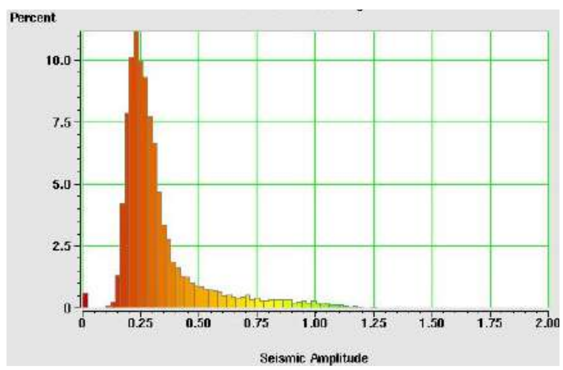

Figure 4.42. Histogram of NRMS PP 2003-2004 after application of time-shifts and cross-normalization (gain) to PP-2004.

4.4.3 Time-variant time-shifts

After testing different sets of parameters, this final stage in cross-equalization was performed by using a sliding window for correlation 100 ms long and starting at 650 ms. This correlation window had a 1ms step and this correlation was done using 650 windows in order to cover all the seismic events-packages of interest (lower overburden, tight-gas sands interval and coals interval). The time-variant time shifts were designed to be applied to PP 2004, and the resulting volume is shown along with PP 2003 on Figure 4.43, and this was used to calculate the PP 2004-2003 differences shown on Figure 4.44

before and after applying these time-variant time shifts. Again there is no outstanding improvement in the repeatability of the surveys after the application of this last cross-equalization step, but observation of NRMS after the time-variant time-shifts as shown on Figures 4.45 and 4.46 allow interpreting that the main NRMS peak shifted towards values slightly lower than 0.25, which means an improvement of the PP 2003-2004 surveys repeatability.

A final assessment of the PP 2003-2004 cross-equalization can be done by seeing the PP 2004-2003 before and after cross-equalization shown on Figure 4.47. There is a strong degree of attenuation of the differences in the static window after cross-equalization. This also is confirmed by the comparison of the NRMS before and after cross-equalization seen on Figure 4.48, where the series of processes allowed obtained a more uniform distribution of lower NRMS values, which is translated in an improvement of the repeatability of these surveys.

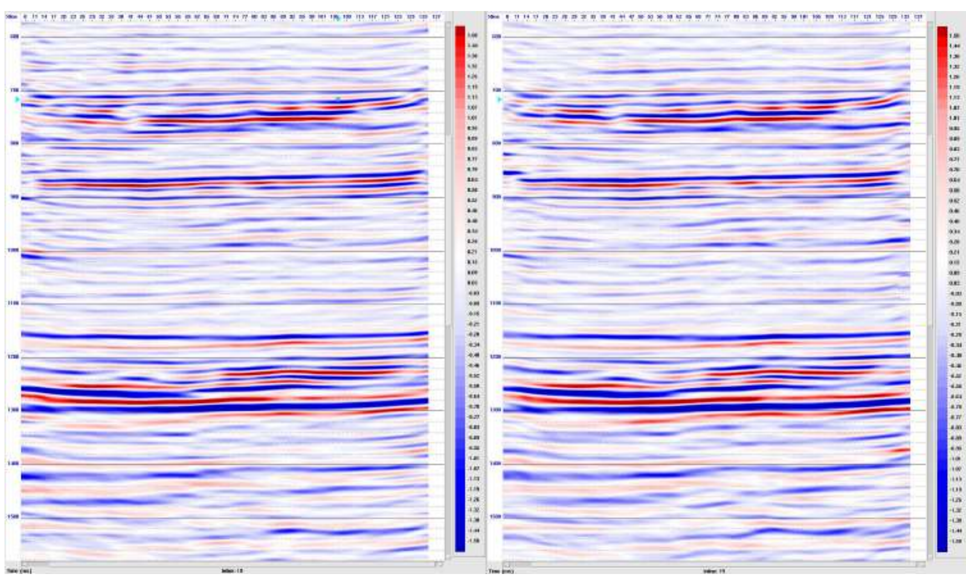

Figure 4.43. Inline 19: PP-2003 (left) and PP-2004 (right), after application of static time shifts, cross-normalization (gain) and time-variant time-shifts to PP-2004.

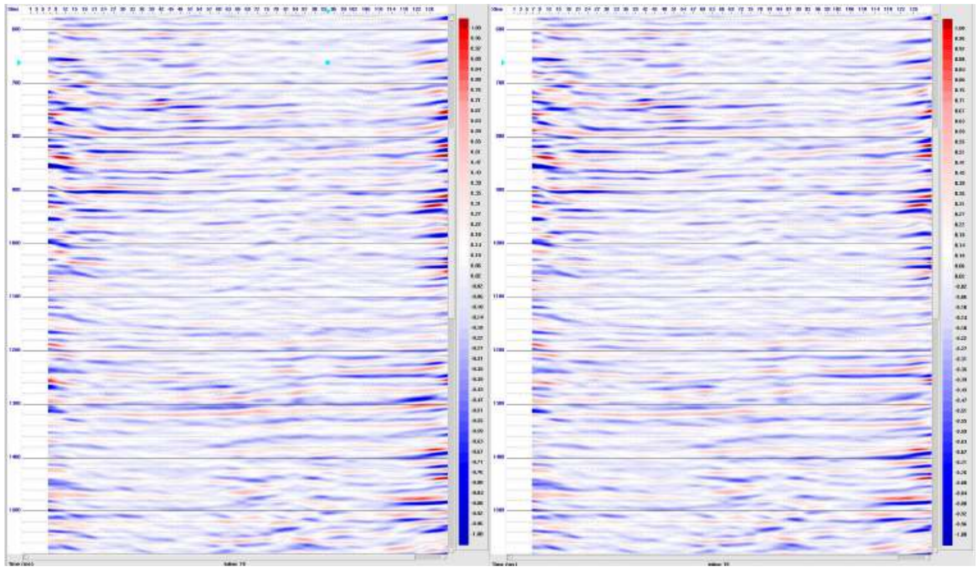

Figure 4.44. Inline 19: Difference PP 2004-2003 after application of time–shifts and cross-normalization (gain) (left), and after application of time–shifts, cross-normalization (gain) and time-variant time-shifts to PP-2004 (right).

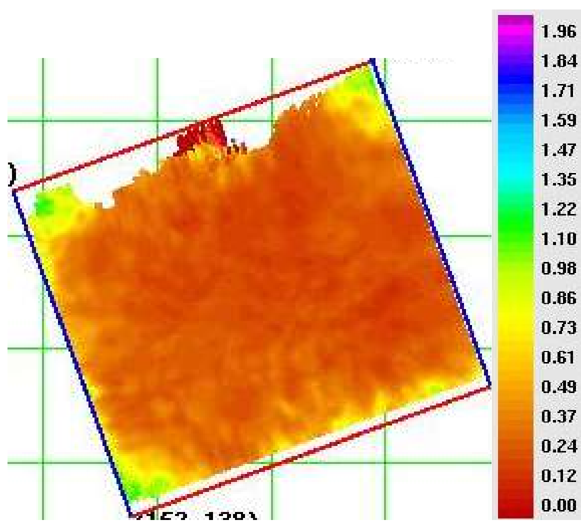

Figure 4.45. NRMS PP 2003-2004 after application of time-shifts, cross-normalization (gain) and time-variant time-shifts to PP-2004.

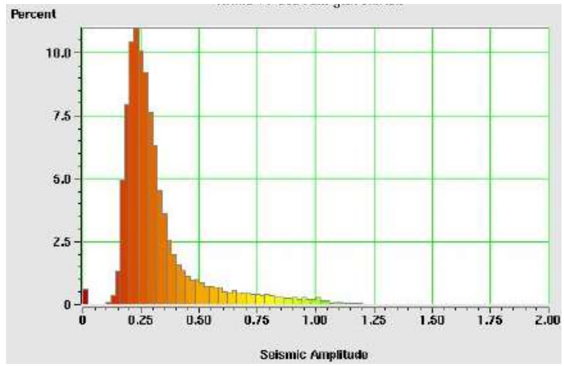

Figure 4.46. Histogram of NRMS PP 2003-2004 after application of time-shifts, cross-normalization (gain) and time-variant time-shifts to PP-2004.

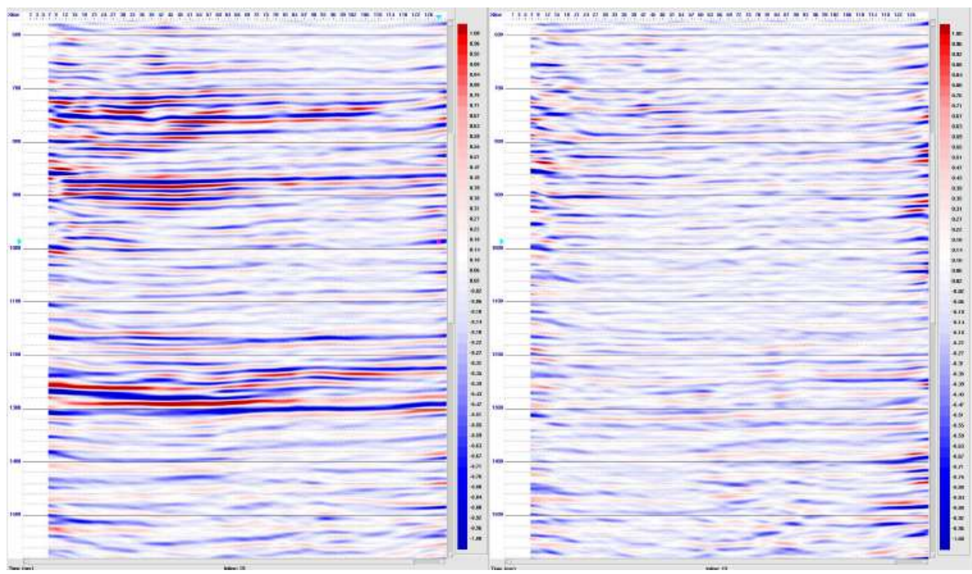

Figure 4.47. Inline 19: Difference PP 2004-2003 before cross-equalization (left) and after cross-equalization (right).

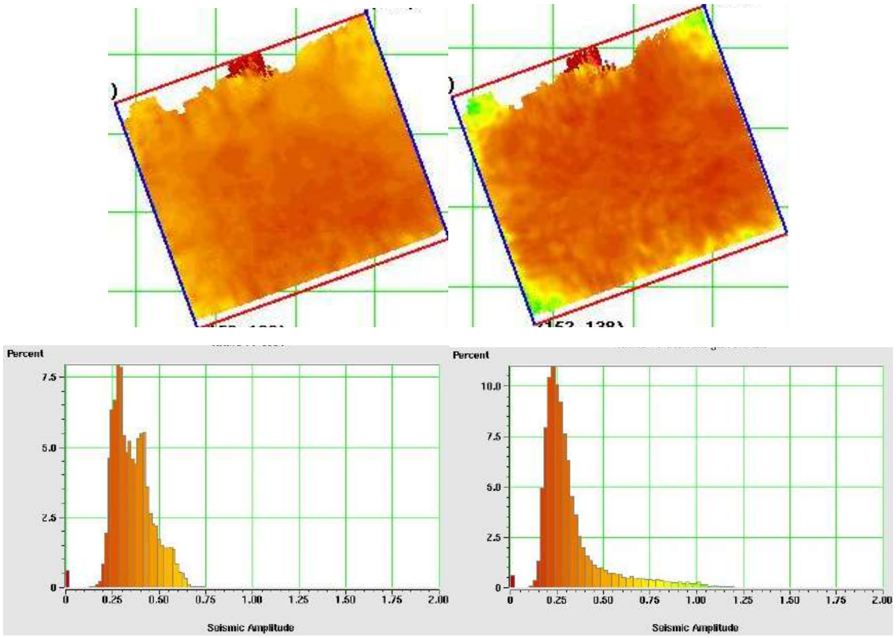

Figure 4.48. NRMS PP 2003-2004 map views before (upper left) and after cross-equalization (upper right). Histograms before (lower left) and after cross-equalization (lower right).

4.5 High-Frequency Noise in pure shear (S11 & S22) datasets

Before performing the S11 and S22 cross-equalization, a scope of the amplitude spectra for all the volumes showed a broad range of relatively high frequencies (~25 Hz-50 Hz) having moderate amplitudes that are associated with noise as shown on Figure 4.49.

In order to confirm that this range of frequency (25 Hz-50 Hz) is associated with noise, a spectral balancing was performed in order to boost these frequencies and make their contribution to data comparable to the contribution of lower frequencies. The corresponding balanced amplitude spectrum is shown on Figure 4.50.

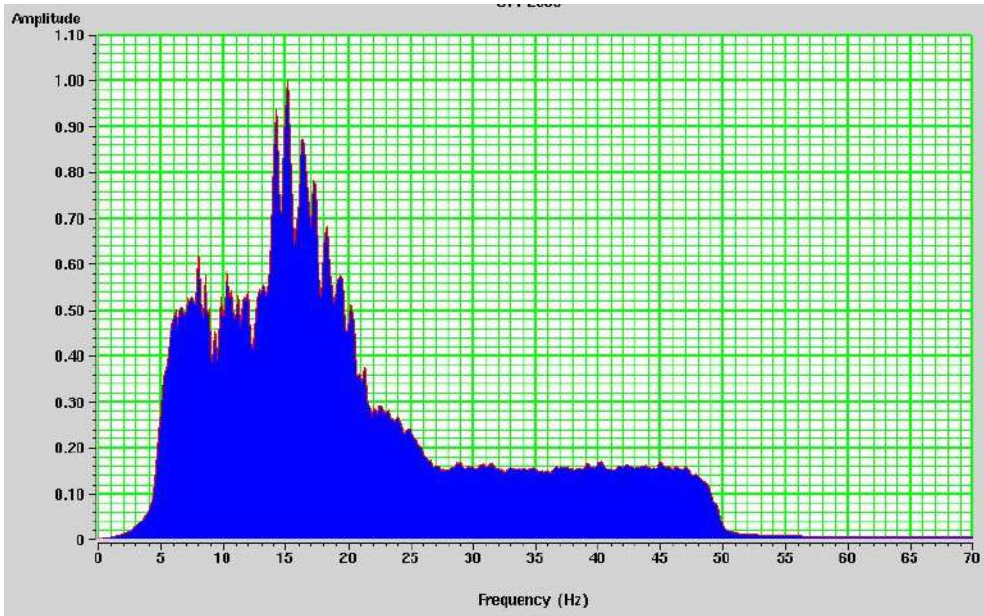

Figure 4.49. S11-2003 amplitude spectra showing potential high-frequency noise.

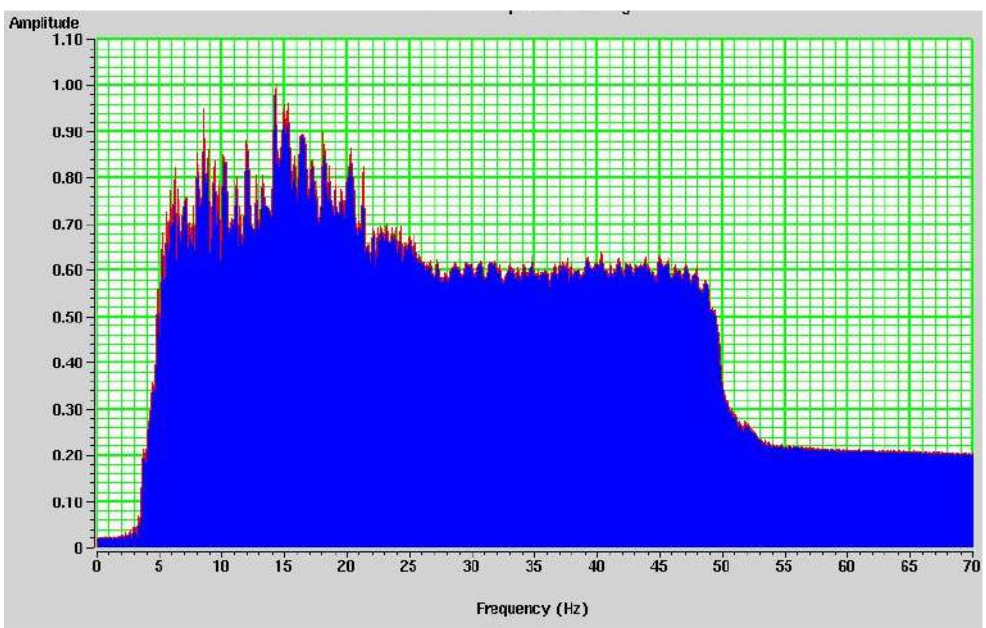

Figure 4.50. S11-2003 amplitude spectrum after application of spectral balancing.

This dataset is shown on Figure 4.51 before and after the application of the spectral balancing. From the comparison it can be stated that the frequency range 25-50 Hz does not contribute to the improvement of the signal-noise ratio. In fact it may contribute to reducing this ratio. I applied a low-pass filter (0-0-25-30 Hz) in order to have this noise attenuated on the datasets before continuing their corresponding cross-equalization.

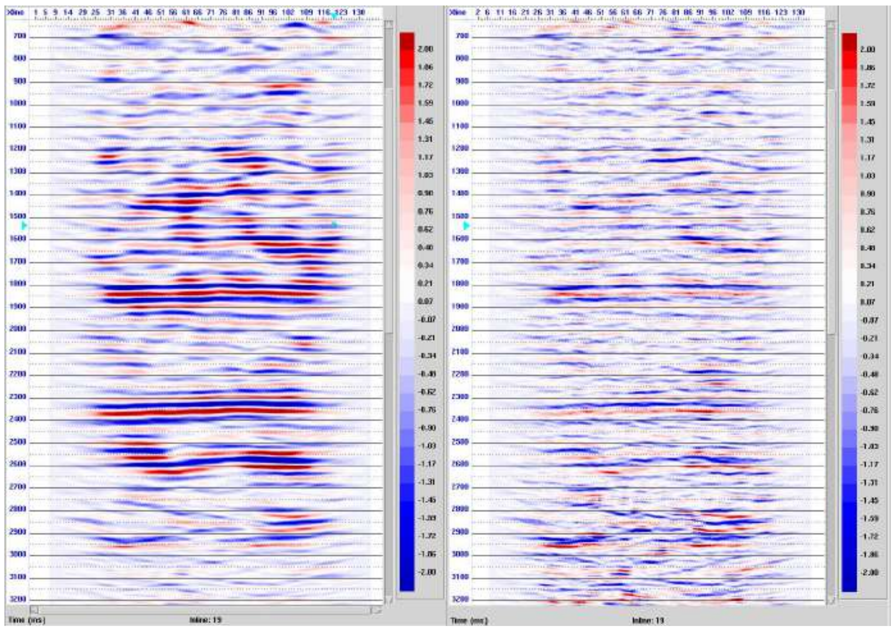

Figure 4.51. S11-2003 raw data (left) and after spectral balancing (right).

4.6 Cross-Equalization S11-2006 to S11-2003

The S11 cross-equalization follows the same order used for the PP cross-equalization. After different tests, I chose a S11 static window of 1800-1900 ms. Figure 4.52 shows both S11-2003 and 2006 volumes before cross-equalization, and Figure 4.53 shows the NRMS map at this stage with its corresponding histogram seen on Figure 4.54. An overall NRMS=0.3 indicates that both acquisition and processing provided a good degree of data repeatability for these datasets. Repeatability was later improved by cross-equalization.

4.6.1 Static Time-shift

The time shifts to the 2006 data were applied by calculating the cross-correlation between the 2006 and 2003 data using only the samples of the traces within the static window. The maximum allowed time shift was set on 20 ms. The maximum correlation found on a trace-by-trace basis is shown on Figure 4.55. Its corresponding histogram is shown on Figure 4.56. In map view there is a uniform distribution (except in the survey's border) of high cross-correlation values as seen on the corresponding histogram with most of the values being higher than 0.9. This display shows good repeatability except for the low fold area on the survey borders.

The calculated and applied time-shifts are seen on Figure 4.57 as a map view and Figure 4.58 as its corresponding histogram. The value distribution of time shifts does not show any preferential time-shift trend as seen on PP cross-equalizations, which means that time-lapse velocity anomalies in the overburden are less outstanding in S11 than P-wave. These time-shifts were applied to the corresponding traces of the S11-2006 volume, so both the base S11-2003 and shifted S11-2006 are shown on Figure 4.59. Since the applied time shifts were still very small, there is no obvious change on the S11-2006 dataset that can be seen by the naked-eye.

The difference S11 2006-2003 before and after the application of the static time shifts is shown on Figure 4.60. The attenuation of differences on the overlying levels of the S11 static window is not effective enough. As a matter of fact there are time-lapse differences in the overburden that outweigh those at the reservoir level. This could be due to the fact that right above UMVS event (< 1800 ms) there is a rapid loss of fold (Casey and Davis, 2007) that affects the signal-noise ratio of these shallow events and affects negatively the performance of the S11 cross-equalization. This analysis applies for all the S11 and S22 cross-equalizations.

The most appropriate way to assess the quality of the cross-equalization operators is by using NRMS as shown on Figure 4.61, with its corresponding histogram depicted on Figure 4.62. The map view (Figure 4.61) presents more uniformly distributed lower NRMS values, and the histogram shows a unique peaked distribution of values around 0.25, which is slightly better when considering the wider initial distribution of NRMS values.

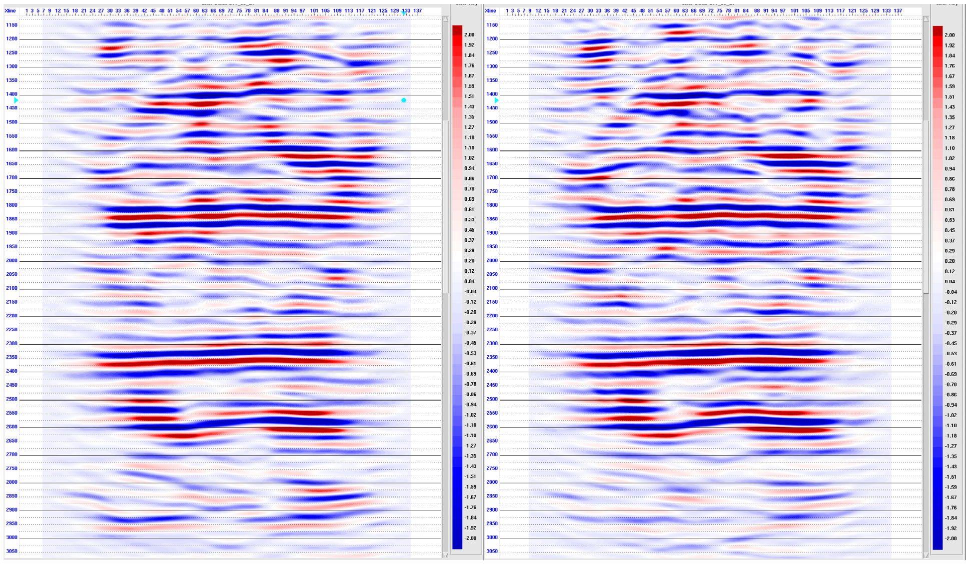

Figure 4.52. Inline 19: S11-2003 (left) and S11-2006 (right).

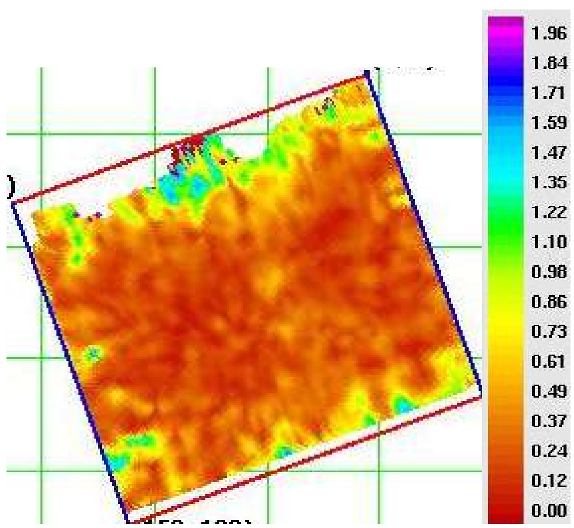

Figure 4.53. NRMS S11 2003-2006 for filtered raw data.

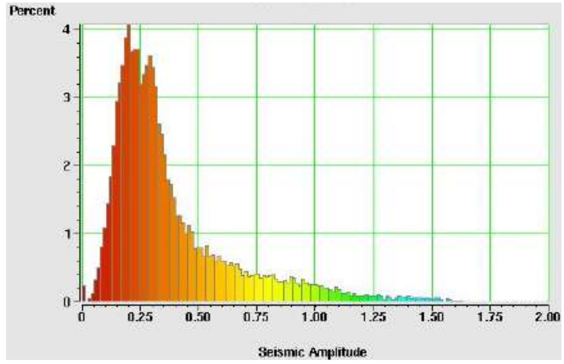

Figure 4.54. Histogram of NRMS S11 2003-2006 for filtered raw data.

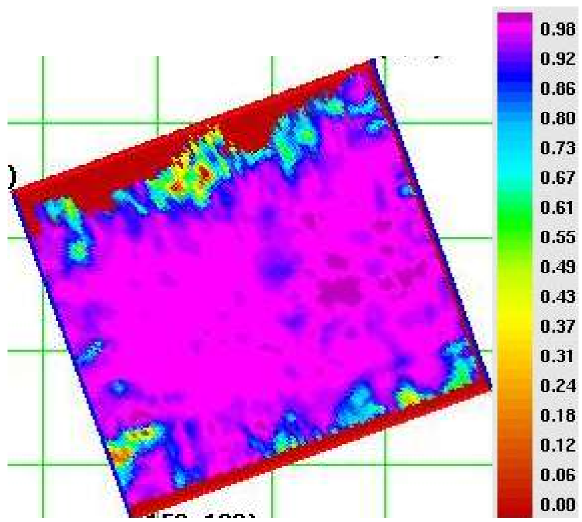

Figure 4.55. Maximum cross-correlation (S11-2003 & 2006) map distribution expressed in fraction.

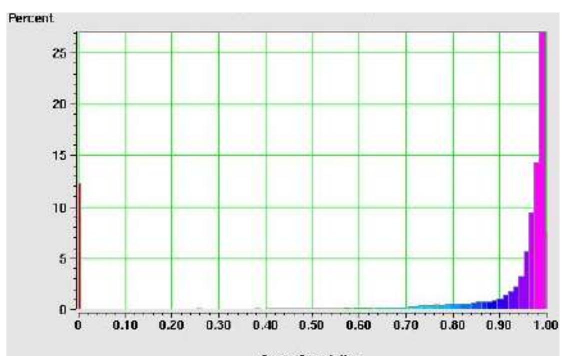

Figure 4.56. Maximum cross-correlation (S11-2003 & 2006) histogram, expressed in fraction.

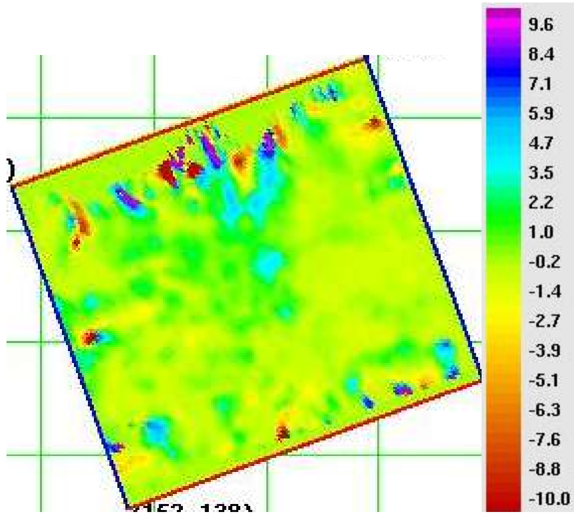

Figure 4.57. Time-shifts applied to S11-2006 relative to S11-2003.

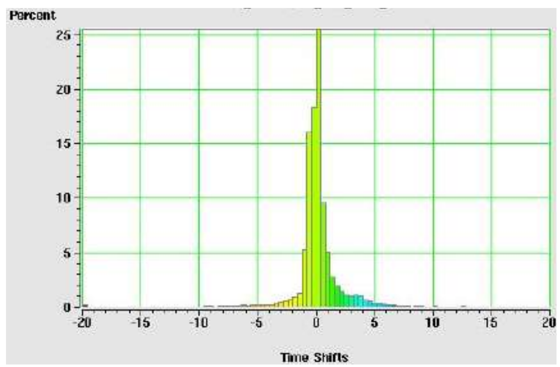

Figure 4.58. Histogram of time-shifts applied to S11-2006 relative to S11-2003.

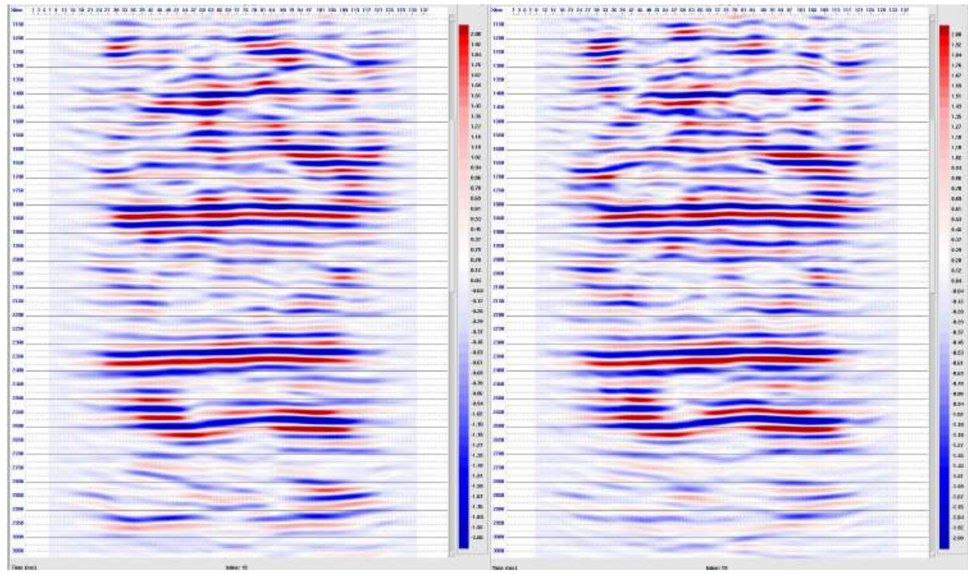

Figure 4.59. Inline 19: S11-2003 (left) and S11-2006 (right), after application of static time shifts to S11-2006.

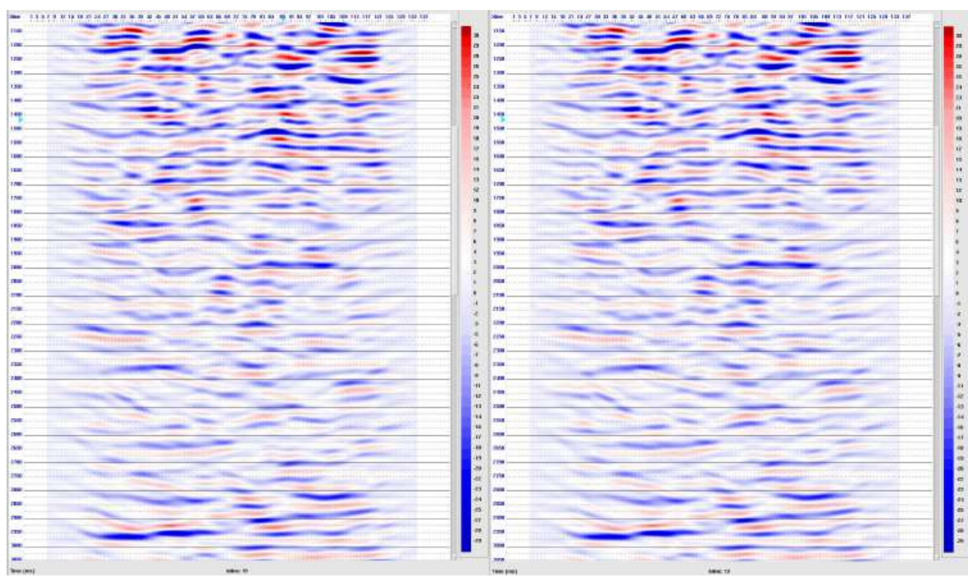

Figure 4.60. Inline 19: Difference S11 2006-2003 for filtered raw data (left) and after application of static time shifts to S11-2006 (right).

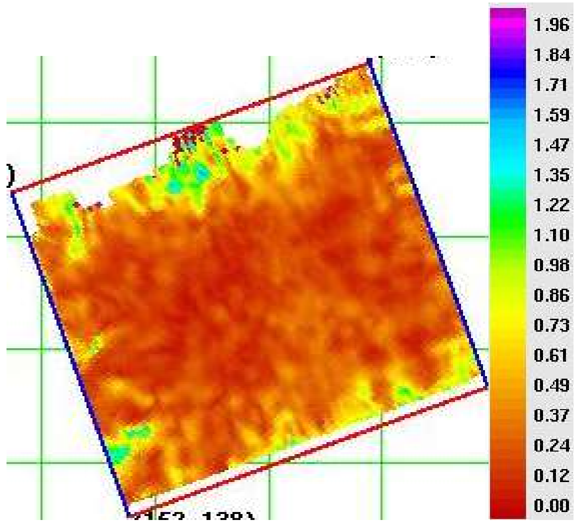

Figure 4.61. NRMS S11 2003-2006 after application of time-shifts to S11-2006.

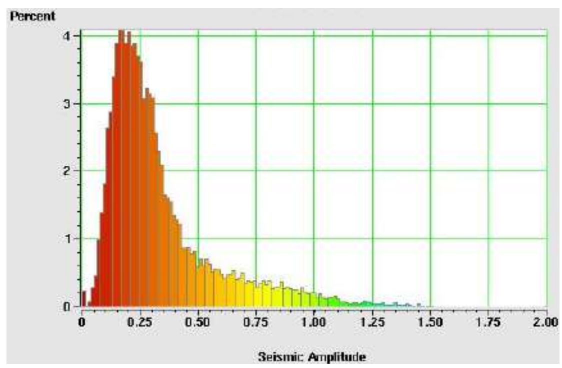

Figure 4.62. Histogram of NRMS S11 2003-2006 after application of time-shifts to S11-2006.

4.6.2 Cross-Normalization (Gain)

The amplitude matching between the two surveys was done by calculating the gain factors in a trace-by-trace basis within the static window. A map view of these gain factors is depicted on Figure 4.63 and its corresponding histogram is shown on figure 4.64. From these figures it can be seen that the scaling of amplitudes applied to S11-2006 dataset to match the S11-2003 dataset are slightly greater than 1. This is indicative of either different coupling/gain or higher time lapse sensitivity in the overburden in terms of amplitudes for S11 wave mode compared to that of the PP wave mode.

These gain factors were applied to their corresponding traces on the S11-2006 volume, with results shown along with S11-2003 on Figure 4.65. Using this resulting volume I calculated the S11 2006-2003 difference after applying the gain to S11-2006 and it can be compared to the difference before the application of the gain as seen on Figure 4.66. There are more attenuated differences between 1800-1900 ms compared to the previous case (static time-shifts). The resulting NRMS on Figures 4.67 and 4.68 supports the previous appreciation, where there are more uniformly area distributed lower NRMS values, and a narrower distribution peak around NRMS=0.15. There is an outstanding improvement in the repeatability of the surveys.

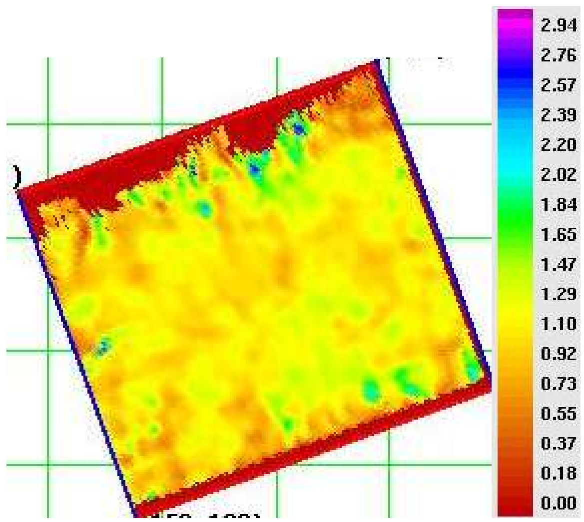

Figure 4.63. Gain factor (trace-by-trace) applied to the S11-2006 volume.

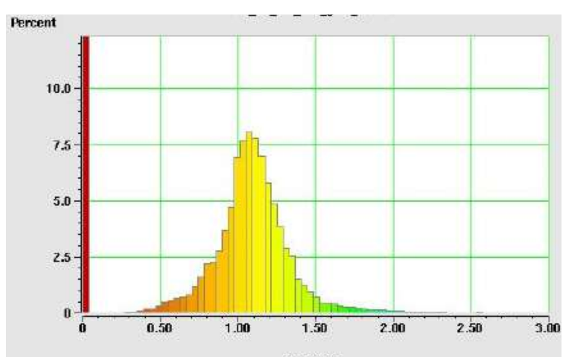

Figure 4.64. Histogram of the gain factor (trace-by-trace) applied to the S11-2006 volume.

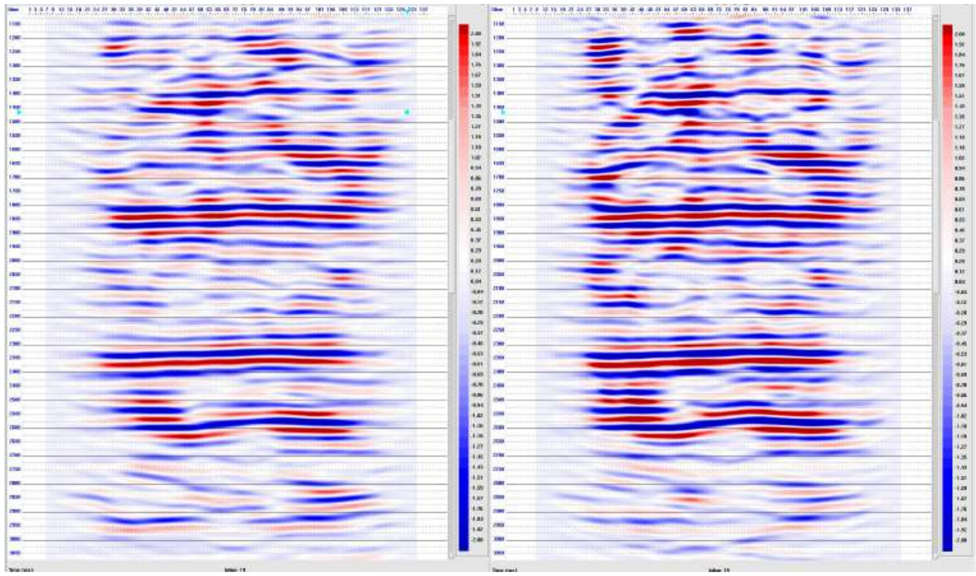

Figure 4.65. Inline 19: S11-2003 (left) and S11-2006 (right), after application of static time shifts and cross-normalization (gain) to S11-2006.

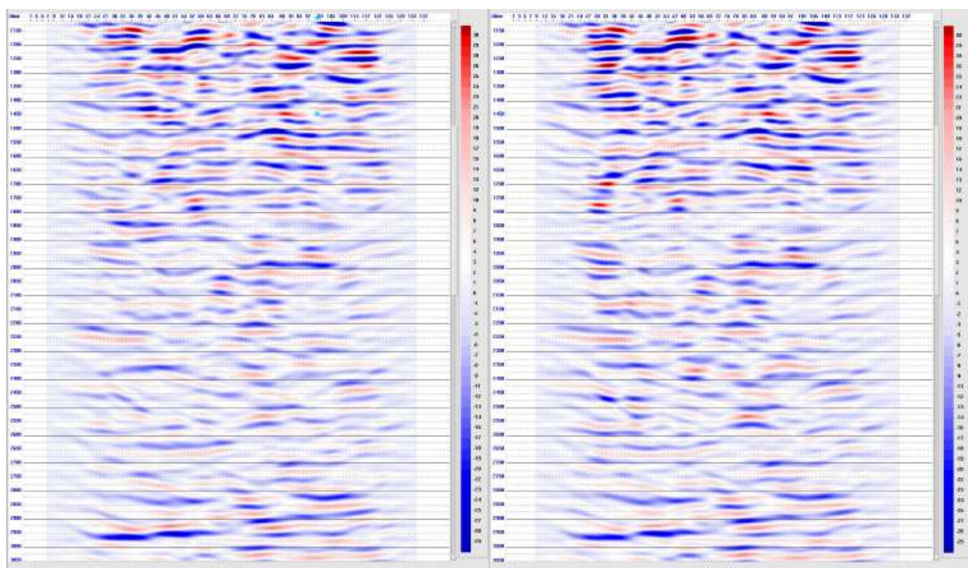

Figure 4.66. Inline 19: Difference S11 2006-2003 after application of static time shifts (left) and after application of time–shifts and cross-normalization (gain) to S11-2006 (right).

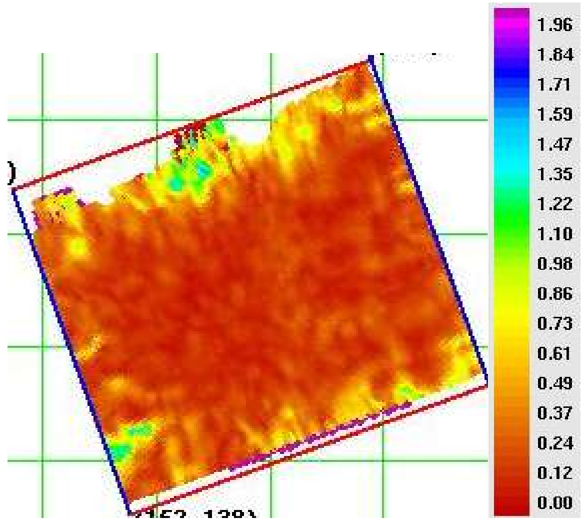

Figure 4.67. NRMS S11 2003-2006 after application of time-shifts and cross-normalization (gain) to S11-2006.

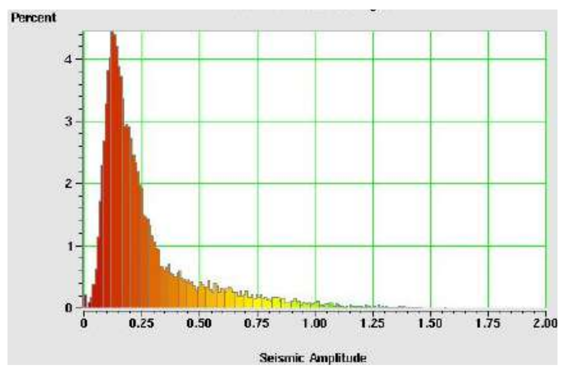

Figure 4.68. Histogram of NRMS S11 2003-2006 after application of time-shifts and cross-normalization (gain) to S11-2006.

4.6.3 Time-variant time-shifts

After the test of different sets of parameters, the final stage in cross-equalization was performed by using a sliding window for correlation being 200 ms long and starting at 1500 ms. This correlation window had a 1ms step and this correlation was done using 1000 windows in order to cover all the seismic events-packages of interest (lower overburden, tight-gas sands interval and coals interval). The time-variant time shifts were designed to be applied to S11 2006, and the resulting volume is shown along with S11 2003 on Figure 4.69.This volume was used to calculate the S11 2006-2003 differences shown on Figure 4.70 before and after applying these time-variant time shifts. There is no appreciable improvement in the repeatability of the surveys after the application of this last cross-equalization step. Observation of NRMS after the time-variant time-shifts as shown on Figures 4.71 and 4.72 allow interpreting that the main NRMS peak shifted towards values lower than 0.15 and becomes slightly narrower, which means an improvement of the S11 2003-2006 survey repeatability.

A final assessment of the S11 2003-2006 cross-equalization can be done by seeing the S11 2006-2003 before and after cross-equalization shown on Figure 4.73. The degree of attenuation of differences can only be appreciated in the static window after cross-equalization. A better assessment of the repeatability improvement by cross-equalization is expressed through the NRMS before and after cross-equalization seen on Figure 4.74, where the series of processes allowed obtained a more uniform distribution of lower NRMS values, which is translated as an improvement of the repeatability of these surveys.

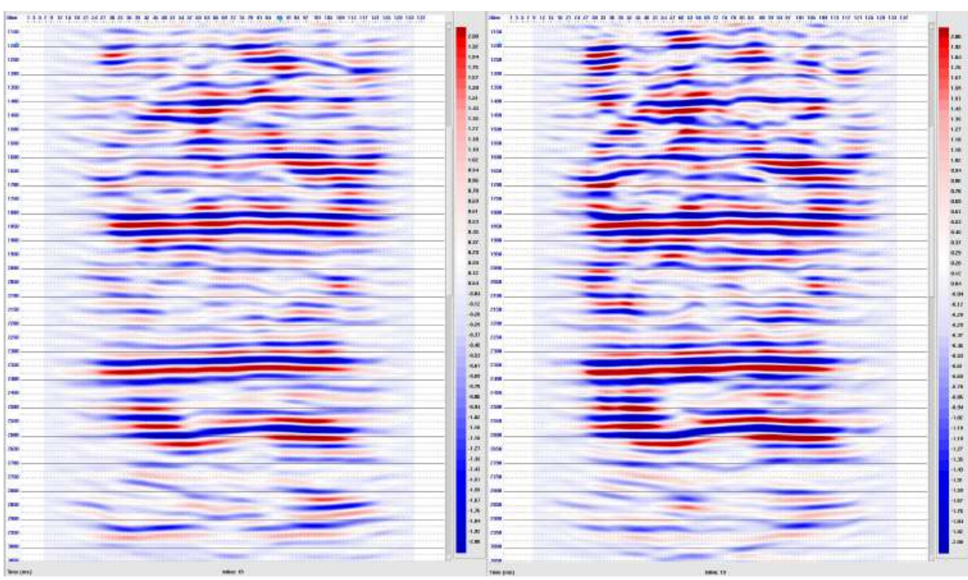

Figure 4.69. Inline 19: S11-2003 (left) and S11-2006 (right), after application of static time shifts, cross-normalization (gain) and time-variant time-shifts to S11-2006.

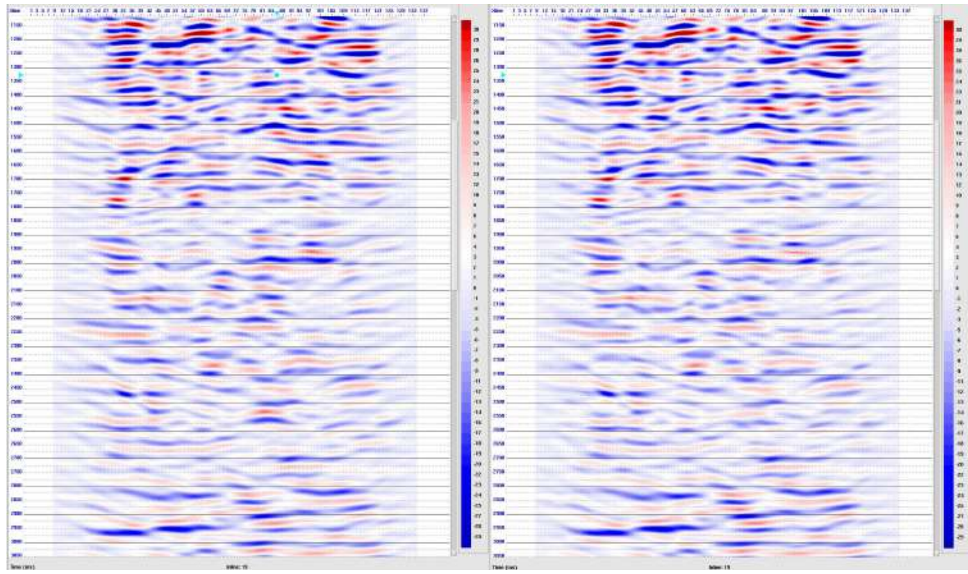

Figure 4.70. Inline 19: Difference S11 2006-2003 after application of time–shifts and cross-normalization (gain) (left), and after application of time–shifts, cross-normalization (gain) and time-variant time-shifts to S11-2006 (right).

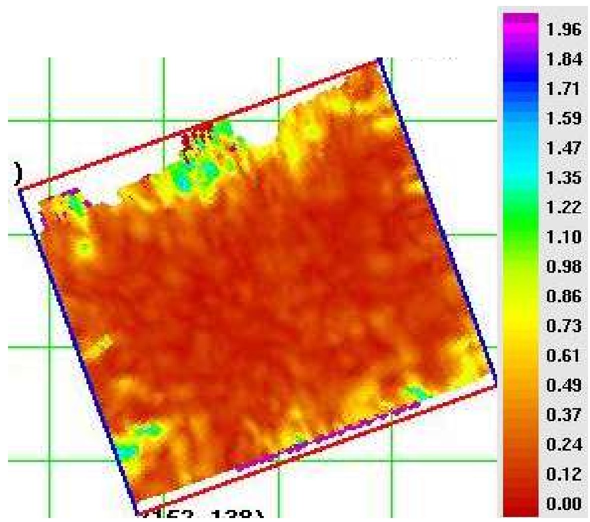

Figure 4.71. NRMS S11 2003-2006 after application of time-shifts, cross-normalization (gain) and time-variant time-shifts to S11-2006.

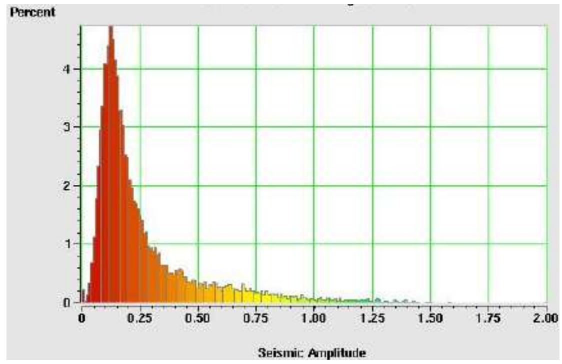

Figure 4.72. Histogram of NRMS S11 2003-2006 after application of time-shifts, cross-normalization (gain) and time-variant time-shifts to S11-2006.

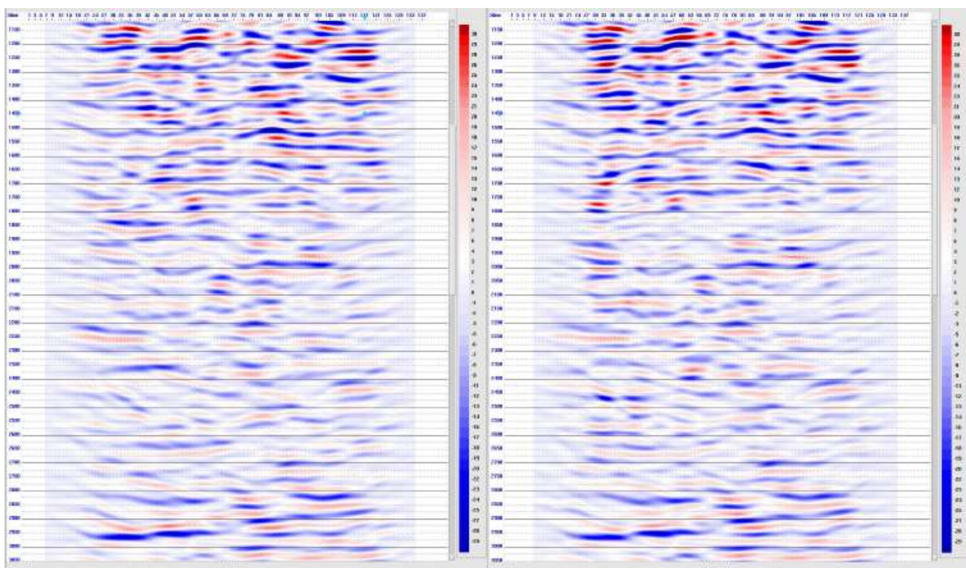

Figure 4.73. Inline 19: Difference S11 2006-2003 before cross-equalization (left) and after cross-equalization (right).

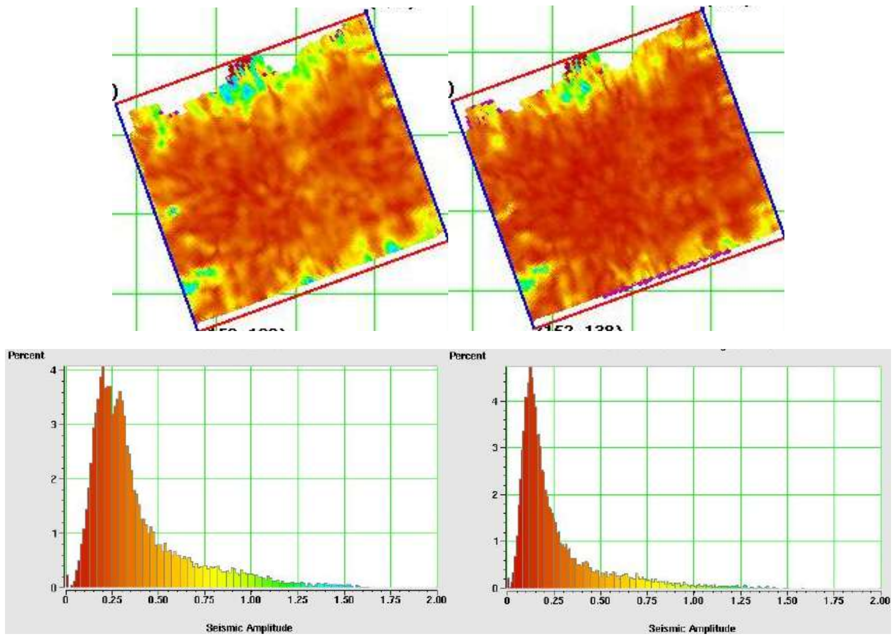

Figure 4.74. NRMS S11 2003-2006 map views before (upper left) and after cross-equalization (upper right). Histograms before (lower left) and after cross-equalization (lower right).

4.7 Cross-Equalization S11-2004 to S11-2003

In order to keep consistency, for this cross-equalization I kept the same parameters used for S11 2003-2006 cross-equalization, including the 1800-1900 ms static window, and using the band-pass (0-0-25-30 Hz) filtered volumes as input. Figure 4.75 shows both S11-2003 and 2004 volumes before cross-equalization, and Figure 4.76 shows the NRMS map view at this stage along with its corresponding histogram seen on Figure 4.77. Compared to the initial S11 2003-2006, the survey repeatability of the S11 2003-2004 is relatively poor considering the wide range of variation of NRMS values probably due to the rainy conditions during 2004 acquisition that affected the overburden. However, the series of cross-equalization processes make substantial improvement of the repeatability of these volumes.

4.7.1 Static Time-shift

The time shifts to the 2004 data were applied by calculating the cross-correlation between the 2004 and 2003 data using only the trace samples within the static window. The maximum allowed time shift was set on 20 ms. The maximum correlation found in a trace by trace basis is shown on Figure 4.78, and its corresponding histogram on Figure 4.79. Both figures show the distribution of high cross-correlation values between the 2003 and 2004 surveys within the static window, which could confirms the initial fair repeatability of the surveys.

The calculated and applied time-shifts are seen on Figure 4.80 as a map view and Figure 4.81 as its corresponding histogram. There is a wide distribution of positive time-shifts, which means that the events within the static window for S11 2004 have earlier arrival times than those for S11 2003. This is a result of a time-lapse changing overburden, due to the previously mentioned anomalous conditions during the 2004 acquisition. In case we assume a time-lapse changing overburden, the average fast-shear wave velocity in 2004 is generally faster than 2003. These time-shifts were applied to the corresponding traces of the S11-2004 volume, so both the base S11-2003 and shifted S11-2004 are shown on Figure 4.82.

The difference between S11 2004-2003 before and after the application of the static time shifts is shown on Figure 4.83. Despite the overburden and low fold influence in the cross-equalization mentioned earlier, the S11 2004-2003 after the application of static time-shifts shows an outstanding attenuation of differences even above the static window, so the static time-shift operator by itself is a reliable source of improvement of repeatability in this case. Based on NRMS results shown on Figure 4.84, with its corresponding histogram depicted on Figure 4.85 a substantial improvement is seen. The map view (Figure 4.84) shows a concentration of low NRMS values in the center of the survey (area of maximum CMP fold), and the histogram shows a narrower distribution of values.

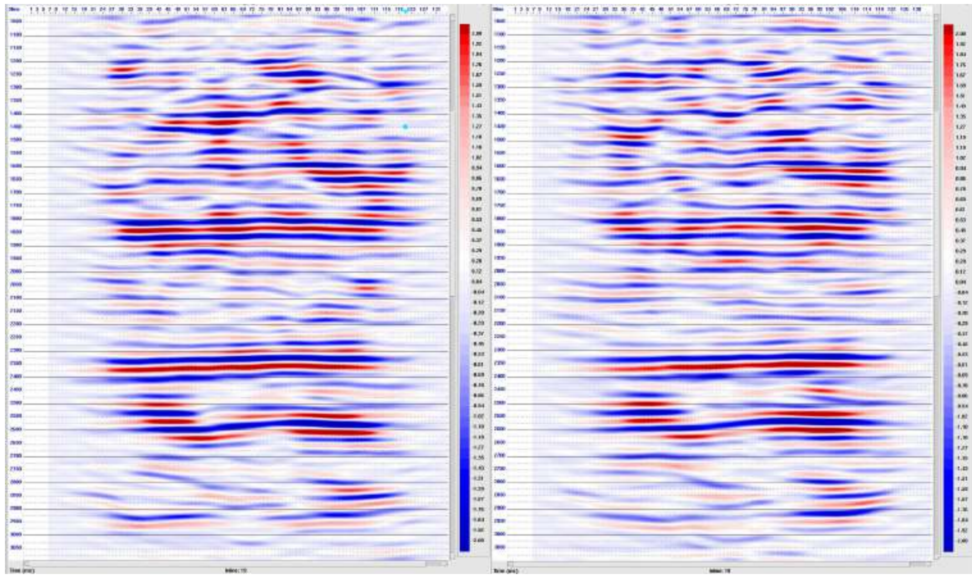

Figure 4.75. Inline 19: S11-2003 (left) and S11-2004 (right).

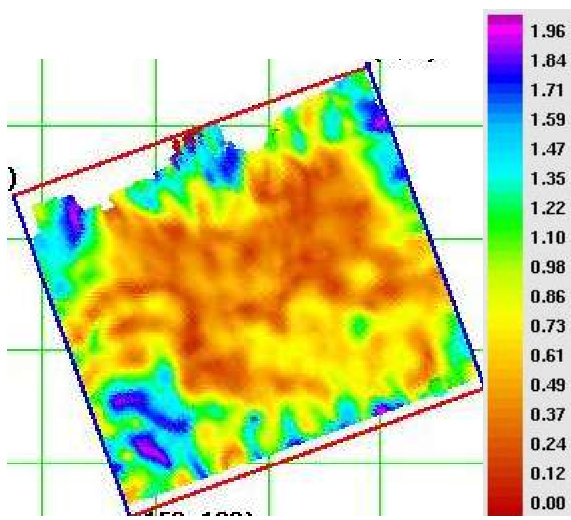

Figure 4.76. NRMS S11 2003-2004 for filtered raw data.

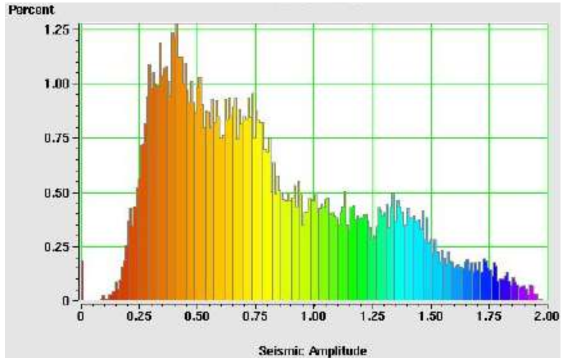

Figure 4.77. Histogram of NRMS S11 2003-2004 for filtered raw data.

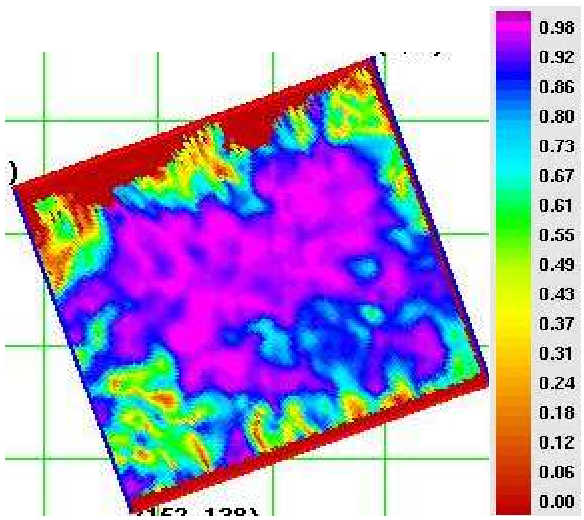

Figure 4.78. Maximum cross-correlation (S11-2003 & 2004) map distribution expressed in fraction.

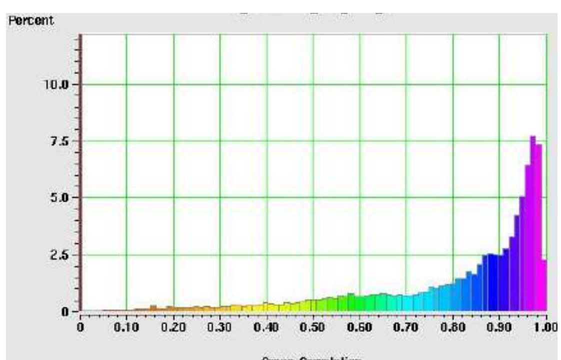

Figure 4.79. Maximum cross-correlation (S11-2003 & 2004) histogram, expressed in fraction.

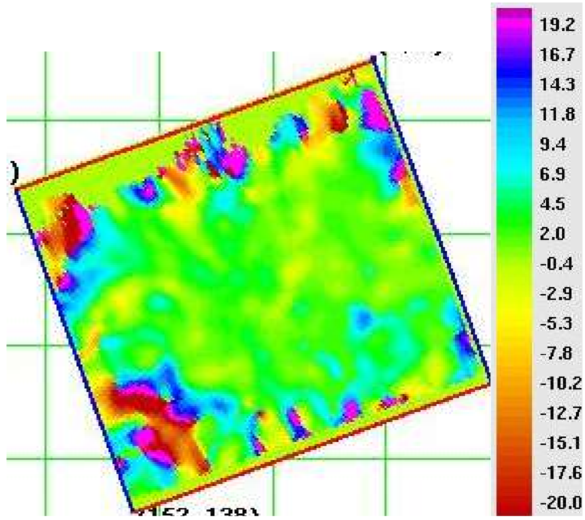

Figure 4.80. Time-shifts applied to S11-2004 relative to S11-2003.

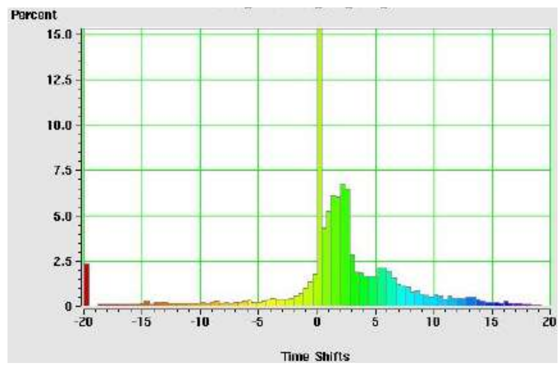

Figure 4.81. Histogram of time-shifts applied to S11-2004 relative to S11-2003.

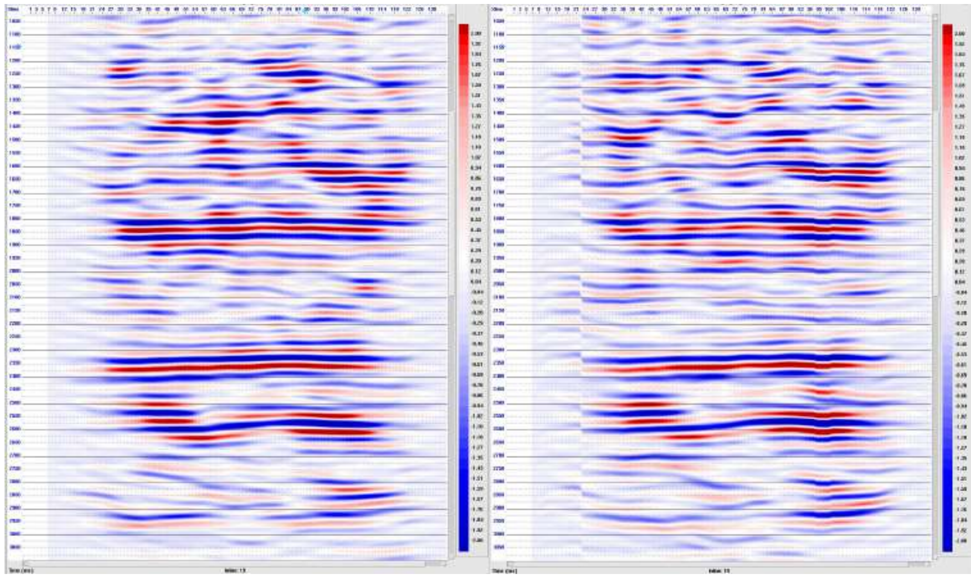

Figure 4.82. Inline 19: S11-2003 (left) and S11-2004 (right), after application of static time shifts to S11-2004.

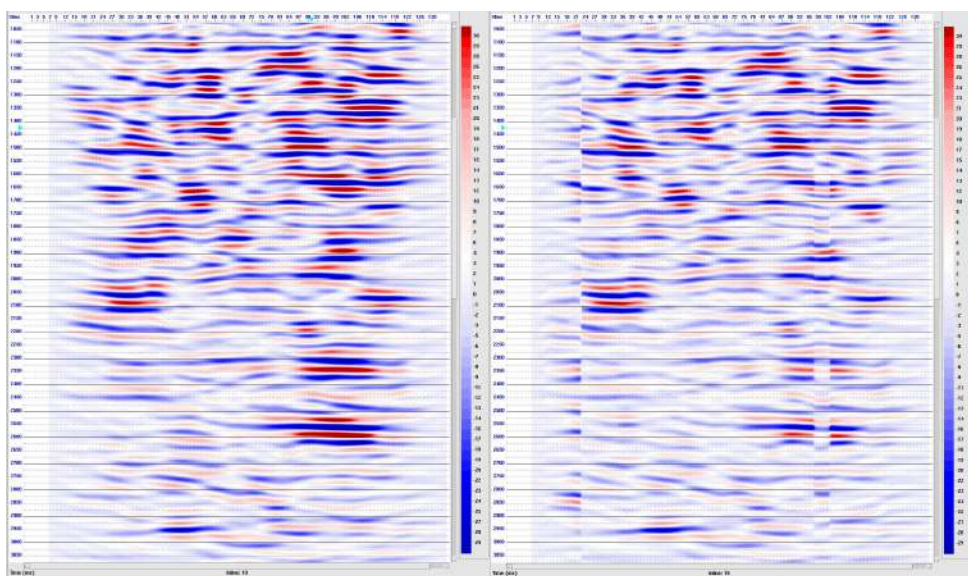

Figure 4.83. Inline 19: Difference S11 2004-2003 for filtered raw data (left) and after application of static time shifts to S11-2004 (right).

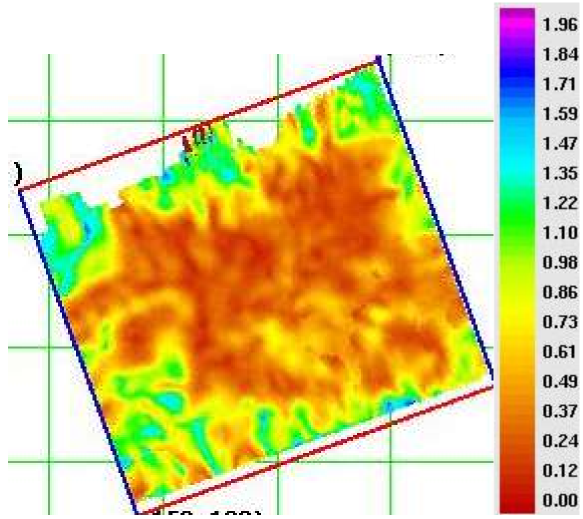

Figure 4.84. NRMS S11 2003-2004 after application of time-shifts to S11-2004.

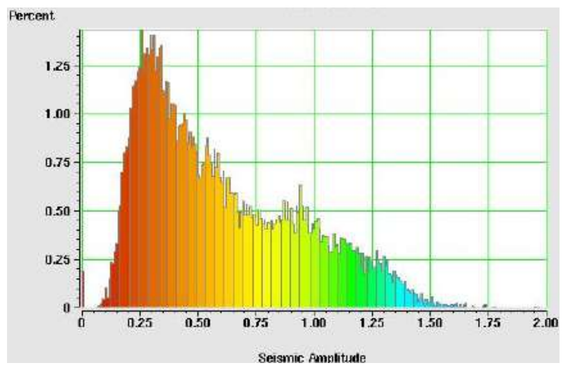

Figure 4.85. Histogram of NRMS S11 2003-2004 after application of time-shifts to S11-2004.

4.7.2 Cross-Normalization (Gain)

The amplitude matching between the two surveys was done by calculating the gain factors in a trace-by-trace basis within the static window. A map view of these gain factors is depicted on Figure 4.86 and its corresponding histogram on Figure 4.87. From these figures it can be seen that the scaling of amplitudes applied to S11-2006 dataset to match the S11-2003 dataset is slightly greater than 1. These could be indicative of a better match of both surveys (2003 & 2004) in terms of amplitudes.

These gain factors were applied to their corresponding traces on the S11-2004 volume, with results shown along with S11-2003 on Figure 4.88. Using this resulting volume, I calculated the S11 2004-2003 difference after applying the gain to S11-2004 and compared the difference before the application of the gain as seen on Figure 4.89. More attenuated anomalies occur between 1800-1900 ms compared to the previous case (static time-shifts). Also a better degree of isolation of time-lapse anomalies occurs at the reservoir level (1900-2400 ms). The resulting NRMS on Figures 4.90 and 4.91 depict both area and value distribution improvement. The NRMS value distribution seen on the histogram is narrower and contains a well defined peak around 0.25, which is considered a milestone on the road to improvement of the S11-2004 repeatability in reference to S11-2003 survey.

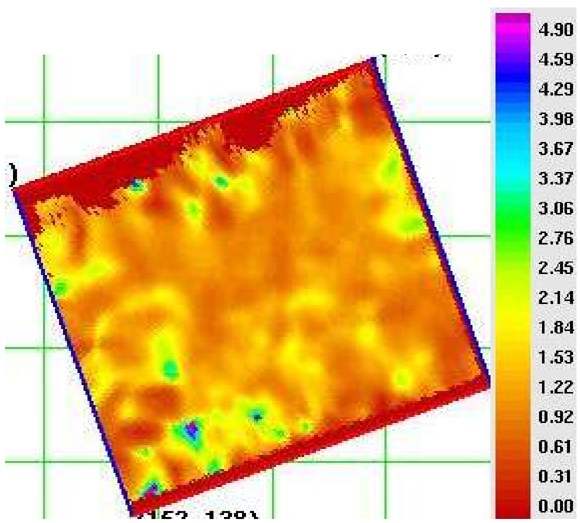

Figure 4.86. Gain factor (trace-by-trace) applied to the S11-2004 volume.

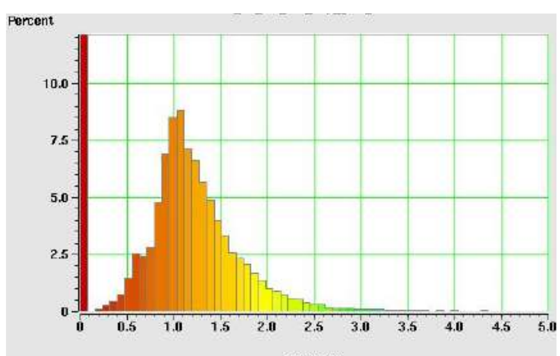

Figure 4.87. Histogram of the gain factor (trace-by-trace) applied to the S11-2004 volume.

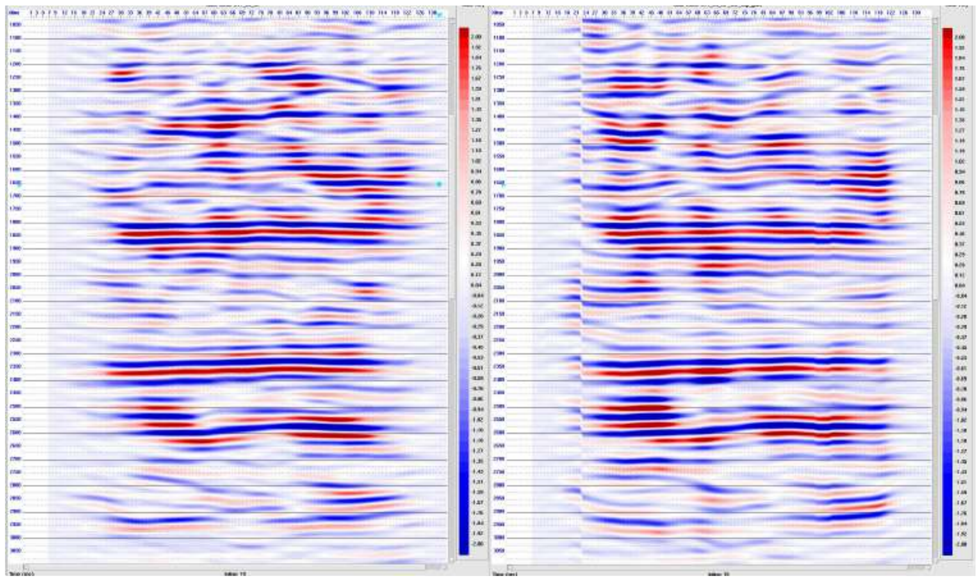

Figure 4.88. Inline 19: S11-2003 (left) and S11-2004 (right), after application of static time shifts and cross-normalization (gain) to S11-2004.

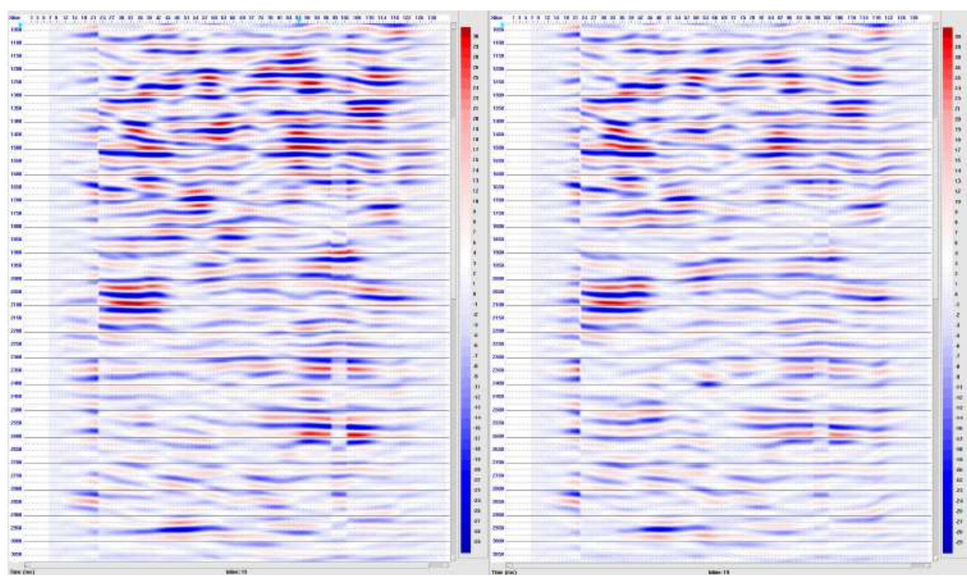

Figure 4.89. Inline 19: Difference S11 2004-2003 after application of static time shifts (left) and after application of time–shifts and cross-normalization (gain) to S11-2004 (right).

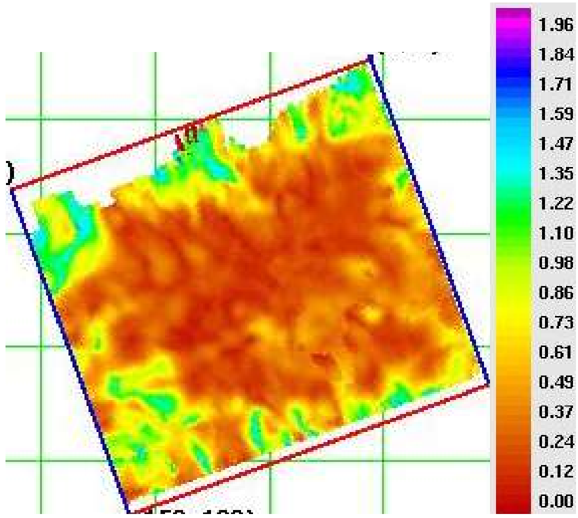

Figure 4.90. NRMS S11 2003-2004 after application of time-shifts and cross-normalization (gain) to S11-2004.

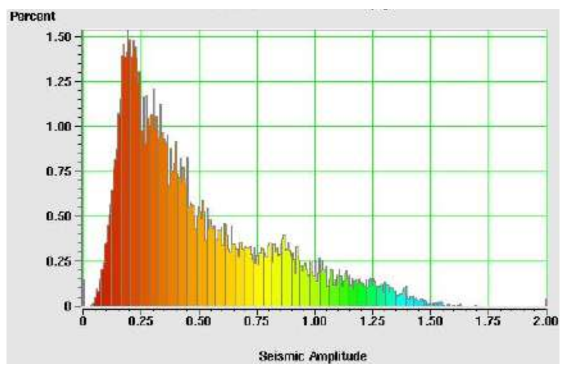

Figure 4.91. Histogram of NRMS S11 2003-2004 after application of time-shifts and cross-normalization (gain) to S11-2004.

4.7.3 Time-variant time-shifts

For this stage, I used the same set of parameters for S11 2003-2006: a sliding window for correlation 200 ms long and starting at 1500 ms. This correlation window had a 1ms step and was done using 1000 windows in order to cover all the seismic events-packages of interest (lower overburden, tight-gas sands interval and coals interval). The time-variant time shifts were designed to be applied to S11 2004, and the resulting volume is shown along with S11 2003 on Figure 4.92. I calculated the S11 2004-2003 differences shown on Figure 4.93 before and after applying these time-variant time shifts. In both cases (Figure 4.92 and 4.93) it can be observed that the “strip-bands” caused by the static time-shifts were largely attenuated by the time-variant time-shifts. Observation of NRMS after the time-variant time-shifts is shown in Figures 4.94 and 4.95. They show there is a slightly better areal distribution of lower NRMS values, despite the fact that the main peak on the NRMS histogram does not shift towards 0. The value distribution represented on the histogram becomes narrower. This observation indicates an improvement of the S11 2003-2004 repeatability.

A final assessment of the S11 2003-2004 cross-equalization occurs by seeing the S11 2004-2003 before and after cross-equalization shown on Figure 4.96. The degree of attenuation of differences is appreciated in most of the time section after cross-equalization. A better assessment of the repeatability improvement by cross-equalization is expressed through the NRMS before and after cross-equalization seen on Figure 4.97, where the series of processes provided a more uniform distribution of lower NRMS values except close to the borders of the survey. In general, lower NRMS values compared to the initial stage as seen on the corresponding histograms, indicating an improvement of the repeatability of these surveys. The improvement is lower compared to the S11 2003-2006 case, but attributed to the unusual weather conditions involving the 2004 survey.

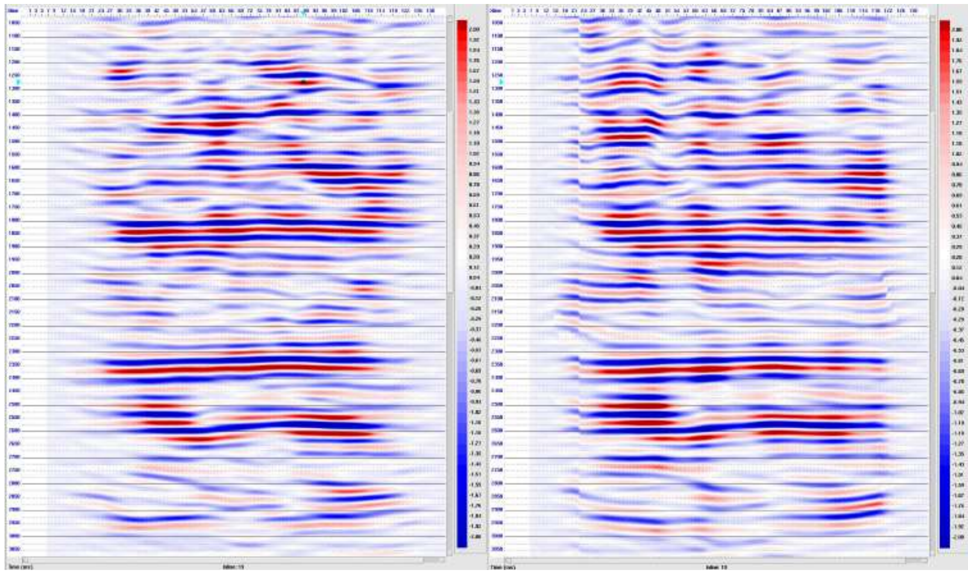

Figure 4.92. Inline 19: S11-2003 (left) and S11-2004 (right), after application of static time shifts, cross-normalization (gain) and time-variant time-shifts to S11-2004.

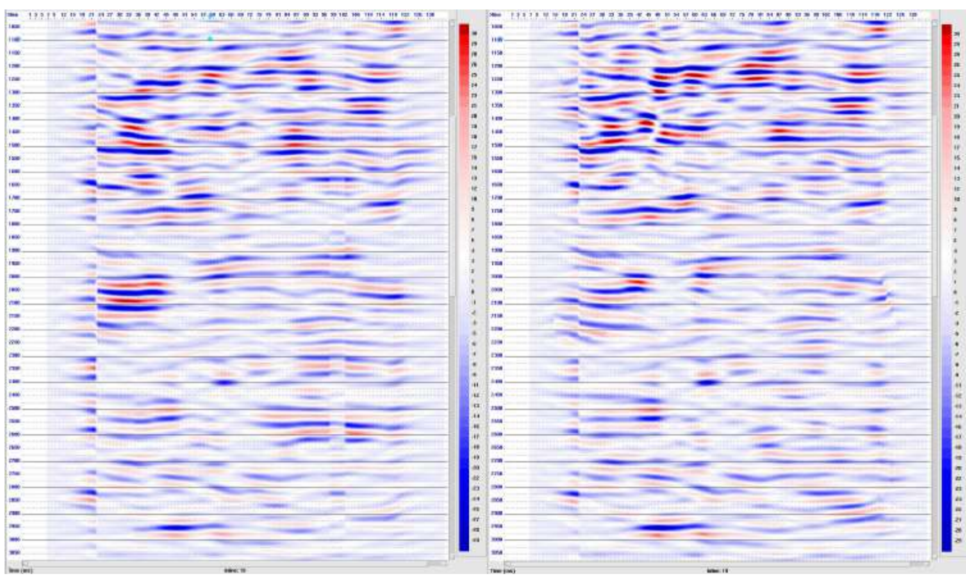

Figure 4.93. Inline 19: Difference S11 2004-2003 after application of time–shifts and cross-normalization (gain) (left), and after application of time–shifts, cross-normalization (gain) and time-variant time-shifts to S11-2004 (right).

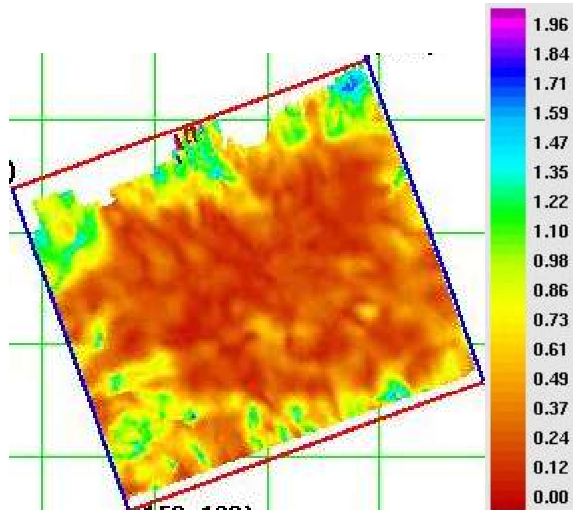

Figure 4.94. NRMS S11 2003-2004 after application of time-shifts, cross-normalization (gain) and time-variant time-shifts to S11-2004.

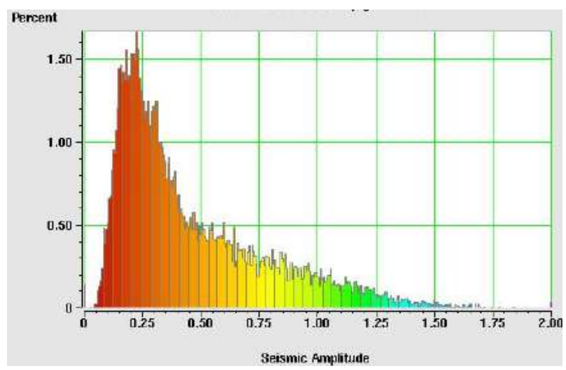

Figure 4.95. Histogram of NRMS S11 2003-2004 after application of time-shifts, cross-normalization (gain) and time-variant time-shifts to S11-2004.

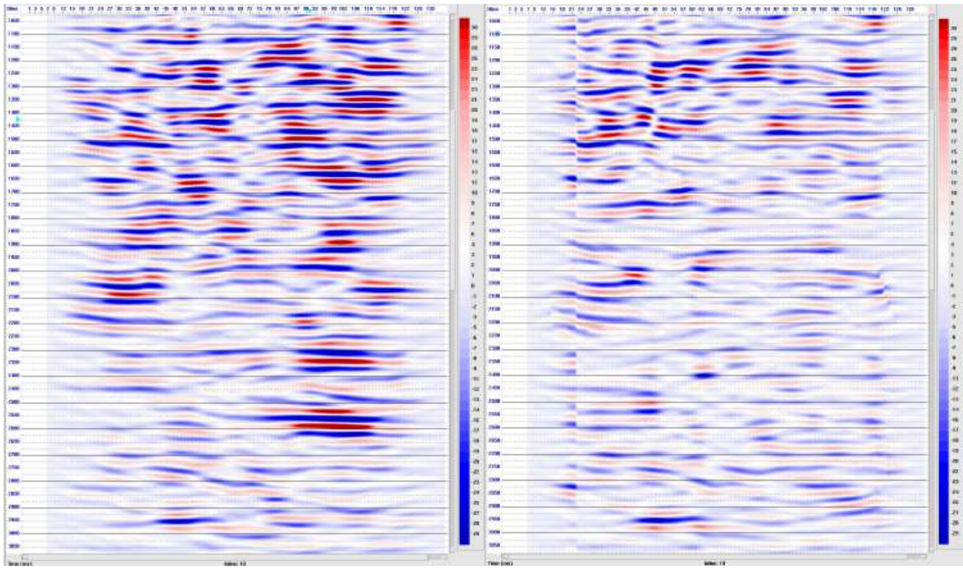

Figure 4.96. Inline 19: Difference S11 2004-2003 before cross-equalization (left) and after cross-equalization (right).

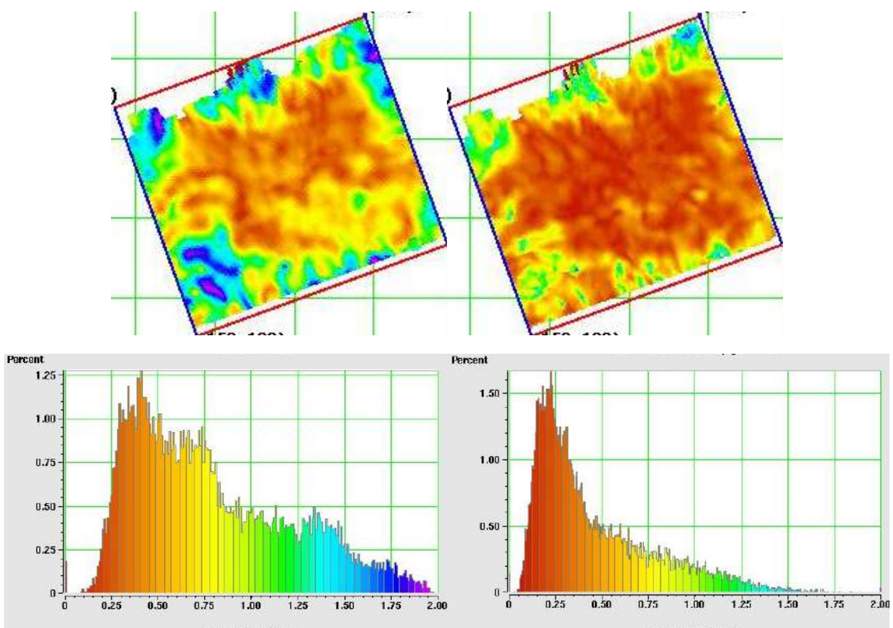

Figure 4.97. NRMS S11 2003-2004 map views before (upper left) and after cross-equalization (upper right). Histograms before (lower left) and after cross-equalization (lower right).

4.8 Cross-Equalization S22-2006 to S22-2003

For the slow-shear wave mode (S22) cross-equalization I used the same order of processes previously done in the PP and S11 cases. Also the input volumes were those band pass filtered (0-0-25-30 Hz) in order to attenuate high frequency noise. After different tests, and considering slightly larger arrival times for this wave-mode, the S22 static window was set on 1800-1950 ms. Figure 4.98 shows both S22-2003 and 2006 volumes before cross-equalization, and Figure 4.99 shows the NRMS map at this stage with its corresponding histogram seen on Figure 4.100. An overall NRMS slightly higher than 0.25 with a good areal distribution (map view) as well as a peak value distribution (histogram) shows that both acquisition and processing provided a good degree of data repeatability for these datasets.

4.8.1 Static Time-shift

Time shifts to the 2006 data were applied by calculating the cross-correlation between the 2006 and 2003 data using only the samples of the traces within the static window. The maximum allowed time shift was set on 20 ms. The maximum correlation found in a trace by traces basis is shown on Figure 4.101, and its corresponding histogram on Figure 4.102. From the map view there is a uniform distribution (except in the survey's borders) of high cross-correlation values as seen on its corresponding histogram with most of the values being higher than 0.9.

The calculated and applied time-shifts are seen on Figure 4.103 as a map view and Figure 4.104 as its corresponding histogram. The value distribution of time shifts around 0 ms is evidence of either no time-lapse velocity changes in the overburden or an overall better repeatability between the S22 2003-2006 surveys. These time-shifts were applied to the corresponding traces of the S22-2006 volume, so both the base S22-2003 and shifted S22-2006 are shown on Figure 4.105. Since the applied time shifts were still very small, there is no obvious change on the S22-2006 dataset that can be seen by the naked-eye.

The difference S22 2006-2003 before and after the application of the static time shifts is shown on Figure 4.106. The attenuation of differences on the overlying levels of the S22 static window shows improvement compared to the S11 case, and also the reservoir differences at this stage in S22 data look enhanced compared to the differences before application of static time-shifts. This fact is going to be supported by the remaining S22 cross-equalization results and the post-stack inversion results as well.

The most appropriate way to assess the quality of the cross-equalization operator is by using NRMS as shown on Figure 4.107, with its corresponding histogram depicted on figure 4.108. The map view (Figure 4.107) presents more uniformly distributed lower NRMS values, and the histogram shows a unique peaked distribution of values lower than 0.25.

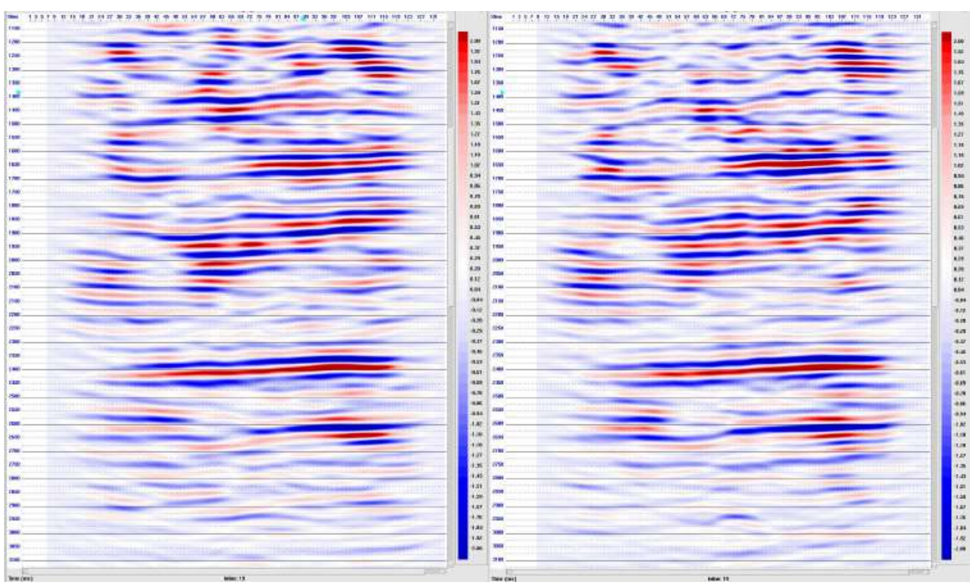

Figure 4.98. Inline 19: S22-2003 (left) and S22-2006 (right).

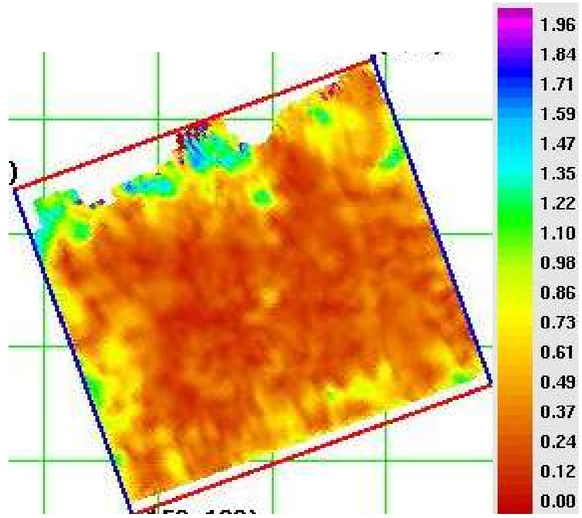

Figure 4.99. NRMS S22 2003-2006 for filtered raw data.

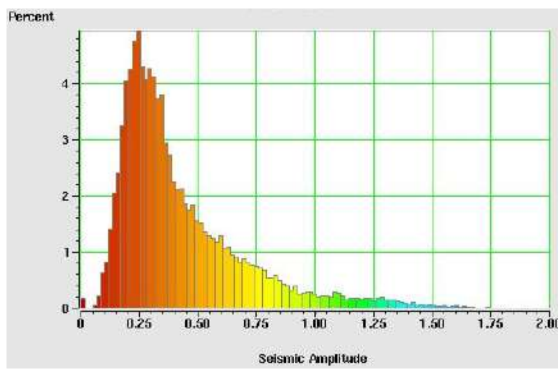

Figure 4.100. Histogram of NRMS S22 2003-2006 for filtered raw data.

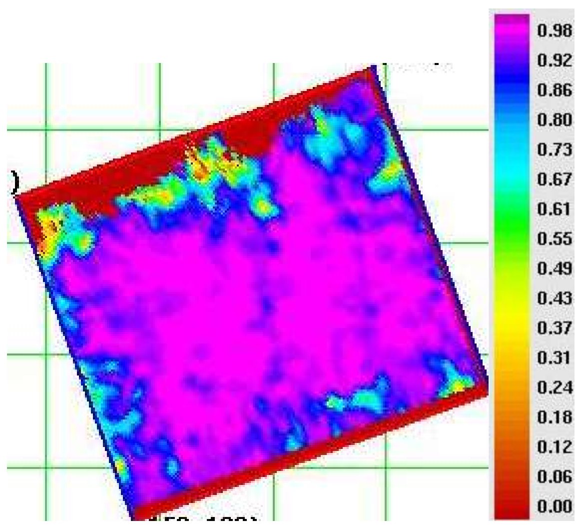

Figure 4.101. Maximum cross-correlation (S22-2003 & 2006) map distribution expressed in fraction.

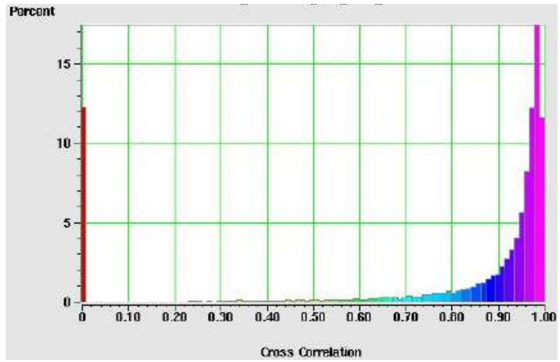

Figure 4.102. Maximum cross-correlation (S22-2003 & 2006) histogram, expressed in fraction.

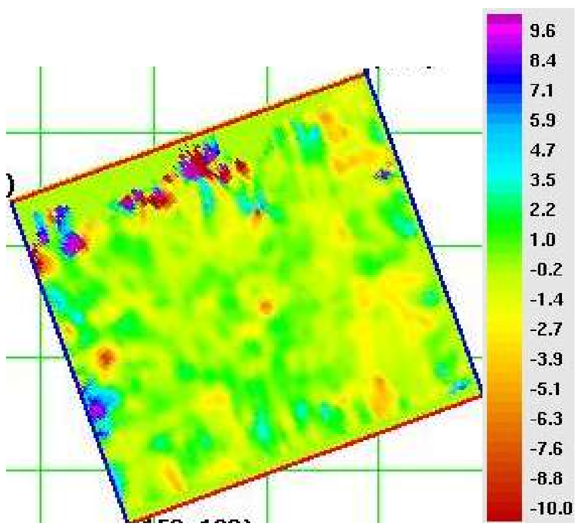

Figure 4.103. Time-shifts applied to S22-2006 relative to S22-2003.

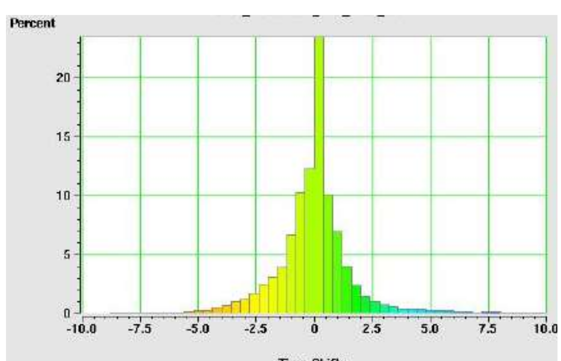

Figure 4.104. Histogram of time-shifts applied to S22-2006 relative to S22-2003.

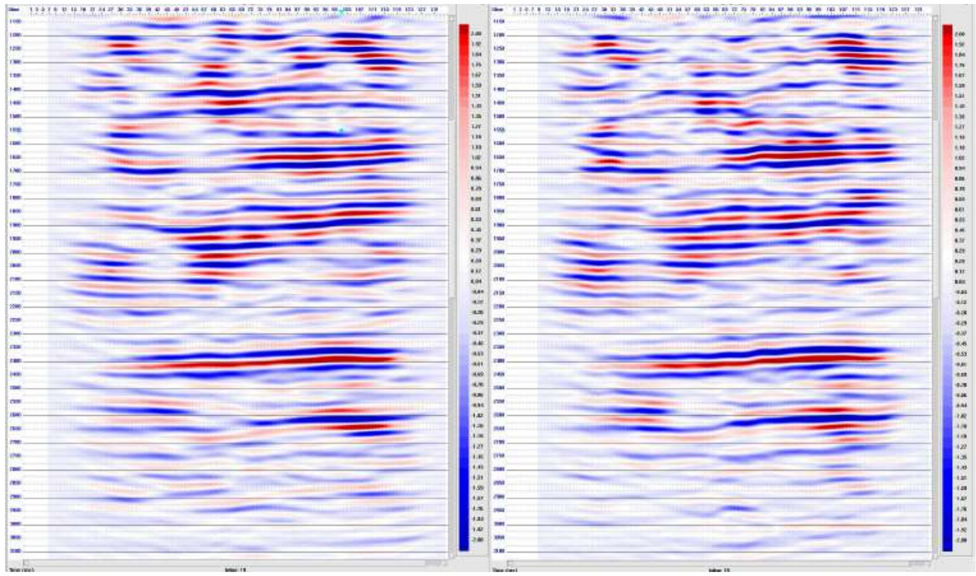

Figure 4.105. Inline 19: S22-2003 (left) and S22-2006 (right), after application of static time shifts to S22-2006.

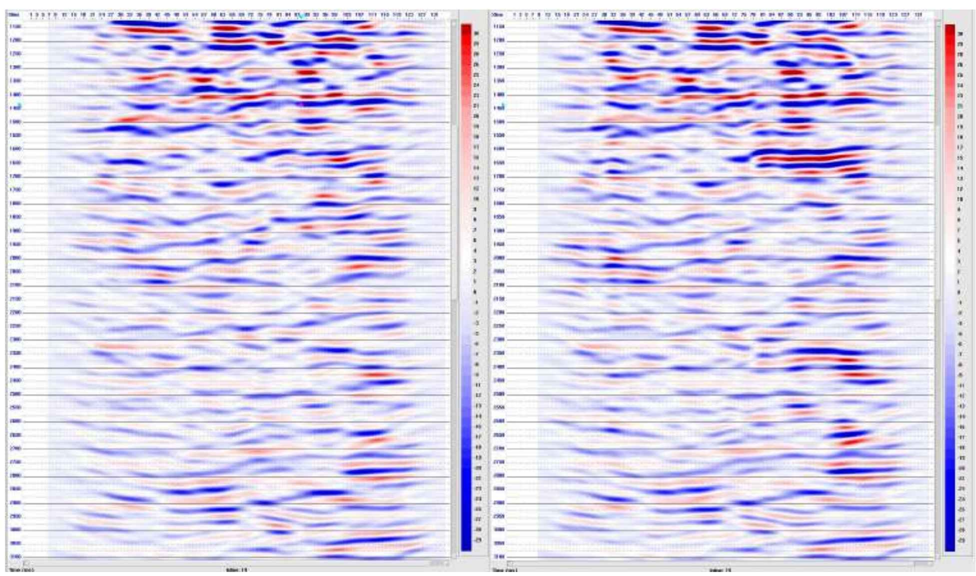

Figure 4.106. Inline 19: Difference S22 2006-2003 for filtered raw data (left) and after application of static time shifts to S22-2006 (right).

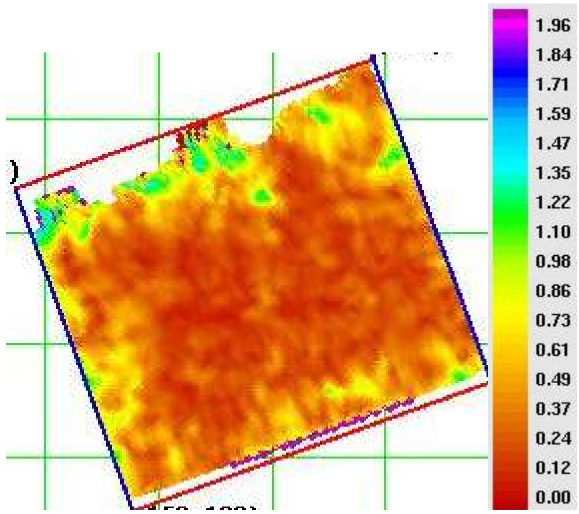

Figure 4.107. NRMS S22 2003-2006 after application of time-shifts to S22-2006.

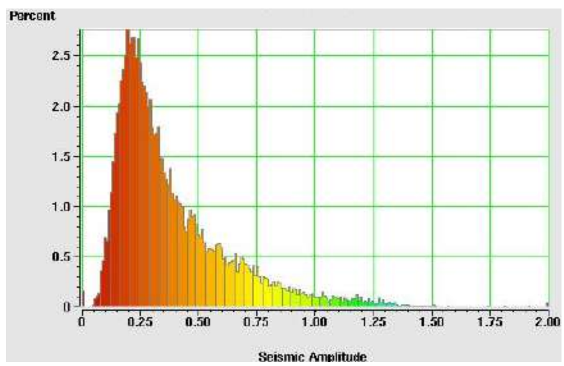

Figure 4.108. Histogram of NRMS S22 2003-2006 after application of time-shifts to S22-2006.

4.8.2 Cross-Normalization (Gain)

The amplitude matching between the two surveys was done by calculating the gain factors on a trace-by-trace basis within the static window. A map view of these gain factors is depicted on Figure 4.109 and its corresponding histogram on Figure 4.110. The scaling of amplitudes applied to S22-2006 dataset to match the S22-2003 dataset is slightly greater than 1, which is an indication that a different coupling occurred.

These gain factors were applied to their corresponding traces on the S22-2006 volume, which results are shown along with S22-2003 on Figure 4.111. Using this resulting volume I calculated the S22 2006-2003 difference after applying the gain to S22-2006 and can be compared to the difference before the application of the gain as seen on Figure 4.112. More attenuated anomalies between 1800-1950 ms occurs compared to the previous case (static time-shifts), as well as more attenuated differences in the shallower overburden (< 1800 ms). The resulting NRMS on Figures 4.113 and 4.114 indicates more uniformly area distributed lower NRMS values, and a narrower distribution peaked around NRMS=0.2.

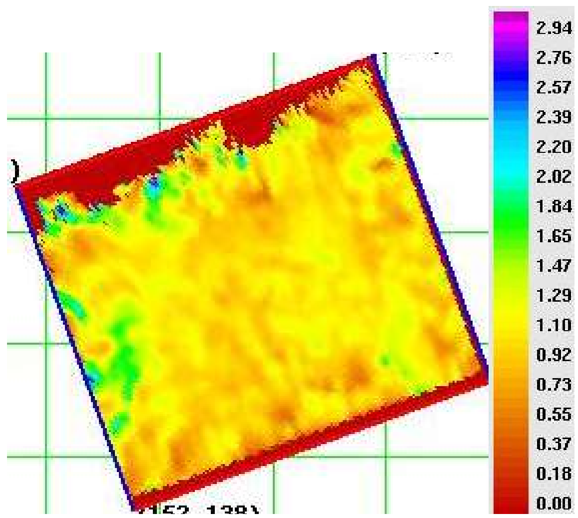

Figure 4.109. Gain factor (trace-by-trace) applied to the S22-2006 volume.

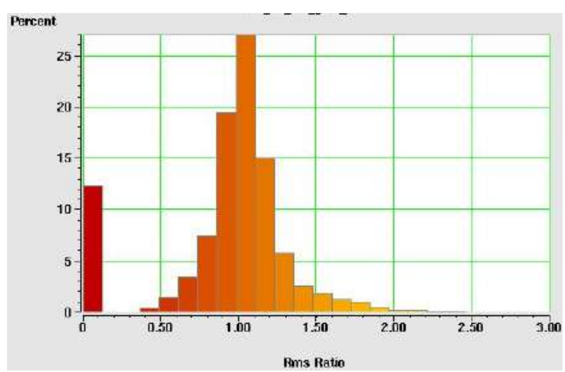

Figure 4.110. Histogram of the gain factor (trace-by-trace) applied to the S22-2006 volume.

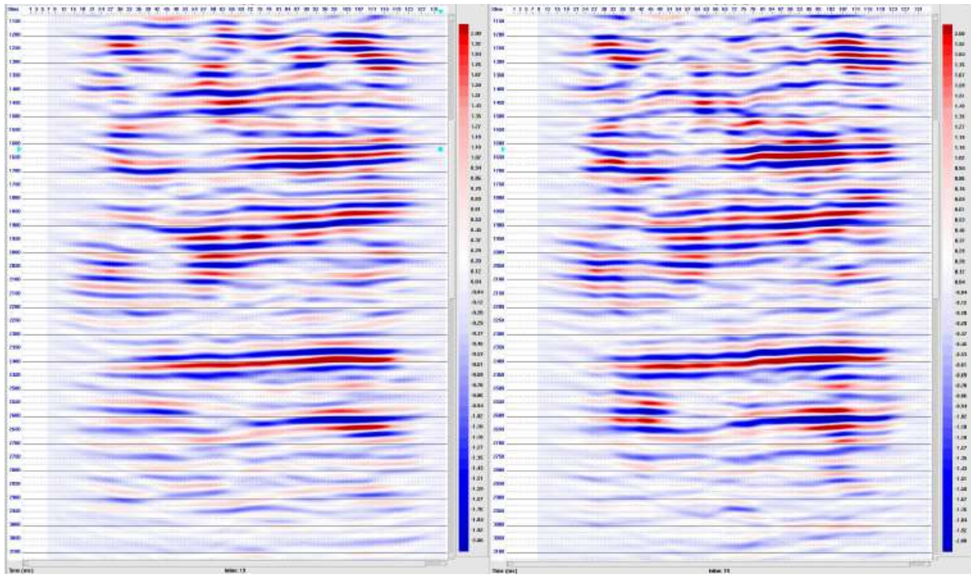

Figure 4.111. Inline 19: S22-2003 (left) and S22-2006 (right), after application of static time shifts and cross-normalization (gain) to S22-2006.

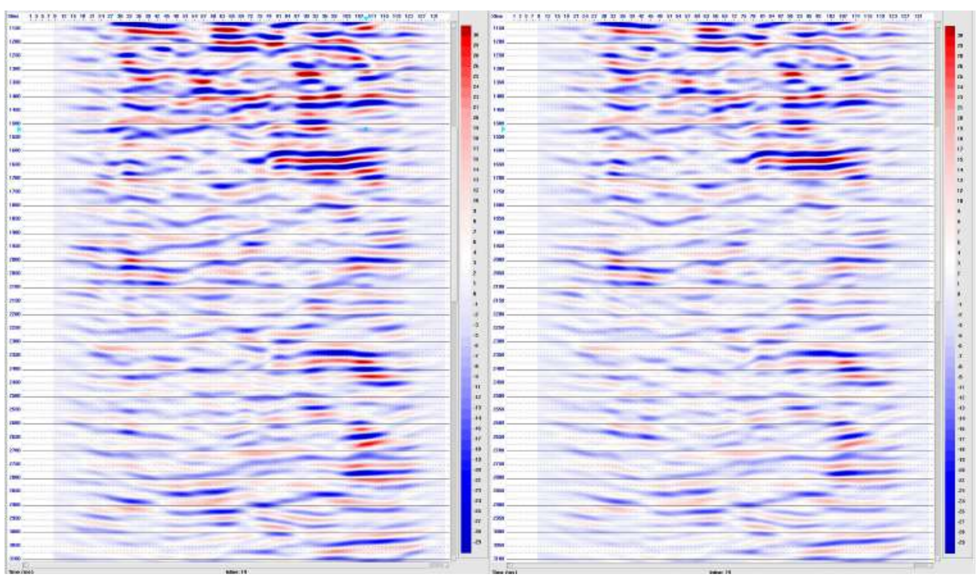

Figure 4.112. Inline 19: Difference S22 2006-2003 after application of static time shifts (left) and after application of time–shifts and cross-normalization (gain) to S22-2006 (right).

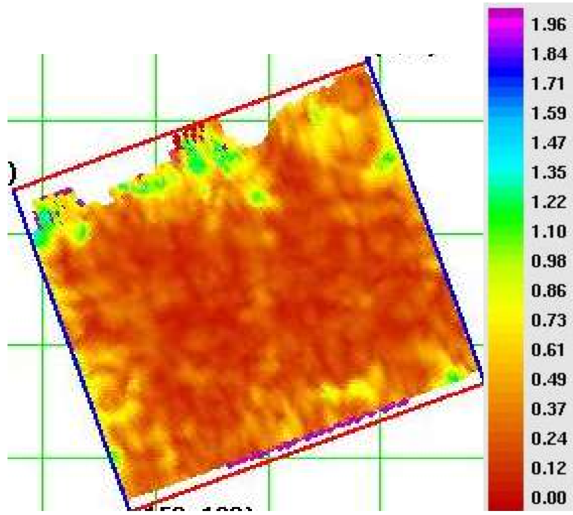

Figure 4.113. NRMS S22 2003-2006 after application of time-shifts and cross-normalization (gain) to S22-2006.

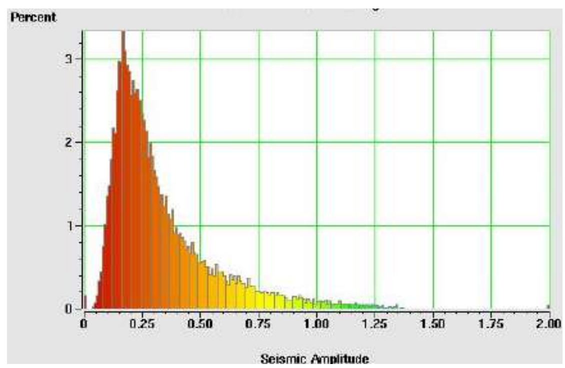

Figure 4.114. Histogram of NRMS S22 2003-2006 after application of time-shifts and cross-normalization (gain) to S22-2006.

4.8.3 Time-variant time-shifts

After the test of different sets of parameters, this final stage in cross-equalization was performed by using a sliding window for correlation being 200 ms long and starting at 1500 ms. This correlation window had a 1ms step and this correlation was done using 1000 windows in order to cover all the seismic events-packages of interest (lower overburden, tight-gas sands interval and coals interval). The time-variant time shifts were designed to be applied to S22 2006, and the resulting volume is shown along with S22 2003 on Figure 4.115, and this was used to calculate the S22 2006-2003 differences shown on Figure 4.116 before and after applying these time-variant time shifts. There is an appreciable improvement in the repeatability of the surveys after the application of this last cross-equalization step by seeing how good the shallow overburden differences were additionally attenuated. The NRMS after the time-variant time-shifts shown on Figures 4.117 and 4.118 allows interpreting that the main NRMS peak shifted towards values close to 0.15 and becomes slightly narrower, which means an improvement on the S22 2003-2006 surveys repeatability.

A final assessment of the S22 2003-2006 cross-equalization can be done by seeing the S22 2006-2003 before and after cross-equalization shown on Figure 4.119, where the degree of attenuation of the differences is seen after cross-equalization. A better assessment of the repeatability improvement by cross-equalization is expressed through the NRMS before and after cross-equalization seen on Figure 4.120, where the series of processes allowed obtaining a more uniform distribution of lower NRMS values, which is translated in an improvement of the repeatability of these surveys.

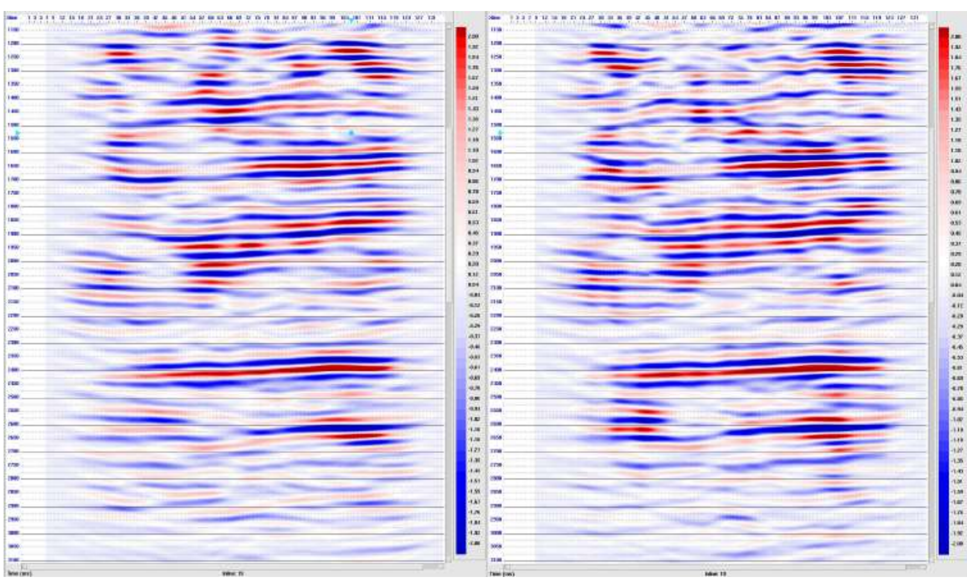

Figure 4.115. Inline 19: S22-2003 (left) and S22-2006 (right), after application of static time shifts, cross-normalization (gain) and time-variant time-shifts to S22-2006.

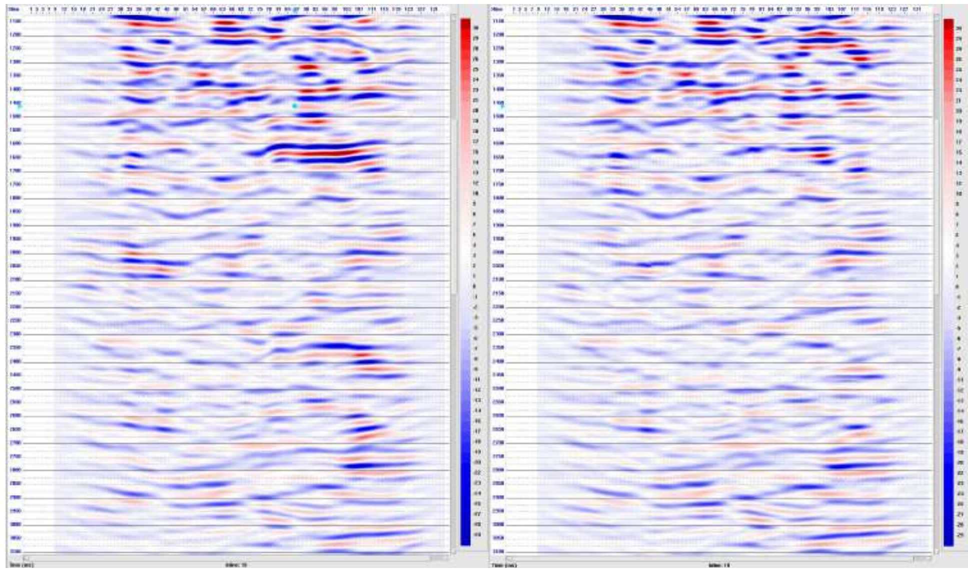

Figure 4.116. Inline 19: Difference S22 2006-2003 after application of time–shifts and cross-normalization (gain) (left), and after application of time–shifts, cross-normalization (gain) and time-variant time-shifts to S22-2006 (right).

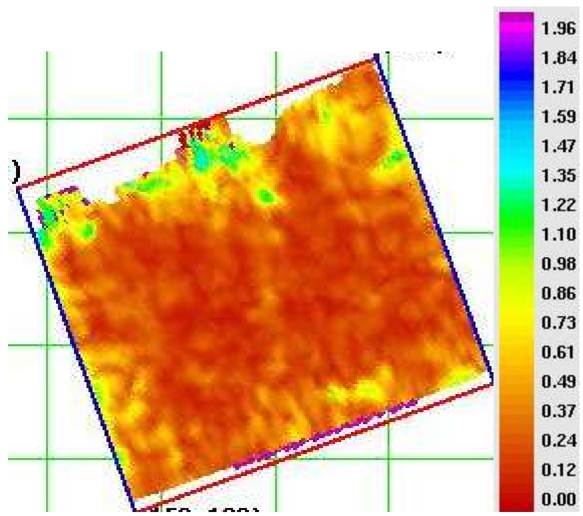

Figure 4.117. NRMS S22 2003-2006 after application of time-shifts, cross-normalization (gain) and time-variant time-shifts to S22-2006.

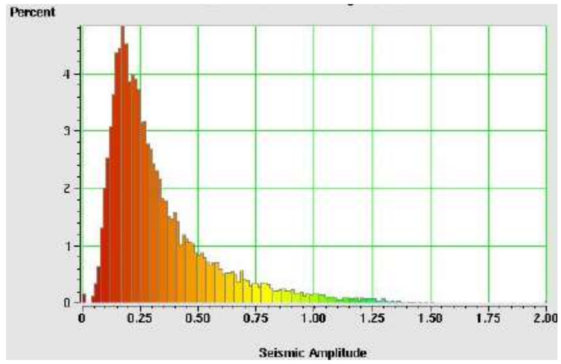

Figure 4.118. Histogram of NRMS S22 2003-2006 after application of time-shifts, cross-normalization (gain) and time-variant time-shifts to S22-2006.

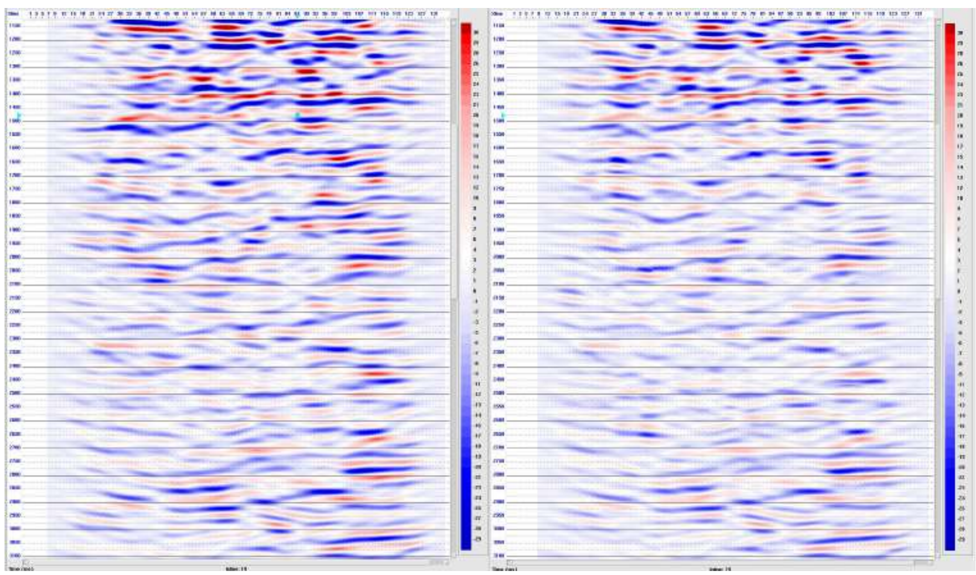

Figure 4.119. Inline 19: Difference S22 2006-2003 before cross-equalization (left) and after cross-equalization (right).

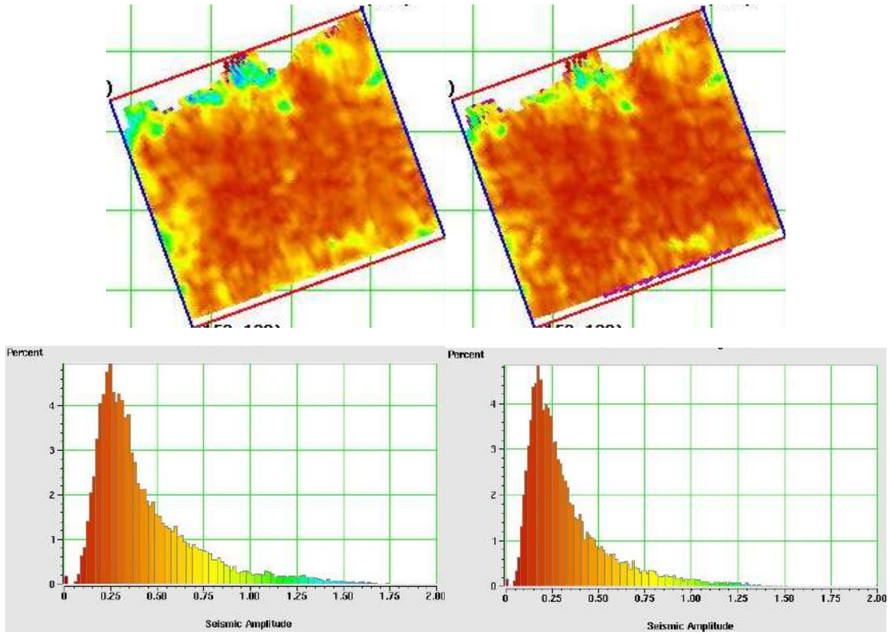

Figure 4.120. NRMS S22 2003-2006 map views before (upper left) and after cross-equalization (upper right). Histograms before (lower left) and after cross-equalization (lower right).

4.9 Cross-Equalization S22-2004 to S22-2003

In order to keep consistency, for the 2003-2004 cross-equalization I used the same parameters for S22 2003-2006 cross-equalization, including the 1800-1950 ms static window, and the band-pass (0-0-25-30 Hz) filtered volumes as input. Figure 4.121 shows both S22-2003 and 2004 volumes before cross-equalization, and Figure 4.122 shows the NRMS map view at this stage along with its corresponding histogram seen on Figure 4.123. Compared to the S22 2003-2006, the survey repeatability of S22 2003-2004 is initially lower than 2003-2006 considering the wide range of variation of NRMS values and its main peak being higher than 0.5. However, after a series of cross-equalization processes a comparable level of similarity between 2003-2006 and 2003-2004 in the static window between these surveys is obtained.

4.9.1 Static Time-shift

Time shifts to the 2004 data were applied by calculating the cross-correlation between the 2004 and 2003 data using only the samples of the traces within the static window. The maximum allowed time shift was set on 20 ms. The maximum correlation found on a trace-by-trace basis is shown on Figure 4.124, and its corresponding histogram is shown on Figure 4.125. Both figures show a fair distribution of high cross-correlation values between the 2003 and 2004 surveys within the static window, which could confirms the initial fair repeatability of those surveys.

The calculated and applied time-shifts are seen on Figure 4.126 as a map view and Figure 4.127 as its corresponding histogram. Like the S11 2003-2004 cross-equalization case, there is a wide distribution of positive time-shifts, which means that the events within the static window for S22 2004 have earlier arrival times than those for S22 2003. This in fact could be a result of a time-lapse changing overburden, or acquisition artifacts due to the previously mentioned anomalous conditions during the 2004 acquisition. In case we assume a changing overburden, its average slow-shear wave velocity in 2004 is in general faster than that for the 2003 case. These time-shifts were applied to the corresponding traces of the S22-2004 volume, so both the base S22-2003 and shifted S22-2004 are shown on Figure 4.128.

The difference S22 2004-2003 before and after the application of the static time shifts is shown on Figure 4.129. Despite the overburden low fold influence in the cross-equalization mentioned earlier, the S22 2004-2003 after the application of static time-shifts shows an outstanding attenuation of differences even above the static window, so the static time-shift operator by itself is a reliable source of improvement of repeatability in this case.

Based on NRMS results shown on Figure 4.130, with the corresponding histogram depicted on Figure 4.131, I observe that the repeatability has been improved through the application of static time-shifts, since the main NRMS peak has been shifted towards lower NRMS values (~0.35) with a narrower distribution of values.

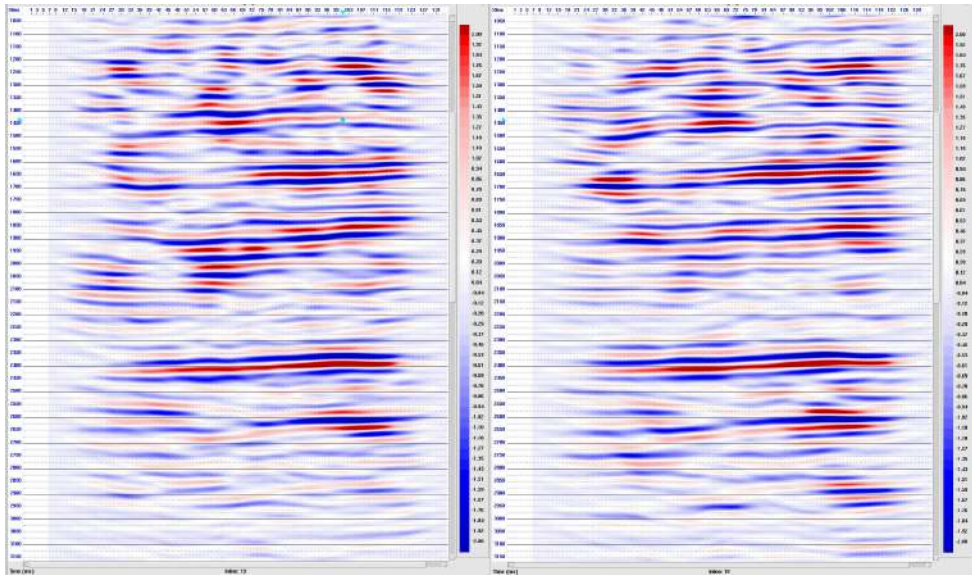

Figure 4.121. Inline 19: S22-2003 (left) and S22-2004 (right).

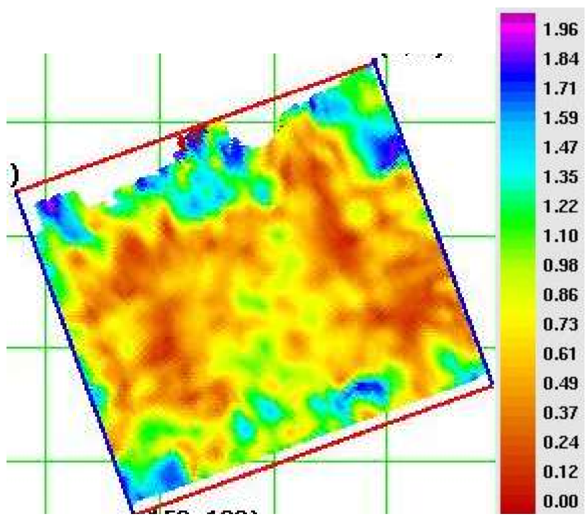

Figure 4.122. NRMS S22 2003-2004 for filtered raw data.

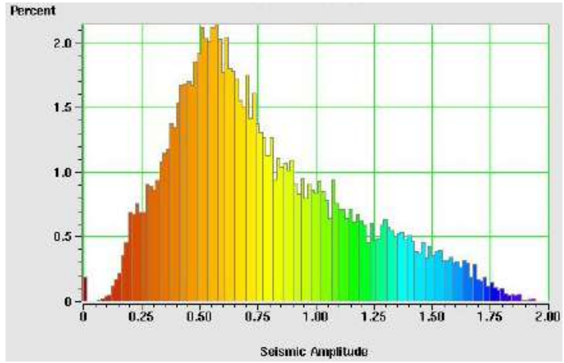

Figure 4.123. Histogram of NRMS S22 2003-2004 for filtered raw data.

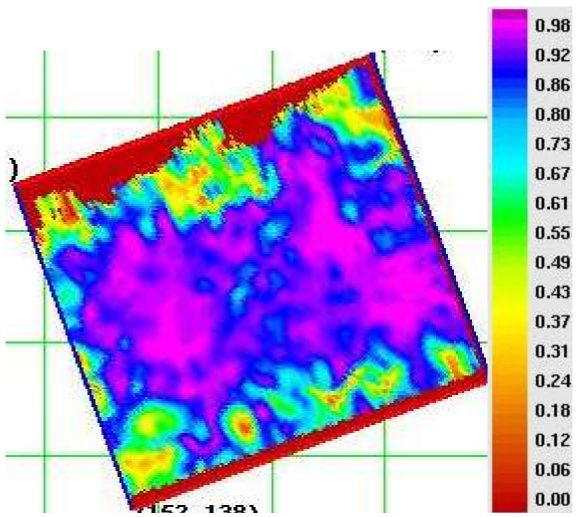

Figure 4.124. Maximum cross-correlation (S22-2003 & 2004) map distribution expressed in fraction.

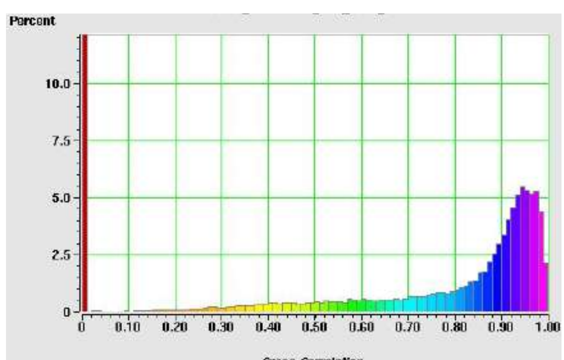

Figure 4.125. Maximum cross-correlation (S22-2003 & 2004) histogram, expressed in fraction.

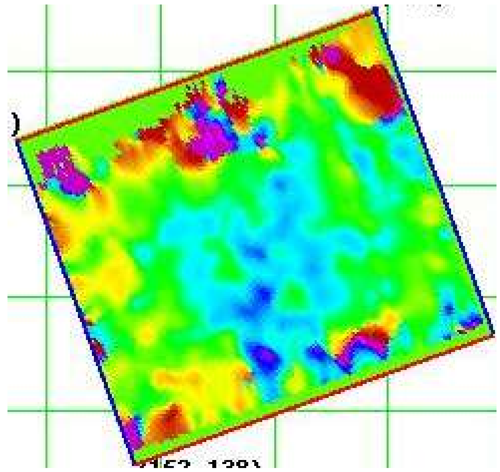

Figure 4.126. Time-shifts applied to S22-2004 relative to S22-2003.

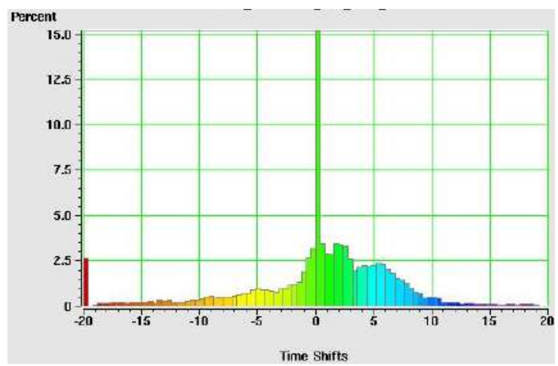

Figure 4.127. Histogram of time-shifts applied to S22-2004 relative to S22-2003.

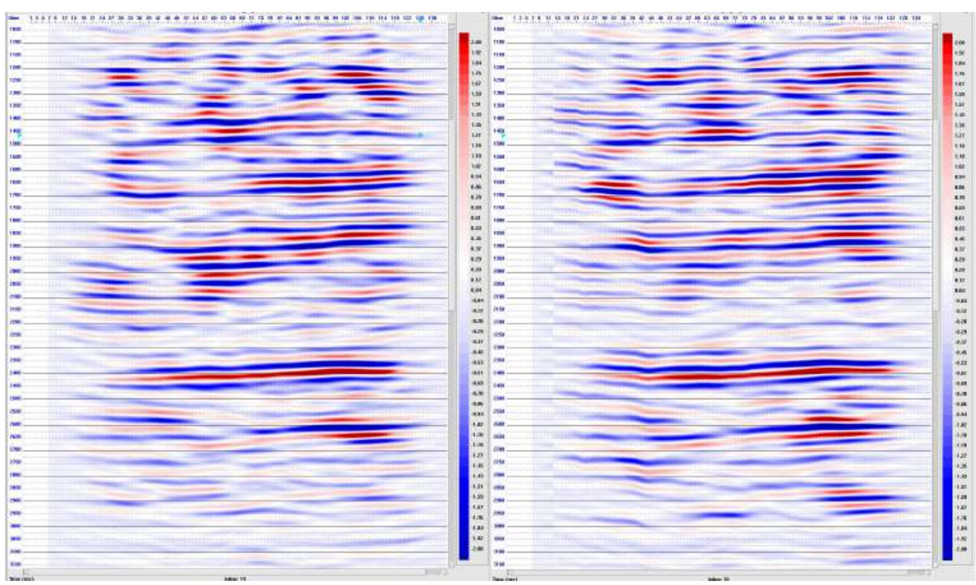

Figure 4.128. Inline 19: S22-2003 (left) and S22-2004 (right), after application of static time shifts to S22-2004.

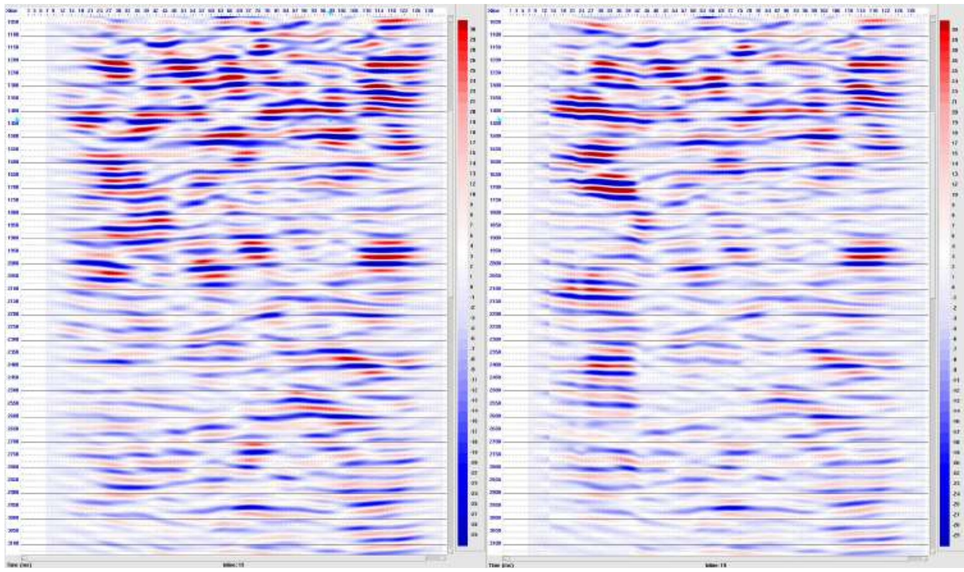

Figure 4.129. Inline 19: Difference S22 2004-2003 for filtered raw data (left) and after application of static time shifts to S22-2004 (right).

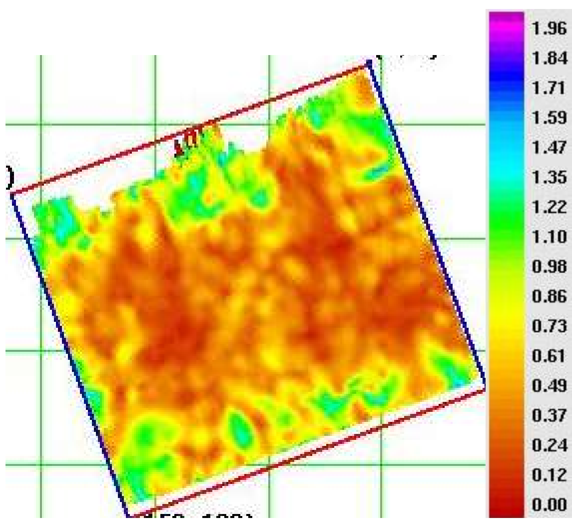

Figure 4.130. NRMS S22 2003-2004 after application of time-shifts to S22-2004.

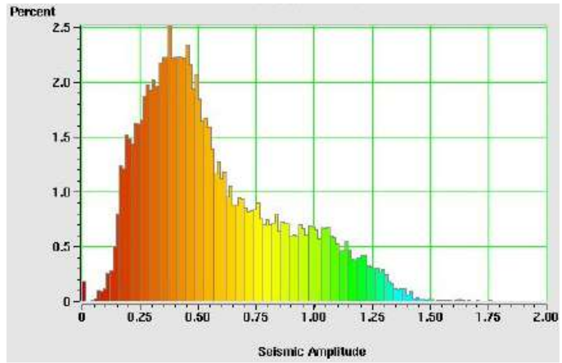

Figure 4.131. Histogram of NRMS S22 2003-2004 after application of time-shifts to S22-2004.

4.9.2 Cross-Normalization (Gain)

The amplitude matching between the two surveys was done by calculating the gain factors in a trace-by-trace basis within the static window. A map view of these gain factors is depicted on Figure 4.132 and its corresponding histogram on Figure 4.133. From these figures it is shown that the scaling of amplitudes applied to S22-2004 dataset to match the S22-2003 dataset is slightly greater than 1. This is a sign of the good degree of repeatability of both surveys (2003 & 2004) in terms of amplitudes.

These gain factors were applied to their corresponding traces on the S22-2004 volume, with results shown along with S22-2003 on Figure 4.134. Using this resulting volume I calculated the S22 2004-2003 difference after applying the gain to S22-2004 and it can be compared to the difference before the application of the gain as seen on Figure 4.135. More attenuated anomalies occur between 1800-1950 ms compared to the previous case (static time-shifts). Also a better degree of isolation of time-lapse anomalies at reservoir level (1950-2400 ms) is observed. The resulting NRMS on Figures 4.136 and 4.137 depicts both areal and value distribution improvement characterized by more uniform area distribution, lower peak value and narrower histogram.

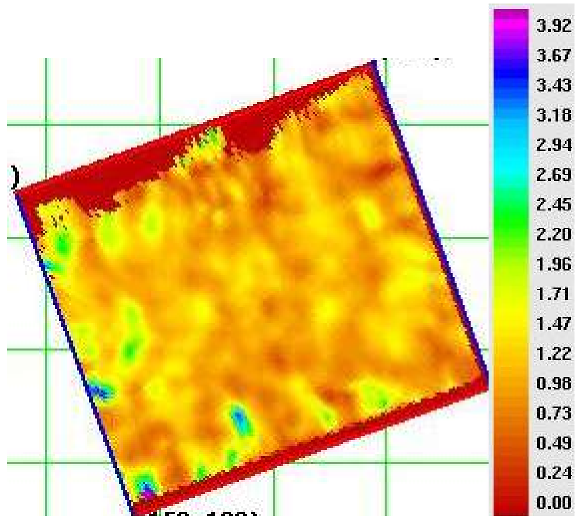

Figure 4.132. Gain factor (trace-by-trace) applied to the S22-2004 volume.

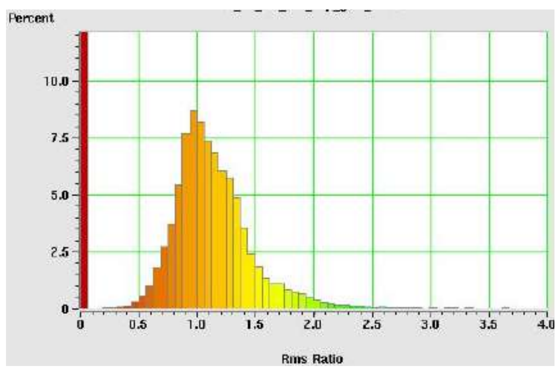

Figure 4.133. Histogram of the gain factor (trace-by-trace) applied to the S22-2004 volume.

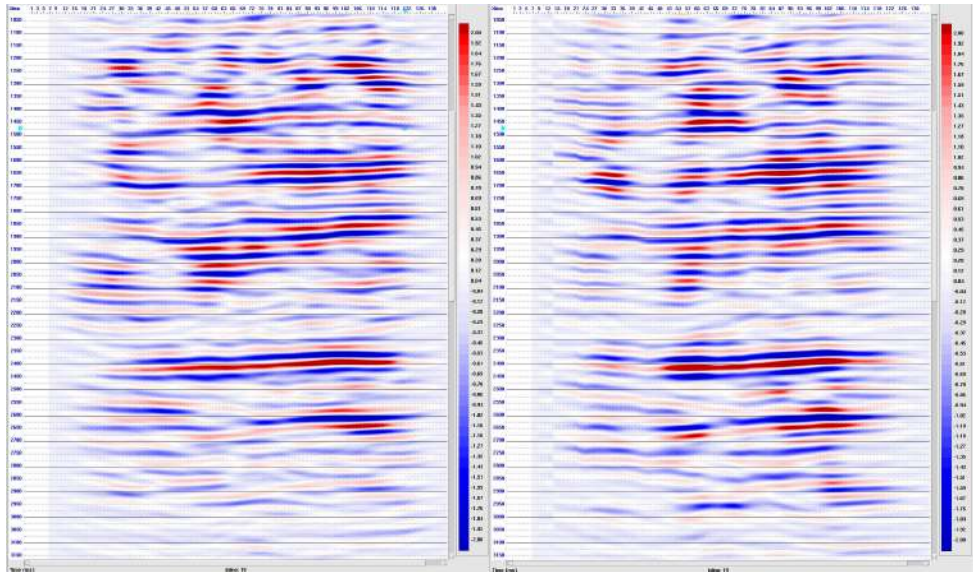

Figure 4.134. Inline 19: S22-2003 (left) and S22-2004 (right), after application of static time shifts and cross-normalization (gain) to S22-2004.

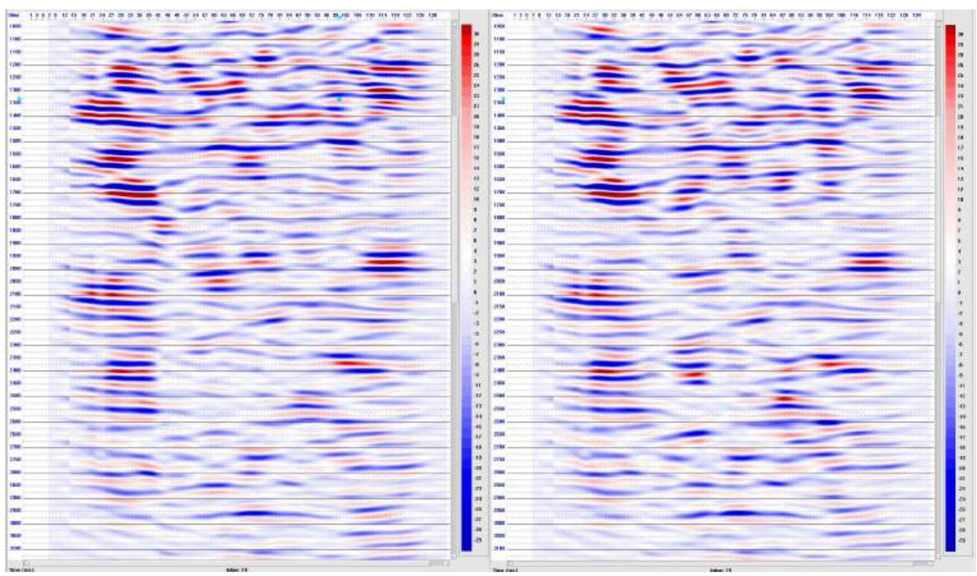

Figure 4.135. Inline 19: Difference S22 2004-2003 after application of static time shifts (left) and after application of time–shifts and cross-normalization (gain) to S22-2004 (right).

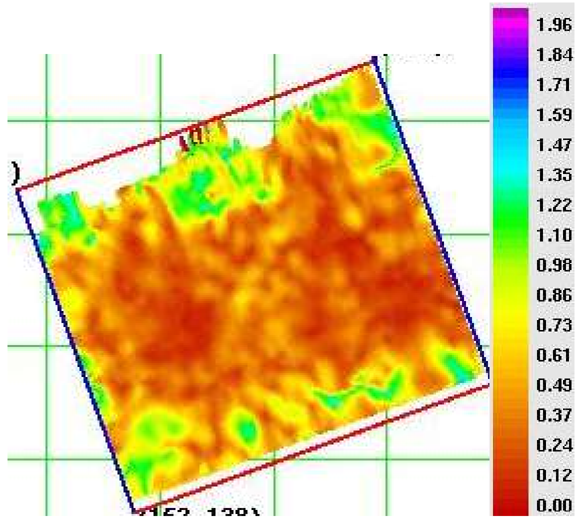

Figure 4.136. NRMS S22 2003-2004 after application of time-shifts and cross-normalization (gain) to S22-2004.

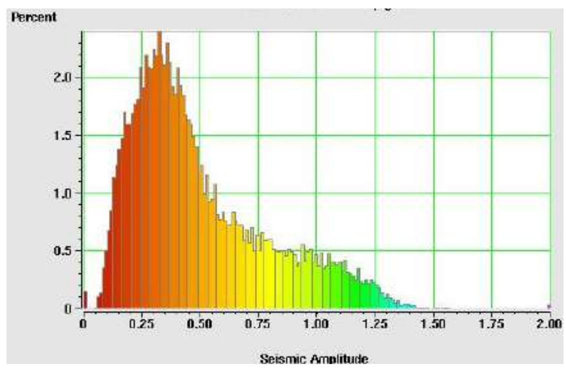

Figure 4.137. Histogram of NRMS S22 2003-2004 after application of time-shifts and cross-normalization (gain) to S22-2004.

4.9.3 Time-variant time-shifts

For this stage I used the same set of parameters used for S22 2003-2006: a sliding window for correlation 200 ms long and starting at 1500 ms. This correlation window had a 1ms step and was performed using 1000 windows in order to cover all the seismic events-packages of interest (lower overburden, tight-gas sands interval and coals interval). The time-variant time shifts were designed to be applied to S22 2004, and the resulting volume is shown along with S22 2003 on Figure 4.138. The S22 2004-2003 differences are shown on Figure 4.139 before and after applying the time-variant time shifts. Differences in the static window are more attenuated and the deeper differences (>

1950 ms) have been better isolated. Observation of NRMS after the time-variant time-shifts as shown on Figures 4.140 and 4.141 allow seeing a slightly better areal distribution of the lower NRMS values. The main peak on NRMS histogram shifts towards 0.25, and the values distribution represented on this histogram becomes narrower. This observation indicates an improvement of the S22 2003-2004 repeatability.

A final assessment of the S22 2003-2004 cross-equalization can be done by seeing the S22 2004-2003 before and after cross-equalization shown on Figure 4.142. The degree of attenuation of the differences can be appreciated in most of the time section after cross-equalization, including a better isolation of time-lapse anomalies at the reservoir level. A better assessment of the repeatability improvement by cross-equalization is expressed through the NRMS before and after cross-equalization seen on Figure 4.143, where the series of processes provided for a more uniform distribution of lower NRMS values except close to the borders of the survey. Seeing lower NRMS values compared to the initial stage as seen on the corresponding histograms, being this case (S22 2003-2004 cross-equalization) demonstrate the most outstanding case of improvement of survey repeatability using cross-equalization seen on this project.

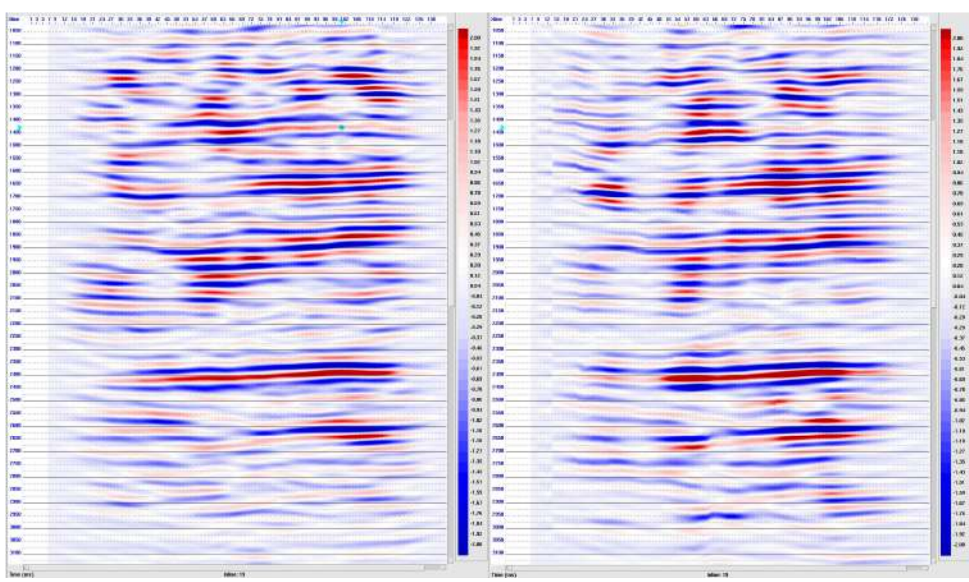

Figure 4.138. Inline 19: S22-2003 (left) and S22-2004 (right), after application of static time shifts, cross-normalization (gain) and time-variant time-shifts to S22-2004.

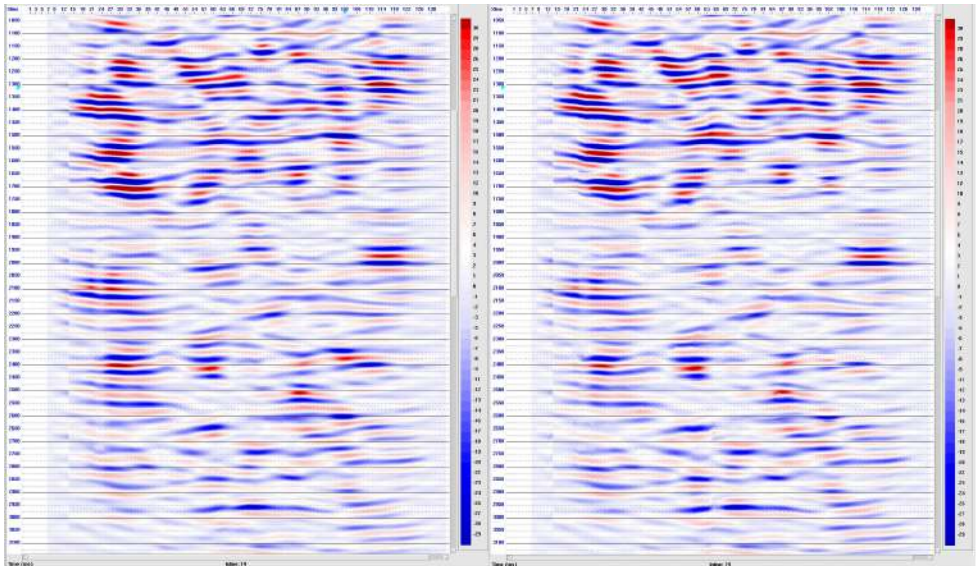

Figure 4.139. Inline 19: Difference S22 2004-2003 after application of time–shifts and cross-normalization (gain) (left), and after application of time–shifts, cross-normalization (gain) and time-variant time-shifts to S22-2004 (right).

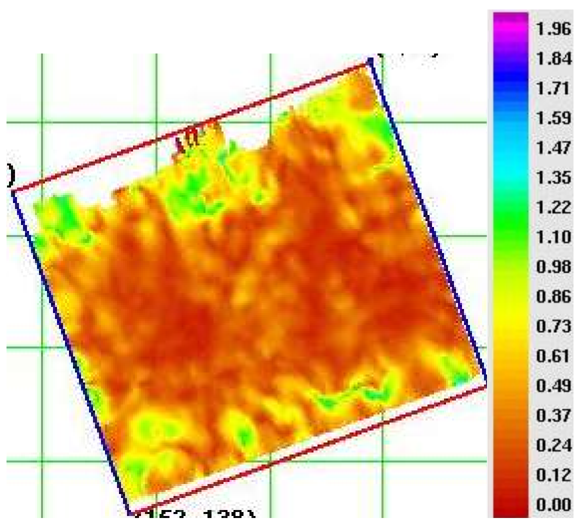

Figure 4.140. NRMS S22 2003-2004 after application of time-shifts, cross-normalization (gain) and time-variant time-shifts to S22-2004.

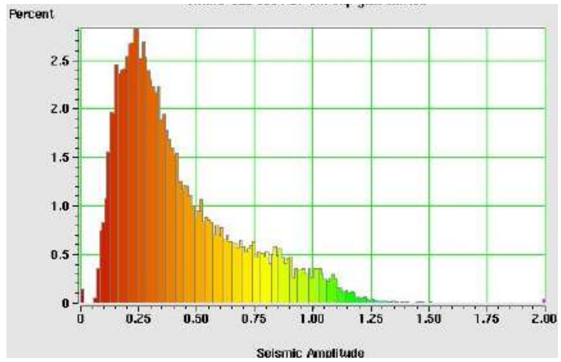

Figure 4.141. Histogram of NRMS S22 2003-2004 after application of time-shifts, cross-normalization (gain) and time-variant time-shifts to S22-2004.

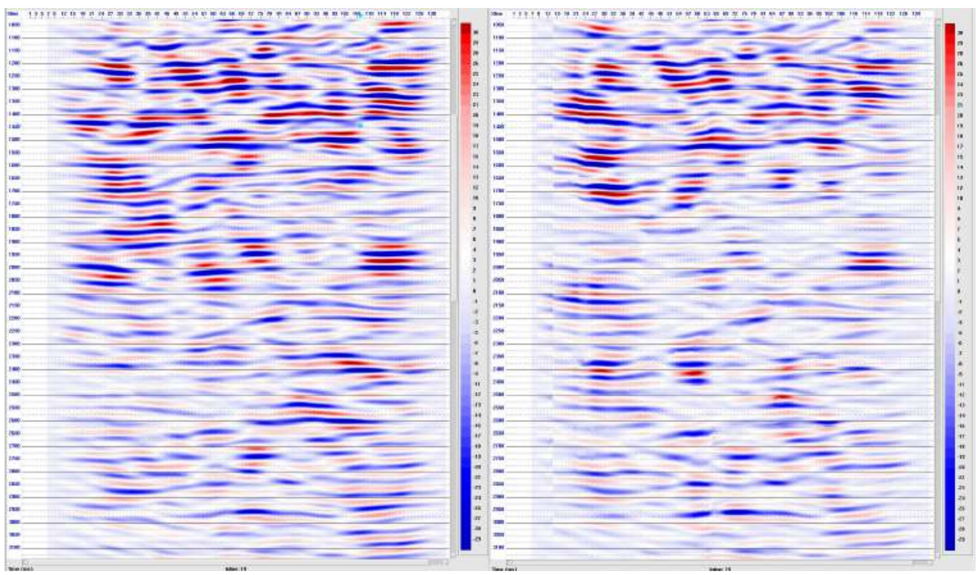

Figure 4.142. Inline 19: Difference S22 2004-2003 before cross-equalization (left) and after cross-equalization (right).

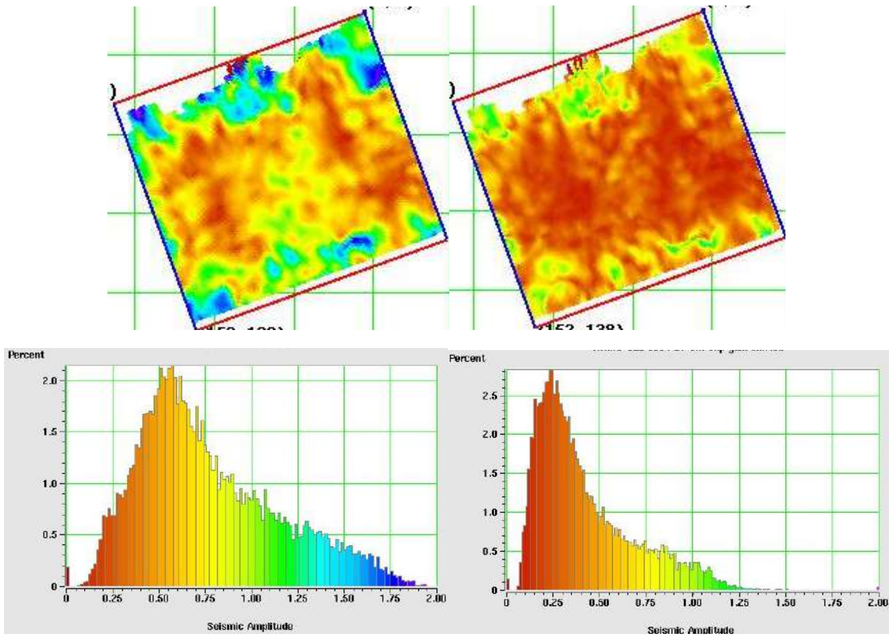

Figure 4.143. NRMS S22 2003-2004 map views before (upper left) and after cross-equalization (upper right). Histograms before (lower left) and after cross-equalization (lower right).

4.10 Summary

Although there are different degrees of improvement, all cross-equalization procedures improved the repeatability of the surveys based on the attenuation of differences within the static window and the enhancement of the differences within the reservoir. In all cases (PP, S11 and S22) it has been shown that the 2004 monitor survey presented a lower quality of cross-equalization results (indeed, lower repeatability) compared to the 2006 monitor survey since acquisition conditions during the 2004 survey were affected by rainfall.

It is necessary to determine a level of confidence during the interpretation of time-lapse anomalies by estimating an approximate level of noise on data in a time-lapse basis which would allow setting a threshold for interpreting time-lapse anomalies. The quality control of cross-equalization expressed as NRMS map view has shown that the fringe area (survey’s borders) has been low-quality cross-equalized, but the effect of this area on the rest of the survey during cross-equalization is minimum or absent due to the trace-by-trace nature of most of the operators. Approximately this fringe extends around 5 traces (~ 200 ft) inside the survey area from the borders, which could help estimating the level of volume cropping for time-lapse interpretation.

CHAPTER 5
POST-STACK SEISMIC INVERSION FOR P- AND S- IMPEDANCE

5.1 Fundamentals

As stated in Chapters 1 and 2, the method I used for calculating V_P/V_S volumes is based on the determination of impedances volumes (P- and S- impedance) to be obtained by post-stack inversion of multi-component seismic data.

Geophysical inverse modeling or inversion is defined as a procedure to determine a model that could have given rise to observed effects (Sheriff, 2002). In the case of post-stack seismic inversion, the technique principle objective is to transform seismic reflection data into a quantitative property that describes the subsurface, traditionally acoustic impedance (P-impedance or Z_P) in the case of P-wave data and/or shear-wave impedance (Z_S) in the case multi-component seismic is available (Pendrel, 2006).

5.2 Inversion Strategy in Rulison Field

Post-stack seismic inversion requires datasets other than seismic (sonic logs, density logs and time-depth relationships) in order to constrain the results. In this case, I used the logs from the control well RU-7, whose relative location is shown on Figure 5.1. There are different algorithms/routines for inversion. The inversion scheme I used is model-based inversion, which works by perturbing an initial-guess model and obtaining modeled seismic data on each iteration until the difference between observed and modeled data has been minimized. In order to perform the forward modeling of the data on each iteration, it is necessary to have an accurate knowledge of the wavelet in the seismic data. Figure 5.2 shows a general workflow for this kind of inversion.

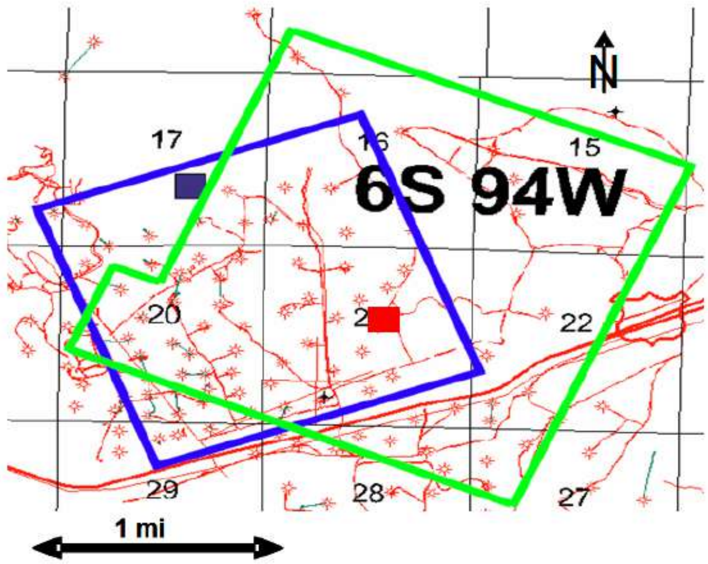

Figure 5.1. Relative location of control well RU-7. Rulison 4D-9C survey outline shown on blue and RU-7 well represented by red-filled square.

I performed model-based inversion due to the following reasons:

- The range of impedance change is expected to be small in magnitude, so accuracy in impedance calculation is usually best suited using model-based inversion.

- By using the same initial model and wavelet while inverting the volumes for a particular wave mode I avoid introducing time-lapse anomalies not related to the reservoir development.

I performed the inversion in three main stages corresponding to each wave mode involved (PP, S11 and S22) using the previously cross-equalized data and Hampson & Russell STRATA® inversion software. Within each of these stages, I inverted the corresponding 2003, 2004 and 2006 volumes using a common initial model and wavelet. Each stage is characterized by the following steps:

- Build the synthetic seismogram from the control well RU-7.
- Horizon picking.
- Initial model building.
- Determination of inversion parameters.
- Full inversion (2003, 2004 and 2006).

The details of these stages are presented in the following sections.

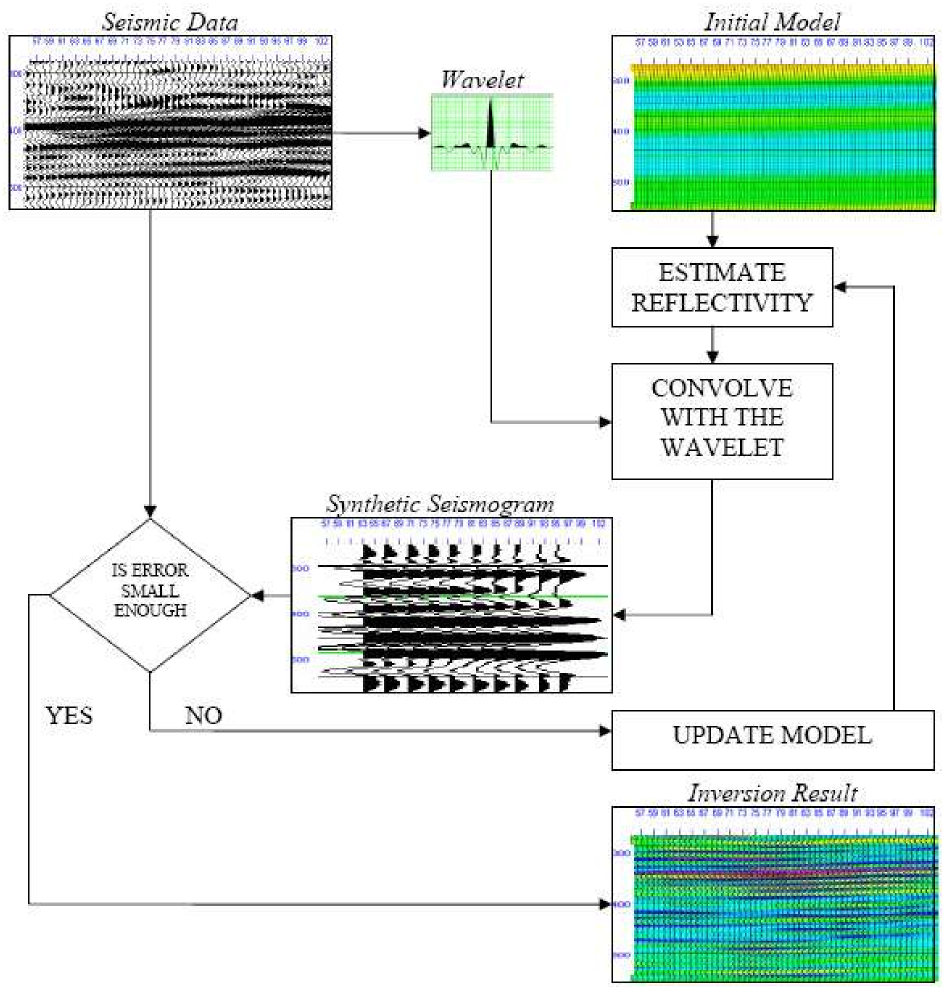

Figure 5.2. Model-based inversion workflow (from Guliyev, 2007)

5.3 Inversion of P-wave seismic data

This inversion was carried out using the previously cross-equalized PP volumes considering their full frequency bandwidth in order to keep a resolution comparable to that of the pure shear volumes. This premise is further explained in the next chapter.

5.3.1 P-wave Synthetic Seismogram and Horizon Picking

Using the check shot data, and sonic and density logs I built a synthetic seismogram for P-wave data as shown on Figure 5.3. The goals of this step are:

- Estimate wavelet and obtain a corrected sonic log.
- Identify seismic events that correlate geologic markers (UMVS and Top Cameo).

This synthetic seismogram allowed 73% of correlation with the observed PP-2003 seismic data, and this correlation is the same for PP-2004 and 2006. This seismogram was built using a zero-phase statistical wavelet which time, frequency and phase responses are shown on Figure 5.4.

The main geological markers, UMVS and Top Cameo, were identified in the synthetic seismogram and interpreted in their corresponding seismic onset, allowing obtaining their corresponding time maps for P-wave data as seen on Figures 5.5 (UMVS) and 5.6 (Cameo). These horizons are used for extrapolation of well-log impedances in order to build the initial model for inversion.

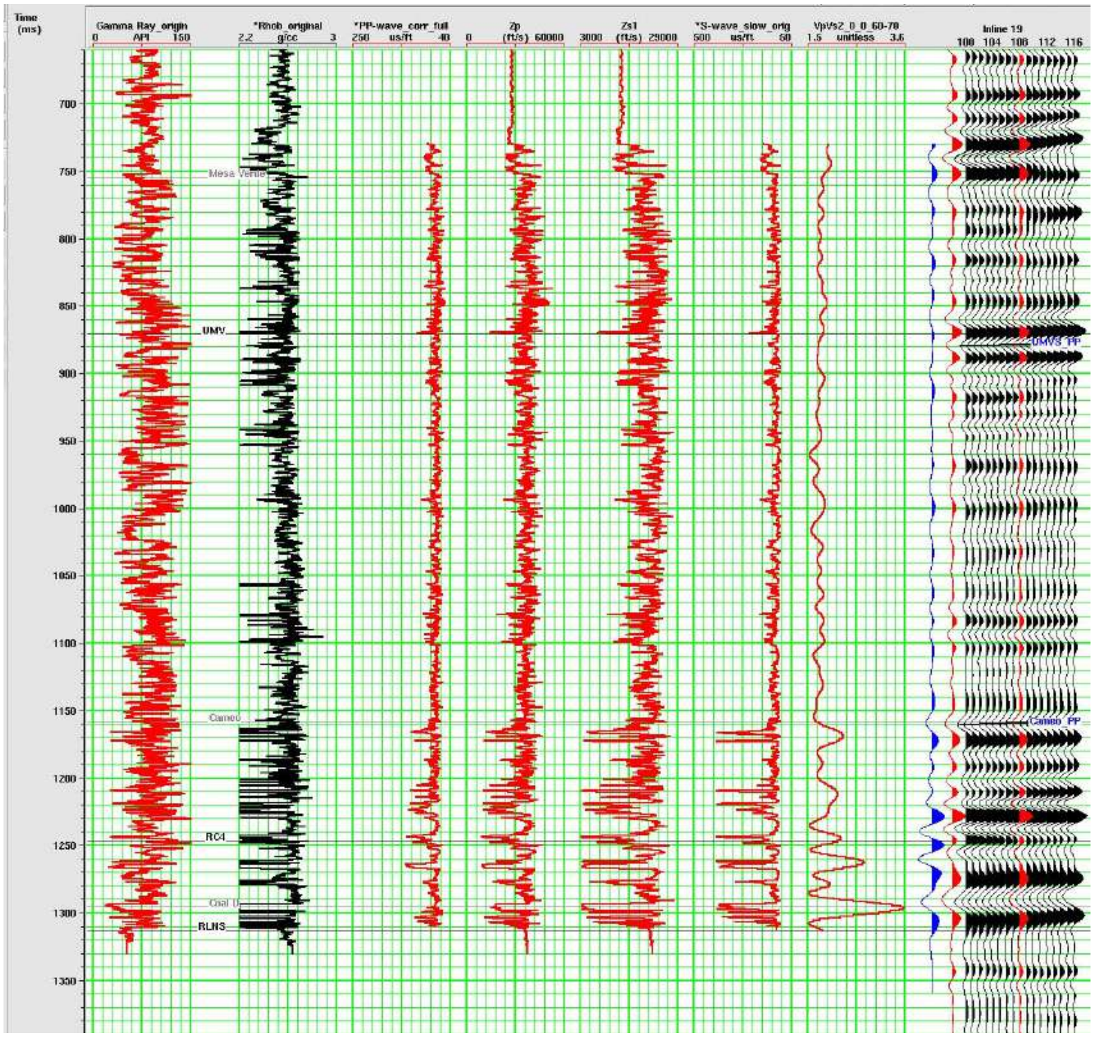

Figure 5.3. Synthetic seismogram (blue trace) for PP-2003 (black and red traces).

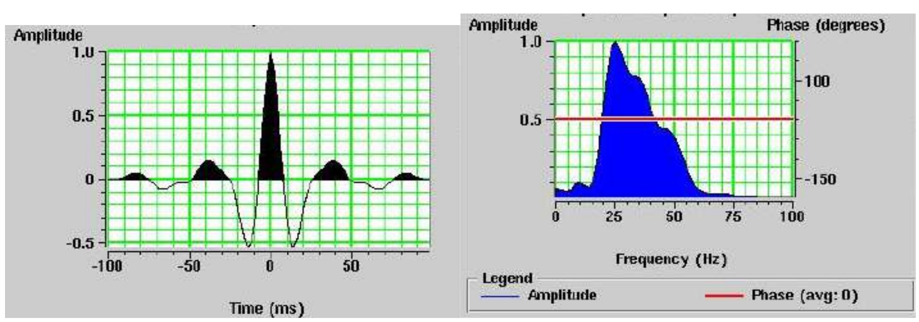

Figure 5.4. Statistical wavelet responses on time (left), frequency (right blue) and phase (right red).

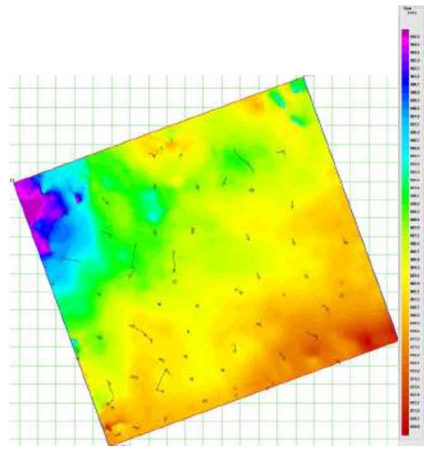

Figure 5.5. UMVS time structural map for P-wave data.

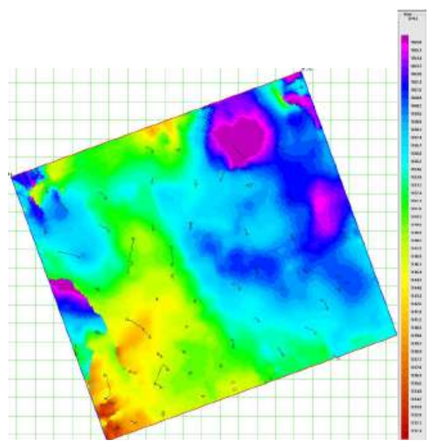

Figure 5.6. Top Cameo time structural map for P-wave data.

5.3.2 Building the Initial P-wave Model

The P-impedance initial model was built using the UMVS and Cameo horizons previously shown in order to extrapolate the impedance values away from control well RU-7. These impedance values are those corresponding to the P-impedance log calculated using the corrected P-wave sonic log and the density log. This impedance log was low-pass filtered (0-10 Hz) in order to avoid introducing details in the inversion output that come from the initial model instead of seismic data, keeping only the low frequency component absent on seismic data. This initial P-impedance model is shown on Figure 5.7.

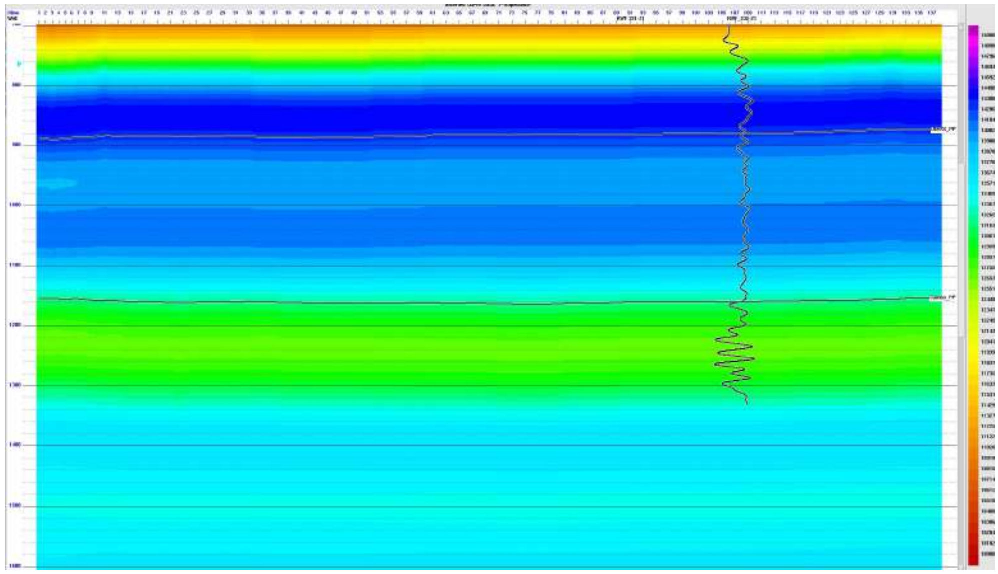

Figure 5.7. IL-19. Initial P-impedance model with RU-7 low-pass filtered impedance log overlaid.

5.3.3 Determination of P-wave Inversion Parameters and Inversion Results

Using the initial P-impedance model is possible to test different inversion parameters at the RU-7 location, until I found the optimum parameter set. Figure 5.8 depicts the inversion results at RU-7 location using the optimum set of parameters.

This test was done using the PP-2003 seismic data (base survey) but is very similar to those of PP-2004 and PP-2006. That is why it is possible to keep the same parameters for inversion of the three datasets. I allowed +/- 30% of variation from the initial model through five (5) iterations using a scaler adjustment factor of 0.9 and 1% of pre-whitening.

The inversion achieved its goal of recovering an impedance model similar to the impedance log at the well location at 0-60 Hz bandwidth, and all the details on the inversion results are derived from seismic data, not from the initial model which has been highly smoothed due to the low-pass frequency filtering. The correlation between the P-impedance log and the impedance from inversion is over 86% in the interval of interest. Most of the mismatches occur in the Cameo coal interval (1150-1350 ms), which could be caused by inaccurate measurements of the well log due to instability of the well-bore in the coals.

Having the inversion parameters defined, as well as the initial model and the wavelet, I inverted the PP-2003, 2004 and 2006 volumes using the model-based inversion algorithm. Corresponding results are shown on Figures 5.9, 5.10 and 5.11.

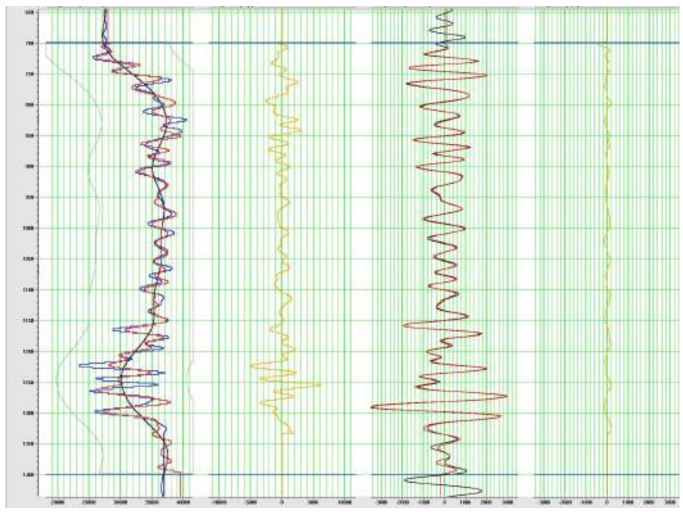

Figure 5.8. Inversion Results at RU-7 location. Track 1 (left): Initial Model (black), original P-impedance log (blue) and inversion result (red). Track 2 (left-center): Error on Impedance (yellow). Track 3 (center-right): Seismic trace (black), modeled trace (red). Track 4 (right): Error on traces (yellow).

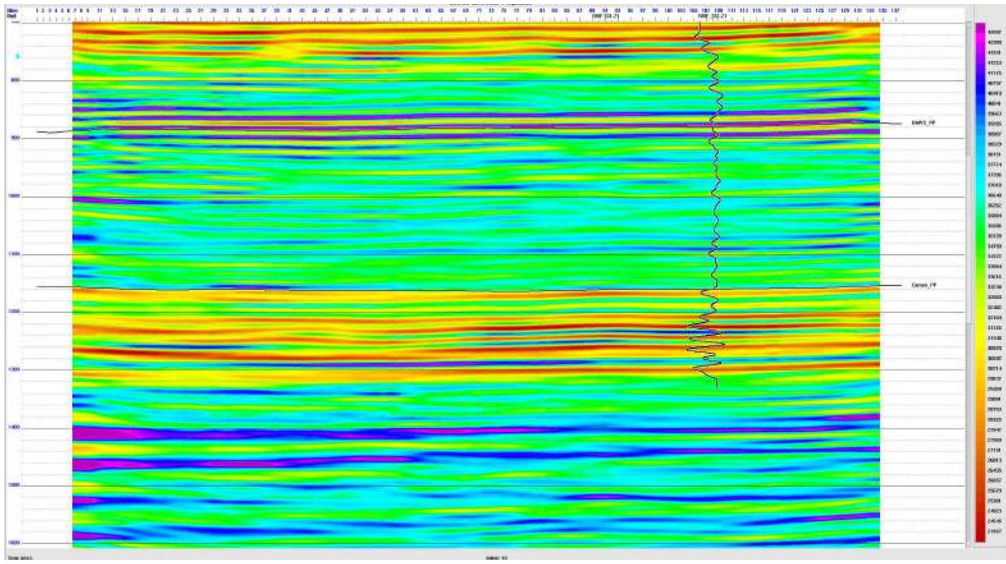

Figure 5.9. IL-19. PP-2003 Inversion result (P-impedance) with RU-7 low-pass filtered impedance log overlaid.

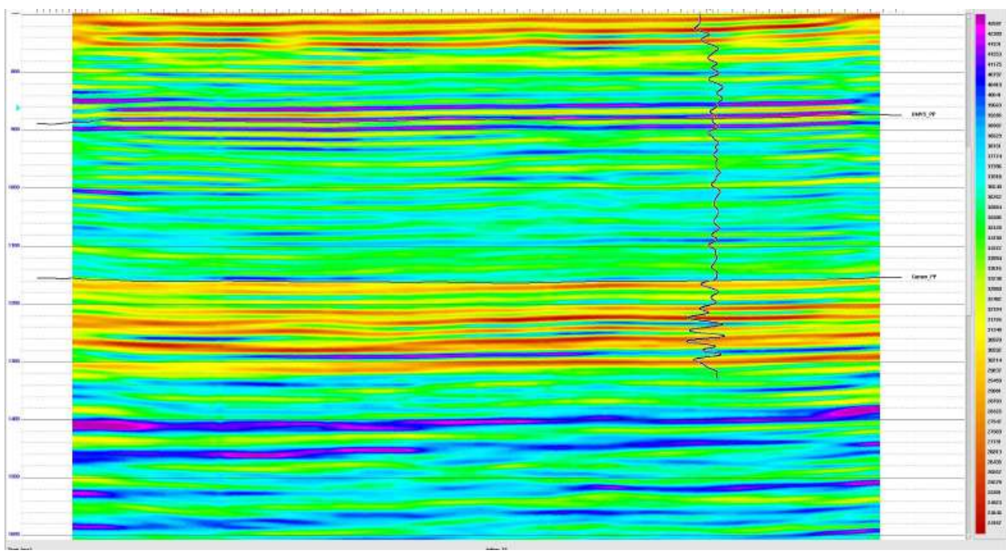

Figure 5.10. IL-19. PP-2004 Inversion result (P-impedance) with RU-7 low-pass filtered impedance log overlaid.

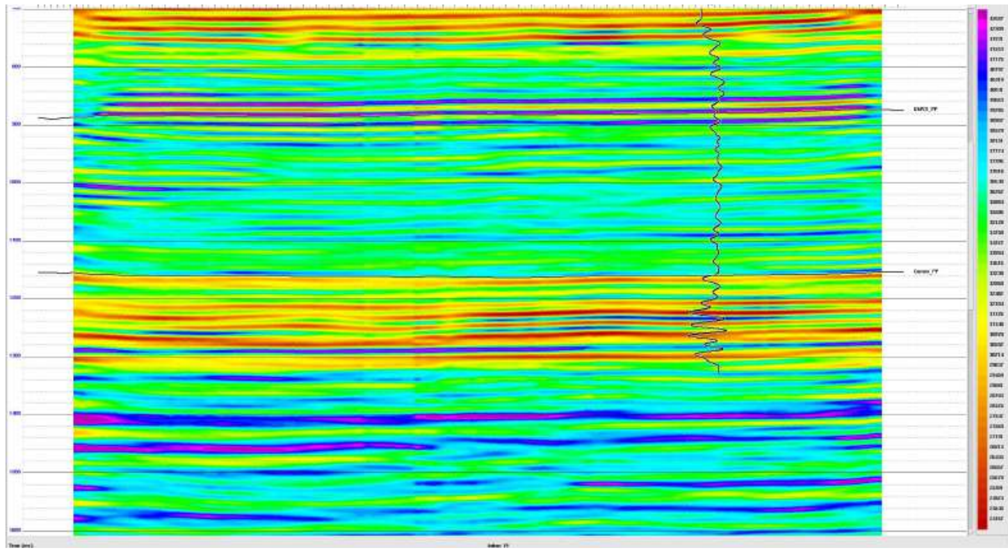

Figure 5.11. IL-19. PP-2006 Inversion result (P-impedance) with RU-7 low-pass filtered impedance log overlaid.

5.4 Inversion of S11-wave seismic data

The inversion of both pure-shear wave-modes faces an additional step related to the approximate correlation of events on S11 time in order to perform a large synthetic trace stretch during the synthetic seismogram construction. Figure 5.12 shows both PP-2003 and S11-2003 datasets in a side-by-side comparison at PP time (ms) assuming V_P/V_S=2 for time domain conversion.

This visual correlation of packages (seismic facies) done also on S11 time allowed modifying the time-depth relationship in order to start the well-seismic tie of events on the natural domain of the S11 seismic data.

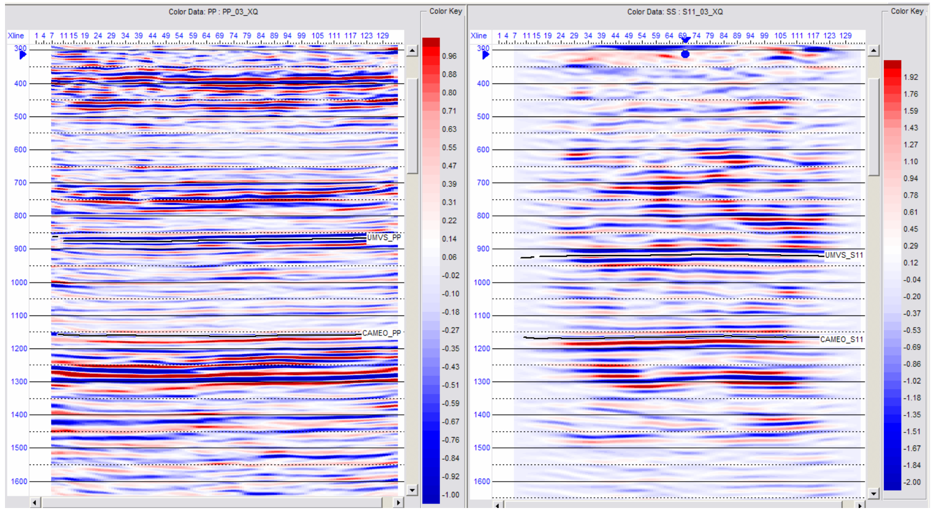

Figure 5.12. IL-19. PP-2003 (left) and S11-2003 (right) at PP time (ms).

5.4.1 S11-wave Synthetic Seismogram and Horizon Picking

Using the modified time-depth curve, and the fast-shear sonic and density logs I built a synthetic seismogram for S11-wave data as shown on Figure 5.13. This synthetic seismogram allowed 73% of correlation with the observed S11-2003 seismic data, and this correlation is the same for S11-2004 and 2006. This seismogram was built using a -24º- average phase statistical wavelet which time, frequency and phase responses are shown on Figure 5.14.

The main geological markers, UMVS and Top Cameo, were identified in the synthetic seismogram and interpreted in their corresponding seismic onset, allowing obtaining their corresponding time maps for S11-wave data as seen on Figures 5.15 (UMVS) and 5.16 (Cameo).

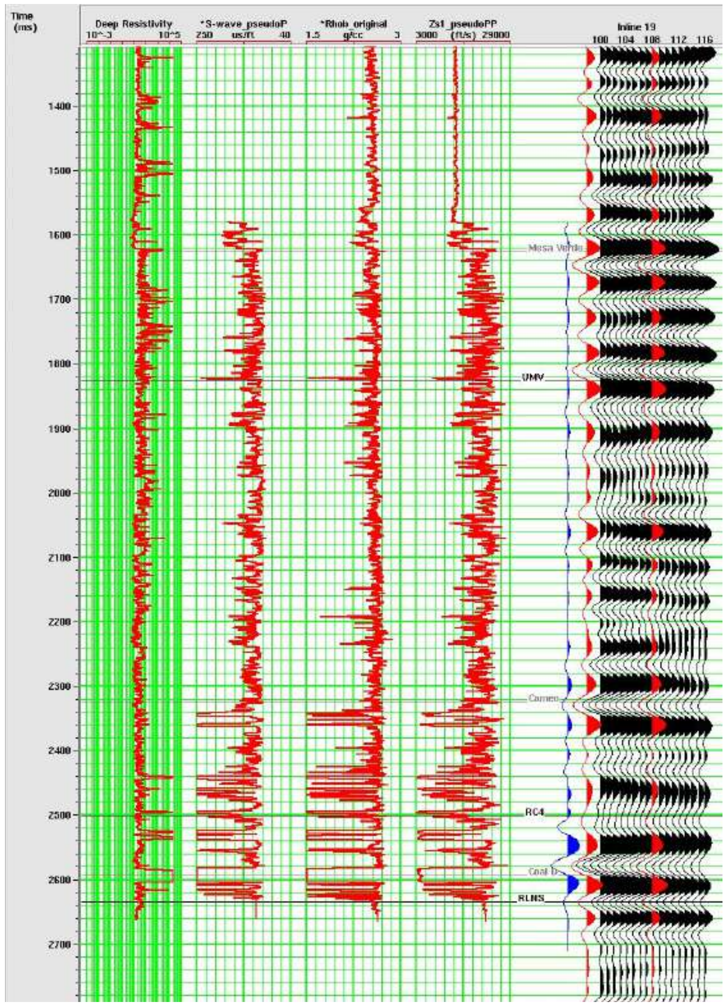

Figure 5.13. Synthetic seismogram (blue trace) for S11-2003 (black and red traces).

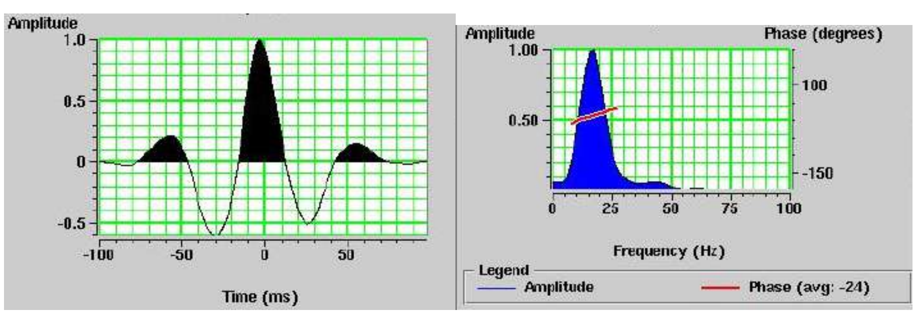

Figure 5.14. Statistical wavelet responses on time (upper), frequency (lower blue) and phase (lower red).

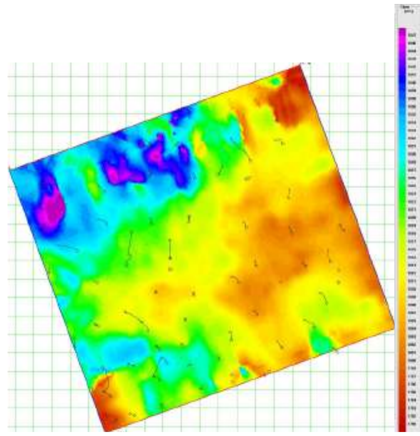

Figure 5.15. UMVS time structural map for S11-wave data.

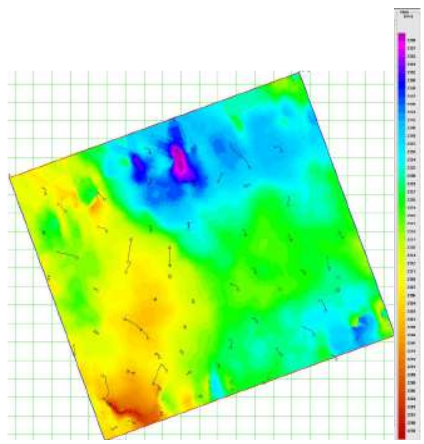

Figure 5.16. Top Cameo time structural map for S11-wave data.

5.4.2 Building the Initial S11-wave Model

The S11-impedance initial model was built using the UMVS and Cameo horizons previously shown in order to extrapolate the impedance values away from control well RU-7. These impedance values are those corresponding to the S11-impedance log calculated using the corrected S11-wave sonic log (fast shear) and the density log. This impedance log was low-pass filtered (0-4 Hz) in order to avoid introducing details in the inversion output that come from the initial model instead of seismic data, keeping only the low frequency component absent on seismic data. This initial S11-impedance model is shown on Figure 5.17.

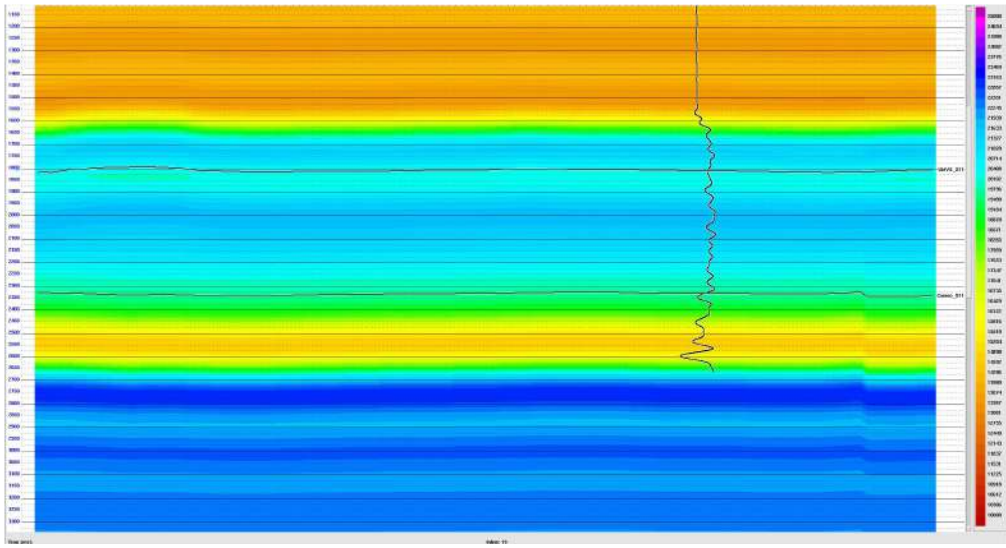

Figure 5.17. IL-19. Initial S11-impedance model with RU-7 low-pass filtered impedance log overlaid.

5.4.3 Determination of S11-wave Inversion Parameters and Inversion Results

Using the initial S11-impedance model I tested different inversion parameters at the RU-7 location until I found the optimum set. Figure 5.18 depicts the inversion results at RU-7 location using the optimum parameters set.

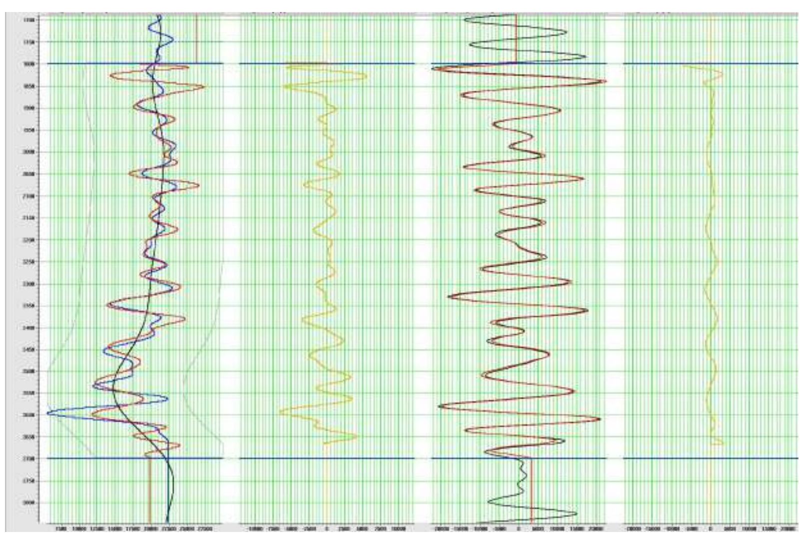

Figure 5.18. Inversion Results at RU-7 location. Track 1 (left): Initial Model (black), original S11-impedance log (blue) and inversion result (red). Track 2 (left-center): Error on Impedance (yellow). Track 3 (center-right): Seismic trace (black), modeled trace (red). Track 4 (right): Error on traces (yellow).

This test was done using the S11-2003 seismic data (base survey) but is very similar to those of S11-2004 and S11-2006. As a result, I kept the same parameters for inversion for all three datasets. I allowed +/- 50% of variation from the initial model through five (5) iterations using a scaler adjustment factor of 0.6 and 1% of pre-whitening.

The inversion achieved its goal of recovering an impedance model similar to the impedance log at the well location at 0-30 Hz bandwidth, and all the details on the inversion results are derived from seismic data, not from the initial model which has been highly smoothed due to the low-pass frequency filtering. The correlation between the S11-impedance log and the impedance from inversion is over 73% in the interval of interest. Most of the mismatches occur in the Cameo coal interval (2300-2700 ms), which could be caused by inaccurate measurements of the well log due to instability of the well-bore in the coals. Having the inversion parameters defined, as well as the initial model and the wavelet I inverted the S11-2003, 2004 and 2006 volumes using the model-based inversion algorithm, and their corresponding results are shown on Figures 5.19, 5.20 and 5.21.

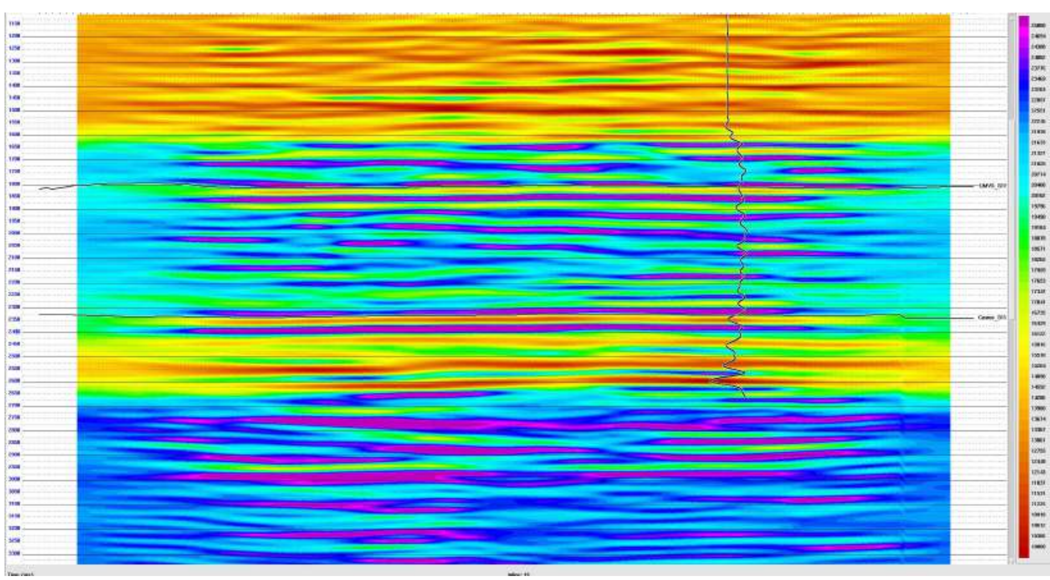

Figure 5.19. IL-19. S11-2003 Inversion result (S11-impedance) with RU-7 low-pass filtered impedance log overlaid.

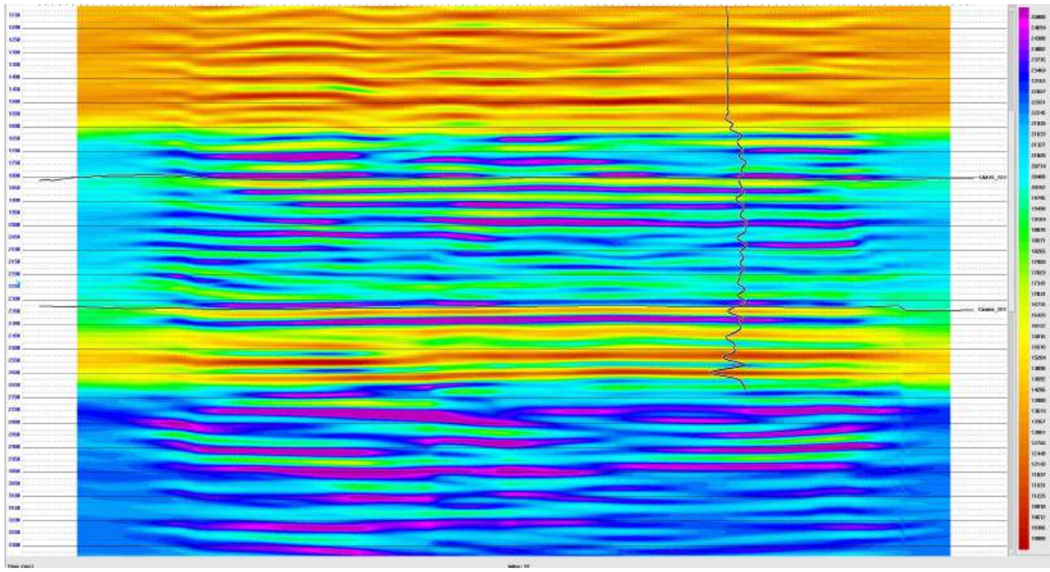

Figure 5.20. IL-19. S11-2004 Inversion result (S11-impedance) with RU-7 low-pass filtered impedance log overlaid.

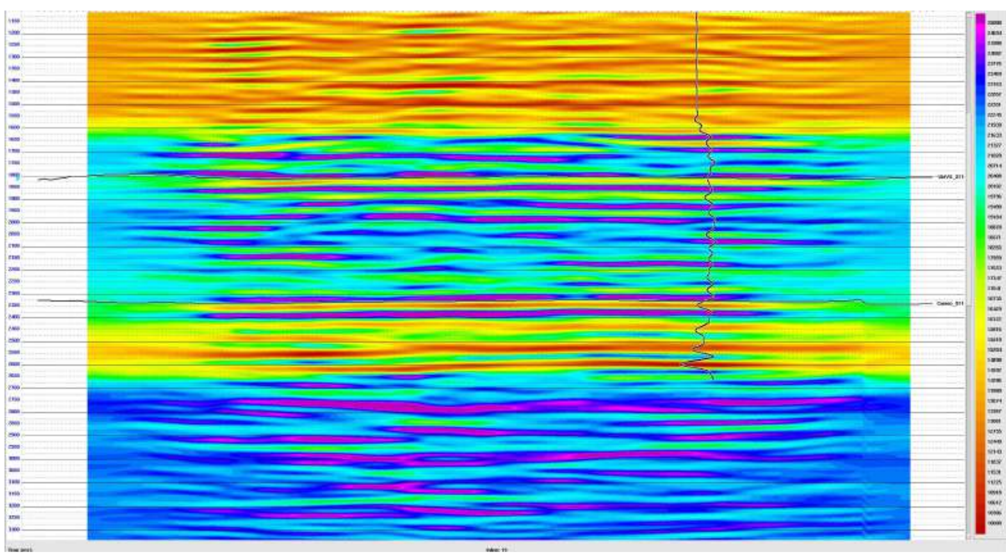

Figure 5.21. IL-19. S11-2006 Inversion result (S11-impedance) with RU-7 low-pass filtered impedance log overlaid.

5.5 Inversion of S22-wave seismic data

The inversion of both pure-shear wave-modes faces an additional step related to the approximate correlation of events on S22 time in order to perform a large synthetic trace stretch during the synthetic seismogram construction. Figure 5.22 shows both PP-2003 and S22-2003 datasets in a side-by-side comparison at PP time (ms) V_P/V_S=2 for time domain conversion.

This visual correlation of packages (seismic facies) done also on S22 time allowed modifying the time-depth relationship in order to start the well-seismic tie of events on the natural domain of the S22 seismic data.

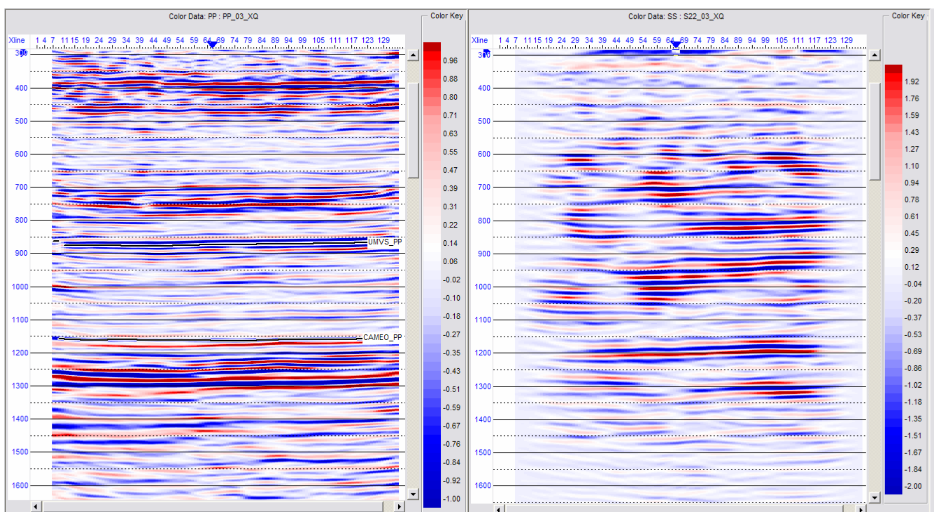

Figure 5.22. IL-19. PP-2003 (left) and S22-2003 (right) at PP time (ms)

5.5.1 S22-wave Synthetic Seismogram and Horizon Picking

Using the modified time-depth curve, and the slow-shear sonic and density logs I built a synthetic seismogram for S22-wave data as shown on Figure 5.23. This synthetic seismogram provided 78% of correlation with the observed S22-2003 seismic data, and this correlation is the same for S22-2004 and 2006. This seismogram was built using a -24º- average phase statistical wavelet which time, frequency and phase responses are shown on figure 5.24. The main geological markers, UMVS and Top Cameo, are identified on the synthetic seismogram. Their time maps for S22-wave data are seen on Figures 5.25 (UMVS) and 5.26 (Cameo).

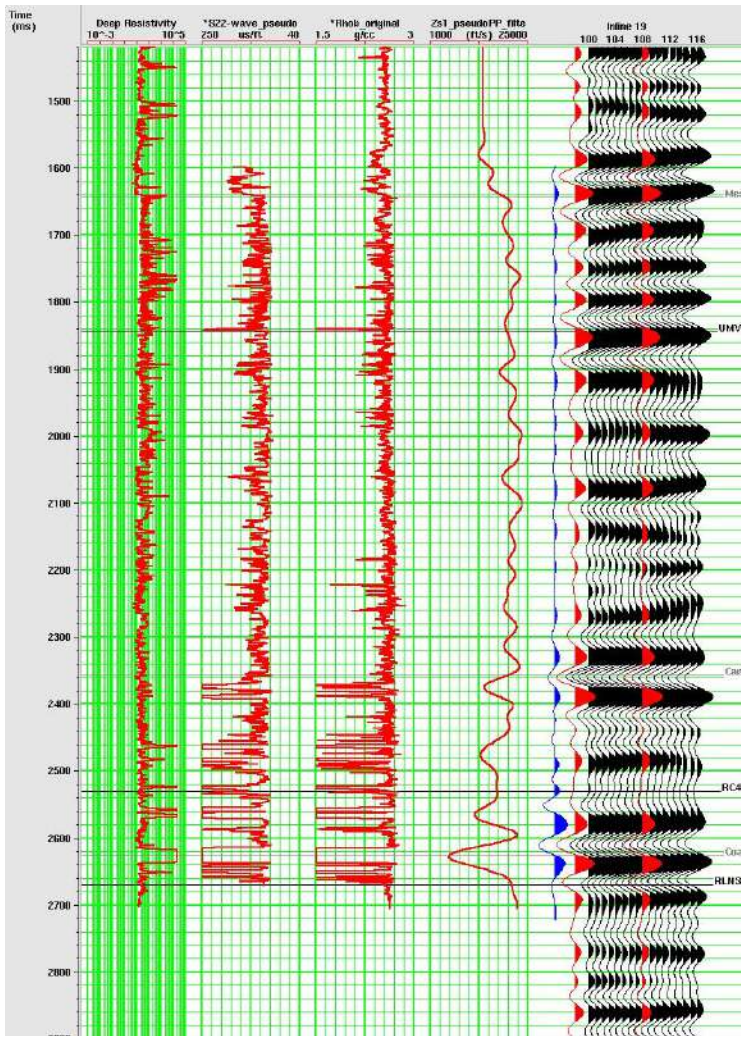

Figure 5.23. Synthetic seismogram (blue trace) for S22-2003 (black and red traces).

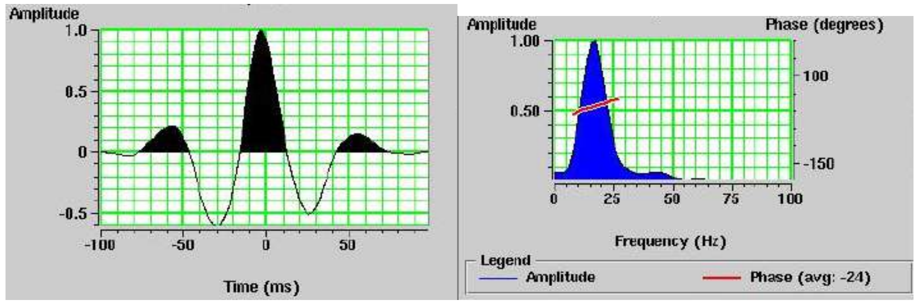

Figure 5.24. Statistical wavelet responses on time (upper), frequency (lower blue) and phase (lower red).

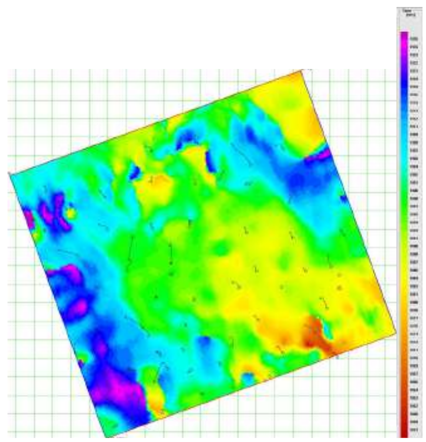

Figure 5.25. UMVS time structural map for S22-wave data.

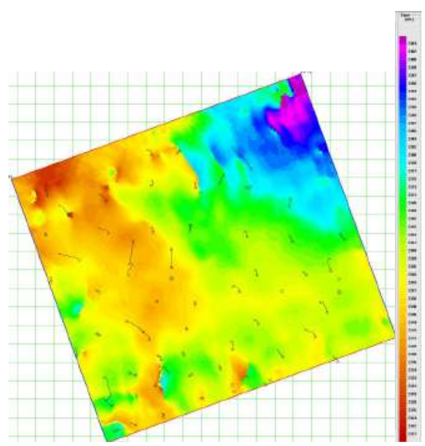

Figure 5.26. Top Cameo time structural map for S22-wave data.

5.5.2 Building the Initial S22-wave Model

The S22-impedance initial model was built using the UMVS and Cameo horizons previously shown in order to extrapolate the impedance values away from control well RU-7. These impedance values are those corresponding to the S22-impedance log calculated using the corrected S22-wave sonic log (slow shear) and the density log. Like previous cases, this impedance log was low-pass filtered (0-4 Hz). This initial S22-impedance model is shown on Figure 5.27.

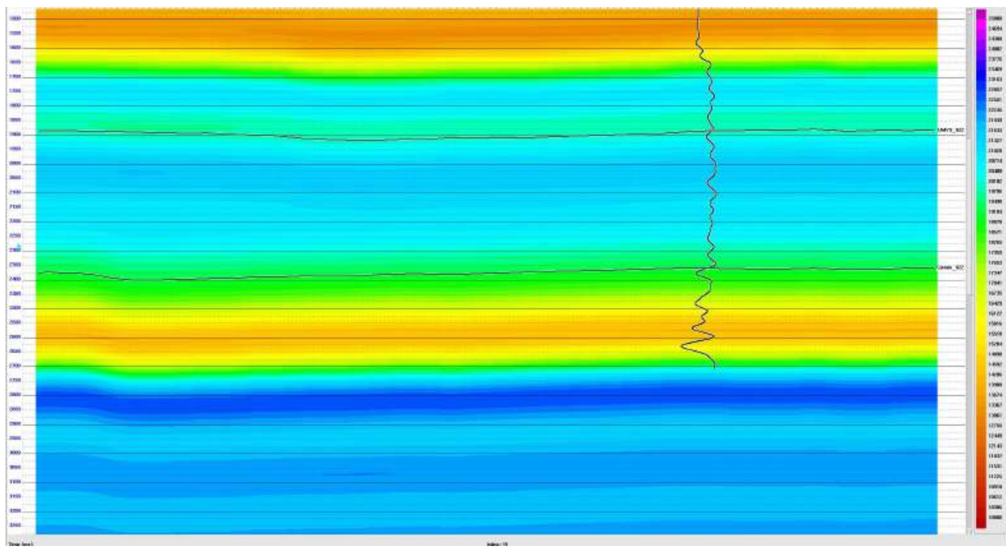

Figure 5.27. IL-19. Initial S22-impedance model with RU-7 low-pass filtered impedance log overlaid.

5.5.3 Determination of S22-wave Inversion Parameters and Inversion Results

Using the initial S22-impedance model I tested different inversion parameters at the RU-7 location, until I found the optimum set. Figure 5.28 depicts the inversion results at RU-7 location using that optimum parameters set.

This test was done using the S22-2003 seismic data (base survey) but is very similar to those of S22-2004 and S22-2006, reason why is possible to keep the same parameters for inversion of the three datasets. I allowed +/- 50% of variation from the initial model through five (5) iterations using a scaler adjustment factor of 0.55 and 1% of pre-whitening.

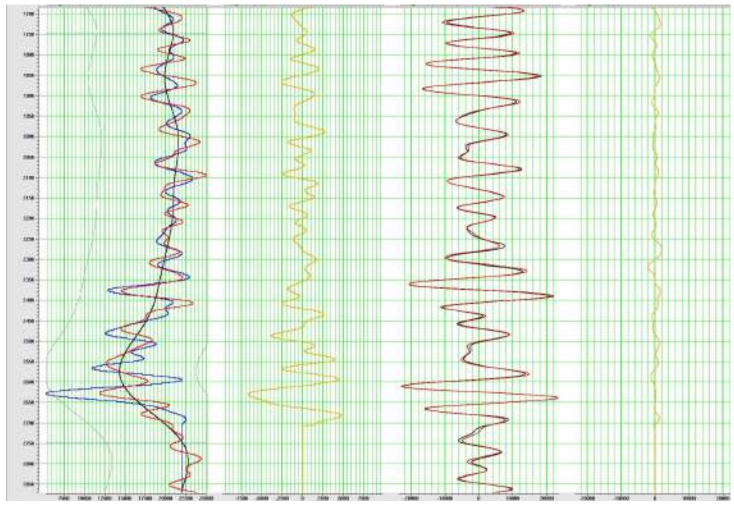

Figure 5.28. Inversion Results at RU-7 location. Track 1 (left): Initial Model (black), original S22-impedance log (blue) and inversion result (red). Track 2 (left-center): Error on Impedance (yellow). Track 3 (center-right): Seismic trace (black), modeled trace (red). Track 4 (right): Error on traces (yellow).

The inversion achieved its goal of recovering an impedance model similar to the impedance log at the well location at 0-30 Hz bandwidth, and all the details on the inversion results are derived from seismic data, not from the initial model which has been highly smoothed due to the low-pass frequency filtering. The correlation among the S22-impedance log and the impedance from inversion is over 89% in the interval of interest. Most of the mismatches occur in the Cameo coal interval (2300-2700 ms), which may be caused by inaccurate measurements of the well log due to instability of the well-bore in the coals.

Having the inversion parameters defined, as well as the initial model and the wavelet, I inverted the S22-2003, 2004 and 2006 volumes using the model-based inversion algorithm, and their corresponding results are shown on figures 5.29, 5.30 and 5.31.

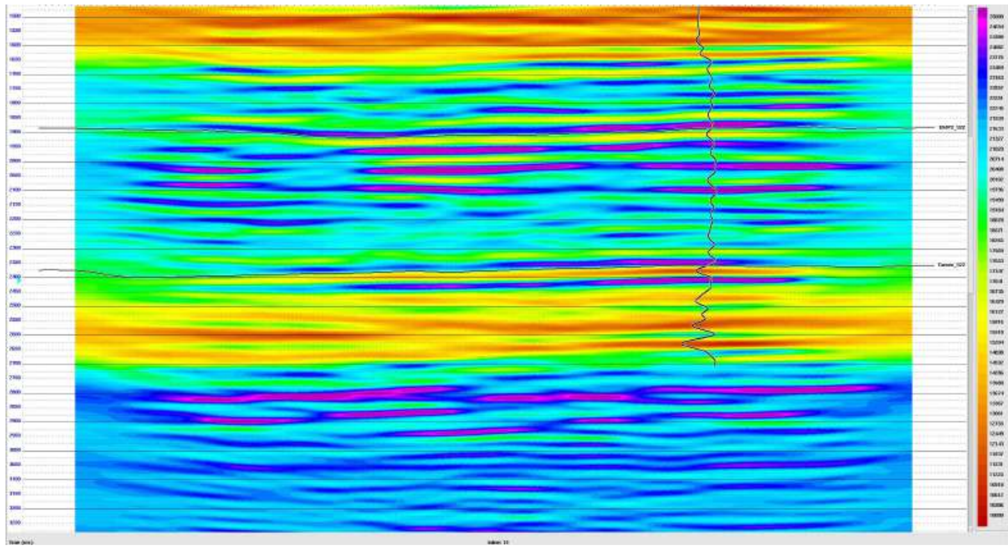

Figure 5.29. IL-19. S22-2003 Inversion result (S22-impedance) with RU-7 low-pass filtered impedance log overlaid.

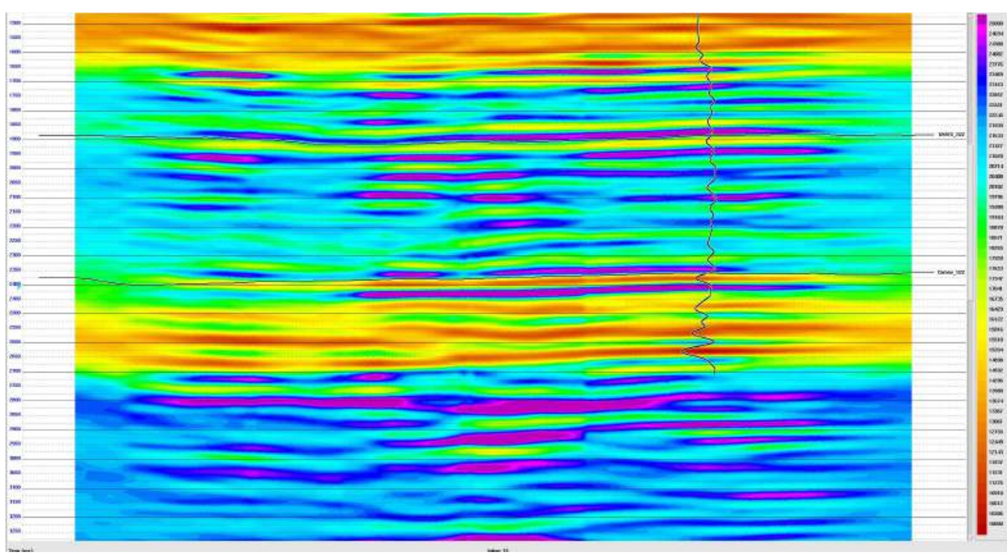

Figure 5.30. IL-19. S22-2004 Inversion result (S22-impedance) with RU-7 low-pass filtered impedance log overlaid.

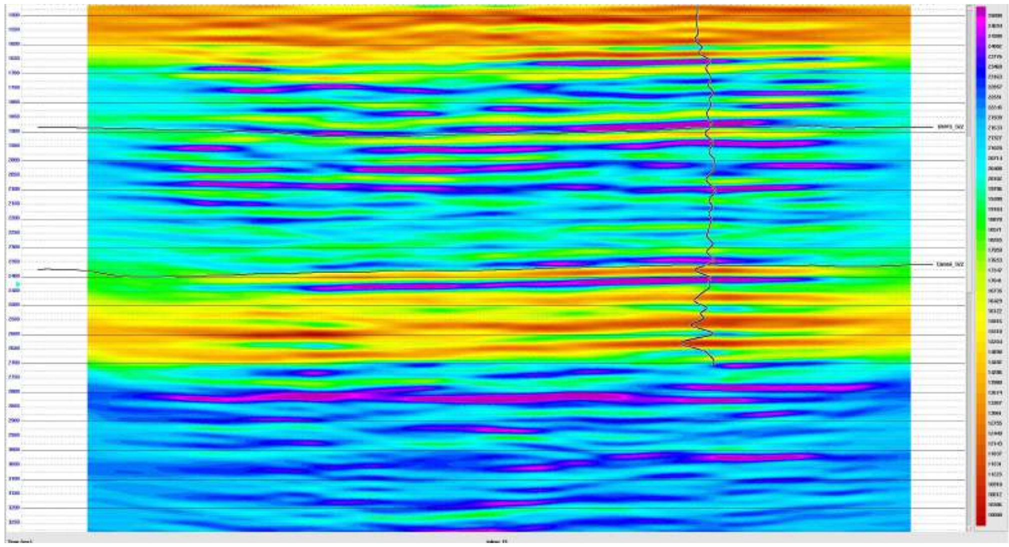

Figure 5.31. IL-19. S22-2006 Inversion result (S22-impedance) with RU-7 low-pass filtered impedance log overlaid.

5.6 Summary

Inversion is a necessary tool for quantitative time-lapse analysis of reservoir since it provides a property (impedance) related to a layer that can be correlated to the most important reservoir properties, such as lithology, fluid-content and pressure, and facilitates better estimations of reservoir properties such as porosity and net pay, in a way that would not be possible by using post-stack seismic attributes alone, which are related to an interface still containing an important influence of the wavelet. In addition, inversion improves seismic resolution by attenuating the side-lobe ringing of the wavelet in the data.

As mentioned in Chapters 1 and 2, inversion is a necessary step towards the determination of time-lapse V_P/V_S volumes based on the ratio of the P- and S-impedances. Both P- and S-wave (fast and slow) impedances were obtained using the model-based inversion algorithm, obtaining a high degree of correlation between the impedance log and the inversion result on each wave mode: 86% for P-wave, 73% for S11-wave and 89% for S22-wave mode. The different level of correlation for S11 and S22 seismic datasets, being lower for the S11 wave-mode, could be indicative that a much better estimation of wavelet for S11 is required for future studies. A way to accomplish this goal can be wavelet estimation from VSP multi-component data, which can help explaining the effect of anisotropy on the wavelet signature.

The time-lapse consistency of the inversion on each wave mode is granted by using the cross-equalized volumes as input, and using the same initial model and wavelet for inversion of all vintages within each wave mode, in order to ensure that time-lapse impedance differences are derived from seismic data and not from different initial models for each vintage.

CHAPTER 6
VERTICAL DOMAIN CONVERSION

6.1 Introduction

The difference in arrival times for the same depth-equivalent events for P- and S-wave modes is caused by the difference in the P- and S- wave velocities that give rise to such arrival times. In order to properly compare events in both seismic wave modes it is necessary to have them at the same vertical common scale, being time or depth. This task is achieved by the multi-component registration, which will allow the proper division of Z_P by Z_S in order to provide the V_P/V_S volumes.

6.2 Multi-Component Registration

The registration was performed using Transform TerraMorph® Software, which performs a 3-D interactive registration of seismic events. First, I registered PP-S11 2003 to PP time obtaining an additional output volume called $\gamma_1=V_P/V_{S1}$. Since the 2004 and 2006 volumes have undergone time-variant time shifts relative to their corresponding base surveys, the registration for PP-S11 for those vintages can use the same γ_1 volume for automated registration. Later I proceeded in the same way for the PP-S22 2003 registration obtaining the $\gamma_2=V_P/V_{S2}$ volume, then applied for registration of the PP-S22 2004 and 2006 volumes to PP time.

The γ_1 and γ_2 volumes are the result from extrapolating sparse V_P/V_S values through the survey space. These γ values are calculated based on the interactive correlation of seismic events between the two wave modes being registered. This interactive correlation is performed at different common CMP locations, allowing both areal and spatial extrapolation of such tie-points. A previous knowledge of the gross correlation of events between the seismic modes is needed. Despite the different reflectivity, both wave modes show similarities in terms of the gross seismic facies that can help in correlating packages (Hardage and Aluka, 2006; Roth, 2006). This comparison of seismic facies can be accompanied by a gross-registration using an average $\boldsymbol{V_P/V_S}$ ratio, in this case $\boldsymbol{V_P/V_S}$=2, which is consistent to the values obtained from core samples and dipole sonic logs (Rojas, 2005), as seen on the actual seismic data on Figure 6.1. This figure shows both PP and S11 seismic sections for the IL19 on PP time scale using $\boldsymbol{V_P/V_S}$=2 in order to plot both volumes in the gross equivalent vertical scale. It can be appreciated that both datasets show strong events associated to the top and the bottom of the main reservoir interval, as well as the absence of major reflections within. These observations are still valid when considering S22 data as shown on Figure 6.2.

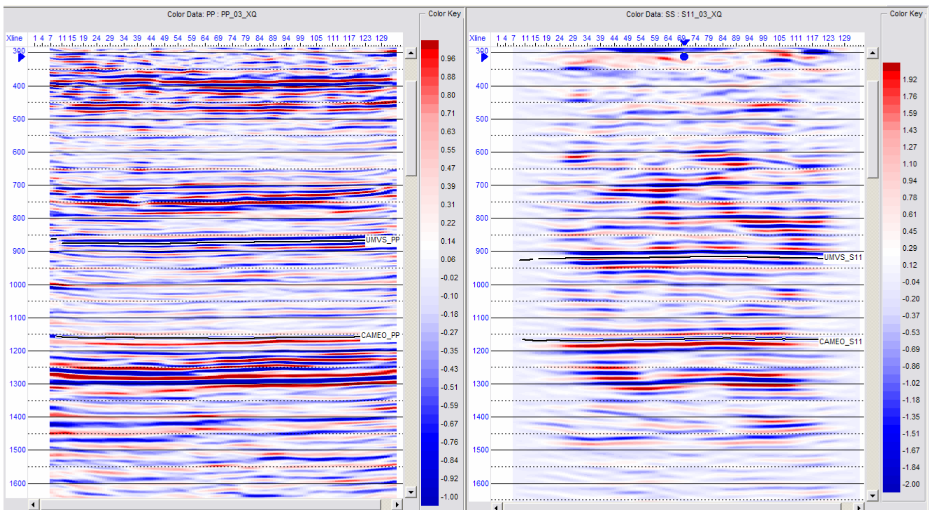

Figure 6.1. Gross correlation between PP & S11 seismic data on PP time using $\boldsymbol{V_P/V_S}$ *=2. PP on left and S11 on right.*

This premise is consistent with the comparison of synthetic seismogram signatures for PP, S11 and S22 wave modes as seen on Figure 6.3. These seismic-well ties also show consistent seismic onsets for the two main markers (UMVS and Cameo) which ensure the correlation of seismic polarity during automated correlation of events between the different wave-modes.

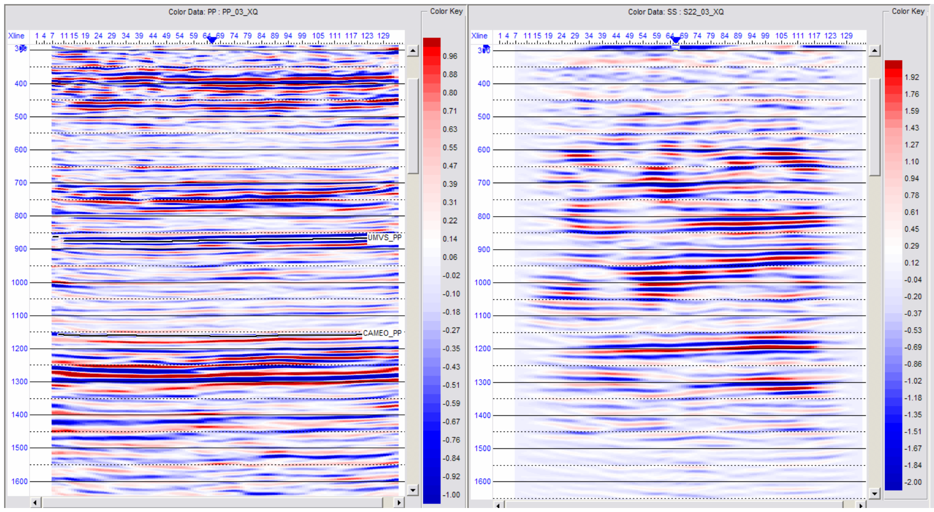

Figure 6.2. Gross correlation between PP & S22 seismic data on PP time using V_P/V_S *=2. PP on left and S22 on right.*

The automated registration process started by picking an event in the SS data (S11 or S22) on its natural time domain and then interactively squeezes this dataset vertically until it is found an event on PP data that visually correlates the picked event on SS data. The amount of visual squeezing is determined by a particular γ value. This dynamic visual registration can be supported by a γ windowed correlation plot as shown on Figure 6.4. This plot helps providing an estimated amount of trace squeezing (γ) required to obtain a maximum correlation of the picked event on SS data relative to events on PP data. In this example, this plot corresponds to the Top Cameo SS event, which requires γ ~3 in order to maximize the correlation with its PP-equivalent event. The obtained γ values are higher than expected (~1.5-2) due to the fact that the software does not handle pure shear data (SS) for registration, so the SS datasets were loaded as PS datasets which generates larger than expected γ values. This procedure accomplishes the registration task, but it might compromise the analysis of the generated γ volumes.

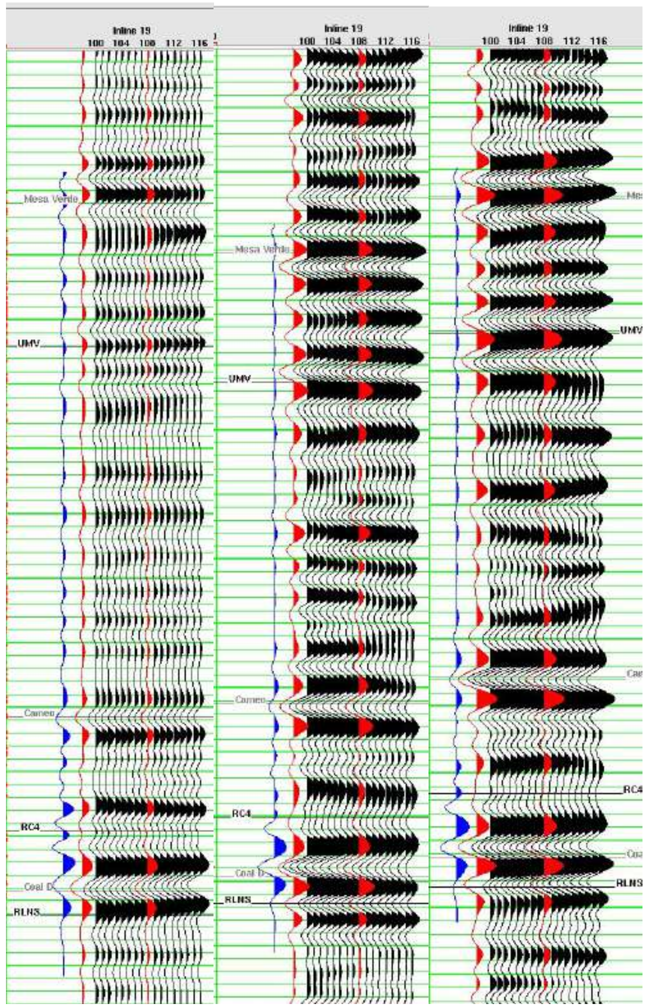

Figure 6.3. Multi-component synthetic seismograms at well RU-7. PP (left track), S11 (middle track) and S22 (right track). Synthetic seismograms represented by blue traces, and red traces are the composite of the corresponding actual seismic data (black).

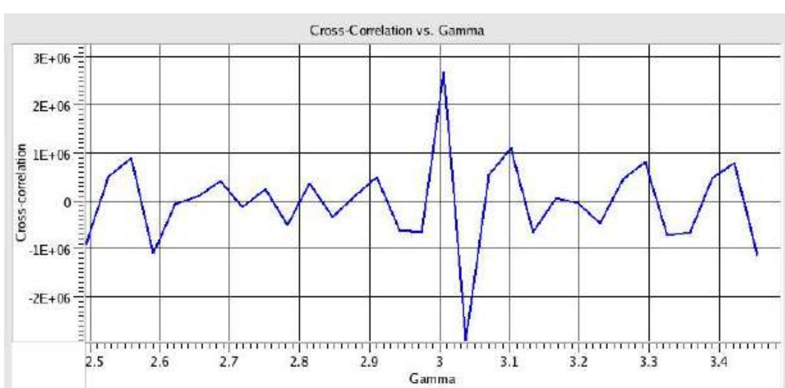

Figure 6.4. γ correlation plot example for Top Cameo event. Cross-correlation between PP and SS (S11 or S22) events (y-axis) and γ values that give rise such correlation values (x-axis).

This automated correlation is performed for few common seismic events in both datasets being involved at sparse CMP locations as shown on Figure 6.5. These locations allowed extrapolating the γvalues in order to obtain the registration of the S11 and S22 volumes relative to PP as shown on Figures 6.6 and 6.7. The quality of the registration is confirmed by applied the corresponding γvalues to the impedance volumes as shown on Figures 6.8 and 6.9, where it can be appreciated the high level of visual correlation among the seismic packages. It has to be noticed that both amplitude and impedance SS traces show visually higher frequency content after registration compared to the frequency content before their registration, due to the squeezing of the traces. This observation impacts the resolution of the different wave-modes, a topic discussed in the next section.

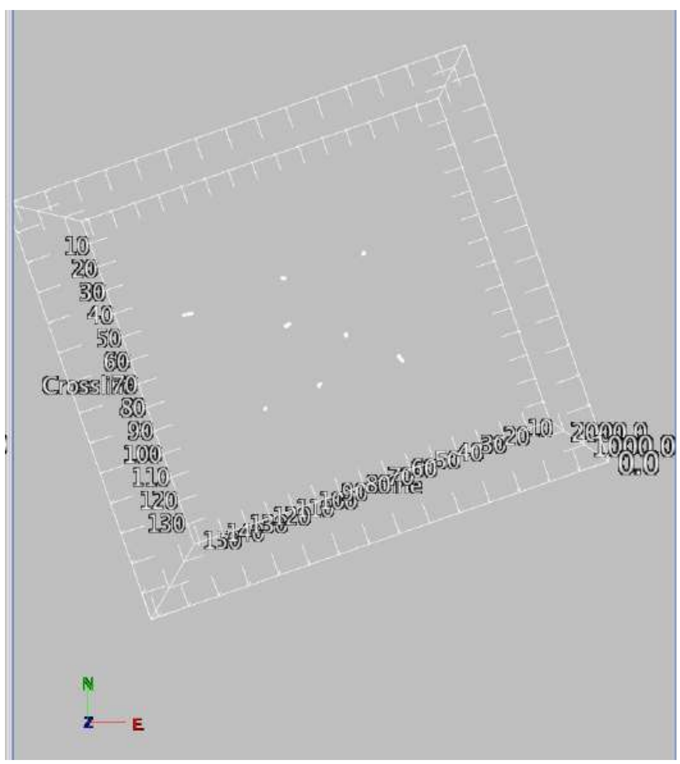

Figure 6.5. Map view of sparse CMP locations for PP-SS events tie.

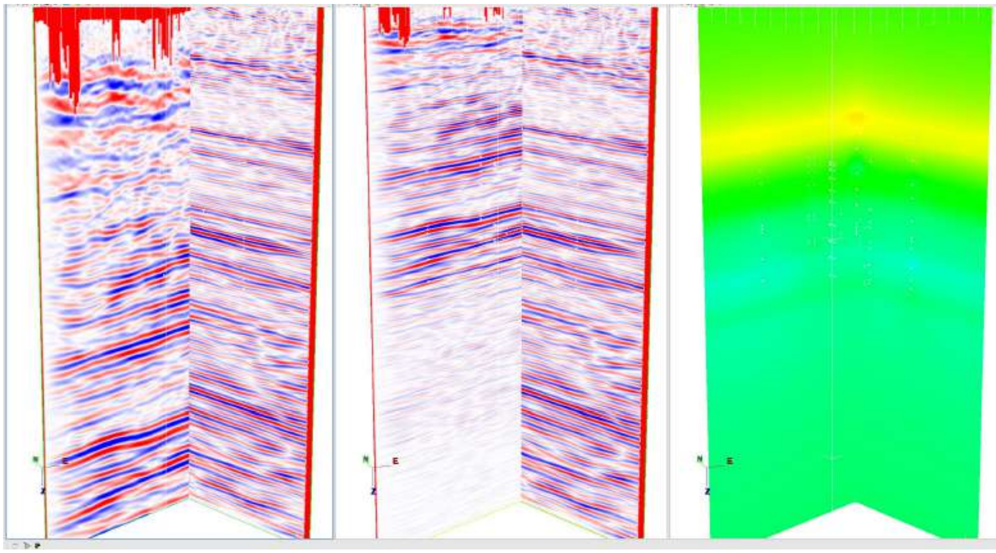

Figure 6.6. PP-S11 registration. Un-registered S11 data relative to PP data (left panel), registered S11 data relative to PP data (middle panel) and extrapolated $\boldsymbol{\gamma_{11}}$ *values (right panel).*

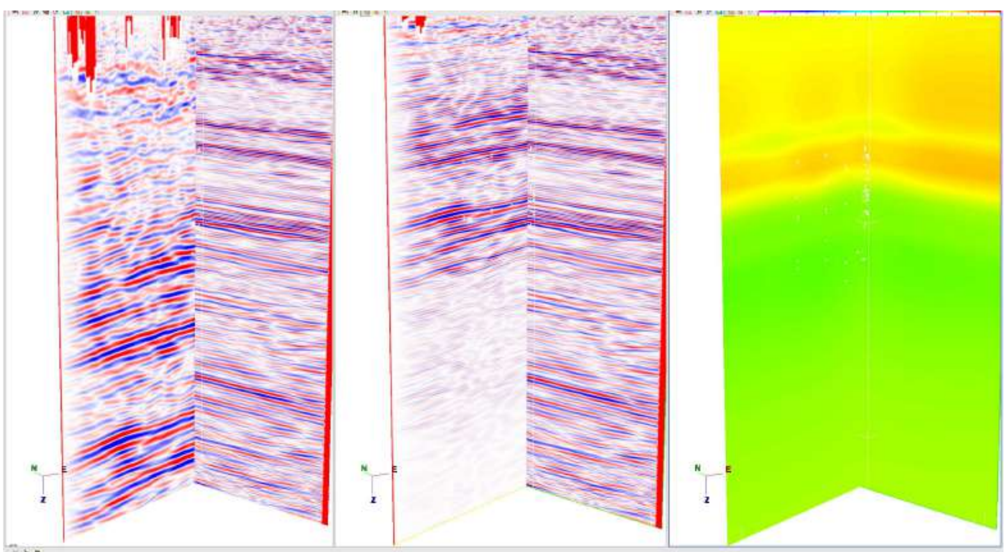

Figure 6.7. PP-S22 registration. Un-registered S22 data relative to PP data (left panel), registered S22 data relative to PP data (middle panel) and extrapolated $\boldsymbol{\gamma_{22}}$ *values (right panel).*

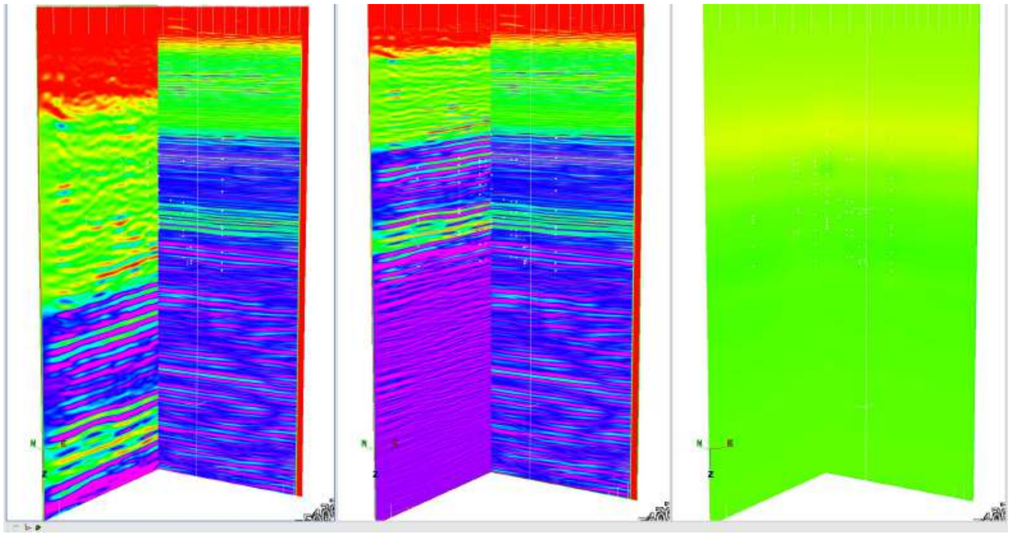

Figure 6.8. $\mathbf{Z_P}$-$\mathbf{Z_{S11}}$ *registration. Un-registered* $\mathbf{Z_{S11}}$ *data relative to* $\mathbf{Z_P}$ *data (left panel), registered* $\mathbf{Z_{S11}}$ *data relative to* $\mathbf{Z_P}$ *data (middle panel) and extrapolated* $\boldsymbol{\gamma_{11}}$ *values (right panel).*

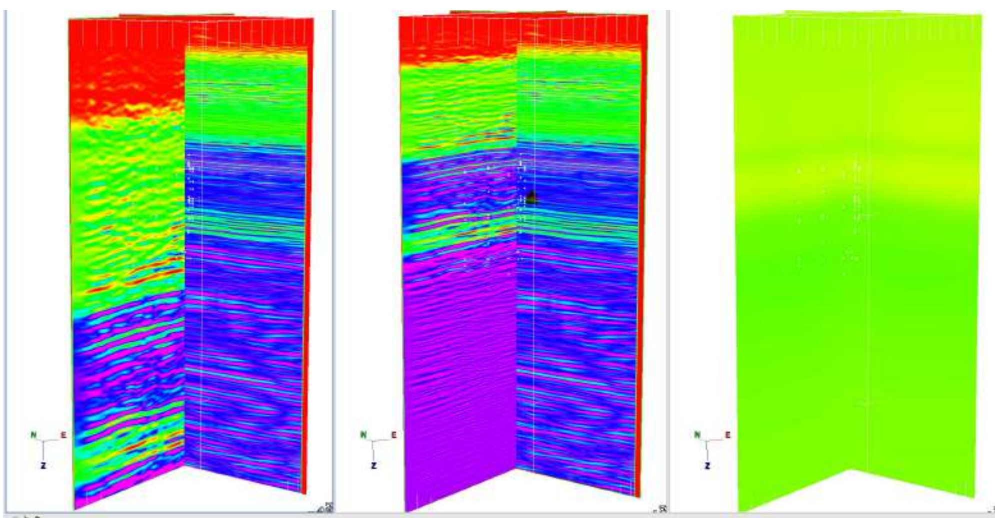

Figure 6.9. $\mathbf{Z_P}$-$\mathbf{Z_{S22}}$ *registration. Un-registered* $\mathbf{Z_{S22}}$ *data relative to* $\mathbf{Z_P}$ *data (left panel), registered* $\mathbf{Z_{S22}}$ *data relative to* $\mathbf{Z_P}$ *data (middle panel) and extrapolated* $\boldsymbol{\gamma_{22}}$ *values (right panel).*

6.3 Multi-component resolution

The resolving power of seismic data is determined by its wavelength $\boldsymbol{\lambda}$ (Widess, 1973), which is a function of its dominant frequency $\boldsymbol{f}$ and target interval velocity $\boldsymbol{V}$ as expressed in equation 6.1.

$$\lambda = \frac{V}{f} \tag{6.1}$$

P- and S- wave seismic data on their original time domains are characterized by different bandwidths, narrower in the case of S-wave as shown on figure 6.10. Equation 6.1 can be applied to both P- and S- wavelengths $\boldsymbol{\lambda_P}$ and $\boldsymbol{\lambda_S}$ considering the corresponding dominant frequencies $\boldsymbol{f_P}$ and $\boldsymbol{f_S}$ and velocities $\boldsymbol{V_P}$ and $\boldsymbol{V_S}$ as shown on equation 6.2 (Garotta, 1985).

$$\frac{\lambda_S}{\lambda_P} = \frac{V_S}{V_P}\frac{f_P}{f_S} \tag{6.2}$$

In case both P- and S- wave seismic data are displayed on their original time domains, $\boldsymbol{V_S/V_P}$ ratio averages 0.5 ($\boldsymbol{V_P/V_S}$~2), and the ratio of the dominant frequencies $\boldsymbol{f_P/f_S}$ ~ 2 ($\boldsymbol{f_P}$~30 Hz and $\boldsymbol{f_S}$~15 Hz). Obtaining $\boldsymbol{\lambda_S}$~$\boldsymbol{\lambda_P}$, which means that both wave-modes almost have the same resolution on their original time domains and bandwidths.

After registration, SS traces have undergone a squeezing process in order to be re-scaled to PP time. This process changed the bandwidth of the registered data (SS') as shown on Figure 6.11, where both PP and SS' match the low-cut frequency and have comparable dominant frequency (~30-35 Hz). Also the SS' amplitude spectrum has been broadened to a high-cut frequency ~ 60 Hz from the original 30 Hz. The high-cut filter applied to SS data before cross-equalization (0-0-25-30 Hz) might have prevented a better match of higher frequencies.

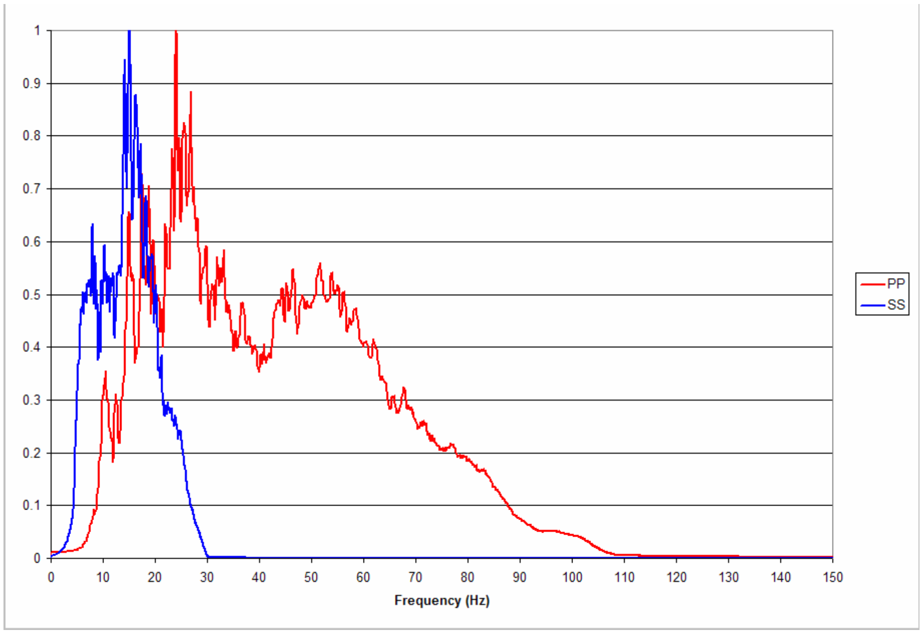

Figure 6.10. Multi-component amplitude spectrum before registration. PP spectrum (red) and SS spectrum (blue).

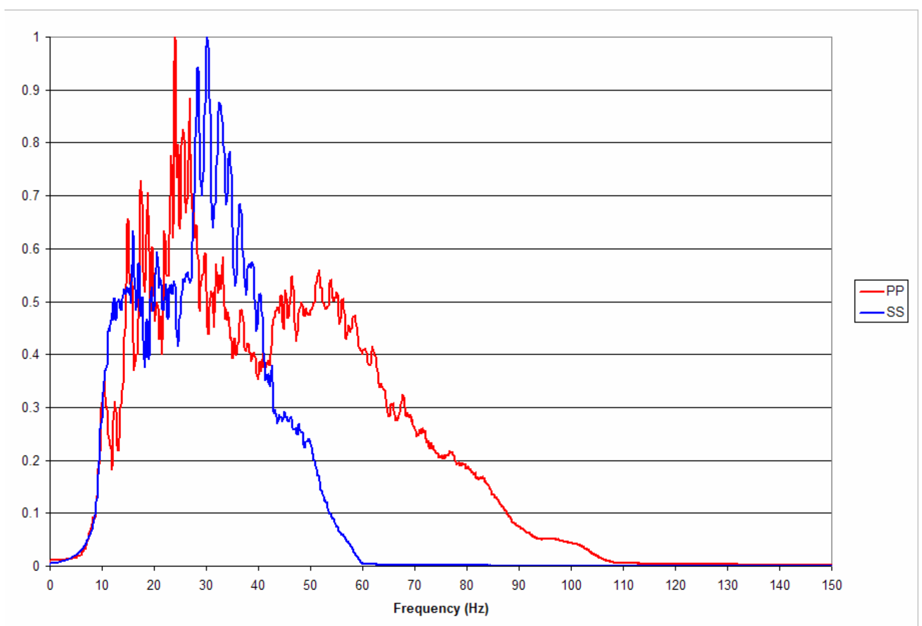

Figure 6.11. Multi-component amplitude spectrum after registration. PP spectrum (red) and SS spectrum (blue).

Once SS data have been registered, the effect of shear velocity on differential arrival times has disappeared, which means that SS' arrival times correspond to P-wave velocity, making $\boldsymbol{V_P/V_S}$=1. Since dominant frequencies of PP and SS' have also been matched (f_P/f_S ~ 1), therefore λ_S~λ_P according to equation 6.1, so both wave modes can be also considered to have the same resolution when SS data is registered.

Considering the Rayleigh criterion, the minimum resolvable thickness b can be estimated according equation 6.2 (Lines and Newrick, 2004).

$$b = \frac{\lambda_P}{4} = \frac{1}{4}\frac{V_P}{f_P} \tag{6.2}$$

Since it has been proved the equivalence of both PP and SS wavelengths, b is going to represent the resolution for both datasets. In this case V_P is the average of interval velocity at reservoir level (~12,500 ft/sec) and f_P the dominant frequency (f_P ~ 30 Hz), which provides a limit of vertical seismic resolution b~ 105 ft.

The lateral resolution of data is estimated by calculating the Fresnel zone diameter F_D for un-migrated datasets using the Berkhout criterion (Lines and Newrick, 2004) as a function of the target depth Z and dominant wavelength λ, as shown on equation 6.3.

$$F_D \cong \sqrt{\lambda Z} \tag{6.3}$$

Considering λ= 420 ft and Z~ 4940 ft- 6930 ft then the Fresnel zone diameter at reservoir level for un-migrated will range 1400-1700 ft. In case of ideal migrated datasets, it is expected that F_D~ $\lambda/4$ (Lines and Newrick, 2004), so the Fresnel zone diameter could be around 105 ft for migrated datasets. This is going to represent the minimum spatial feature that could be resolved using theses datasets.

Both lateral and vertical resolution limits just estimated correspond to seismic amplitude data. In case of impedance data from seismic inversion, as a rule of thumb the tuning thickness is about one-third of that for amplitude data (Steve Hill, personal communication), so considering this rule the vertical resolution is improved from about 105 ft to 35 ft.

6.4 Depth Conversion

An appropriate depth image is one of the ultimate goals of seismic interpretation, especially considering it as an input for further reservoir description processes, such as geo-statistical and geo-mechanical modeling. The depth conversion I carried out was based on the 3D velocity modeling of average velocities from control well RU-7, extrapolated through the survey using the time horizons for UMV shale (UMVS) and Cameo interpreted on the PP wave-mode. This velocity model is shown on figure 6.12, and it must be noticed the smooth lateral and vertical gradient which reflects the lack of structural complexity that might have affected the velocity modeling.

The quality control of the depth conversion was performed by comparing the actual (well logs) and predicted (depth-converted seismic) main geological tops (UMVS and Cameo). Table 6.1 contains such comparison including the control well RU-7 and RU-1. The latter was not used for velocity model in order to use it for testing of the depth conversion accuracy. The prediction of depths from seismic can be considered satisfactory, especially considering the fact that the absolute depth errors are lower than the tuning thickness for amplitude data (~105 ft) which can be considered as a threshold for depth estimation accuracy.

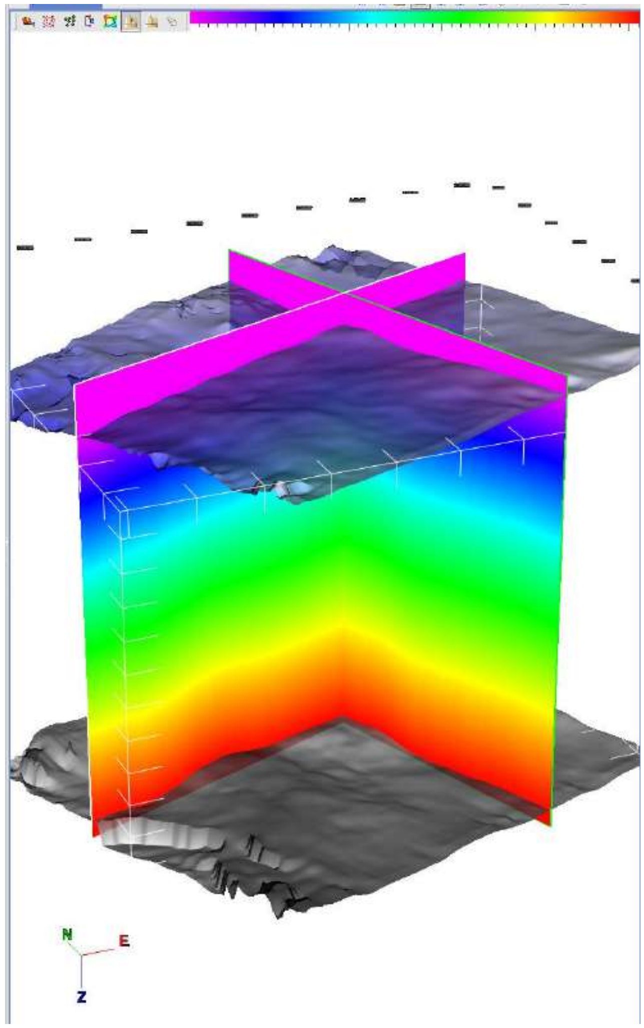

Figure 6.12. Average velocity model for depth conversion displayed in PP time.

Well	Top Name	Actual pick depth (ft)	Predicted pick depth (ft)	Depth error (ft)
RU-7	UMVS	4932	5003	-71
RU-7	CAMEO	6938	6951	-13
RU-1	UMVS	5061	5078	-17
RU-1	CAMEO	6859	6903	-44

Table 6.1. Actual versus seismic-predicted depths for main seismic events.

6.5 Summary

The registration of multi-component volumes based on automated technology and visual correlation of major seismic facies packages achieved the goal of re-scale the shear-wave volumes to the PP time scale. This is a key procedure to perform the division of $\boldsymbol{Z_P}$ and $\boldsymbol{Z_S}$ in order to generate $\boldsymbol{V_P/V_S}$ volumes consistent on their vertical scale and values.

The analysis of data has supported the fact that PP and SS wavelengths are comparable, which means that their vertical resolutions are similar when considering their dominant frequencies both un-registered and registered. The seismic amplitude tuning thickness (resolution) is about 105 ft, while seismic impedance resolution is about 35 ft.

The modeling of average velocities using the UMVS and Cameo PP horizons and the time-depth relationship from well RU-7 has shown to be satisfactory to convert seismic volumes from time to depth, based on the comparison of actual and seismic-predicted well tops with errors below tuning thickness.

CHAPTER 7
INTEGRATED INTERPRETATION

7.1 Introduction

After multi-component registration, I obtained two V_P/V_S volumes (fast or V_P/V_{S1}, and slow or V_P/V_{S2}) for each vintage (2003, 2004 and 2006). Examples of fast and slow V_P/V_S are shown on Figure 7.1. It can be noticed that there is a correlation between the cleanest and thickest sand packages seen on GR logs (low-pass filtered) and the low V_P/V_S values expressed as hot colors in the sections for both V_P/V_S modes, more evident for V_P/V_{S1}. It also can be appreciated the high V_P/V_S values in the Cameo interval, mainly associated to the coal intervals. These observations support the feasibility to describe sand distribution using V_P/V_S volumes.

Comparison of V_P/V_S traces with low-pass filtered V_P/V_S logs at RU-7 location is shown on Figure 7.2. It can be appreciated the overall good match among the log and the corresponding nearby V_P/V_S trace.

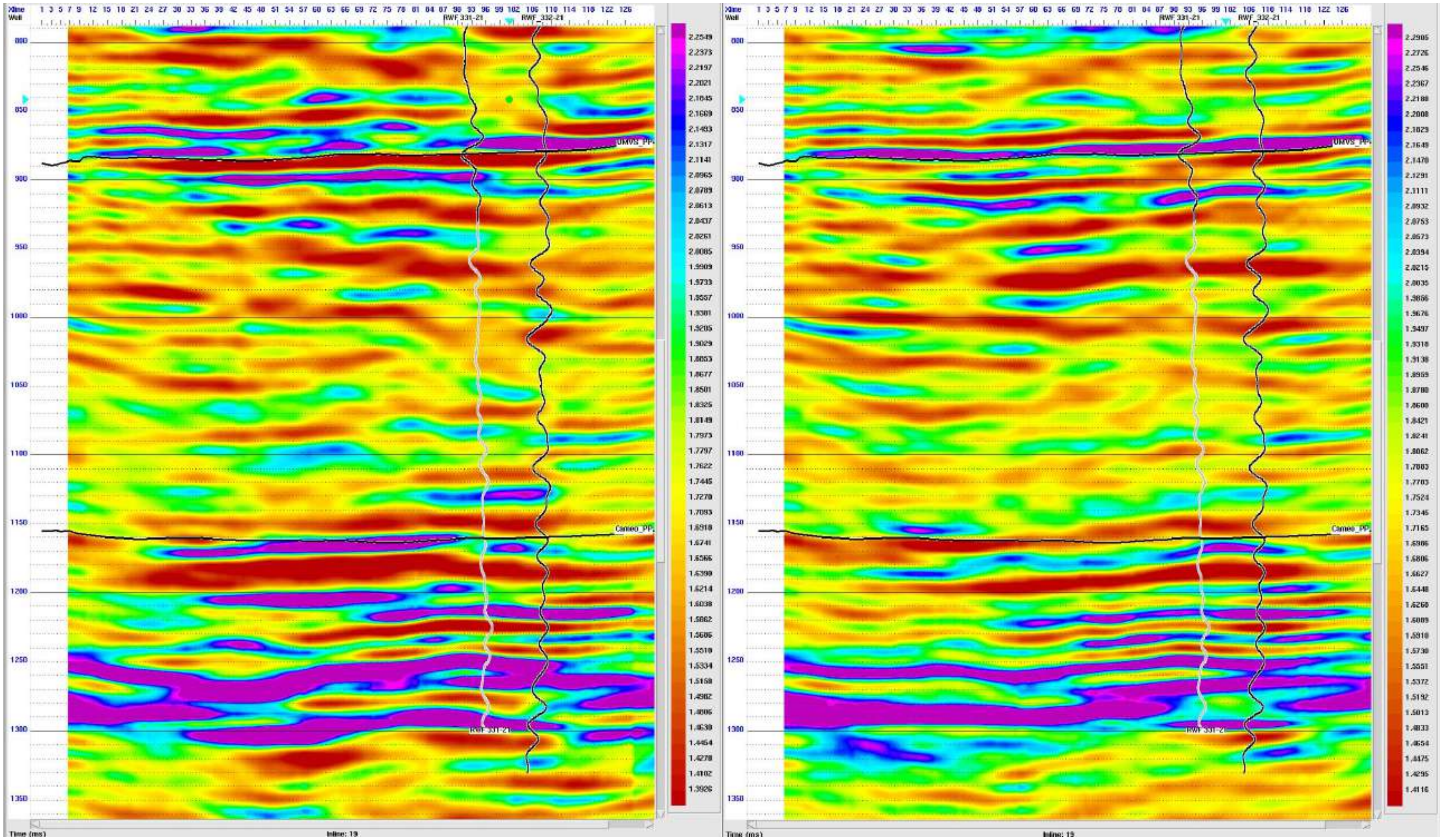

Figure 7.1. IL-19 showing $\mathbf{V_P/V_{S1}}$ 2003 (left) and $\mathbf{V_P/V_{S2}}$ 2003 (right). GR logs (filtered) are shown overlying the well paths.

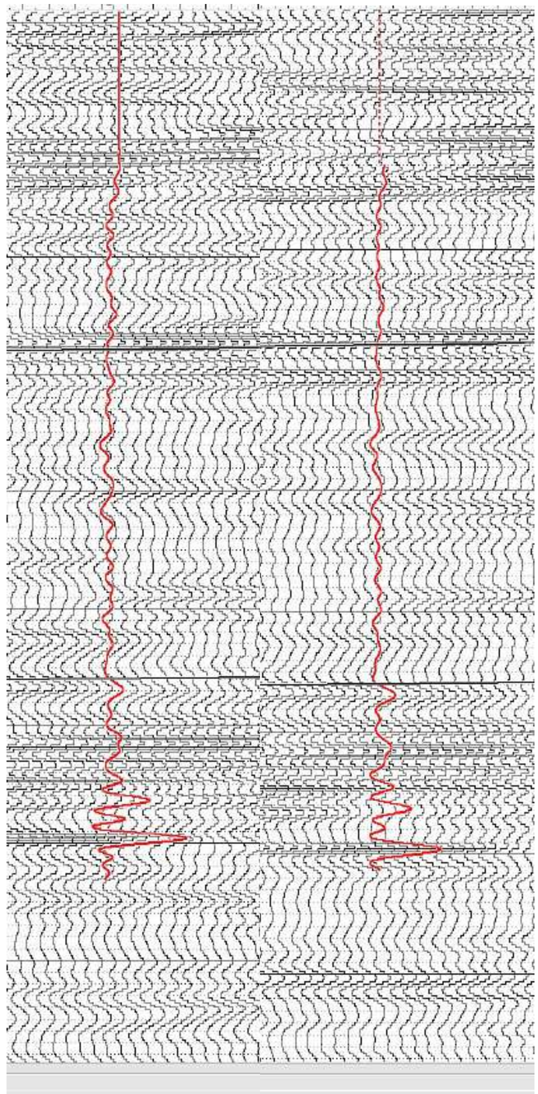

Figure 7.2. Correlation at RU-7 location between V_P/V_S from seismic (black) and well logs (red). V_P/V_{S1} (left) and V_P/V_{S2} (right).

7.2 Reservoir Pressure Prediction

The determination of reservoir pressure volumes is based on the premises shown on Chapter 3. Using the mapping function shown in equation 3.4, the overburden pressure volume Pc shown on figure 3.1 and equation 3.2, I obtained reservoir pressure volumes from the time-lapse V_P/V_{S2} volumes. In order to evaluate the results, I compared the reservoir pressure values obtained from 2006 seismic (P_P') with the mini-frac pressure test (P_P) at well RU-5 acquired in June 2006 (Wikel, 2008), which relative location to RCP study area is shown on Figure 7.3. Figure 7.4 depicts a $\boldsymbol{P_P}$*'* 2006 depth seismic section of the containing the testing well.

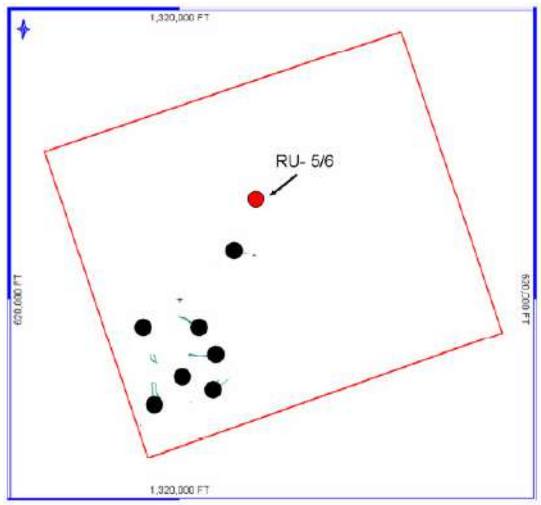

Figure 7.3. Diagram showing location of earlier pressure tests to the location of well RU-5/and RU-6 (two wells from one pad) within the RCP study area. Black dots denote the locations of previous pressure tests that were completed by Williams (from Wikel, 2008).

A quantitative comparison between predicted and actual reservoir pressures can be made by considering values on Table 7.1.

Tested Depth (ft)	$\boldsymbol{P_P}$ or actual pressure (psi)	$\boldsymbol{P_P}$*'* or predicted pressure (psi)	$\boldsymbol{V_P/V_{S2}}$	$\boldsymbol{\Delta P_P}$ (psi)
5822.5	-1978	5951	1.73389	-7929
6200	-2643	5290	1.74192	-7933
6263.5	-2981	5180	1.86212	-8161
6849	-3677	4290	1.6935	-7967
7237	-4026	-9600	1.23284	5574

Table 7.1. Actual versus predicted reservoir pressure at well location RU-5.

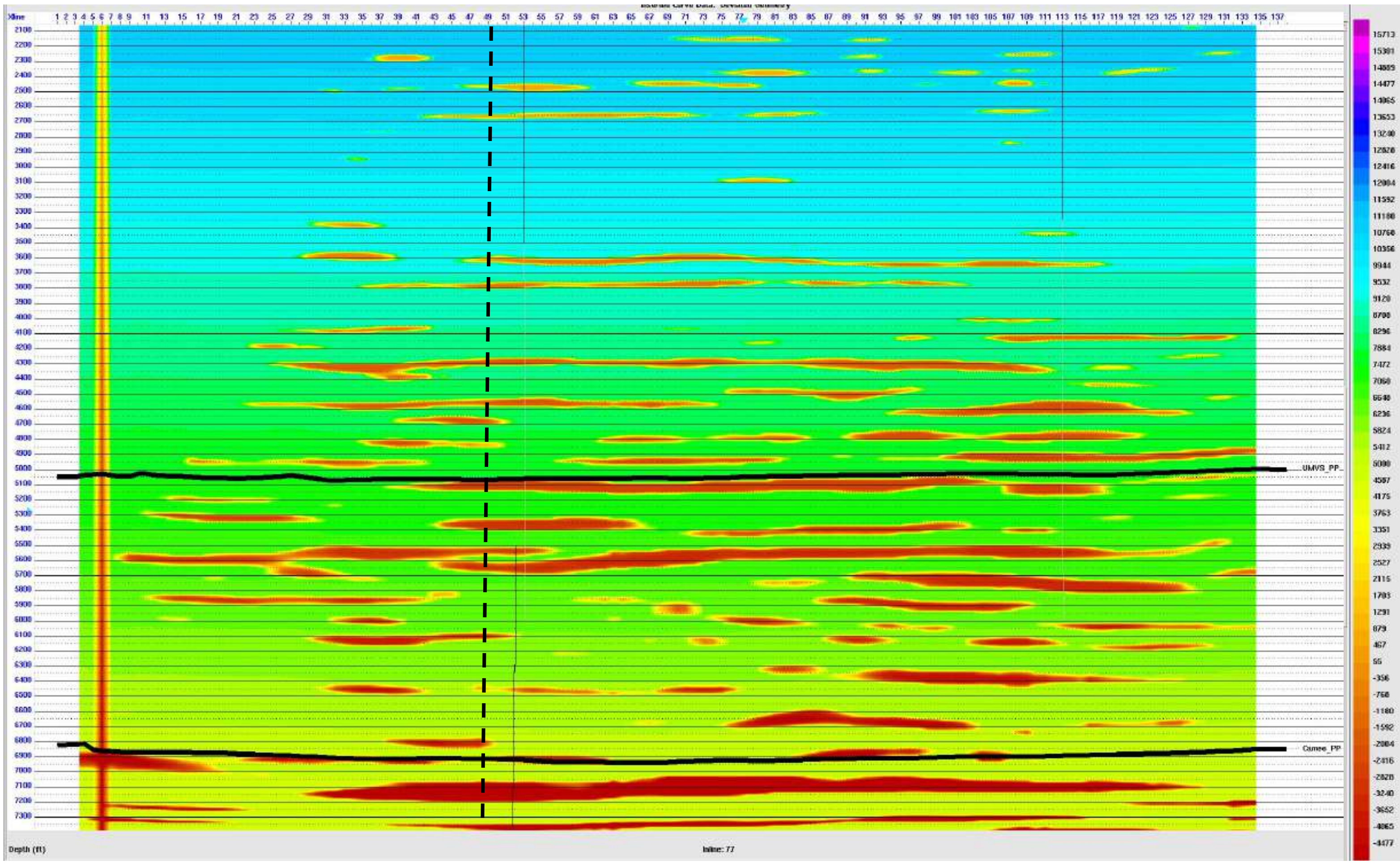

Figure 7.4. IL 77 $\mathbf{P_P}$' 2006 depth converted section including testing well RU-5 (vertical dashed line).

It can be noticed that there is no match between the actual and predicted pressures for well location RU-5. The more plausible reason for such large mismatch can be stated by the lack of sensitivity of V_P/V_S to pressure on depleted zones (high effective pressure) as shown on Figures 3.4 and 3.5. Figure 7.5 shows the RU-5 pressure test relative to the gradient pressure in the field, which shows that all the intervals of sands tested have been partially depleted (Wikel, 2008). The two (2) deepest test points correspond to Cameo intervals, which contains coals in the reservoir which was not taken in account during core lab measurements (Rojas, 2005) therefore, can not be mapped from the V_P/V_S domain to the Pe domain using the same mapping function used in this project.

In order to continue assessing the predicted pressure P_P', I selected different wells with higher reservoir pressure measurements. The wells RU-8, RU-9 and RU-10 contain some sand intervals with relatively high pressures (≥ 3000 psi) in the UMVS-Cameo interval that can be compared to the predicted reservoir pressure PP'. Figure 7.6 shows a cross-plot of actual versus predicted pressure at those intervals, the black line represents the linear fit to the points having a line gradient m~1, which means that in most of the cases the seismic predicted reservoir pressure P_P' tracks the actual reservoir pressure in cases of reservoir pressure higher than 3000 psi. This result agrees the core lab ultrasonic measurements (Rojas, 2005) and the pressure prediction posted in terms of V_P/V_S mapping to Pe in chapter 3, since the V_P/V_S sensitivity at higher reservoir pressure (lower effective pressure) is higher.

These results allowed me to conclude that reservoir pressure derived from V_P/V_S volumes is useful to quantify high pressure zones related to low V_P/V_S values that can be mapped to the effective pressure domain with the certainty and stability provided by the mapping function used on this case. The uncertainty on mapping is lost for V_P/V_S values higher than 1.6 which correspond to depleted zones where the sensitivity of V_P/V_S to effective pressure is minimized. One of the variables for P_P' calculation is the Biot's constant n=0.7 (Wikel, 2008), which might be considered as a value that varies in space instead of constant.

Another shortcoming on this reservoir pressure prediction procedure may be the mapping function itself, since it was determined from ultrasonic core plug measurements that accomplished the following experimental conditions:

- Ultrasonic measurements: The range of frequencies used on these measurements is not comparable to the range of surface seismic frequencies, and it is well known the frequency dependency of seismic velocities, so the resulting velocity measurements do not totally agree the surface seismic velocities under the same effective stress conditions. A way to mitigate such effect could be through the determination of velocities from time-lapse VSP coupled with pressure tests in the same well location.

- Uniform lithofacies: The samples correspond to 10% porosity sand. Sands with different porosity or different clay content may allow the derivation of a slightly different mapping function. The way to control such facies variability might be through spatially-variable Biot's constant.

- Anisotropy: The samples are un-fractured, but the reservoir is fractured. The selection of the slow-mode of shear-wave seismic to predict reservoir pressure might not be totally correct in terms of pressure quantification, especially considering cases where some reservoir intervals have a fracture pattern orientation different from the orientation used during Alford rotation of the volumes, changing the level of sensitivity of the volumes to pressure.

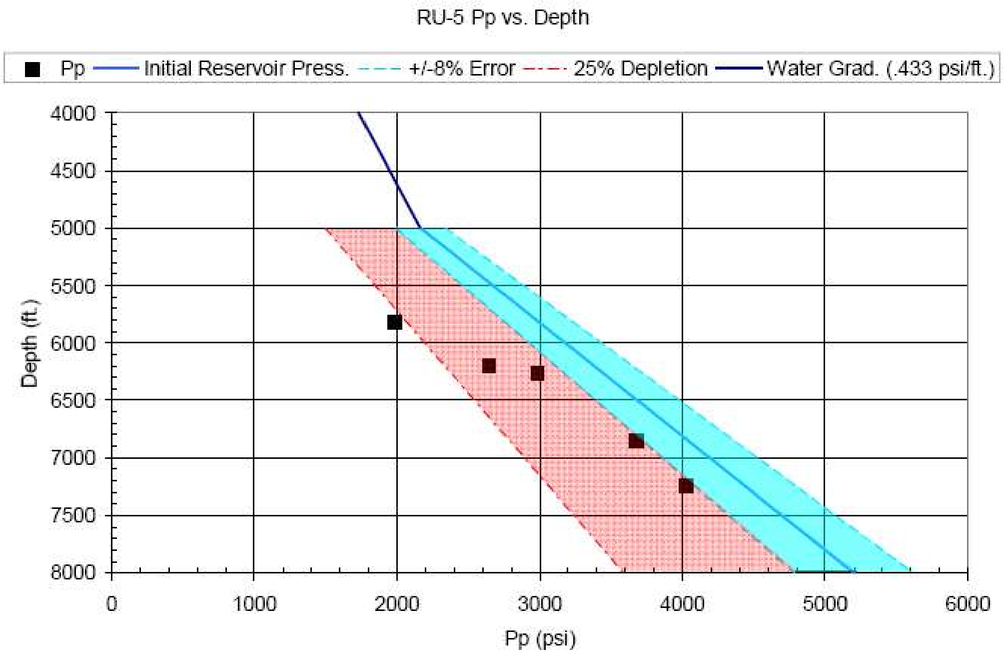

Figure 7.5. Chart showing pore pressure along with the virgin pore pressure gradient from Williams. The blue window is 8% error that was calculated by Williams. The red window shows partial depletion while the red dashed line denotes 25% depletion (from Wikel, 2008).

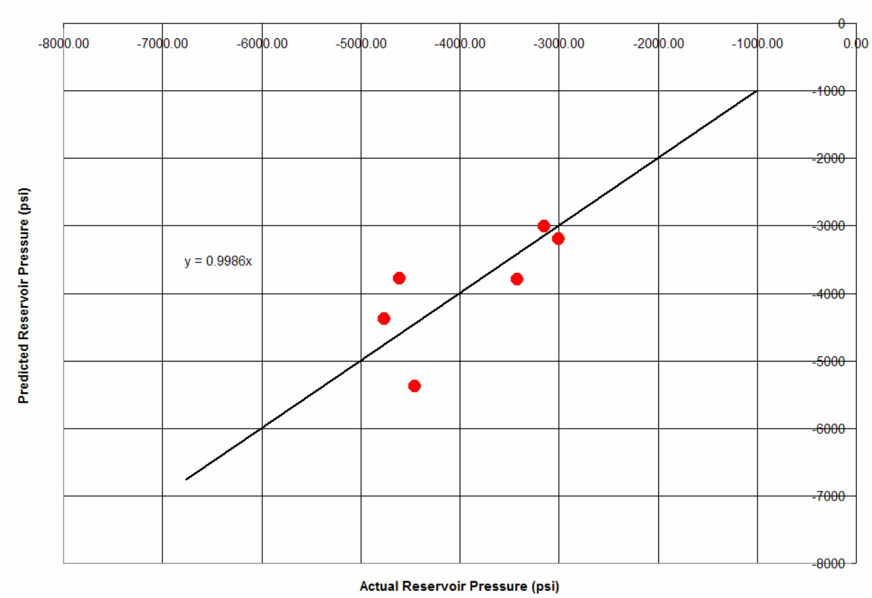

Figure 7.6. Actual versus predicted reservoir pressure cross-plot at different high pressure intervals and well locations tested.

7.3 Time-lapse Results

Previous research work, using the 2003 and 2004 vintages for PP (Keighley, 2006) and S11 & S22 datasets (Rumon, 2006) showed that time-lapse anomalies can be interpreted on those volumes. However, these anomalies are subtle due to the fact that pressure drops due to production are not large enough to be imaged using time-lapse surveys acquired within one-year monitoring lapse. This observation is supported by the modeled pressure in the reservoir (Wikel, 2008) as shown on Figure 7.7, which shows that reservoir pressure drops ~100 psi during 2003-2004, but it declines ~300 psi during 2003-2006.

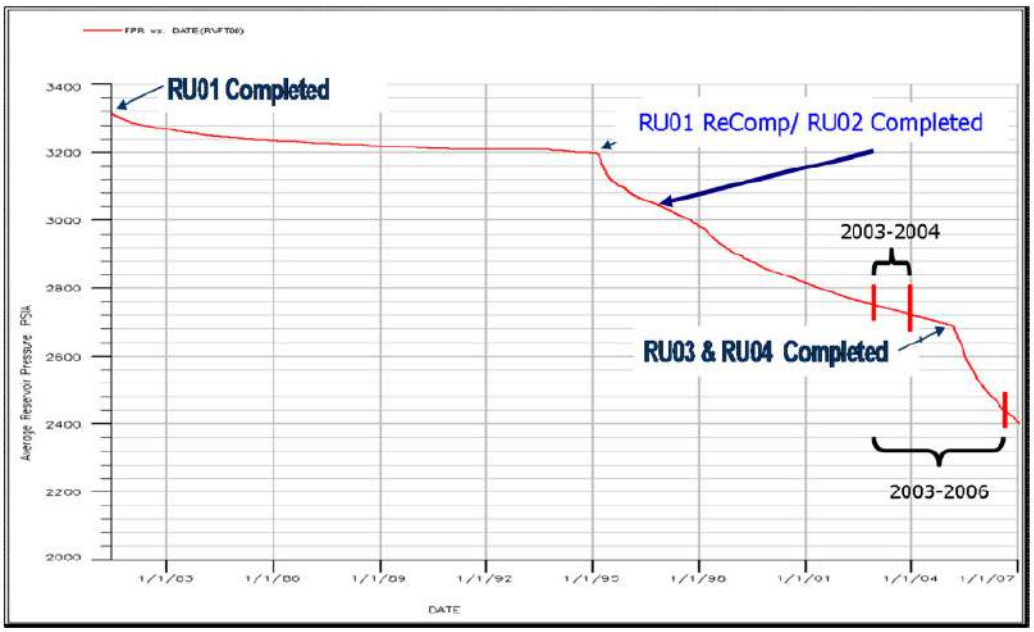

Figure 7.7: Chart highlighting average pressure within the production model with drilling events and time-lapse seismic surveys. The y-axis shows pressure in psia and the x-axis shows the date. Courtesy of Schlumberger DCS Denver (from Wikel, 2008).

These observations agree the time-lapse results considering only the 2003-2006 lapse using P- and S- wave data separately as shown on Figures 7.8 and 7.9. The displayed well (RU-7) depicts its shear-wave splitting log calculated from the cross-dipole sonic log in order to compare the high shear wave splitting (large deflection of the curve) associated with high fracture density related to time-lapse anomalies. It can be noticed that the time-lapse anomalies located within the UMVS-Cameo interval are fewer and more areal constrained to the well RU-7 compared to those time-lapse anomalies underlying the Cameo top, and there is a high correlation between the shear-wave splitting and the vertical location of the anomalies, which agrees the premise that higher crack density increases permeability, therefore it makes it easier to drain. Since all the wells are characterized by a commingled completion, is not possible to allocate production to each reservoir interval. However, cumulative production could provide some hints about the source of time-lapse anomalies. The well RU-7 was drilled during the 2004 campaign so it is a good candidate for time-lapse analysis using the 2003 and 2006 vintages since these two surveys may show time-lapse anomalies associated to the perturbation caused by this well, however, the cumulative production of this well can be considered modest (317 MMCF). This may lead to conclude that these outstanding anomalies are due to the fact that there is no uniform distribution of production from each interval within the UMVS-Cameo section, and the large anomalies underlying Cameo top can be the product of the drainage area interference of RU-7 and other nearby producing wells.

In order to determine how interpretable a time-lapse anomaly is, it was considered a time-lapse background noise level about +/- 6% (Meza, 2007b), which means that any time-lapse difference equal or lower than this threshold is going to be considered noise. Figure 7.10 shows the 2003-2006 time-lapse $\boldsymbol{V_P/V_S}$ (fast and slow) difference for the same section shown on Figures 7.8 and 7.9 considering the level of background noise in the colorbar, considering only the positive anomalies associated to time-lapse depletion. The first observation is that anomalies are more constrained laterally compared to the anomalies observed on $\boldsymbol{Z_P}$ and $\boldsymbol{Z_S}$ data on Figures 7.8 and 7.9 respectively, even those underlying Cameo top. Some of the anomalies are relative to the RU-7 well path, which support that some of those anomalies are caused by production from this well.

Both $\boldsymbol{Z_P}$ and $\boldsymbol{Z_S}$ cases showed more anomalies below Cameo top than in UMVS-Cameo interval, but in the case of $\boldsymbol{V_P/V_S}$ ratio the number of anomalies in both intervals could be comparable, at least in this section view. The first conclusion derived from this observation is that despite $\boldsymbol{Z_P}$ and/or $\boldsymbol{Z_S}$ are changing in a determined location, $\boldsymbol{V_P/V_S}$ does not. Changes of $\boldsymbol{Z_P}$ and $\boldsymbol{Z_S}$ occur in a effective stress window related to low reservoir pressure (high effective pressure) where despite of changes on $\boldsymbol{Z_P}$ and $\boldsymbol{Z_S}$ impedances, $\boldsymbol{V_P/V_S}$ is almost constant as seen on Figure 7.11. These results are shown on a previous section of this report (section 7.2). The time-lapse changes of $\boldsymbol{V_P/V_S}$ are caused by a change of pressure scenarios as follows:

- A reservoir interval (sand) depleted on the baseline vintage is recharged with gas when monitor vintage was acquired. Negative change of $\boldsymbol{Z_P}$, $\boldsymbol{Z_S}$ (fast and slow) and $\boldsymbol{V_P/V_S}$ (fast and slow).

- A sand at initial pressure/overpressure conditions at time of baseline survey has been partially depleted at monitor survey acquisition time. Positive change of $\boldsymbol{Z_P}$, $\boldsymbol{Z_S}$ (fast and slow) and $\boldsymbol{V_P/V_S}$ (fast and slow).

- A sand initially at overpressure conditions during baseline survey acquisition has not been depleted enough to be out of the overpressure window during monitor acquisition. Positive change of $\boldsymbol{Z_P}$, $\boldsymbol{Z_S}$ (fast and slow) and $\boldsymbol{V_P/V_S}$ (fast and slow).

These three scenarios are considered to be realistic due to overpressure and re-migration of gas from Cameo interval through the fracture network (Davis, 2006) as shown on Figure 7.12.

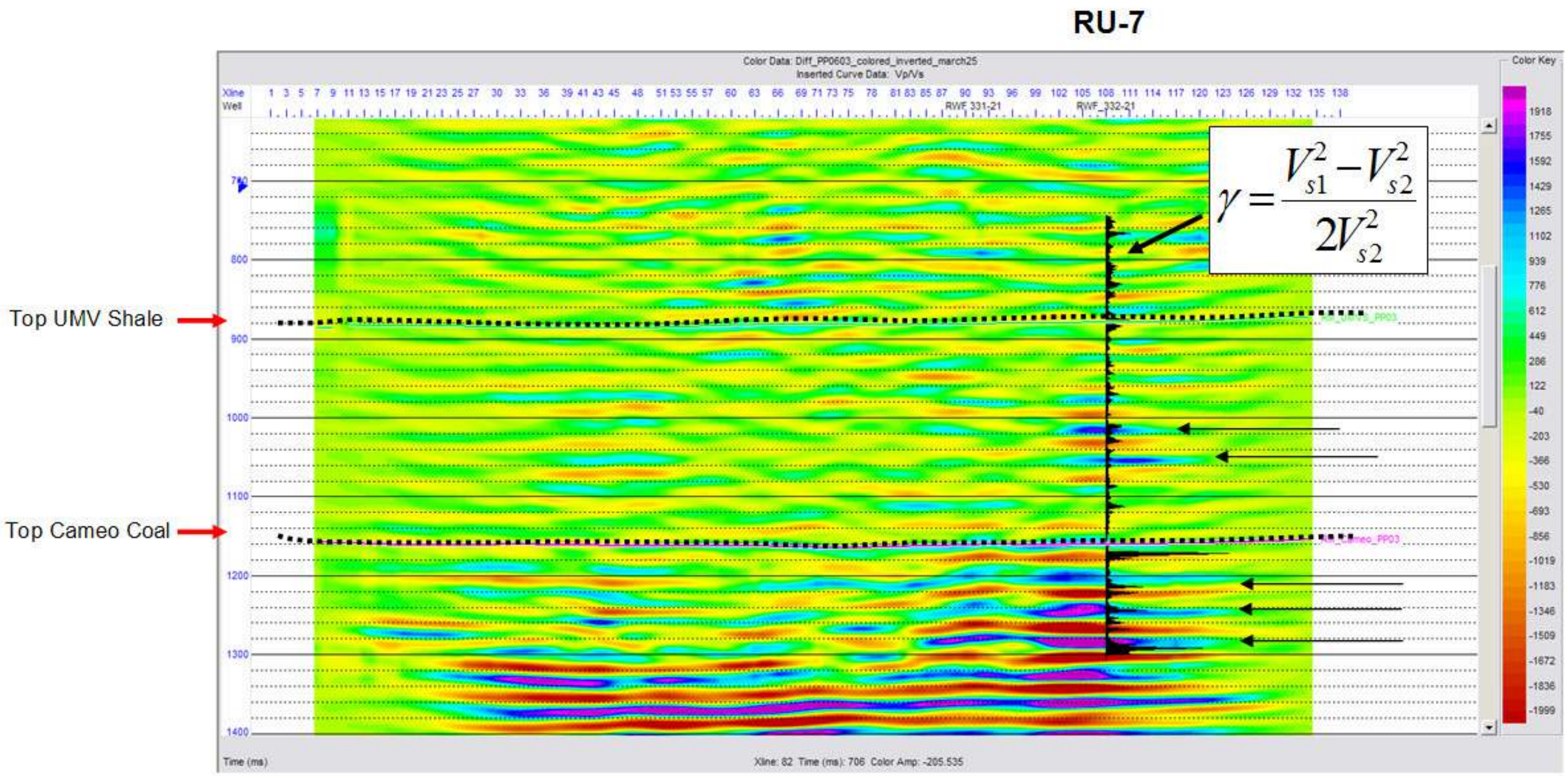

Figure 7.8: IL-19 P-impedance absolute difference 2003-2006 (from Meza, 2007a).

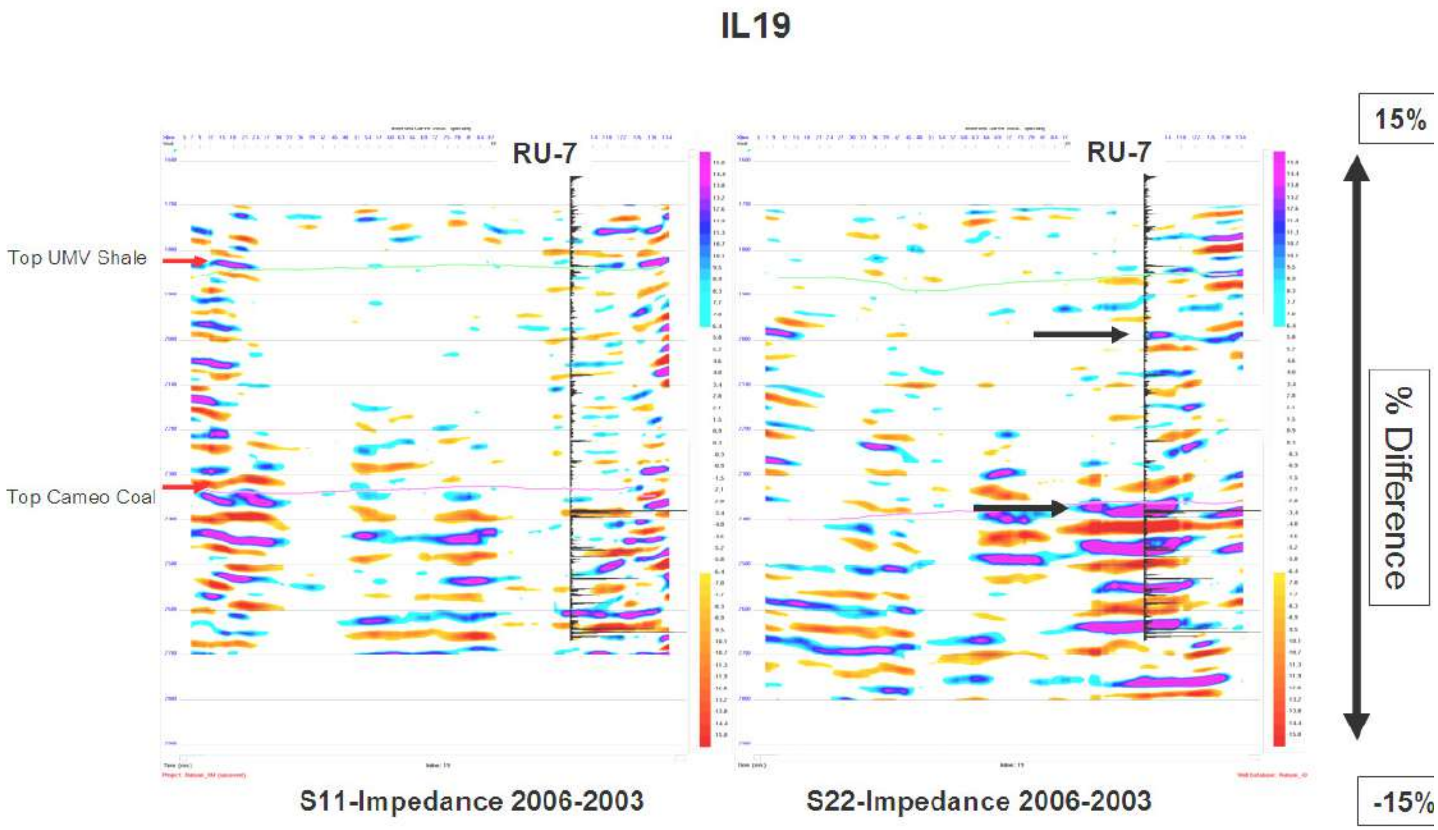

Figure 7.9: IL-19 S11-impedance relative (%) difference 2003-2006 for S11 (left) and S22 (right). (from Meza, 2007b)

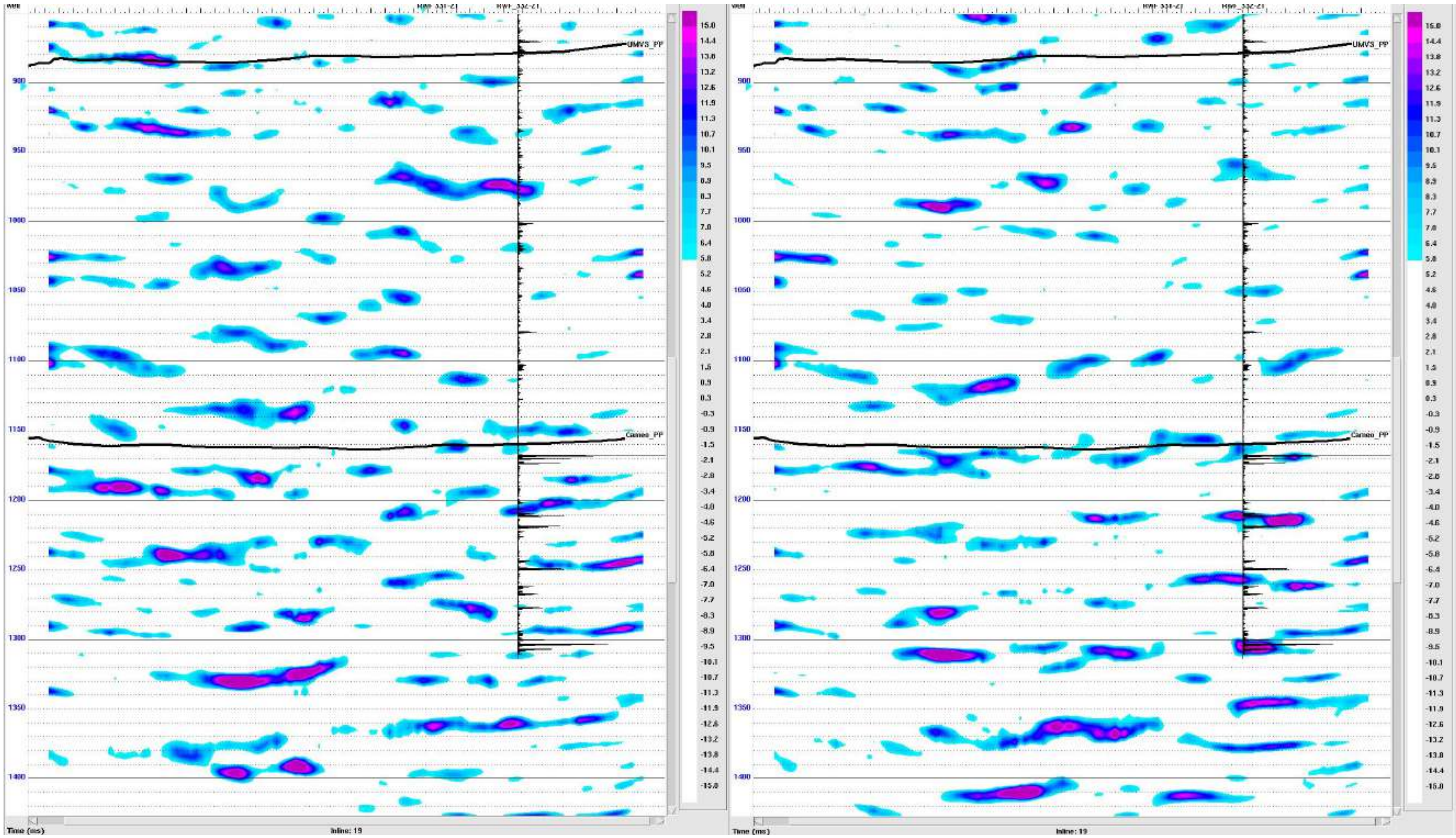

Figure 7.10: IL-19 V_P/V_S relative (%) difference 2003-2006 for fast mode (left) and slow mode (right).

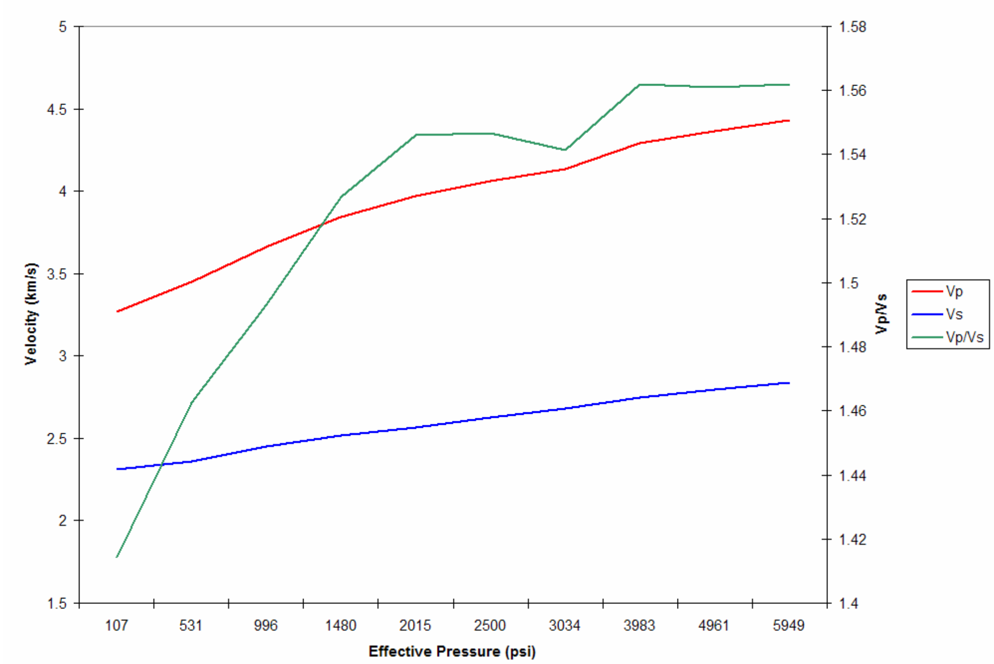

*Figure 7.11: Core lab ultrasonic measurements (Rojas, 2005) of **V_P**, **V_S** and **V_P/V_S** variation with effective pressure.*

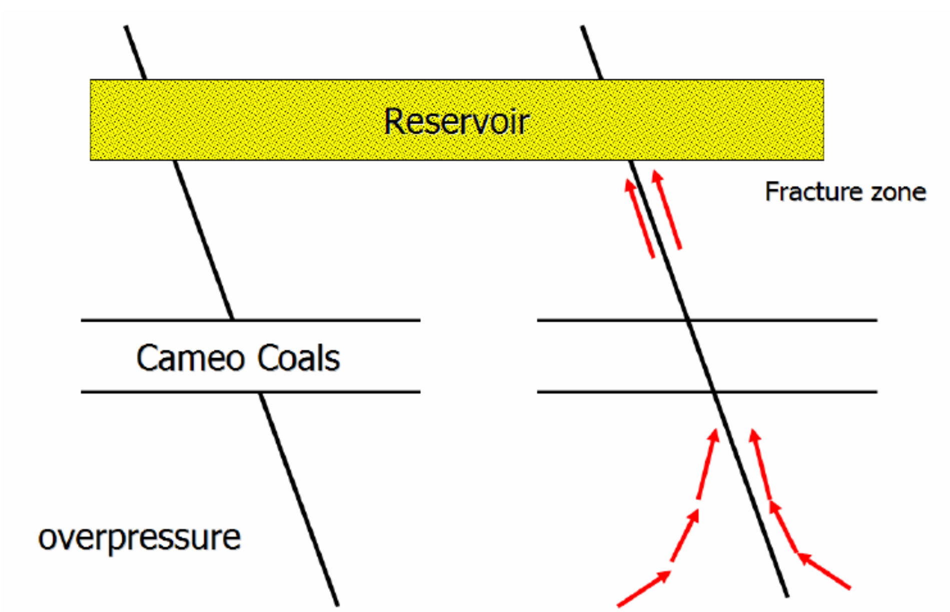

Figure 7.12: Gas remigration through the fault and fracture network (modified from Davis, 2006).

It must be noticed that $\boldsymbol{V_P/V_{S1}}$ shows time-lapse anomalies not present on $\boldsymbol{V_P/V_{S2}}$ according to Figure 7.10. This is indicative that certain fast-shear attributes (amplitude, impedance and/or $\boldsymbol{V_P/V_S}$) may be more time-lapse sensitive in some areas compared to others depending on the fracture orientation changes in the reservoir, or due to the presence of two or more interconnected fracture sets in the eastern area of the field (Vasconcelos et al, 2007). This is supported by Figures 7.13 and 7.14 that show map views of the maximum time-lapse change within the UMVS-Cameo interval for $\boldsymbol{V_P/V_S}$ fast and slow respectively. It can be seen that there almost no coincidence among the largest anomalies in both modes, and also is supported the observation about the lateral constraining of the anomalies to what may be drainage areas from producing wells.

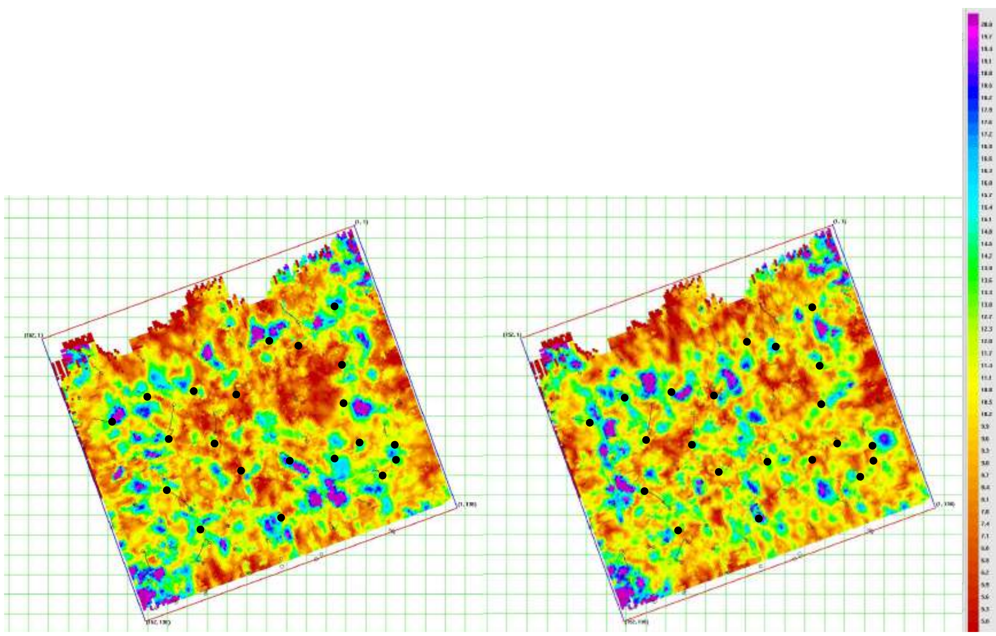

*Figure 7.13: Maximum time-lapse relative difference (2003-2006) map view within the UMVS-Cameo interval for **V_P/V_S**. Fast mode (left) and slow mode (right).*

Time-lapse data, especially the S22 2003 and 2006 vintages have shown to be consistent with the 3D geomechanical model being built in the area (Wikel, 2008) showing the pressure drop due to two (2) new wells drilled during the lapse. The well RU-4 is part of this 3D geomechanical modeling and is shown on the 2003-2006 relative differences for $\boldsymbol{V_P/V_S}$ in Figure 7.14. It can be appreciated that slow $\boldsymbol{V_P/V_S}$ shows more anomalies within the UMVS-Cameo interval than the fast mode, therefore, it is thought that fracturing in this area of the survey has one preferential direction (Vasconcelos, 2007), and both modes show anomalies below top Cameo, supporting the hypothesis of multiple set fracturing at these levels (Davis et al, 2007).

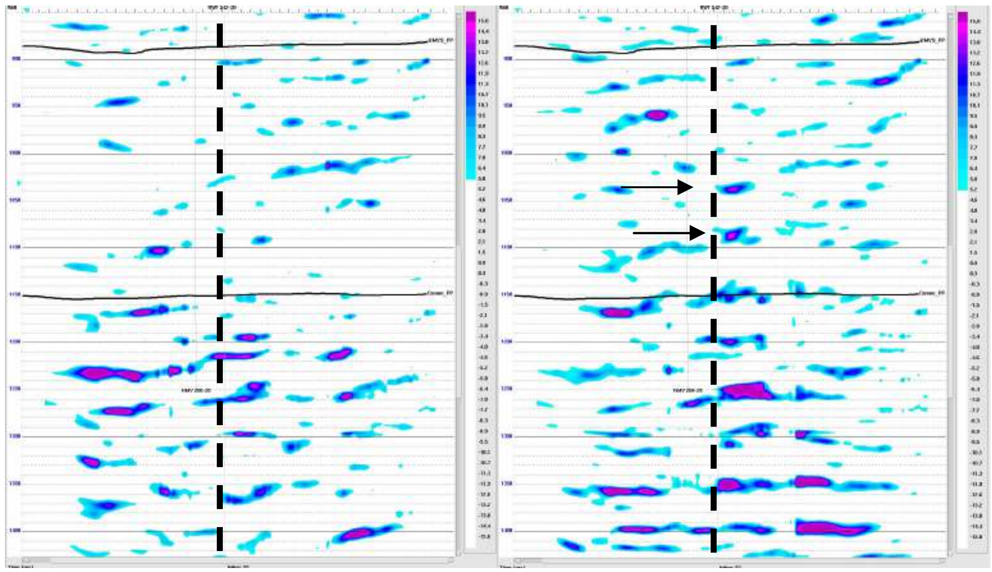

Figure 7.14: IL-93 V_P/V_S relative (%) difference 2003-2006 for fast mode (left) and slow mode (right). RU-4 is represented as a black dashed line.

Horizontal slices at arrow locations in Figure 7.14 are shown on Figure 7.15 and 7.16. Both anomalies are constrained to the south of the well RU-4. This might be indicative of a non-uniform hydraulic fracturing during RU-4 completion leading to a no-uniform growth of such fractures affecting the drainage pattern (Riley, 2007) or may be the product of intersecting drainage areas with well RU-1. In addition, it is interesting to notice on these images the several anomalies at those depth levels at different locations which may match the drained areas of some wells during 2003-2006.

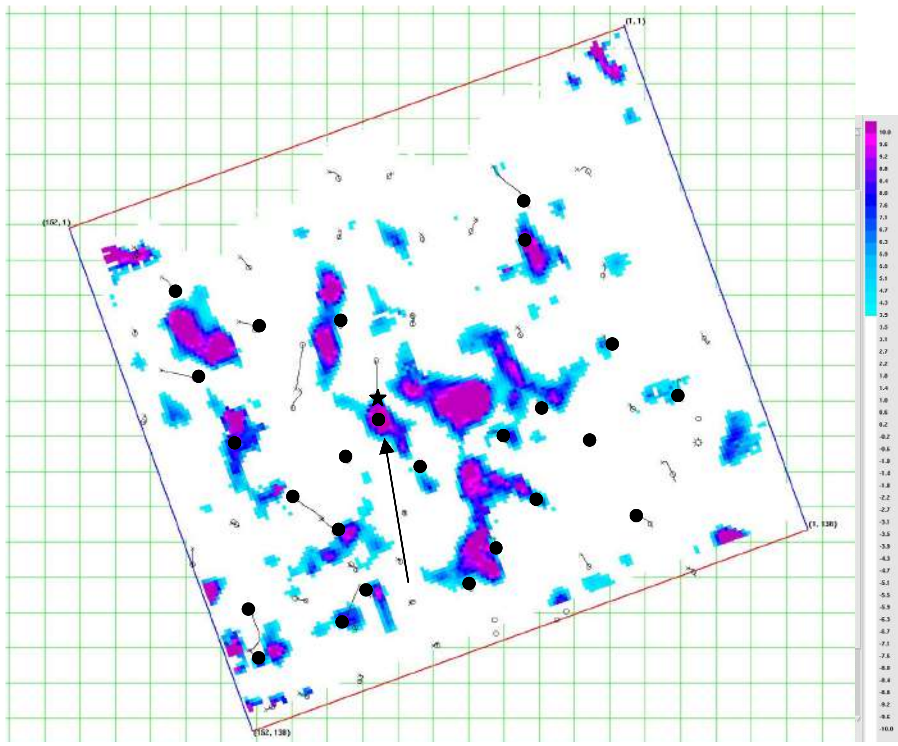

Figure 7.15: Depth slice @ 6200 ft showing extension of relative 2003-2006 V_P/V_{S2} anomalies. Well RU-4 represented as a black star.

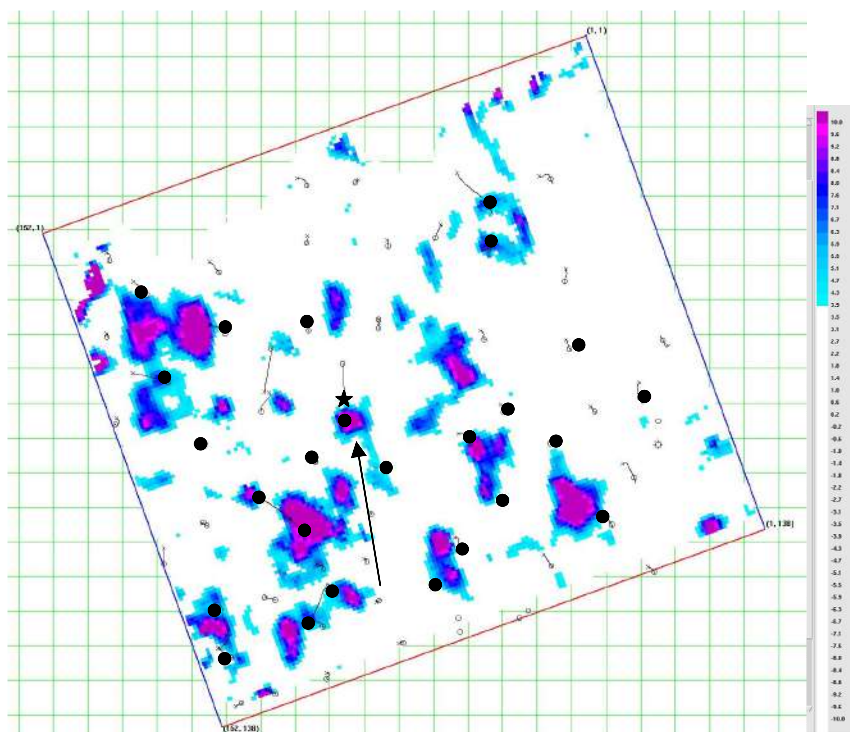

Figure 7.16: Depth slice @ 6500 ft showing extension of relative 2003-2006 V_P/V_{S2} anomalies. Well RU-4 represented as a black star.

Unlike V_P/V_S, time-lapse reservoir pressure changes from seismic cannot be properly imaged as seen on Figure 7.17. This may be a consequence of some of the pressure prediction shortcomings cited in section 7.2. Therefore; any quantitative appraisal of reservoir pressures based on these seismic data may be compromised.

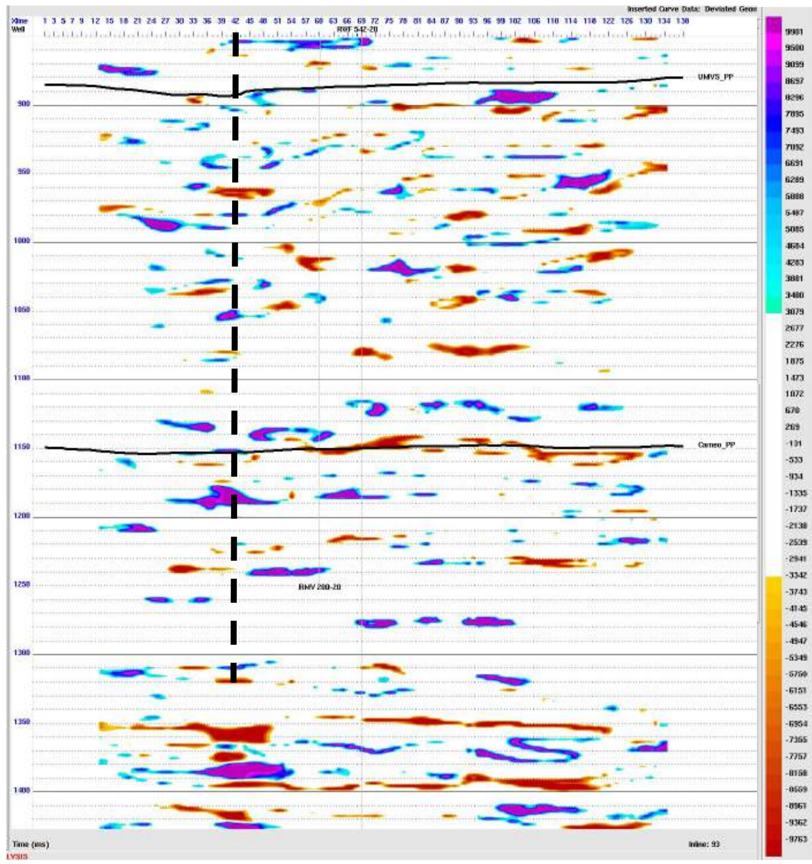

Figure 7.17: IL-93 Reservoir pressure absolute difference 2003-2006 for slow mode (right). RU-4 is represented as a black dashed line.

7.4 Classification of Time-lapse V_P/V_S anomalies

In the previous section it was shown that the magnitude and sign of the time-lapse V_P/V_S anomalies is not conclusive relative to pressure regime change that originated it. Based on V_P/V_S versus effective stress curve for Rulison field as shown in Figure 7.11, reservoir pressure volumes estimated from seismic may have some shortcomings that prevent us from determining the actual pressure regime of a certain interval. Figures 7.18 and 7.19 show the V_P/V_S versus effective pressure curve, this time showing the two (2) possible scenarios for time-lapse anomalies based on V_P/V_S data. Based on this premise I propose a classification scheme for these time-lapse anomalies, described as follows:

I proposed that a type I anomaly occurring on baseline and monitor surveys show effective pressure within the over-pressure window (effective pressure ranges from 0-2000 psi) as shown on Figure 7.18, being higher the reservoir pressure for the base survey (red dot).

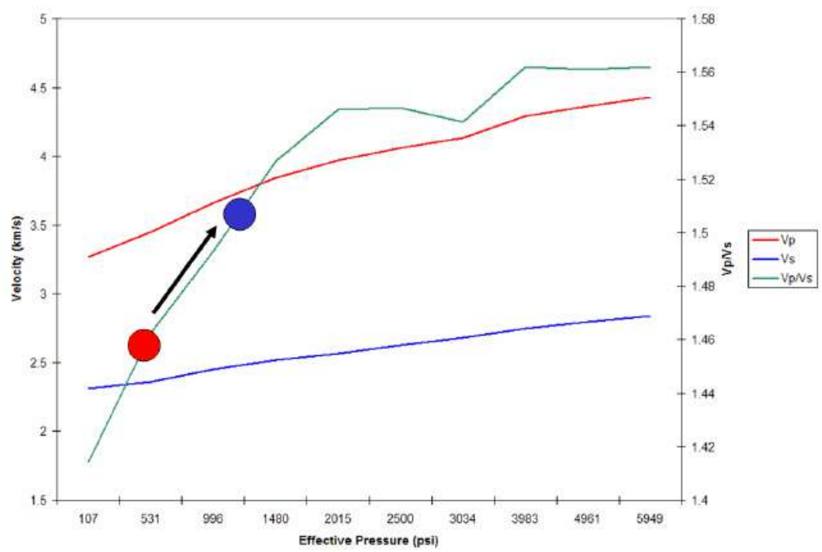

Figure 7.18: V_P/V_S versus effective stress showing depletion scenario for Type I time-lapse anomaly (red dot for base survey and blue dot for monitor survey).

Type II anomaly occurs in case the initial stage is within the over-pressure window (red dot) and the monitor stage is within the depleted window (blue dot). Both cases consider depletion, which is translated to positive time-lapse anomalies. In case of recharging or pressuring of the reservoir, the anomalies can be classified in the same way but considering only the negative ones.

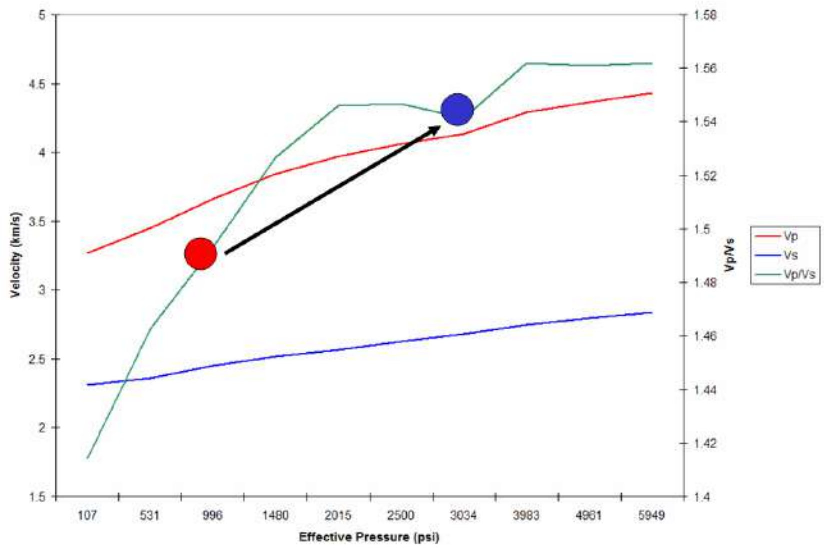

*Figure 7.19: **V_P/V_S** versus effective stress showing depletion scenario for Type II time-lapse anomaly (red dot for base survey and blue dot for monitor survey).*

Following the same fashion used for anomalies classification used on classical AVO analysis (Castagna and Swan, 1997), I propose the use of cross-plots of monitor versus baseline ***V_P/V_S*** in order to highlight the anomalies in the seismic sections according to the proposed classification. These anomalies can be interpreted in the cross-plot as shown on Figure 7.20, considering the type I and II anomalies for depletion and recharging scenarios.

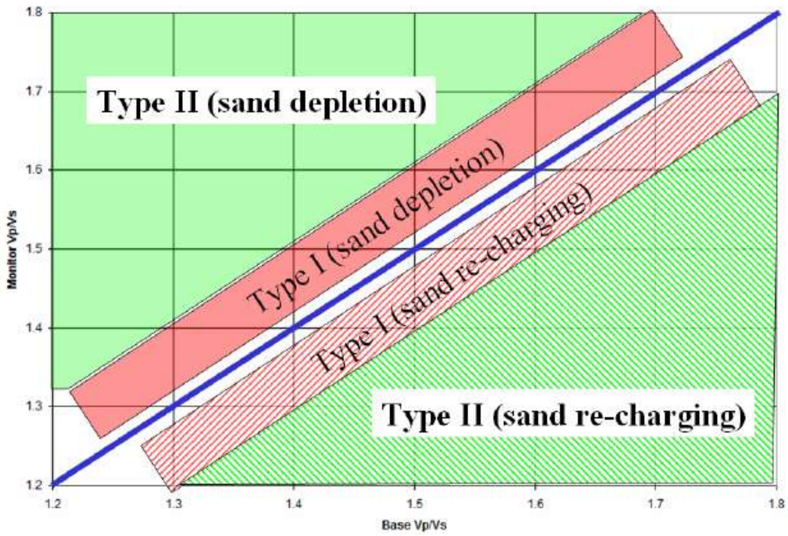

Figure 7.20. Scheme for cross-plotting of monitor versus baseline survey V_P/V_S. Type I (red) and Type II yellow) anomalies for depletion case in solid colors, and re-charging case in dashed-pattern. Background trend (no V_P/V_S anomalies) represented by the blue line.

Once a similar scheme is applied in the real data cross-plot, the V_P/V_S anomalies can be highlighted in the vertical sections in order to identify them according to the types previously defined. The corresponding results of the classification scheme can be seen on Figures 7.21-7.23. Type I anomalies are highlighted in red and type II anomalies in green. In case of Figure 7.21, the well RU-7 (dashed vertical line) has several anomalies close to it, but the upper reservoir anomalies are type I, which means that they have not been depleted enough to abandon the "over-pressure" regime, while the anomaly located at the final depth of the well is type II, which means that that level has been considerably depleted. It also can be appreciated in all figures that there are cases of lateral change of classification within an anomaly, which may lead to consider re-completions at those intervals or even new wells due to potential bypassed high-pressure zones. This analysis is subject to the cross-plotting and filtering performed in the monitor-base V_P/V_S domain which was difficult, so some anomalies could not have been classified, so future efforts may be needed to improve the utility of this tool.

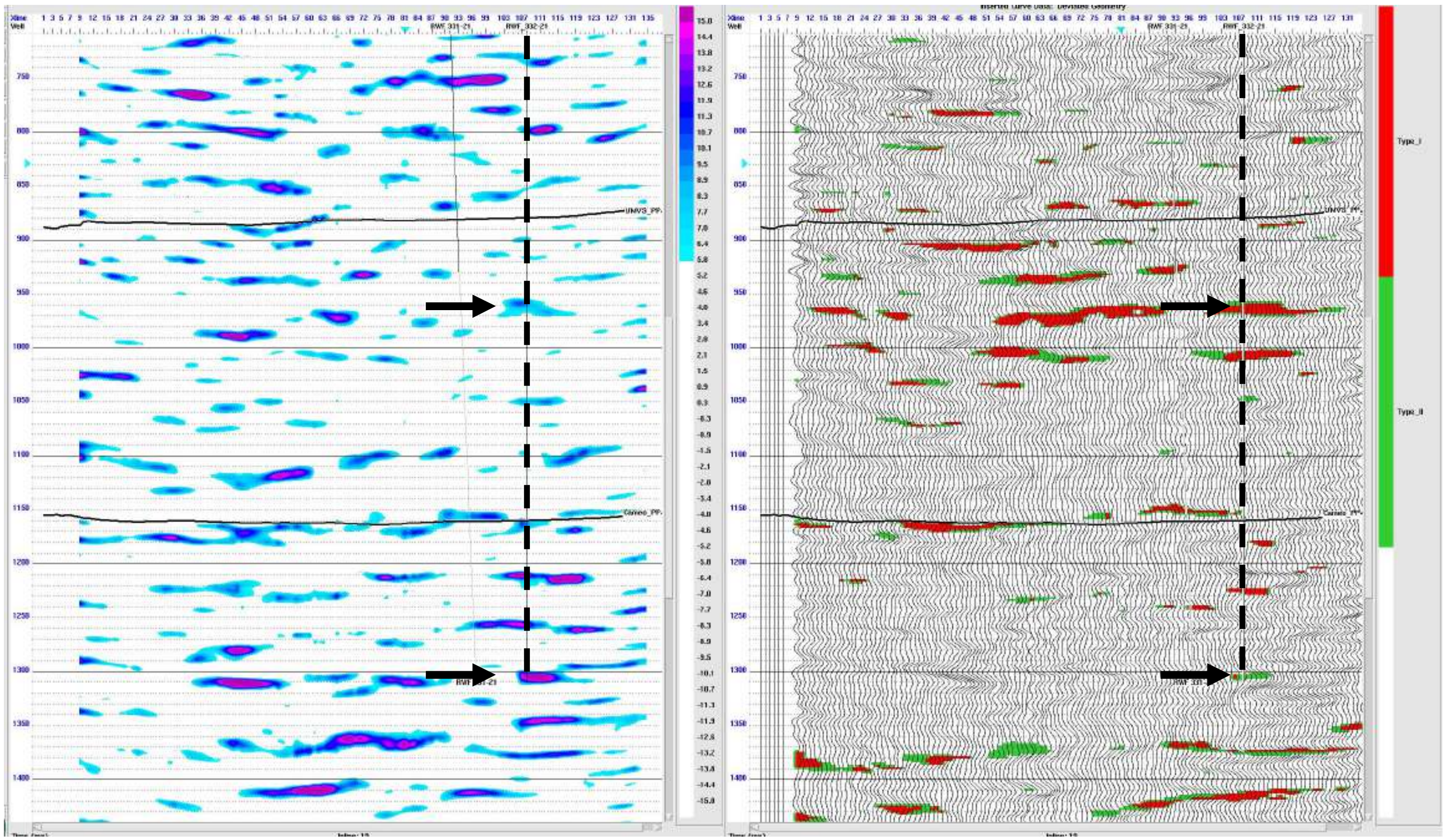

Figure 7.21. IL-19 showing $\mathbf{V_P/V_{S2}}$ *2003-2006 time lapse relative (%) anomalies (left), and classification (right). Type I (red) and Type II (green).*

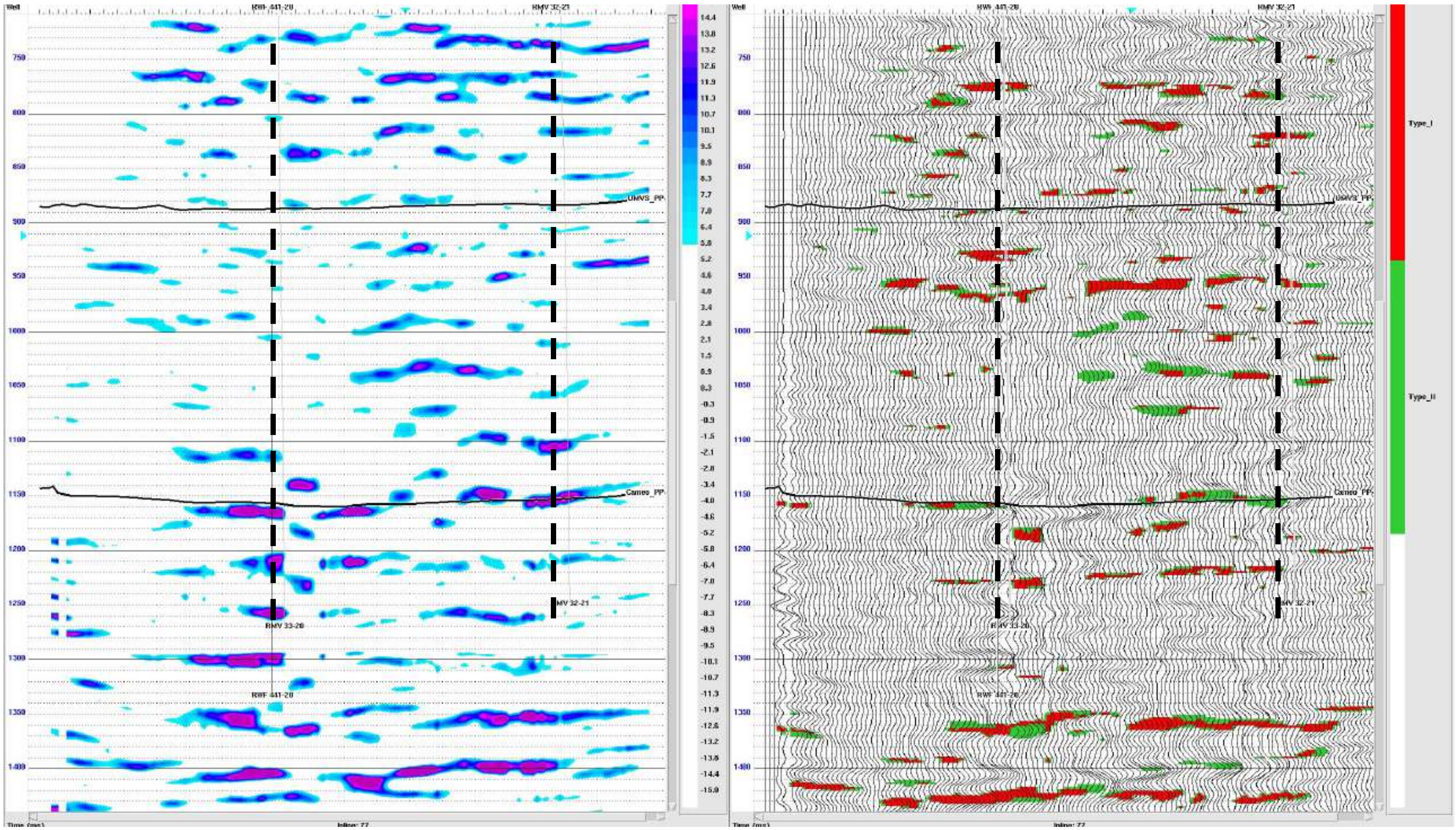

Figure 7.22. IL-77 showing V_P/V_{S2} 2003-2006 time lapse relative (%) anomalies (left), and classification (right). Type I (red) and Type II (green).

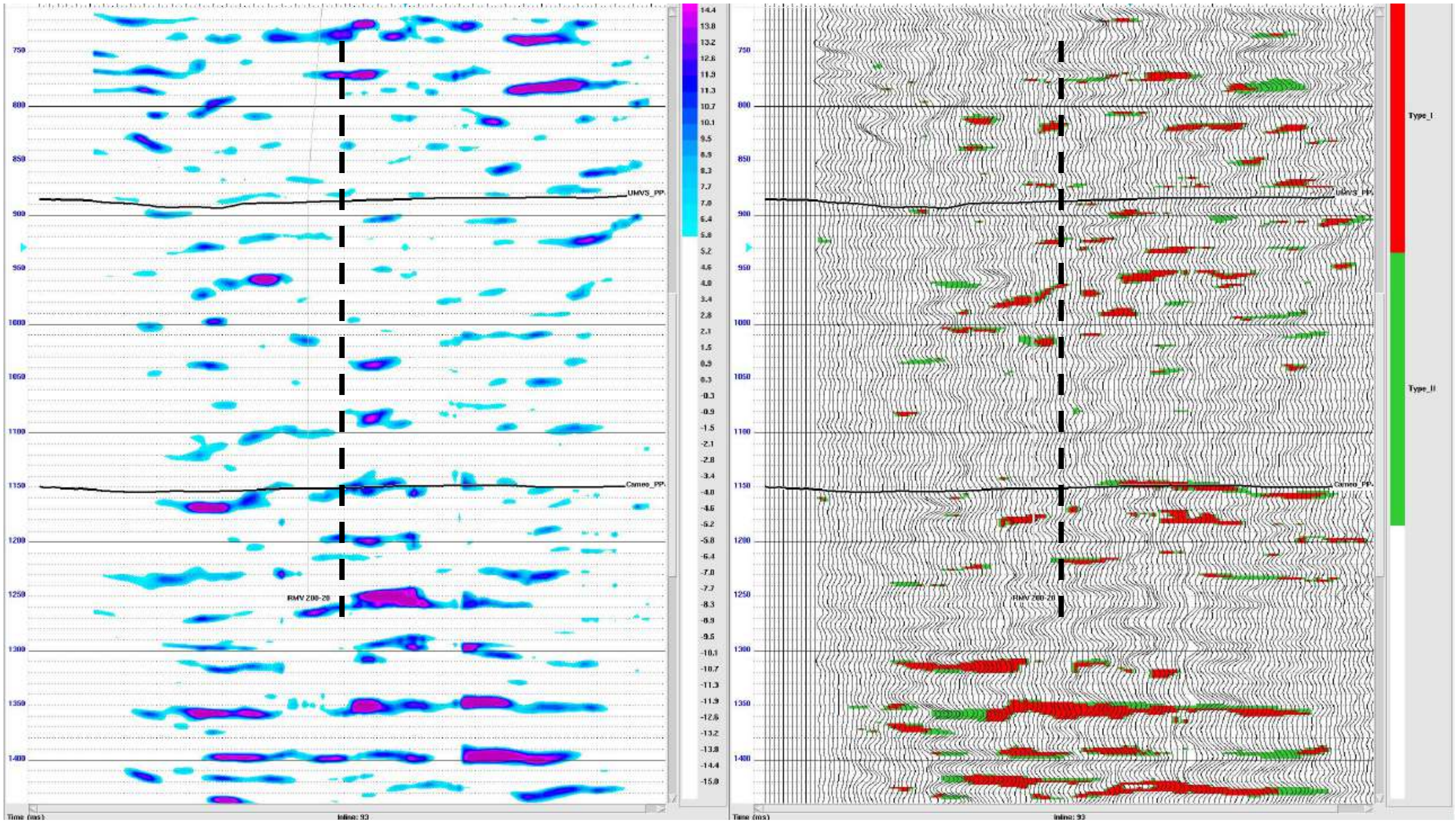

Figure 7.23. IL-93 showing V_P/V_{S2} 2003-2006 time lapse relative (%) anomalies (left), and classification (right). Type I (red) and Type II (green).

7.5 Lithology description using impedance-filtered V_P/V_S

As stated in Chapter 3 according to RU-7 well log data, cross-plots of $\boldsymbol{Z_P}$ vs $\boldsymbol{Z_{S\ 1/2}}$ using a discriminator color code like shale volume may help improve lithology discrimination. I evaluated this possibility by using the 2006 volumes considering that a seismic survey that imaged a subsurface containing less gas may help reduce the ambiguity of the $\boldsymbol{V_P/V_S}$ dependence on lithology, fluids and pressure.

I applied the filter in the $\boldsymbol{Z_P}$ vs $\boldsymbol{Z_{S1}}$ cross-plot to the $\boldsymbol{Z_P}$ and $\boldsymbol{Z_{S1}}$ 2006 data in order to obtain displays of impedance-filtered $\boldsymbol{V_P/V_S}$ as shown on Figures 7.24 and 7.25. Both figures show the regular $\boldsymbol{V_P/V_{S1}}$ volume color-coded with low values (< 1.76) in the left side, and the impedance-filtered $\boldsymbol{V_P/V_S}$ is shown in the right side with the potential “sands” highlighted in red. The first thing to notice is that the filtered $\boldsymbol{V_P/V_S}$ image is more conservative for sands than regular $\boldsymbol{V_P/V_S}$ as expected. Second, there is an overall good match with the major sand trends shown on GR logs. This overall appearance confirms the general vertical stratigraphy in the area, where more blocky and continuous sands are found in the upper reservoir, becoming thinner and isolated at the bottom (Cumella and Ostby, 2003).

The impedance-filtered $\boldsymbol{V_P/V_S}$ shows the spatial distribution of sands at 0-60 Hz bandwidth, so details seen on GR logs cannot be interpreted on $\boldsymbol{V_P/V_S}$. However, this attribute can play a main role in a geo-statistical model in terms of constraining the probabilistic lithology distribution based on well-logs alone. These results may be improved by a better choice of the filter in the $\boldsymbol{Z_P}$ - $\boldsymbol{Z_{S1}}$ space and/or using more sophisticated visualization and multi-attribute analysis tools leading to the construction of geobodies.

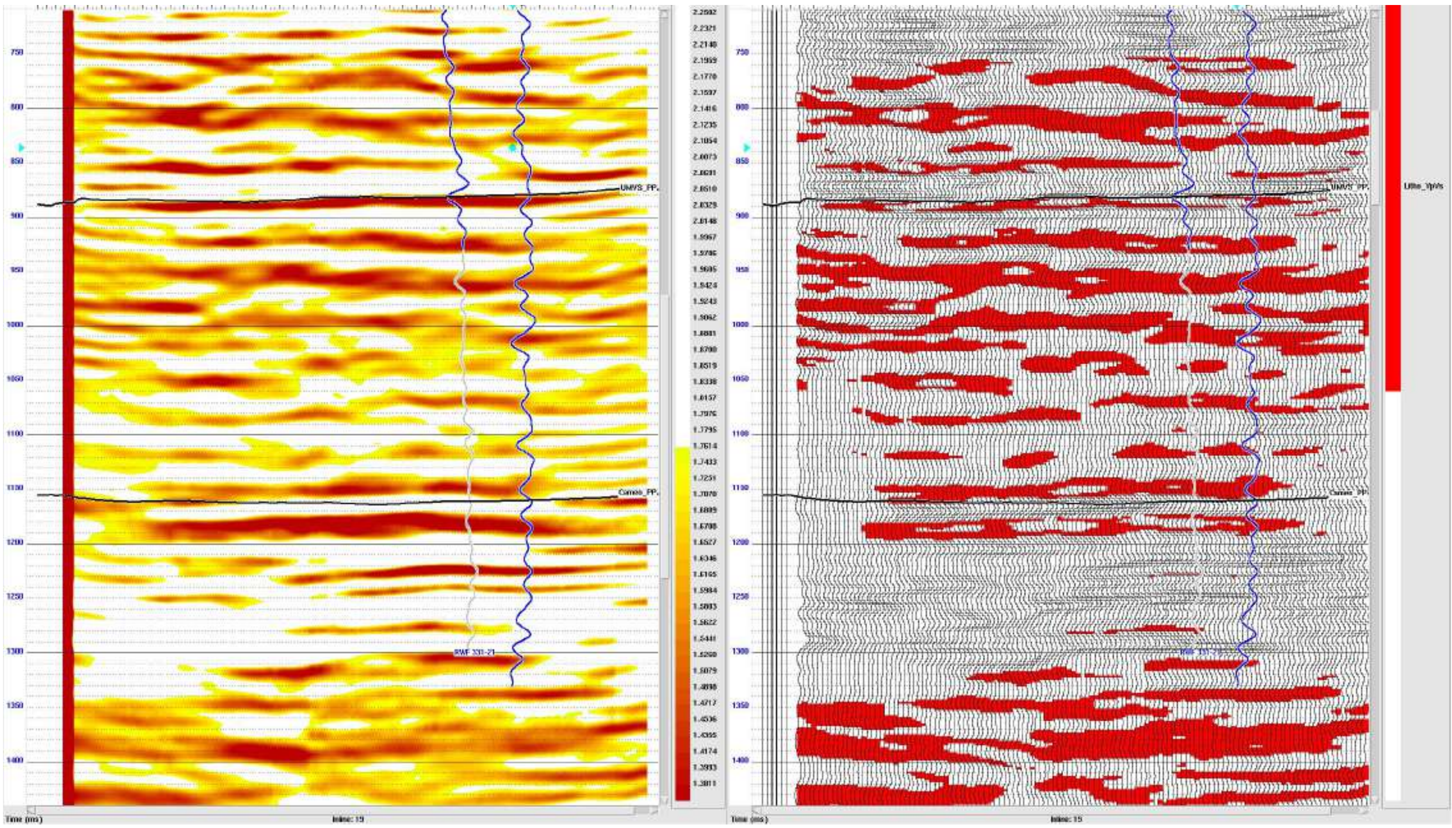

*Figure 7.24: IL-19 Low **V_P/V_{S1}** 2006 values only (left) and Impedance-filtered **V_P/V_{S1}** 2006 (right).*

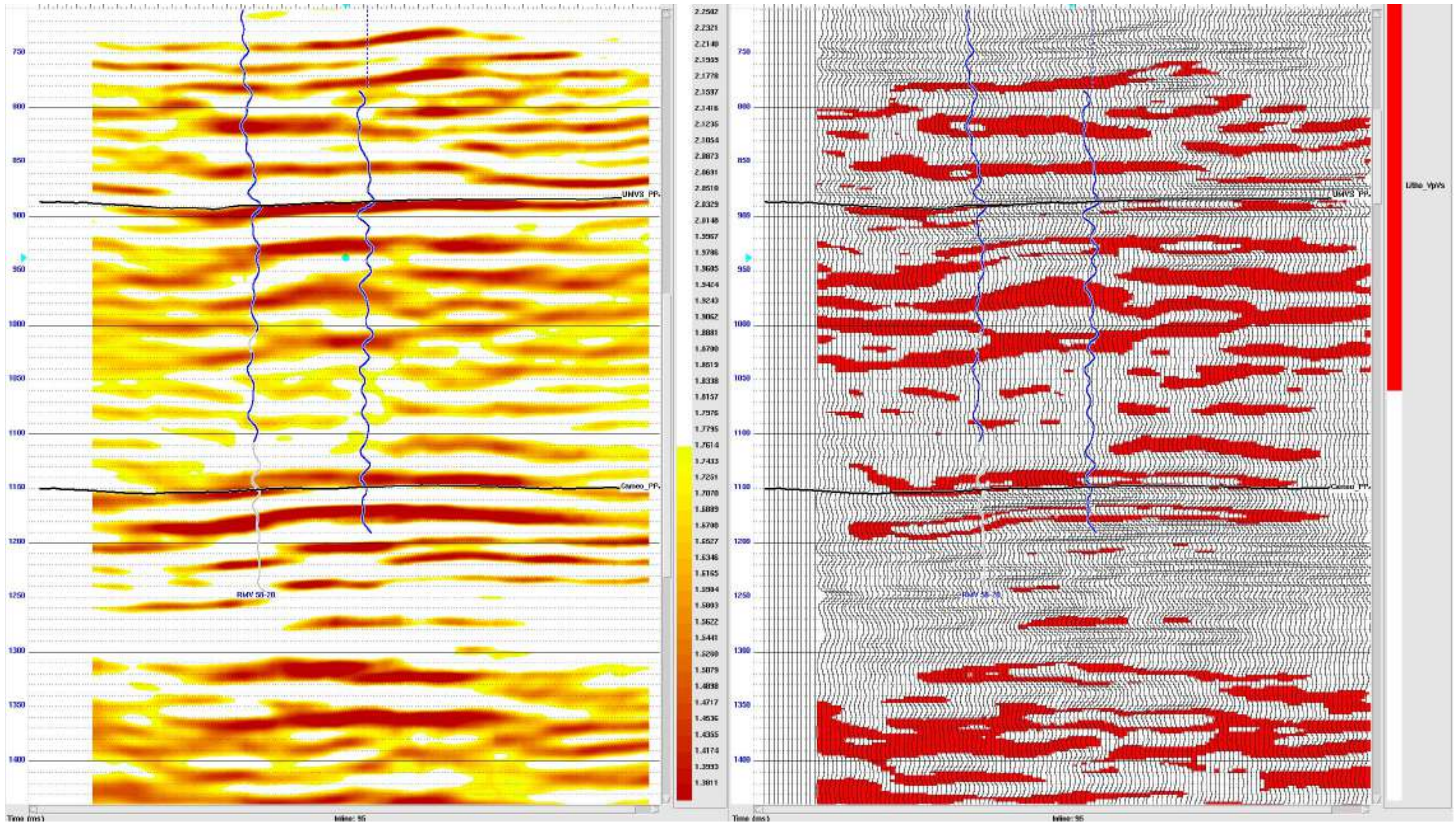

Figure 7.25: IL-95 Low $\mathbf{V_P/V_{S1}}$ 2006 values only (left) and Impedance-filtered $\mathbf{V_P/V_{S1}}$ 2006 (right).

CHAPTER 8
CONCLUSIONS AND RECOMMENDATIONS

8.1 Conclusions

From the analysis of the results I conclude that:

- $\boldsymbol{V_P/V_S}$ ratio is a powerful time-lapse tool for tight-gas sandstone reservoirs. Enhanced imaging of time-lapse $\boldsymbol{V_P/V_S}$ anomalies relate to drainage patterns of producing wells. Both $\boldsymbol{V_P/V_S}$ modes (fast and slow) need to be taken into account due to changes in the preferential orientation of fracture sets.

- These time-lapse anomalies are not centered in the related producing wells, so this observation may lead to consider either complex hydraulic fracturing or interference with a nearby well at the same interval, or stratigraphic control on production.

- Reservoir pressure prediction works when predicting absolute reservoir pressure in those intervals characterized by low effective pressure (high reservoir pressure). The method fails to predict absolute reservoir pressure in cases of considerable depletion. These observations are consistent with the $\boldsymbol{V_P/V_S}$ behavior observed in core lab measurements (Rojas, 2005).

- A classification scheme for $\boldsymbol{V_P/V_S}$ time-lapse anomalies is necessary to determine the actual pressure regime (depleted, or still in over-pressure). Type I anomalies represent sweet spots to be considered for future development.

- Lithology prediction is improved by using the impedance-filtered $\boldsymbol{V_P/V_S}$ for sands in the UMVS-Cameo interval.

8.2 Recommendations

This project demonstrated the feasibility of using V_P/V_S as a tool for dynamic and static reservoir characterization. Some enhancements can be implemented to improve the accuracy of this tool:

- Use of 4D-9C VSP in order to determine a V_P/V_S -Pe mapping function at seismic bandwidth that can be coupled with pressure tests in the same well location. This would allow obtaining anisotropic mapping functions. 4D well-logging also might be an option to be considered for control of the velocity changes in time-lapse depending on the presence of well casing.

- Biot's constant as a function of space location might help since it would consider the variability of porosity throughout the space.

- Implement the impedance-filtered V_P/V_S by using visualization and multi-attribute analysis tools as well, in addition to better "flag" logs, also considering the case of coals that need to be characterized using this method.

- Perform pre-stack simultaneous inversion of P-wave seismic data in order to obtain P- and S- wave impedances and determine V_P/V_S. This may allow comparison of results and determine the feasibility of this kind of analysis based on 4D-9C datasets, especially considering unconventional reservoirs.

- Improve the classification scheme I proposed here by performing more accurate cross-plotting and filtering, also considering the use of visualization and multi-attribute analysis tools.

- Pressure prediction might be also improved by performing the lithology discrimination on V_P/V_S volumes before any pressure estimation based on seismic.

- Different forms of V_P/V_S can feed different models in the reservoir. For example V_P/V_S converted on Poisson's ratio (σ) volume, in addition to time-lapse anomalies (classified or un-classified) and pressure volumes can improve substantially the 3D geo-mechanical model. Geostatistical models may be constrained by the impedance-filtered V_P/V_S, and the reservoir simulation, especially the history matching, can be constrained by the time-lapse anomalies in order to allocate production.

REFERENCES

- Aki, K. and P. Richards, 2002. Quantitative Seismology. 2nd ed.
- Amundsen, L. and M. Landrø, 2007a. 4D Seismic: Status and Future challenges, Part I: Status. GEOExPro Vol. 4, No. 5. October 2007.
- Amundsen, L. and M. Landrø, 2007b. 4D Seismic: Status and Future challenges, Part II: Challenges. GEOExPro Vol. 4, No. 6. December 2007.
- Bakulin, A., Grechka, V. and I. Tsvankin, 2000. Estimation of fracture parameters from reflection seismic data-part I: HTI model due to a single fracture set. Geophysics Vol. 65 No. 6. November-December 2000.
- Casey, M. and T. Davis, 2007. Time-lapse shear-wave splitting: monitoring hydraulic fracturing of a tight gas reservoir. SEG San Antonio Annual meeting expanded abstracts.
- Castagna, J. and H. Swan, 1997. Principles of AVO crossplotting. The Leading Edge, April.
- Chopra, S. and A. Huffman, 2006. Velocity determination for pore-pressure prediction. The leading edge. December 2006.
- Cluff, R. and K. Graff, 2003. Production history plots for Piceance Basin oil and gas fields. RMAG 2003 Piceance Basin guidebook, 2003.
- Cumella, S. and D. Ostby, 2003. Geology of the basin-centered gas accumulation, Piceance basin, Colorado. RMAG 2003 Piceance Basin guidebook, 2003.
- Davis, T., 2006. Multicomponent 4-D seismic reservoir characterization of tight gas sands, Rulison Field, Colorado. SEG 2006 meeting expanded abstracts.
- Davis, T., Benson, R., Ansorger, C. and S. Roche, 2007. Coal bed methane seismic monitoring, Rulison field, Colorado. SEG 2007 meeting expanded abstracts.
- Dewar, J., 2001. Rock Physics for the rest of us - an informal discussion. CSEG Recorder. May 2001.

- Dutta, N., Mukerji, T., Prasad, M. and J. Dvorkin, 2002. Seismic detection and estimation of overpressures part II: field applications. CSEG Recorder, September 2002.
- Eastwood, R. and J. Castagna, 1986. Interpretation of Vp/Vs ratios from sonic logs, in Shear-wave exploration, SEG Geophysical developments series.
- Garotta, R., 1985. Observation of shear waves and correlation with P events, in handbook of geophysical exploration, vol 15B: Seismic shear waves applications.
- Grechka, V. and M. Kachanov, 2006a. Seismic characterization of multiple fracture sets: Does orthotropy suffice? Geophysics, Vol. 71 No. 3. May-June 2006 (a).
- Grechka, V. and M. Kachanov, 2006b. Effective elasticity of fractured rocks: a snapshot of the work in progress. Geophysics, Vol. 71 No. 6. November-December 2006 (b).
- Guliyev, E., 2007, M.S., Vp/Vs estimation from multicomponent seismic data for improved characterization of a tight sandstone gas reservoir, Rulison Field, Colorado.
- Hardage, B. and I. Aluka, 2006. Elastic wavefield seismic stratigraphy. AAPG Search and Discovery, # 40183.
- Hoffmann, R., Xu, X., Batzle, M., Prasad, M., Furre, A. and A. Pillitteri, 2005. Effective pressure or what is the effect of pressure?. The leading edge. December 2005.
- Keighley, D., 2006, M.S, P-wave time-lapse seismic data interpretation at Rulison field, Piceance Basin, Colorado.
- Kragh, E. and P. Christie, 2002. Seismic repeatability, normalized rms, and predictability. SEG The Leading Edge July 2002.
- Lines, L. and R. Newrick, 2004. Fundamentals of Geophysical Interpretation. SEG geophysical monograph series.
- Matesic, M., 2007. Structural and stratigraphic controls on Mesaverde reservoir performance: Rulison field, Garfield County, Colorado: M.S. thesis, Colorado School of Mines. 2007.

- Meza, R., 2007a. Time-lapse Vp/Vs analysis for reservoir characterization, Rulison field, Colorado. RCP Spring 2007 sponsors meeting booklet.
- Meza, R., 2007b. Time-lapse Vp/Vs analysis for reservoir characterization, Rulison field, Colorado. RCP Fall 2007 sponsors meeting booklet.
- Mukerji, T., Dutta, N., Prasad, M. and J. Dvorkin, 2002. Seismic detection and estimation of overpressures part I: the rock physics basis. CSEG Recorder, September 2002.
- Pendrel, J., 2006. Seismic inversion- still the best tool for reservoir characterization. CSEG Recorder January 2006.
- Riley, R., 2007. Micro-macro seismic: enhanced fracturing through integration, Rulison field, Colorado. MS thesis.
- Rojas, E., 2005, M.S., Elastic rock properties of tight gas sandstones for reservoir characterization at Rulison Field, Colorado.
- Roth, M., 2006. Practical Interpretation of multi-component seismic data. CSEG Recorder, May 2006.
- Rumon, M., 2006, M.S., Shearwave time-lapse monitoring of a tight gas reservoir, Rulison Field, Colorado.
- Sayers, C., Den Boer, L., Nagy, Z. and P. Hooyman, 2006. Well-constrained seismic estimation of pore pressure with uncertainty. The leading edge. December 2006.
- Schoenberg, M. and C. Sayers, 1995. Seismic anisotropy of fractured rock. Geophysics, Vol. 60, No. 1. January-February 1995.
- Sheriff, R. 2002. Encyclopedic dictionary of applied geophysics. SEG geophysical references series 13, 4th edition.
- Tatham, R., 1985. Shear waves and lithology, in handbook of geophysical exploration, vol 15B: Seismic shear waves applications.
- Tsvankin, I, 1997. Anisotropic parameters and P-wave velocity for orthorhombic media. Geophysics Vol. 62, No. 4, July-August 1997.
- Vasconcelos, I. and V. Grechka, 2007. Seismic characterization of multiple fracture sets at Rulison field, Colorado. Geophysics, Vol. 72, No. 2. March-April 2007.

- Widess, M., 1973. How thin is a thin bed? Geophysics, Vol. 38, No. 6. December.
- Wikel, K., 2008. 3D geomechanical modeling of a tight gas reservoir, Rulison field, Piceance basin, Colorado. MS thesis.